On light at the nanoscale:

Plasmonic resonances and plasmon-emitter coupling

A. Cuartero-González

Departamento de Física Teórica de la Materia Condensada
Universidad Autónoma de Madrid

Universidad Autónoma de Madrid

Departamento de Física Teórica de la Materia Condensada

Condensed Matter Physics Center (IFIMAC)

ON LIGHT AT THE NANOSCALE

Plasmonic resonances and plasmon-exciton coupling

Álvaro Cuartero González

Dissertation submitted in partial fulfillment of the
requirements for the degree of Doctor of Philosophy

Supervised by:

Antonio Isaac Fernández Domínguez

Madrid, June 2021

Sigamos por esa senda
a ver qué luz encontramos,
esa luz que está en la tierra
y que nosotros apagamos.[1]

---

[1] Todo es de color. Lole y Manuel

Prefacio

A las decenas de páginas que contienen la cristalización del trabajo de casi un lustro es costumbre añadir una sección al margen de los detalles técnicos y académicos. Suele ser este un texto breve, como compendio del tránsito emocional que ha envuelto las derivaciones, los análisis, las figuras y los *papers*.

A mi director de tesis, Antonio Fernández Domínguez, no le hago justicia escriba cinco líneas o veinte folios. Creo que el vínculo ha superado lo profesional, probablemente debido a la confianza que depositó al permitirme trabajar mano a mano junto a él durante todos estos años y donde cada uno de nosotros ha intentado enseñar y aprender *el oficio*, respectivamente. Espero haber estado a la altura mínima exigida en este camino, continuación de una saga con varios siglos de andadura. Asimismo, quiero recordar y agradecer al prof. Guillermo Acuña, por tantas discusiones en torno a la nanofotónica, que nunca ha dejado de ofrecernos su ayuda, desde Braunschweig o Fribourg, y cuyos proyectos experimentales fueron parte fundamental de mi trabajo sobre todo al inicio de la tesis.

It is true and essential to acknowledge the members of the jury, who kindly accepted our request to evaluate this thesis. Thanks to Roberto Otero, Johannes Feist, Angela Demetriadou, Miguel Navarro-Cía, Ana Asenjo-García, José Antonio Sánchez-Gil and Carlos González-Ballestero for your time and your willingness to attend the defense.

Paso ahora a mis compañeros, los pasados y los presentes, quién sabe si los habrá futuros en el tiempo corto que me quede en el 301. Del primer día recuerdo el pasillo escondido y el aspecto que presentaba la que iba a ser mi mesa, porque toda mesa por ocupar tiene un halo de ruina, con par de folios viejos como sello para un lugar que tuvo vida y viene a ser repoblado. Gracias desde la más estricta verticalidad a Carlos, Javier (dP) y Javi (G), que me enseñaron las urdimbres subterráneas del mundo académico, de los que intenté aprender lo indecible y que siempre han estado ahí. Todos los días al mediodía, Rubén, Víctor y Sergio daban al comedor un aspecto de patio de Monipodio, lleno de lenguas afiladas y anécdotas alegales. ¡Poca paz para tanta guerra! No puedo dejar de recordar aquí al conjunto de biólogos moleculares, Predes, Antonio y Filip, que hicieron tambalearse nuestras pocas nociones del concepto emergencia en esa magia negra que esconde la auto-replicación del ADN. Me hago cargo de mi parte en las veces que nuestro escándalo de voces rompió vuestro ritmo de trabajo, sobre todo el de nuestras compañeras de almuerzo, las siempre cañeras Ana, Elena, Silvia y Rocío. Of course, I cannot forget the stay of Dr. Rui-Qi Li in our office.

El paso de los años dio pie a la marcha de casi toda la vieja guardia, prácticamente al mismo tiempo que mudé mis bártulos por seis meses a las llanuras polvorientas al costado del río Grande. Al prof. Alejandro Manjavacas, muchas gracias por el trato personal y profesional que me brindó desde el instante inicial en el que nuestros correos se cruzaron. Dr. Paul and Dr. Keith, thank you for both your hospitality and including me in any plan related to gun powder since the first day. Ms. LZ, from Valles Caldera to the Mexican border, thank you for every kilometer and every party you took me, you know *this train'll stop at Tucumcari*. Thanks to Siva and the soccer team, Julián, Mohamad and all the people in the PandA and PAIS departments.

A mi vuelta de Nuevo México, la situación por todos bien conocida cambió el ritmo del despacho, impidiéndonos seguir desarrollando el culto de nuestros altares y sus tradiciones. A Miguel, el señalado como siguiente (con esto no quiero meter presión), gracias por cada segundo de discusiones y líneas de pensamiento, espero no se desvanezcan en la incertidumbre del futuro. A Iñaki, nuestra promesa, gracias por tus lecturas concienzudas de partes del manuscrito y por tu agudeza cada vez que hemos tenido que atacar un problema. A los más jóvenes, Jaime y Alberto, que vagan por senderos parecidos a los míos, que tengáis suerte con todo obstáculo con el que os crucéis. Espero haber podido ayudar en lo que hayáis necesitado tal y como me ayudaron los que por delante de mí fueron.

Saliendo de nuestro lóbrego pasillo y subiendo las escaleras, quiero recordar a todos los que por el departamento pasaron, en especial estudiantes y posdocs, que tanta vida dieron, desde el humor absurdo y los memes a grupos de whatsapp furtivos de Guille, José y Nerea. María y Raúl, mis quintos y sufridos compañeros de algunos de los Rinconetes citados, ya sabéis que siempre a tope. Gracias pues a Marc, que nos ha dado perlas filosóficas, científicas y políticas a todos los niveles y a mis compañeros de laboratorios, algunos de ellos profesores, Juan Antonio, Esteban, Adolfo, Carlos Tejedor, Rafa Delgado y Elena del Valle. Asimismo, no puedo dejar de recordar y agradecer a Laura Ramos y Almudena Conde, que desde el despacho de la sexta planta tanta ayuda y guía nos han dado en los procedimientos administrativos con Rectorado y el Ministerio.

Dos espíritus libres que han servido muchas veces como guía, Rocío y Clàudia, que tanta Luz que dieron al módulo 5. Por la realización de todos vuestros (y algunos nuestros) proyectos, porque hay ciencia, hay vida y hay arte.

Llego a las puertas del módulo y abandono el edificio. A Mónica, gracias por todos estos años de análisis y consejo sobre lo que pasaba puertas afuera y puertas adentro, que así sigan siendo. Qué puedo sino colmar de infinitas coronas de laurel y flores las sienes de Hernán, mi primo, eterna cafeína, con el que tantos caminos de hierro anduve, de Cantoblanco a la Mancha. Espero haber aportado por lo menos una mínima parte de lo que de los dos he recibido.

No obstante, todo esto empezó hace mucho tiempo. Desde mis primeros años en el instituto, la Física fue una de las materias fundamentales en mi vida como estudiante, dentro y fuera de las clases. Gracias a todos los profesores de Física y Química que por aquellas aulas pasaron. De tales, quiero recordar a J. Garrigós y R. Martínez que embaucaron, aparte de mí, al reciente Dr. Felipe-Navarro, hablando extracurricularmente de orbitales, fuerzas, ecuaciones diferenciales y transformadas de todo tipo, aún sin que tuviésemos mucha idea de los rudimentos más básicos de las matemáticas. De los primeros años de la Facultad en Valencia saco charlas infinitas y un conjunto de quintos forjado a las orillas del Rin. Suerte especial para S y mi apreciada Let, en el camino académico que les queda por transitar. Con las eternas colegas del Erasmus, Claudia y Bea, pareja de bromas estelares, se perfiló el momento actual desde Blackett Laboratory. Y hoy no estaría haciendo un previo para una tesis de plasmones sin dos de mis supervisores en el campo de la nanofotónica, Vincenzo Giannini y Rubén Esteban, en Londres y San Sebastián, respectivamente.

A mis compadres de Albacete, con los que hemos roto balones y zapatillas en el asfalto, en las pistas de cualquier deporte y últimamente en los caminos polvorientos. A CM, por tirar del carro en absoluta igualdad y sin pensar en lo que cueste, por ser absolutamente fundamental. A la parte que por ella toca, que ha tratado siempre de hacer las circunstancias más fáciles. A toda la familia, presente y recuerdo de los que pusieron su esfuerzo en la construcción de lo que hoy es. A mi hermana y a mis padres, cuyo impacto en el pasado, presente y futuro es imposible de medir, la razón primera y última de todo.

Quizá no ha sido del todo breve.

De Madrid a otros campos un poco más al sur, verano de 2021.

Contents

Abstract

English

In the context of condensed matter physics, the manipulation of the interaction between light and matter constitutes one of the most fruitful and promising fields in the dawn of Physics of the XXIst century. The development of the solid-state based technologies allowed the advances towards the control of the electromagnetic interactions between matter excitations and light, with special interest in the possibilities that occur in the limit where quantum emitters can store and release energy quanta one by one. The tailoring of light emission is well known since the middle of the XXth century through the coupling between the emitter and the electromagnetic modes in its surroundings. If we attend to the generation of light in the optical regime, the spatial scales shrink down to the nanometer range, where just a few thousands of atoms can support electromagnetic resonances. In this way, different metallodielectric structures can shape the emission of quantum light sources. In particular, plasmonic resonances, sustained by the collective motion of quasifree eletrons in metal-dielectric interfaces, permit the modification of the local density of states that allows for the de-excitation of the quantum emitter. At the same time, metallic nanoresonators are able to act as optical nanoantennas, converting very efficiently propagating light from the far-field into evanescent modes confined with nanometric resolution and enhancing the excitation of quantum emitters by light. The field of nanophotonics, based on the manipulation of electromagnetic waves at the nanoscale, has been postulated as a key step of the development of optoelectronics and nanotechnology in the XXIst century.

In the first part of the thesis, we center our study on the interaction between plasmons and excitons in an archetypal plasmonic cavity, formed by a single nanoparticle separated only by a few nanometers from a metallic substrate. The research in metamaterials gave place to the development of theoretical methods for the obtention of analytical solutions of Maxwell's equations. In particular, we will make use of the Transformation Optics formalism to study solutions of the Laplace's equation, limit of the Maxwell's set in nanometric environments under the quasistatic approximation. By means of this procedure, we obtain a fully analytical characterization of the light-matter coupling for two types of quantum emitters, distinguished by the nature of their transition, dipolar and quadrupolar. Moreover, we use this approach to reveal the possible impact of finite-size effects in the optical properties of the emitter, to describe the population dynamics in a spontaneous emission configuration and to calculate the far-field scattering spectrum of the hybrid plasmon-emitter system. Our findings reveal the similarities and differences between the light-matter coupling phenomenology for bright and dark excitons in nanocavities.

In the second part, we proceed to introduce a degree of complexity in the initial system formed by the cavity and a single emitter in the two-level approximation. Firstly, we consider the case of having more than one emitter in the cavity. We make use of a perturbative solution for the dyadic Green's function tensor, where the presence of the second emitter has a distorting character in the bare cavity light-matter coupling. We model the response of the distorting emitter in terms of a lineal model through an effective polarizability. Applying this scheme, we study two different plasmonic cavities, testing the results with numerical simulations. Our findings reveal that the distorting emitter induces new contributions to the density of states and we provide an interpretation of these results in terms of a Hamiltonian formalism. Secondly, we consider a single emitter in the cavity but with a three-level structure, where the excited states present different transition momenta, dipolar and quadrupolar ones. The description of the light-matter coupling is obtained analytically, focusing on both the dynamics of the light-allowed state and the scattering cross-section of the hybrid system. Our results evidence the profound modification of the Purcell enhancement besides the emergence or disappearance of peaks in the scattering spectrum due to the presence of the light-forbidden transition.

In the third part, we put aside the study of the interaction between quantum emitters and plasmonic modes, focusing on the form of the resonances by itself. Extended systems given by the periodic repetition of metallic nanoparticles show different types of resonances. Ones are typically plasmon-like, with large bandwidths, whereas another ones emerge from the electromagnetic interaction between the system constituents, usually termed lattice resonances, characterized by large quality factors. In particular, we analyze the nature of lattice resonances in complex arrays, built from unit cells comprising two different particles. We find that the radiative losses of the resonances supported by this type of structures result in sub- or superradiant modes, with large or small quality factors.

Finally, in the last part of this work, we show our results, based in numerical solutions of Maxwell's equations, in collaboration with the group of Prof. Guillermo Acuña at

Braunschweig and Fribourg. His experimental group carried out several research projects on the nature of light-matter interactions in nanoscale systems built with nanometric precision through DNA origami techniques, allowing measurements in the single molecule limit. First, we present our study about enhancement of radiative Purcell factor in silver dimers. Second, we analyze the influence of plasmonic resonances in energy transfer between fluorescent molecules. Our numerical results shed light into the experimental findings in both projects and were instrumental for their analysis and interpretation.

Castellano

Dentro de la física de la materia condensada, la manipulación de la interacción luz-materia constituye uno de los campos más fructíferos y a la vez prometedores en los inicios de la Física del siglo XXI. En el contexto actual, el desarrollo de las tecnologías basadas en fenomenología del estado sólido permitió los avances hacia el control de las interacciones electromagnéticas entre excitaciones materiales y de luz, con especial interés en las posibilidades que sobrevienen en el límite cuántico, en el que la materia puede almacenar y emitir un cuanto de energía. La manipulación de esta emisión es conocida desde la mitad del siglo XX a través del acoplamiento del emisor con los modos electromagnéticos de su entorno. Si atendemos a la generación de luz en el espectro óptico, las escalas espaciales se reducen radicalmente, hasta la escala de los nanómetros, donde apenas unos miles de átomos pueden dar soporte a la existencia de resonancias electromagnéticas. De esta manera, distintas nanoestructuras metalodieléctricas permiten perfilar la emisión de fuentes de luz cuánticas. En particular, las resonancias de tipo plasmónico, sustentadas por el movimiento colectivo de los electrones cuasi-libres en la interfaz metal-dieléctrico, permiten modificar la densidad local de estados que media la desexcitación del emisor cuántico a través de la emisión de un fotón. Al mismo tiempo, las nanoestructuras metálicas que soportan este tipo de resonancias son capaces de actuar como nanoantenas ópticas, convirtiendo con gran eficacia luz propagante de campo lejano en modos evanescentes confinados con resolución nanométrica y permitiendo la excitación eficiente de emisores cuánticos. El campo de la nanofotónica, basado en la manipulación de ondas electromagnéticas en la escala nanométrica, se ha postulado como un paso fundamental en el desarrollo de la optoelectrónica y de la nanotecnología del siglo XXI.

En la primera parte de la tesis, centramos nuestro estudio en la interacción entre plasmones y excitones en una cavidad plasmónica arquetípica, formada por una sola nanopartícula separada apenas unos nanómetros de un sustrato metálico. La investigación en teoría de metamateriales dio lugar al desarrollo de métodos para la obtención de soluciones analíticas de las ecuaciones de Maxwell. En particular, haremos uso de la Óptica de Transformación para estudiar las soluciones a la ecuación de Laplace, límite de las ecuaciones de Maxwell en entornos nanométricos bajo la aproximación cuasistática. Por medio de este procedimiento, obtenemos una caracterización del acoplamiento para dos tipos de emisores, distinguidos por la naturaleza de sus transiciones, dipolares y cuadrupolares. Asimismo, hacemos uso de este modelo para revelar el posible impacto del tamaño finito de los emisores y mostrar los efectos de la interacción tanto en la

dinámica de la población del estado excitado del emisor como en los espectros de dispersión de campo lejano.

En la segunda parte, procedemos a introducir un grado más de complejidad en el sistema inicial formado por la cavidad y un solo emisor cuántico en la aproximación de dos niveles. Primero, consideramos el problema de tener más de un emisor en la cavidad. Para ello, hacemos uso de una solución perturbativa en términos de la función de Green diádica, donde la presencia del emisor tiene un carácter distorsionador del acoplamiento luz-materia entre el emisor principal y los modos de la cavidad. En nuestra aproximación, la respuesta del segundo emisor es descrita en términos de un modelo lineal a través de una polarizabilidad efectiva. Aplicamos este modelo a dos cavidades plasmónicas distintas y testeamos su validez con simulaciones numéricas. Nuestros resultados evidencian que el emisor distorsionador induce distintas contribuciones modales en la densidad de estados de las cavidades, que conectamos con una descripción en términos de un formalismo Hamiltoniano. A este problema, añadimos el estudio del acoplamiento de un solo emisor en una cavidad, pero con una estructura de tres niveles donde los estados excitados están caracterizados por distintos momentos de transición, dipolar y cuadrupolar, respectivamente. A partir de la descripción completamente analítica de los campos, podemos hacer un análisis exhaustivo de la dinámica de la población del estado dipolar y del espectro de dispersión del sistema. Nuestro estudio revela la profunda modificación del factor Purcell y la aparición o desaparición de resonancias espectro en el espectro de la sección eficaz de dispersión.

En la tercera parte, dejamos de lado el estudio de la interacción entre emisores cuánticos y modos plasmónicos, centrando nuestro interés en la forma de las resonancias. Los sistemas extendidos dados por el ordenamiento periódico de sus constituyentes presentan distintos tipos de resonancias. Unas pueden ser de puramente plasmónico, con un gran ancho de banda, mientras que otras emergen de la interacción electromagnética a lo largo del sistema, están caracterizadas por factores de calidad grandes y reciben el nombre de resonancias de red. En particular, analizamos la naturaleza de este tipo de resonancias en redes complejas, constituidas por celdas unidad formadas por dos partículas distintas, y encontramos que las pérdidas radiativas de los modos de red de este tipo de estructuras resultan en resonancias sub- o superradiantes, caracterizadas por factores de calidad altos o bajos, respectivamente.

Finalmente, en la última parte de este trabajo, mostramos nuestros resultados, basados en soluciones numéricas de las ecuaciones de Maxwell, en colaboración con el grupo del Prof. Guillermo Acuña en las Universidades de Braunschweig y Fribourg. Su grupo llevo a cabo el trabajo experimental en sistemas nanométricos diseñados y construidos por

medio de técnicas de origamis de ADN. Primero, presentamos nuestro estudio sobre la mejora del efecto Purcell radiativo en dímeros plasmónicos. Después, mostramos nuestros análisis sobre la influencia de resonancias plasmónicas en la transferencia de energía entre emisores cuánticos. Nuestros resultados numéricos proveen de soporte teórico al trabajo experimental, alcanzando las mismas conclusiones en ambos casos.

List of acronyms

This is a list of the acronyms used in the text (in alphabetical order).

2D	Two dimensions
3D	Three dimensions
EM	Electromagnetic
FRET	Förster resonance energy transfer
HOMO	Highest occupied molecular orbital
LDOS	Local density of states
LUMO	Lowest unoccupied molecular orbital
LSP	Localized surface plasmon
MIM	Metal-insulator-metal
NPoM	Nanoparticle-on-mirror
PEP	Plasmon-exciton polariton
QE	Quantum emitter
QED	Quantum electrodynamics
cQED	Cavity quantum electrodynamics
mQED	Macroscopic quantum electrodynamics
QNM	Quasinormal mode
RA	Rayleigh anomaly
SP	Surface plasmon
TO	Transformation Optics

1

Introduction

This thesis is devoted to the study of the interaction between light and matter. In order to avoid such generality, we specify that we have focused on the small part which explores how quantum emitters (QEs) respond to electromagnetic (EM) fields at the nanoscale, and particularly, we have made an effort to understand the form of those fields. Therefore, this work inherits a legacy that started with the formulation of classical electrodynamics and nowadays connects the fields of cavity quantum electrodynamics (cQED) and nanophotonics.

This introduction chapter will give a concise overview of the basic ingredients that are customary for the study of this topic. Technical details will be given afterwards in each chapter and final appendices.

1.1. Brief review about light-matter interactions

Our quotidian experience is depicted by both gravitation and electromagnetism. Without any intention of unveiling the deepest principles of Physics, we do understand that the energy loss at the moderate early age of the Universe allowed the coupling between protons and electrons through photons. The strength of this interaction, characterized by the fine structure constant, determines the dominance of EM interactions. Not dominance in the sense of the strongest interaction. The fine structure constant, a parameter that surges in the theory and has to be experimentally fitted [1], permits the chemical bonding, and therefore, the emergence of vital forms in the way we know. Life lives within the energy scales of photons. This fact is the key that has determined the technological revolution in the last three hundred years. We have refined the way we produced sparks with flintstone at the same time we went deeper in the accessible energy scales.

However, the interaction of light with matter was partially understood until the nineteenth century. The series of different works by a dispersed group of scientists (whose name we do not write in order to not forget any of them) for more than one hundred years allowed the Maxwell's milestone [2]. Maxwell's equations settled the basis that governs macroscopic electrodynamics and constitute the classical field theory for EM interactions[1]. The unification of electric and magnetic phenomena set the pace for the understanding of light as EM waves, firstly demonstrated in Ref. [4], able to travel through space free of matter.

The theoretical and experimental advances in classical electrodynamics guided Physics towards an interesting debate. Whereas Maxwell's theory led to the assumption of continuum theories for matter description, at the same time, the results derived from the kinetic theory of gases attracted many physicists to the old-fashioned atomic ideas[2]. The dispute was still on the air when experimental discoveries established the existence of the electron, the basic constituent of charge. The birth of the twentieth century brought the quantum description of nature with it. The earlier quantization of energy suggested by Planck settled a starting point for the quantization of the EM field, which was almost unaffordable at that moment. In the meantime, matter was shown to follow the quantum rules, opening two fruitful branches of research: the macroscopic structure of matter and the structure of atoms and molecules. The interest of the quantum community concerned especially with the latter due to the (at that time) incomprehensible issue of discrete spectral lines, giving rise to the quantum theory of atomic structure formulated in a first step by Bohr [6]. The process of spontaneous decay of an atom, firstly described phenomenologically through the Einstein's A-coefficient, was finally understood in the framework of quantum theory of radiation, soon known as quantum electrodynamics (QED) [7].

After the comprehension of the spontaneous decay mechanism, the research on atom-vacuum interactions opened a new field of physics. The work by Purcell [8] in modifying decay rates in nuclear magnetic resonances answered a question that had been around for forty years: the spontaneous decay rate of a quantum emitter is not an intrinsic property of matter but of the coupled emitter-radiation system. During the following decades, this

---

[1] After Maxwell, several new branches arose as those of microscopic electromagnetism and the concepts of potential and gauge transformations, fundamental for the formulation of quantum theory of light [3].

[2] The development of kinetic theory of gases delivered not only results as diffusion or heat conduction, but also widely-used concepts as the mean free path [5].

result, known as Purcell effect, was considered in different scenarios. Drexhage carried out experiments where the fluorescence of dyes was modified in front of metallic mirrors [9]. In the opposite sense, Kleppner and others studied the inhibition of the decay, decoupling an emitter from its EM environment and therefore, enlarging the lifetime of the excited state [10]. Additionally, the study of stimulated processes brought out the achievement of the laser [11], an indispensable tool for the efficient control of light.

The field of cavity QED rests on the Purcell effect through the modification of the background radiation field in the surroundings of a quantum emitter. It is especially noteworthy the contribution done by the Cohen-Tannoudji's and Haroche's groups in the understanding of the interaction of photons and atoms in confined spaces. These researchers established fundamental concepts such as *dressed atoms* [12] and set the milestone of *strong coupling* regime [13], characterized by the existence of purely quantum hybrid light-matter states where the atom-radiation distinction becomes blurred[3]. Less renowned but not less important, the twentieth century also gave birth to a vast amount of different research lines based on the increasing control of light properties provided fundamentally by the laser. In the last decades, technological advances allowed the manipulation of matter in decreasing spatial ranges, leading to the dawn of nanophotonics, where light and matter interact at the nanometer scale. Thus, we have witnessed the emergence of novel areas such as plasmonics [16–18], photonic crystals [19, 20] and metamaterials [21] that have led to astonishing applications as plasmonic sensing [22], photovoltaics [23], cancer therapy [24] and superresolution microscopy [25]. The vigor of this field stands on how those nanometer resonators respond to the action of the EM field. Free space EM waves can be efficiently coupled to confined EM modes that live in sub-wavelength volumes, providing access to the near-field properties of the fields and revealing unimaginable resolution [26]. Even when the term nanophotonics or nano-optics can remit to an oxymoron [27], this tame and control over light-matter interaction opens future routes for facing light and quantum matter, resulting in single-photon sources [28], hybrid states of light and matter [29] and quantum optical nanocircuits [30].

1.2. Light description: macroscopic electrodynamics

Any kind of interaction between particles can be defined through the concept of field. Instead of describing the situation as a particle *exerting* a force onto another one, it is assumed that the particle creates a field around itself and any particle present in that

---

[3] A very constructing introduction to the historical development of cQED can be read from the leading researchers of the field in Refs. [14, 15].

field would suffer the effect of a force. This nineteenth century concept is one of the most fruitful ideas of Physics, both in classical and quantum descriptions [31]. The equations that govern how the electric and magnetic fields emerge from EM sources constitute the set of Maxwell's equations in vacuum

$$\nabla \cdot \mathbf{E}(\mathbf{r},t) = \frac{\rho(\mathbf{r},t)}{\epsilon_0}, \tag{1.1a}$$

$$\nabla \cdot \mathbf{B}(\mathbf{r},t) = 0, \tag{1.1b}$$

$$\nabla \times \mathbf{E}(\mathbf{r},t) = -\frac{\partial \mathbf{B}(\mathbf{r},t)}{\partial t}, \tag{1.1c}$$

$$\nabla \times \mathbf{B}(\mathbf{r},t) = \mu_0 \mathbf{J}(\mathbf{r},t) + \mu_0 \epsilon_0 \frac{\partial \mathbf{E}(\mathbf{r},t)}{\partial t}. \tag{1.1d}$$

This set of phenomenological equations links two vectorial fields, $\mathbf{E}(\mathbf{r},t)$ (electric field) and $\mathbf{B}(\mathbf{r},t)$ (magnetic induction), and the field sources, the current density $\mathbf{J}(\mathbf{r},t)$ and the charge density $\rho(\mathbf{r},t)$. The discreteness of electric charge is not considered in macroscopic applications where a large amount of elementary charges play a role. The parameters ϵ_0 and μ_0 are the vacuum electric permittivity and magnetic permeability, respectively. Maxwell's equations implicitly contain the continuity equation for source densities $\nabla \cdot \mathbf{J}(\mathbf{r},t) + \partial_t \rho(\mathbf{r},t) = 0$. Apart from those, the interaction of a single charge q (moving at certain velocity $\mathbf{v}(\mathbf{r},t)$) with both $\mathbf{E}(\mathbf{r},t)$ and $\mathbf{B}(\mathbf{r},t)$ should be addressed in terms of the Lorentz force $\mathbf{F}(\mathbf{r},t) = q(\mathbf{E}(\mathbf{r},t) + \mathbf{v}(\mathbf{r},t) \times \mathbf{B}(\mathbf{r},t))$. Maxwell's equations in vacuum are linear, so solutions can be written as linear superposition of fields. These relations define how the fields are created by the sources but one still has to determine the effects of light onto matter. Therefore, Maxwell's set has to be completed with the description of how matter can give rise to effective sources under light illumination.

The presence of a medium in which EM fields can exist leads to the generation of *induced* charges and currents. In a macroscopic way, fields are sustained onto an effective background that represents the media where those fields are different to their value in vacuum. The total densities of charge and current are split into two different contributions $\rho(\mathbf{r},t) = \rho_{\text{ext}}(\mathbf{r},t) + \rho_{\text{ind}}(\mathbf{r},t)$ and $\mathbf{J}(\mathbf{r},t) = \mathbf{J}_{\text{ext}}(\mathbf{r},t) + \mathbf{J}_{\text{ind}}(\mathbf{r},t)$. Both ρ_{ext} and $\mathbf{J}_{\text{ext}}$ constitute the external sources as those in free space. The induced contributions (ρ_{ind}, $\mathbf{J}_{\text{ind}}$) arise from the action of the fields onto material media. For simplicity in this brief approach, we will consider as a first assumption that linear contributions are the dominant ones. In this limit, only the polarization $\mathbf{P}(\mathbf{r},t)$ and magnetization $\mathbf{M}(\mathbf{r},t)$ play a significant role. Thus, the induced contributions can be written as $\rho_{\text{ind}}(\mathbf{r},t) = -\nabla \cdot \mathbf{P}(\mathbf{r},t)$ and $\mathbf{J}_{\text{ind}}(\mathbf{r},t) = \partial_t \mathbf{P}(\mathbf{r},t) + \nabla \times \mathbf{M}(\mathbf{r},t)$. Usually, the induced current is split into two different terms, the current due to moving quasifree electrons (as those in the conduction band of a metal) and the current associated to the bound charges. Therefore, Ohm's law in the linear limit $\mathbf{J}_{\text{free}}(\mathbf{r},t) = \sigma\mathbf{E}(\mathbf{r},t)$ applies to the relation between the conduction current and the electric field.

Rearranging Maxwell's equations including these considerations provides the set of *macroscopic* Maxwell's equations

$$\nabla \cdot \mathbf{D}(\mathbf{r},t) = \rho_{\text{ext}}(\mathbf{r},t), \tag{1.2a}$$

$$\nabla \cdot \mathbf{B}(\mathbf{r},t) = 0, \tag{1.2b}$$

$$\nabla \times \mathbf{E}(\mathbf{r},t) = -\frac{\partial \mathbf{B}(\mathbf{r},t)}{\partial t}, \tag{1.2c}$$

$$\nabla \times \mathbf{H}(\mathbf{r},t) = \mathbf{J}_{\text{ext}}(\mathbf{r},t) + \frac{\partial \mathbf{D}(\mathbf{r},t)}{\partial t}, \tag{1.2d}$$

where the displacement field, $\mathbf{D}(\mathbf{r},t) = \epsilon_0\mathbf{E}(\mathbf{r},t) + \mathbf{P}(\mathbf{r},t)$ and the magnetic field, $\mathbf{H}(\mathbf{r},t) = \mathbf{B}(\mathbf{r},t)/\mu_0 - \mathbf{M}(\mathbf{r},t)$ naturally appear. From the divergence and rotational expressions, $\mathbf{E}(\mathbf{r},t)$ and $\mathbf{H}(\mathbf{r},t)$ are understood as field intensities whereas $\mathbf{D}(\mathbf{r},t)$ and $\mathbf{B}(\mathbf{r},t)$ represent the flux intensities. The description is completed by expressing $\mathbf{P}(\mathbf{r},t)$ and $\mathbf{M}(\mathbf{r},t)$ in terms of the field intensities. Limiting ourselves to isotropic, linear and non magnetic media which exhibit local properties (no spatial dispersion is relevant), the constitutive relations are:

$$\mathbf{D}(\mathbf{r},t) = \epsilon_0 \int \epsilon(t-t')\mathbf{E}(\mathbf{r},t')dt' \tag{1.3a}$$

$$\mathbf{H}(\mathbf{r},t) = \frac{\mathbf{B}(\mathbf{r},t)}{\mu_0}. \tag{1.3b}$$

The EM magnitudes that appear in Maxwell's equations apply to each point of space at a certain instant of time. Invoking the integral Stokes's and Gauss's theorems, the relations between that physical magnitudes can be represented in the integral form. In this way, the equations allow to obtain several conditions that have to be fulfilled by the components of the fields on either side of the interface which separates two media (subscripts 1 and 2), which read

$$\mathbf{n}(\mathbf{D}_1(\mathbf{r},t) - \mathbf{D}_2(\mathbf{r},t)) = \rho_s(\mathbf{r},t), \tag{1.4}$$

$$\mathbf{n}(\mathbf{B}_1(\mathbf{r},t) - \mathbf{B}_2(\mathbf{r},t)) = 0, \tag{1.5}$$

$$\mathbf{n} \times (\mathbf{E}_1(\mathbf{r},t) - \mathbf{E}_2(\mathbf{r},t)) = 0, \tag{1.6}$$

$$\mathbf{n} \times (\mathbf{H}_1(\mathbf{r},t) - \mathbf{H}_2(\mathbf{r},t)) = \mathbf{J}_s(\mathbf{r},t), \tag{1.7}$$

where $\mathbf{J}_s(\mathbf{r},t)$ and $\rho_s(\mathbf{r},t)$ are the surface current and charge densities in the boundary that separates different media. Looking back to the set of vacuum Maxwell's equations in terms of the fields, it is often found, especially in the context of field theories, that those are expressed in terms of potentials, obtaining a smaller number of differential equations. Due to the vanishing character of $\nabla\cdot\mathbf{B}(\mathbf{r},t)$, it is then defined $\mathbf{B}(\mathbf{r},t)=\nabla\times\mathbf{A}(\mathbf{r},t)$, where $\mathbf{A}(\mathbf{r},t)$ is the vector potential. At the same time, the Faraday's law provides an irrotational field given by both $\mathbf{E}(\mathbf{r},t)$ and $\partial_t\mathbf{B}(\mathbf{r},t)$, so we can write $\mathbf{E}(\mathbf{r},t)=-\nabla\Phi(\mathbf{r},t)-\partial_t\mathbf{A}(\mathbf{r},t)$, where the scalar potential $\Phi(\mathbf{r},t)$ explicitly appears. Therefore, the complete set of four equations is written in terms of the potentials as

$$\nabla^2\Phi(\mathbf{r},t)+\frac{\partial}{\partial t}\Big(\nabla\cdot\mathbf{A}(\mathbf{r},t)\Big)=-\frac{\rho(\mathbf{r},t)}{\epsilon_0} \tag{1.8}$$

$$\nabla^2\mathbf{A}(\mathbf{r},t)-\frac{1}{c^2}\frac{\partial^2\mathbf{A}(\mathbf{r},t)}{\partial t^2}-\nabla\Big(\nabla\cdot\mathbf{A}(\mathbf{r},t)+\frac{1}{c^2}\frac{\partial\Phi(\mathbf{r},t)}{\partial t}\Big)=-\mu_0\mathbf{J}(\mathbf{r},t) \tag{1.9}$$

which are still coupled equations. The definition of the potentials is not unique, due to the fact that some transformations ($\mathbf{A}'(\mathbf{r},t)=\mathbf{A}(\mathbf{r},t)+\nabla\Lambda(\mathbf{r},t)$ and $\Phi'(\mathbf{r},t)=\Phi(\mathbf{r},t)-\partial_t\Lambda(\mathbf{r},t)$) conserve the observables $\mathbf{E}(\mathbf{r},t)$ and $\mathbf{B}(\mathbf{r},t)$ derived from them. Such modifications on the potentials are known as *gauge transformations*. In particular, we highlight two paradigmatic cases. First, the Lorenz gauge, where $\Lambda(\mathbf{r},t)$ is chosen to satisfy $\nabla\cdot\mathbf{A}(\mathbf{r},t)+c^{-2}\partial_t\Phi(\mathbf{r},t)=0$, which yields two symmetric inhomogeneous equations for each potential in the form $(\nabla^2-c^{-2}\partial_t^2)\Phi(\mathbf{r},t)=-\rho(\mathbf{r},t)/\epsilon_0$ and $(\nabla^2-c^{-2}\partial_t^2)\mathbf{A}(\mathbf{r},t)=-\mu_0\mathbf{J}(\mathbf{r},t)$. Second, the Coulomb gauge, also known as radiation gauge, where the imposed condition is $\nabla\cdot\mathbf{A}(\mathbf{r},t)=0$. This gauge is noteworthy for the fact that all the radiation phenomena is contained in $\mathbf{A}(\mathbf{r},t)$ since $\nabla^2\Phi(\mathbf{r},t)=\rho(\mathbf{r},t)/\epsilon_0$, which is the Poisson's equation that reflects the electrostatic character of the scalar potential.

It is usually convenient to take advantage of the properties of Fourier Transforms and express the fields in the frequency domain. Furthermore, in the reciprocal space, the formalism of the conversion from convolutions to products can give another form of the constitutive relation but in a simpler way in terms of wavevectors and frequencies instead of space vectors and time. Any vectorial field $\mathbf{F}(\mathbf{r},t)$ (or scalar quantity) can be written in the form

$$\mathbf{F}(\mathbf{r},t)=\int_{-\infty}^{\infty}\mathbf{F}(\mathbf{r},\omega)e^{-i\omega t}d\omega. \tag{1.10}$$

Monochromatic fields can be written as $\mathbf{F}(\mathbf{r},t)=\mathrm{Re}\{\mathbf{F}(\mathbf{r},\omega)e^{-i\omega t}\}$, temporal derivatives in Maxwell's equations are expressed as products $\partial_t=-i\omega$ and the constitutive relations simply read

$$\mathbf{D}(\mathbf{r},\omega) = \epsilon_0\epsilon(\omega)\mathbf{E}(\mathbf{r},\omega), \tag{1.11a}$$

$$\mathbf{H}(\mathbf{r},\omega) = \frac{\mathbf{B}(\mathbf{r},\omega)}{\mu_0}. \tag{1.11b}$$

Maxwell's equations implicitly contain the existence of EM waves. From the curl equations, the wave equation for the electric field in a non-magnetic homogeneous space reads

$$\nabla \times \nabla \times \mathbf{E}(\mathbf{r},\omega) - \epsilon\frac{\omega^2}{c^2}\mathbf{E}(\mathbf{r},\omega) = i\omega\mu_0\mathbf{J}_{\text{ext}}(\mathbf{r},\omega). \tag{1.12}$$

The wave equation is then equivalent to an inhomogeneous equation $\mathcal{L}\mathbf{E}(\mathbf{r},\omega) = \mathbf{J}(\mathbf{r},\omega)$ where $\mathcal{L}$ is a linear operator onto the electric field that does not create dependences on any quadratic power. The most general solution to such an equation is given by the sum of two functions, corresponding to the homogeneous and particular solutions of the equation. Due to the difficulty to find a general solution for the inhomogeneous equation, a simpler idea arises introducing just a point inhomogeneity in the form $\mathcal{L}\mathbf{G}_i(\mathbf{r},\mathbf{r}',\omega) = \delta(\mathbf{r}-\mathbf{r}')\hat{\mathbf{n}}_i$ [32]. $\mathbf{G}_i(\mathbf{r},\mathbf{r}',\omega)$ is the vector field that contains the solution for the vectorial inhomogeneity in the $\hat{\mathbf{n}}_i$ direction. Once this equation is solved, the solution of the wave equation above can be expressed as

$$\mathbf{E}(\mathbf{r},\omega) = \mathbf{E}_0(\mathbf{r},\omega) + i\omega\mu_0\int_V \mathbf{G}(\mathbf{r},\mathbf{r}',\omega)\mathbf{J}_{\text{ext}}(\mathbf{r}',\omega)\mathrm{d}^3\mathbf{r}', \tag{1.13}$$

where $\mathbf{E}_0(\mathbf{r},\omega)$ is the solution to the homogeneous equation and the integral is calculated over the volume of the sources. $\mathbf{G}(\mathbf{r},\mathbf{r}',\omega)$ is the matrix formed by the vectors $\mathbf{G}_i$, known as the *dyadic Green's function*. The generality of this solution can be clarified if we look upon the multipolar expansion of a distribution of charges. If we consider the first term of the expansion, the current density associated to such configuration is given by the temporal variation of the dipole moment in the form[4] $\mathbf{J}(\mathbf{r},\omega) = -i\omega\boldsymbol{\mu}\delta(\mathbf{r}-\mathbf{r}_0)$. This result provides the form for the electric field for an oscillating point-dipole source

$$\mathbf{E}(\mathbf{r},\omega) = \frac{\omega^2}{\epsilon_0 c^2}\mathbf{G}(\mathbf{r},\mathbf{r}_0,\omega)\boldsymbol{\mu}. \tag{1.14}$$

Then, the electric field generated by a point-dipole source is given directly by the dyadic that connects the location of the dipole and the position at which the field is calculated. The elements of the dyadic tensor are just proportional to the field created by a point-dipole source.

---

[4] As it is commonly used in antenna theory, to the lowest order, an oscillating dipole can be modeled as a current density.

The description of light as an EM wave provides access to the correct explanation of many physical phenomena related to light-matter interactions. Nevertheless, as far as we go in decreasing number of photons involved in the interaction, the corpuscular (discrete) behavior of light manifests by itself. A paradigmatic example occurs when we deal with single quantum emitters (see section 1.3), where the interaction is mediated by one single photon. When this is the case, the quantum description of light is needed to account for light-emitter interactions. The canonical quantization procedure constitutes the fundamentals of the field of quantum optics and we are not going to cover it in detail. We refer the reader to Refs. [33, 34], where this formulation of EM theory is treated thoroughly. For our purposes, it is enough to state that the classical Hamiltonian description of the EM fields can be understood as a set of independent harmonic oscillators. Those functions constitute a complete basis and are interpreted as the *modes* of the system, that can be canonically quantized. Therefore, the modes of the classical field decomposition are promoted to the operators in the second quantization scheme. Those operators are able to create or destroy an excitation (photon) of the corresponding mode. Within this formalism, the Hamiltonian of the EM field reads

$$\hat{H}_{\mathrm{R}} = \sum_{l} \hbar\omega_l \left(\hat{a}_l^{\dagger}\hat{a}_l + \frac{1}{2} \right), \tag{1.15}$$

where the sum runs over the whole set of modes of the system, characterized by their energy $\hbar\omega_l$. Besides, $\hat{a}_l^{\dagger}$ and $\hat{a}_l$ are the photon creation and annihilation operators for the l-mode and fulfill the bosonic commutation relations $[\hat{a}_l, \hat{a}_{l'}^{\dagger}] = \delta_{l,l'}$ with the Kronecker delta $\delta_{l,l'}$. Furthermore, they operate onto the photon Fock states (or number states) as

$$\hat{a}_l^{\dagger} \left| n_l \right\rangle = \sqrt{n+1} \left| (n+1)_l \right\rangle , \tag{1.16}$$

$$\hat{a}_l \left| n_l \right\rangle = \sqrt{n} \left| (n-1)_l \right\rangle . \tag{1.17}$$

Note that the term 1/2 in Eq. (1.15) a pure quantum footprint since it represents the vacuum state energy. Note that we are going to measure our energies as a relative quantity, referenced to the vacuum energy.

Throughout this thesis, we will employ this description of the light fields in order to account for their quantum and bosonic nature of photons. Diverse procedures of quantization have been studied in order to take account for the quantum interaction of light and matter. Closed cavities made of lossless materials are accommodated in quantum models in a straightforward manner. Nevertheless, open systems built of lossy materials present problems in direct quantization [35]. In order to overcome those difficulties, we highlight several proposed approaches, which have put the attention in the treatment of the EM environment. In a first place, macroscopic quantum electrodynamics (mQED) accommodate lossy materials and open environments, expressed in terms of the Green's function and based on Langevin noise approaches [36]. mQED founds the field quantization in terms of bosonic operators living a frequency continuum, making the problems involved in the number of degrees of freedom. Then, expansions of the EM response have been tackled in terms of a few quasinormal modes (QNM) [37], yielding quantization schemes for plasmonic resonators [38]. In this way, it is also remarkable the research done in the context of phenomenological approaches, where the mQED continuum is decomposed into several pseudomodes, leading to decompositions of both interacting and non-interacting lossy effective modes [39–42].

1.3. Matter description

The classical description of EM phenomena constituted a landmark in the comprehension of natural physical phenomena, but it is clear that any perception that we have about the existence of EM fields is given through their interaction with matter. The issue that concerns the understanding of matter has accompanied us since the foundations of natural philosophy. As mentioned above, at the end of the nineteenth century, Maxwell's theory introduced a continuum description of the media that *sustain* the EM fields. On the other hand, the conception of fluids as discrete ensembles of solid particles colliding each other provided at that time many results in the context of kinetic gas theory [5, 43]. The successful derivation of properties of gases (viscosity, diffusion, heat conduction) and the mechanical interpretation of thermodynamic magnitudes as temperature gave important support to the atomic hypothesis, that was lacking in Maxwell's picture of light-matter interactions [44]. The unification of macroscopic and microscopic electromagnetism constitutes by itself a wide topic and we remit the reader to Ref. [45] as a comprehensive reference.

As we have already seen, light propagating through a medium is characterized by its corresponding relative permittivity, ϵ, and permeability, μ. The first attempt towards an atomistic description of matter accounting for the microscopic origin of these two physical magnitudes was proposed by H. A. Lorentz with the oscillator model (formed by two charges of opposite sign), with a characteristic resonant frequency [46]. As we will see in subsequent sections, this model leads to expressions for the relative electric permittivity of different media. Bulk solids will not constitute the center of our study of light and matter interactions[5].

---

[5] About the historical development of the topic that we are referring to in both current and previ-

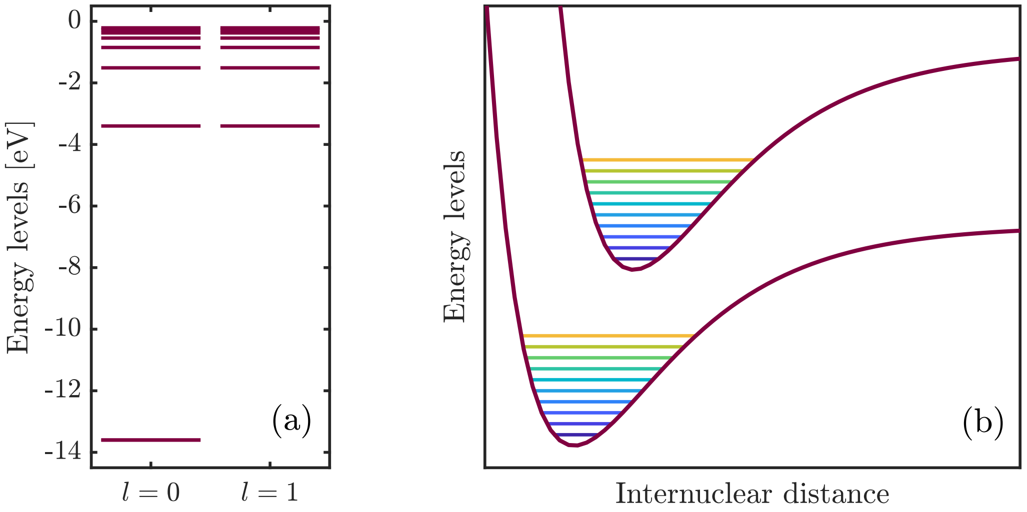

Figure 1.1: Energy structures of matter excitations. (a) Energy levels $E_{n,l}$ for a single-electron (hydrogen-like) atom for different principal number n and angular momentum l. (b) Sketch of two electronic potential energy curves of a diatomic molecule as a function of the internuclear distance. On top of each electronic energy, the vibrational energy spectra of the corresponding state is shown.

In the following, we turn our sight towards systems that sustain matter excitations and emit or absorb photons in a scenario of discrete states and energies[6]. These systems are called *quantum emitters* (QEs) as they can undergo de-excitation by emitting a single photon.

The simplest quantum model of matter corresponds to the hydrogen atom. Applying the Schrödinger equation for one electron and one proton attracting each other through a Coulomb force, a solution for the electron wavefunction is obtained in terms of discrete

---

ous sections, we strongly recommend the book *The Solvay Conferences on physics: Aspects of the development of physics since 1911* [47] where the reader can find that the first five topics of the conferences (organized by H. A. Lorentz) were focused on the nature of radiation, matter and macroscopic properties of matter.

[6] Both quantum-optical and semi-classical descriptions of light-matter interactions present the material component described within a quantized approach. The semi-classical limit, where the EM field is treated within the Maxwell's approach, yields a vast understanding of the processes of absorption and scattering [33], besides it is equivalent to the quantum formalism whenever we consider electrical fields satisfying a classical statistical character. The effects that emerge from the purely quantum nature of radiation are introduced phenomenologically in the semi-classical model through lifetimes.

electronic-type eigenstates[7]. These are determined by the principal quantum number, n, with eigenvalue $E_n = -13.6/n^2$ eV, as plotted in Figure 1.1(a). The atomic spatial length scales are characterized by the Bohr radius, $a_0 = 5.29 \times 10^{-11}$ m.

It is obvious that the atoms are not the only form of quantum matter that we can interact with. Molecules can be described in a similar way, through different states and energy levels associated to those. Nevertheless, as the complexity of material structure increases, new phenomena emerge. There are no just electronic states associated to the electron-nucleus interaction but also energy scales linked to the molecular vibrations and rotations, that, of course, are also quantized. The dominant energy scale is the electronic one, constituted by the potential curves of the molecule. On top of that, the rovibrational spectra appear, associated to the electronic state, as it can be seen in Figure 1.1(b).

The optical properties of typical solids do not usually show a dependence on size, but if we decrease the dimensions of the system, quantum confinement effects arise. This way, the uncertainty associated to a particle moving in a closed system provides an additional energy $\hbar^2/(2m\Delta^2)$, where Δ is the length scale associated to the confinement and m is the effective mass of the particle. The large number of degrees of freedom involved makes the calculation of the energy structure of solids cumbersome, out of the scope of this thesis, even in systems where quantum confinement is relevant. Concisely, the small size of the system leads to quantum confinement effects and provides access to few-body electronic states with discrete spectra. Therefore, we think of atom-like structures, designed in an artificial way. We remark here the quantum dots, nanometric structures formed by semiconductor scaffolding that can be engineered in size to change their optical properties [48–50].

A single photon mediates the transition between the states of a QE. In the case of an atom, the transition is given by the change of orbital of a single electron. Similarly in a molecule, the photo-excitation promotes the electronic configuration from the highest occupied molecular orbital (HOMO) to a higher energy electronic configuration, the lowest unoccupied molecular orbital (LUMO) configuration[8]. Semiconductor structures present the formation of excitons, where the electron-hole pair become bounded to each other. Furthermore, the dielectric conditions of the structure screens the electron-hole

---

[7] The first quantization obtained via using the Schrödinger formalism leads to an ensemble of states whose probability does not depend on time (stationary states). It is necessary to connect this system with another in order to have what we term *transition* to another stationary state, mediated by an absorption or release of energy by the electron.

[8] The complex structure of molecules yields a host of phenomena where the electronic and rovibrational energy structures are coupled each other and lead to intra-molecular processes of relaxation.

Coulomb interaction and allows the hopping between lattice sites. Therefore, the excitation (Wannier-Mott exciton) is delocalized over the emitter.

In their interaction with light, the quantum description of matter is usually given in the two-level approximation. In a first stage, only two electronic states are considered, the ground state, $|g\rangle$ and a *unique* excited one, $|e\rangle$, with a well-defined energy difference, $\hbar\omega_{eg} = E_e - E_g$, close to the photon energy, $\hbar\omega$. This assumption is valid if the energies of the higher excited states of the system, E_i, are far enough in energies from E_e, satisfying $E_i - E_e > \hbar\omega_{eg}$. On the other hand, the rovibrational spectrum associated to those states is also ignored. This can be positively done in simple systems, but in complex molecules, vibrations can substantially interact with the electronic excitation. We emphasize that two-level descriptions fairly capture the de-excitation process in organic molecules [51]. The excited and ground states span the Hilbert space for the exciton wavefunction

$$|\psi\rangle = c_1 |g\rangle + c_2 |e\rangle . \tag{1.18}$$

Their cross projection operators provide the creation, $\hat{\sigma}^\dagger$, and annihilation, $\hat{\sigma}$, operators of an excitation in the quantum emitter, defined as

$$\hat{\sigma}^\dagger = |e\rangle \langle g| , \tag{1.19}$$

$$\hat{\sigma} = |g\rangle \langle e| , \tag{1.20}$$

that follow the anticommutation properties typical of the fermionic systems,

$$\{\hat{\sigma}^\dagger, \hat{\sigma}\} = 1 \tag{1.21}$$

since electronic excitations follow the Pauli Exclusion Principle. The Hamiltonian of this two-level system reads

$$\hat{H}_{\text{TLS}} = \hbar\omega_g |g\rangle \langle g| + \hbar\omega_e |e\rangle \langle e| . \tag{1.22}$$

Since it is usual to define the origin of energies in the ground state where no excitations exist, the Hamiltonian is usually written as

$$\hat{H}_{\text{TLS}} = \hbar\omega_{eg}\hat{\sigma}^\dagger\hat{\sigma}. \tag{1.23}$$

Therefore, the Hamiltonian shows explicitly that the matter excitation becomes characterized by the transition frequency ω_{eg}. Besides, as we will see, in their interaction with light, the influence of the emitter is weighted through its transition moment, a magnitude that can be related to the size of the QE, as we will see in the following sections.

1.4. Emitters, photons and plasmons: Quantum nanophotonics.

Once reviewed the series of fundamental ingredients individually, we proceed to build the picture on which this tesis is based, the study of light-matter interaction at the nanoscale. It does not exist an ideal scenario for the investigation of the associated phenomena over the broad set of possibilities. In the most fundamental conception, the research about the interaction derives from the field of cQED, which has provided most of concepts on which further research relies on. Nevertheless, the range of operability of cQED systems, makes difficult their practical applications. In a quest to reduce the spatial dimensions of those systems, it arose the possibility of handling with energy transitions in the visible range, and therefore, the reduction of system to nanometer scales. Generally, nano-optics and nanophotonics are terms used for describing those systems in which the EM fields length scales and the system size coexist in the nanometric range, giving rise to the coexistence of both near-field and far-field effects. We will use the term quantum nanophotonics to refer this limit, always with the presence of QEs. Not surprisingly, depending on the emitter properties, there exists different types of systems (semiconductor cavities, photonic crystals or plasmonic cavities) whose properties are used to inherit the desired purpose. In our work, we have focused on the light-matter interaction of quantum emitters in *plasmonic cavities*, to which we dedicate the next subsection since it constitutes the fundamental part of this thesis.

1.4.1. Nanoplasmonics. Electrodynamics of metals

The subject of general EM response of different media vastly exceeds the scope of this thesis. Our focus is on optical processes, so we will restrict ourselves to local response approximations since speed of light exceeds the velocities of excitations in solids [52]. When light scatters with extremely nanometric environments, non-local effects can take part in the interaction and the material response under EM fields has to be treated within more complex models, especially at high optical frequencies [53]. In our results, we neglect non-local effects, as they do not have a substantial effect in the spatial regimes explored in this thesis. The limits of strongly-correlated and interacting systems where the classical electron gas model is not valid are neither considered in the common plasmonic systems. For any reader interested in electrodynamics of matter beyond the limits treated in this text, we refer the reader to Refs. [52, 54].

In a local description, when an electric field spans the media, the electrons are excited to a higher energy state by acquiring a net momentum. If the electric field has an harmonic dependence with time through a frequency ω, the set of negative charges can oscillate collectively, giving place to an net polarizability, proportional to the external electric field. The linear relationship between the electric field and the displacement becomes apparent in terms of ϵ, the relative electric permittivity or dielectric function for the metal. The simplest model for describing such a response is obtained by considering free electrons. Those are treated in the classical limit, as particles which do no interact with each other, just characterized by their charge, e, and the average relaxation time $\tau_m = 1/\gamma_m$. The damping constant, γ_m, accounts for electron scattering with the ionic background. The motion of the electrons subjected to an electric field $\mathbf{E}$ is described by

$$m_e \frac{d^2\mathbf{r}}{dt^2} + m_e \gamma_m \frac{d\mathbf{r}}{dt} = -e\mathbf{E}, \tag{1.24}$$

where m_e is the electron mass and the right term is just the electric contribution to the Lorentz force onto the electron. Under the application of an harmonic field $\mathbf{E} = \mathbf{E}_0 e^{-i\omega t}$, the motion has the same temporal dependence and the current associated to the moving electrons can be written as $\mathbf{J}_{\text{cond}} = i\omega N e\mathbf{r} = \sigma_{\text{cond}}(\omega)\mathbf{E}$. The conductivity $\sigma_{\text{cond}}(\omega)$ reads $\sigma_{\text{cond}}(\omega) = \frac{i\omega N e^2}{m_e(\omega^2 + i\gamma_m \omega)}$,where N_e is the density of conduction electrons in the system. The electric permittivity $\epsilon_{\text{cond}}(\omega)$ of such a system is given by

$$\epsilon_{\text{cond}}(\omega) = 1 + \frac{i\sigma_{\text{cond}}(\omega)}{\omega\epsilon_0} = 1 - \frac{\omega_p^2}{\omega^2 + i\gamma_m\omega}. \tag{1.25}$$

Note that we have introduced the plasma frequency $\omega_p = N_e e^2/(\epsilon_0 m_e)$. Eq. (1.25) is known as the Drude dielectric function. This model constitutes a moderately accurate approach for describing intraband processes in metals, since it only includes the purely free charge description within the conducting band. At high frequencies, the boundary between bound and free, or valence and conduction, charges blurs and interband transitions become important. The contribution of valence electrons can be introduced by means of new terms in the permittivity given by Eq. (1.25). These emerge from an equation of motion similar to Eq. (1.24) but with an additional term $m\omega_j^2\mathbf{r}$ representing the binding of the valence electrons. This procedure provides an expression for $\epsilon(\omega)$, which reads

$$\epsilon(\omega) = 1 - \frac{\omega_p^2}{\omega^2 + i\gamma_m\omega} + \sum_j \frac{\tilde{\omega}_j}{\omega_j^2 - \omega^2 - i\gamma_m\omega}, \tag{1.26}$$

where we introduced an effective $\tilde{\omega}_j$, associated to the natural frequency of an interband transition, which would depend on the effective mass and density of electrons. Here we obtain the usual expression for the electric permittivity of a metal, where bound and free contributions become apparent. Usually, at operating frequencies below the plasma frequency where such systems show explicitly their metallic behavior ($\mathrm{Re}\{\epsilon(\omega)\} < 0$), the bound part is usually replaced by a constant ϵ_∞ that effectively accounts for the tails of those resonances beyond ω_p.

1.4.2. Plasmonic modes

When we consider a bulk metallic medium, the response of the system is built on both transversal and longitudinal oscillations of the electron gas. Travelling plane waves inside the plasma are possible at frequencies larger than the plasma frequency $\omega > \omega_p$, whereas longitudinal modes correspond to the collective oscillation of the free electron gas at $\omega = \omega_p$ ($\epsilon_{\text{cond}}(\omega_p) \simeq 0$). If our system presents boundaries, the continuity exigences for the Maxwell's equations fields induce the advent of new modes in the system. The simplest configuration is a planar interface between two different media, dielectric and metallic. The permittivity mismatch at the interface supports the existence of plasmonic modes, EM waves confined to the surface. In a plane non-dispersive dielectric-metal interface, the dispersion relation of the surface plasmon mode (SP)[9] reads

$$k_{\text{SP}} = \frac{\omega}{c}\sqrt{\frac{\epsilon_d \epsilon(\omega)}{\epsilon_d + \epsilon(\omega)}}, \tag{1.27}$$

where ϵ_d is the relative electric permittivity of the dielectric medium. SPs are transverse magnetic modes (the magnetic component is perpendicular to the surface) and must fulfill $\epsilon_d \epsilon(\omega) < 0$ and $\epsilon_d + \epsilon(\omega) < 0$, conditions satisfied by metals at frequencies below ω_p.

In Figure 1.2(a), we represent the dispersion relation of the SPs for a Ag-dielectric constant background ($\epsilon_d = 2$) interface, where Ag has been modeled through a Drude-like permittivity with parameters $\epsilon_\infty = 9.7$ eV, $\hbar\omega_p = 8.91$ eV and $\hbar\gamma_m = 0.06$ eV. Black line plots the so called *light line*, that corresponds to the wavevector of travelling plane waves in the dielectric medium $k = \sqrt{\epsilon_d}\left(\frac{\omega}{c}\right)$. Red and blue lines show the real and imaginary parts of the in-plane component of the SP wavevector, k_{SP}. For frequencies below the surface plasmon frequency[10], $\omega_{\text{SP}} = \omega_p/\sqrt{\epsilon_d + \epsilon_\infty}$, SPs travel along the interface with

---

[9] Those modes are also known under the name Surface Plasmon Polaritons, derived from their nature where both EM field and electrons oscillations are mixed.

[10] We remark that throughout the different figures in the thesis, we will use the convention $\hbar = 1$ for axes related to frequency.

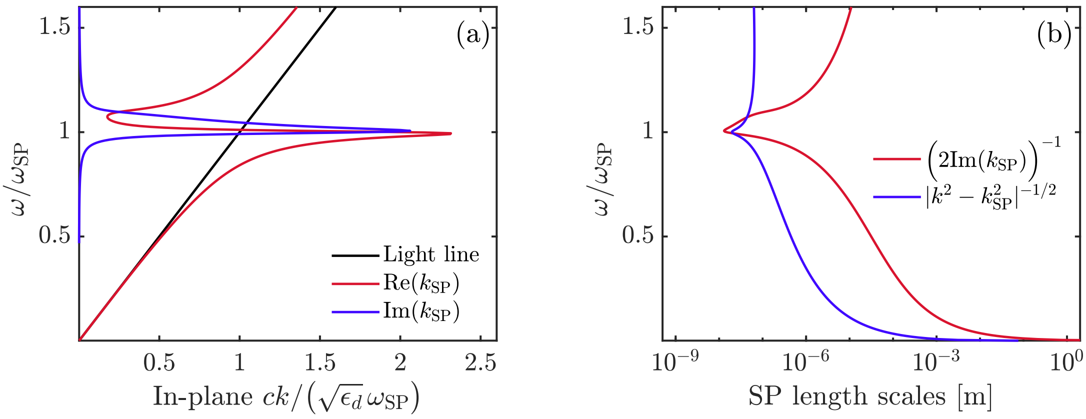

Figure 1.2: SPs resonances. (a) Dispersion relation of SPs propagating in a Ag-dielectric interface. Black line plots the dispersion relation for free space plane waves. Red and blue display the real and imaginary parts of the SP in-plane vector component, k_{SP}, respectively. (b) SPs length scales. Red line shows the propagation length of the SP and blue line represents the decay in the perpendicular direction given by the inverse of the out-of-plane k component.

a wavevector larger than the corresponding to frequency ω in free-space. This means that the SPP cannot be excited directly by an incident plane wave due to momentum mismatch and that the out-of-plane wavevector component $k_\perp = \sqrt{k^2 - k_{\mathrm{SP}}^2}$ has a dominant imaginary part, making the SP mode confined to the interface. For $\omega \ll \omega_{\mathrm{SP}}$, $k_{\mathrm{SP}} \approx k$ and therefore the mode is light-like, i.e. is barely confined. As we reach larger frequencies, the dispersion relation suffers a bending, and the mode acquires an almost electrostatic character $d\omega/dk \approx 0$ at ω_{SP}, that satisfies $\epsilon(\omega_{\mathrm{SP}}) + \epsilon_d = 0$. Due to the lossy nature of metals, there is an upper limit for k_{SP} and a backbending is observed in the dispersion relation. On the other hand, $\mathrm{Im}\{k_{\mathrm{SP}}\}$ reaches a maximum exactly at $\omega = \omega_{\mathrm{SP}}$. Therefore, there is a tradeoff between the maximum confinement and the losses of the system, since the character of the surface plasmon at this limit frequency is very leaky. The spatial confinement and propagation characteristics of SPs derive directly from the different components of the modal wavevector. Both the propagation length of the plasmon, $(2\mathrm{Im}\{k_{\mathrm{SP}}\})^{-1}$ and the exponential decay length $|k_\perp|^{-1}$, plotted in Figure 1.2(b), are minimum at the surface plasmon frequency. For frequencies beyond ω_{SP}, the backbending makes the dispersion relation back to the left-side of the light-line, indicating that the mode propagates inside the material, and the solution resembles that of a dielectric-dielectric interface, corresponding to a Brewster mode (a zero in the corresponding Fresnel coefficient).

The manipulation of boundaries between dielectric and metallic media permits the access to a myriad of EM modes that present plasmonic features. Finite systems can support the existence of plasmonic modes and those have the ability of confining them into finite volumes, giving rise to localized surface plasmon resonances (LSPs). As explained above, the conditions for existence of LSPs emerge from the analysis of the solutions of Maxwell's equations for certain boundary conditions, determined by the geometry of the system. Of course, finding a general solution is far from being trivial, but we can gain insight by considering that the quasistatic limit applies in the nanoscale.

Quasistatics refers to a limit where the spatial length of the system is small compared to the wavelength. This situation, typically in the near-field limit, provides the assumption that the material response is simultaneous [55, 56], yielding the approximation in the velocity of the interaction $c \to \infty$. Hence, as retardation effects do not play a significant role, the temporal and the spatial derivatives in Maxwell's equations are decoupled each other. In our interest, the electric field, $\mathbf{E}(\mathbf{r}, t)$, becomes irrotational and the problem is understood just after finding the scalar potential, $\Phi(\mathbf{r}, t)$ which satisfies the Poisson's equation, and in absence of external charges, $\nabla \cdot \epsilon \nabla \Phi = 0$. The spatial profile of the fields is then instantaneous, just modulated by the time-dependent factor $e^{-i\omega t}$.

Due to its simplicity, we consider as an example the problem of how a nanometric metallic wire, (with its longitudinal axis along z-direction and its section in the xy plane) with radius R, scatters a plane wave. We consider the metallic particle embedded in a dielectric with permittivity ϵ_d. In the quasistatic limit, the plane wave can be approximated by an electric field with constant spatial profile over the nanoparticle extension $\mathbf{E}_0 = E_0 \hat{\mathbf{x}} e^{-i\omega t}$, and the scalar potential outside the wire ($r > R$) has the form

$$\Phi(r > R) = -E_0 r \cos(\phi) - E_0 \frac{R^2}{r} \frac{\epsilon(\omega) - \epsilon_d}{\epsilon(\omega) + \epsilon_d} \cos(\phi), \tag{1.28}$$

where ϕ is the azimuthal angle in the xy plane. It is clear that the second term provides an scattering term which means that free-space plane waves are able to couple to LSPs modes in small particles. In Figure 1.3(a) we plot the spatial profile of the field enhancement in the quasistatic limit for the metallic nanowire ($R = 20\,\text{nm}$) under plane wave illumination ($\lambda = 476\,\text{nm}$), finding large values of $|E|^2/|E_0|^2 \approx 200$ and making explicit that LSPs of small particles collect EM energy from the far-field radiation into small volumes that break the diffraction limit.

In this sub-wavelength scenario, the scattering contribution can be understood as given by an induced dipole moment in the nanowire, $\boldsymbol{\mu}_{\text{ind}} = \alpha_{\text{w}}(\omega) \mathbf{E}_0$ in the form $\phi_{\text{sca}} \propto \frac{\boldsymbol{\mu}_{\text{ind}} \mathbf{r}}{r^2}$

where the polarizability $\alpha_{\mathrm{w}}(\omega)$ reads

$$\alpha_{\mathrm{w}}(\omega) = 2\pi\epsilon_0\epsilon_d R^2 \frac{\epsilon(\omega) - \epsilon_d}{\epsilon(\omega) + \epsilon_d}. \tag{1.29}$$

In the same way, the response of a nanosphere under a plane wave can be described in terms of a polarizability in the form

$$\alpha_{\mathrm{s}}(\omega) = 4\pi\epsilon_0\epsilon_d R^3 \frac{\epsilon(\omega) - \epsilon_d}{\epsilon(\omega) + 2\epsilon_d} \tag{1.30}$$

where it is clear the different scaling with the size and the different spectral position of the LSP resonance in a sphere with respect to the nanowire. In addition, notice that this resonance does not depend on size in the quasistatic limit. Only retardation effects introduce dependences of the LSP frequencies on the nanoparticle size [56]. In Figure 1.3(b) we plot the form of $\alpha_{\mathrm{s}}(\omega)$ for a Ag sphere embedded in a dielectric medium (same parameters as in Figure 1.2), where it is clear the typical lorentzian profile defined by the metal losses. The efficiency of the coupling can be quantified in terms of the absorption and scattering cross-sections for the sphere that read respectively

$$\sigma_{\mathrm{abs}}(\omega) = \frac{\omega}{\epsilon_0\sqrt{\epsilon_d}c}\mathrm{Im}\{\alpha_{\mathrm{s}}(\omega)\}, \qquad \sigma_{\mathrm{sca}}(\omega) = \frac{\omega^4}{6\pi\epsilon_0^2 c^4}|\alpha_{\mathrm{s}}(\omega)|^2 \tag{1.31}$$

The above expressions provide an intuition on how the scattering or absorption response dominate each other in different regimes. From the $\sigma_{\mathrm{abs}}/\sigma_{\mathrm{sca}} \propto (\lambda/R)^3$ dependence it is clear that absorption is more important as the particles are smaller in size. The excitation of LSPs by plane waves makes the interception area that the particle presents to the free-space radiation much larger than the spatial extension of the particle, as can be seen in Figure 1.3(c) which also shows that, for large R ($R \approx 30\,\mathrm{nm}$), scattering overcomes absorption[11].

Nevertheless, single metallic nanoparticles can support more than one plasmonic mode. If we consider larger metal structures, the quasistatic limit is not valid any more and the description of plane wave scattering in terms of a dipolar-like polarizability breaks. The significant phase changes of the driving field over the nanoparticle volume require of a full electrodynamic approach to describe the scattering process, the so known Mie theory [57]. Actually, the metallic resonator supports higher order resonances at larger energies, whose coupling with free space radiation is negligible in the limit $kR \ll 1$.

---

[11] We must indicate that the quasistatic limit offers a restricted version of the polarizability where extinction (both scattering and absorption) is just associated to absorption, and corrections must be included in the $\alpha_{\mathrm{s}}(\omega)$ expression in order to account for scattering contributions.

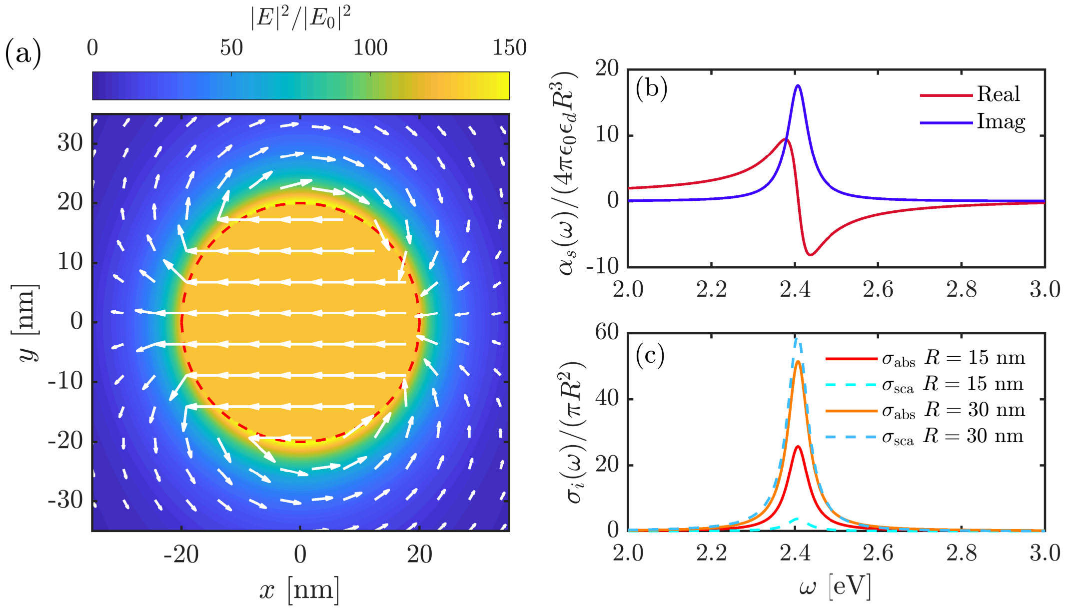

Figure 1.3: LSPs resonances. (a) Spatial distribution of field enhancement $|E|^2/|E_0|^2$ for a Ag wire (perimeter marked in red dashed line) at the frequency of the resonance $\epsilon(\omega) + \epsilon_d \approx 0$ ($\omega = 2.605$ eV, $\lambda = 476$ nm). White arrows represent the magnitude and direction of $\mathbf{E}$. (b) Normalized quasistatic polarizability of a Ag sphere ($R = 15$ nm). (c) Normalized quasistatic absorption (reddish solid lines) and scattering (azure dashed lines) cross-sections for Ag spheres of different size (indicated in the legend).

The mechanism that permits their excitation under plane wave illumination is based on retardation effects between the excitation and the electron response in the metal, making those modes not negligible compared to the lowest-order dipolar one in large particles [58]. As these higher order resonances are weakly coupled to free space radiation, by reciprocity, they radiate much less than the dipolar (bright) plasmon. This fact introduces the denomination of higher order resonances as dark modes, extremely important in the context of near-field phenomena. While plane waves couple inefficiently to them, QEs can interact with dark modes [59, 60].

The plasmon resonances of complex nanostructures formed by a group of individual finite components can be explained in terms of interactions between the plasmon resonances of the elementary constituents. The plasmonic hybridization method [61, 62] provides an elegant and intuitive picture in analogy with the molecular orbital theory. Imposing a Coulomb interaction between the primitive plasmon modes of each structure separately, the new modes are obtained from a Lagrangian description, that can be understood as superpositions of the original ones, and so on the energies associated to those, that can be both redshifted or blueshifted with respect to the originals. The elegance of the plasmon hybridization picture is limited by the need of numerical simulations as an input for the model. The Transformation Optics approach offered a route to derive analytically the optical response of complex structures by applying conformal mapping techniques to the geometry of the plasmonic structure [63], yielding an analytical solution of the electric field associated to the system resonances in agreement with the hybridization scheme [63, 64]. Under these ideas, the plasmonic modes of multiple structures have been investigated within analytical and quasi-analytical Transformation Optics approaches [23, 65–67].

1.4.3. Theoretical description of light-matter interactions

From the theoretical point of view, the issue of understanding the foundations of light-matter interaction requires of the full quantum description of both light and matter as well as their interaction. QED sets an exact full quantum field theory approach for treating the interaction between distributions of charged particles and EM fields, with photons and matter excitations (in general, excitons) as its building blocks. Nevertheless, its generality results in an imbalance for our purposes. Nanophotonics operates at *low* energies within the optical regime, involving macroscopic elements that also can display dispersive features in their response. Those specific characteristics can be treated within the mQED approach, that leads to a field quantization in large structures, determined by the solutions to classical macroscopic Maxwell's equations, contained in the Green's function.

In the previous section, we mentioned that, in the quasiresonant interaction limit, a QE in the two-level approximation is characterized by the set of excited-ground states ($|e; g\rangle$) and their transition frequency ω_{eg}. If an electric field with frequency ω interacts with a quantized two-level system (assuming $\omega \sim \omega_{eg}$), we remark two phenomena: absorption and emission. Absorption and stimulated emission processes are closely related since the presence of the field mediates the transition from the initial state to the other. However, there is another process, much more fascinating, the so-called spontaneous emission. In absence of EM fields or EM energy density, the QE can decay from its excited state to the ground one. To understand this process, we must realize that the QE does not constitute a system by itself but a compound formed by the QE and EM vacuum field. The concept of isolated system is no completely compatible with the description of a quantum system. Quantum nature makes customary the study of a system considering its interaction with the 'rest of the universe', encapsulated under the term *environment*.

The analysis of this problem considers the complete system, formed by the sub-system under our attention, $\mathcal{S}$, and the environment, $\mathcal{E}$. This approach is known as theory of open quantum systems. We emphasize that the general approach to this topic is far from being trivial and the separation $\mathcal{S} \longleftrightarrow \mathcal{E}$ becomes difficult when every energy scale in the problem is similar each other. As we will see, we avoid such complications and refer exclusively to the *Markovian* limit of the theory.

The states of the light-matter system are the tensor product of the two-dimensional space associated to the two-level system, $|e; g\rangle$, and the Fock states, $|n\rangle$, written in a shorthand notation as

$$|\mathrm{TLS}, n\rangle = |\mathrm{TLS}\rangle \otimes |n\rangle \,, \tag{1.32}$$

where the first position corresponds to the matter component and the second indicates the number of excitations in the EM field.

The spontaneous emission rate, γ, can be obtained from the dynamics of an initially populated excited state *weakly* coupled to a continuum of photonic modes devoid of photons. The Fermi's Golden Rule for the *total* decay of $|e, 0\rangle$ into the EM continuum reads [33, 68]

$$\gamma = \frac{2\pi}{\hbar^2} \sum_{\mathbf{q}} |\langle g, 1_{\mathbf{q}}| \hat{H}_I |e, 0\rangle|^2 \delta(\omega_q - \omega_{eg}), \tag{1.33}$$

where $\hat{H}_I$ is the interaction Hamiltonian of the system. The summation over $\mathbf{q}$ runs over the set of different field states $|g; 1_{\mathbf{q}}\rangle$ with one photon of energy $\hbar\omega_q$ and the QE in the ground state [55]. It offers an intuition about the *density of states*, a fundamental magnitude that characterizes the strength of light-matter coupling. This approach provides a microscopic origin of the spontaneous emission mechanism[12].

The multipolar classical Hamiltonian that describes the interaction between an electric field $\mathbf{E}$ and a neutral distribution of charges reads

$$H_{\mathrm{I}} = -\boldsymbol{\mu}\mathbf{E} - \frac{1}{2}(\mathbf{Q}\nabla)\mathbf{E} + ..., \tag{1.34}$$

where we have just shown the first two terms explicitly, where $\boldsymbol{\mu}$ and $\mathbf{Q}$ are the electric dipolar and quadrupolar moments of the charge distribution. Then, by the simple inspection of Eq. (1.34) it becomes apparent that the H_{I} dependence on both matter and

---

[12] We highlight the original version of this result, the spontaneous decay rate for an emitter in free space, given by Wigner and Weisskopf [69], since it sketched the road for the theoretical description of irreversibility in the quantum theory by using the continuum of modes, key of the theory of open quantum systems.

electric fields gives access to the tailoring of light-matter interactions. In the vicinities of a nanostructure, the solution of the Maxwell's equations would result in electric fields different to those of free space, as we have seen in the case of plasmons. The enhancement or suppression of the decay rates of QEs through the manipulation of $|\langle g, 1_{\mathbf{q}}| \hat{H}_{\mathrm{I}} |e, 0\rangle|^2$ is known as the Purcell effect. To measure the intensity of this effect, a figure of merit is the Purcell factor

$$P_f(\omega) = \frac{\gamma}{\gamma_0}, \tag{1.35}$$

which normalizes the decay rate to that of free space, γ_0. This result makes clear that the decay rate of an emitter is not its intrinsic property but it depends on its environment.

We can think of quantized excitations in matter in the simple picture of electrons confined in a box. The length scale of electron confinement has a quadratic relation with the wavelength of the emitted photon and energies in the optical regime correspond to spatial confinements around the nanometer scale, giving a large mismatch between both spatial parameters [70]. This mismatch leads to the small cross-sections of single QEs and prevents a fast radiative decay rate of the excited state. Plasmonic resonators are suitable to work as optical nanoantennas, confining the fields into small spaces and connecting very efficiently the near EM fields and radiation [71, 72].

If we consider the QE in the dipolar limit, the interaction Hamiltonian reads $\hat{H}_I = -\hat{\boldsymbol{\mu}}\hat{\mathbf{E}}$ and γ can be written [55]

$$\gamma = \frac{2\omega_{eg}}{3\hbar\epsilon_0}\mu^2\rho_\mu(\mathbf{r}, \omega_{eg}) \tag{1.36}$$

where $\mu = \langle e| \hat{\boldsymbol{\mu}} |g\rangle$ is the transition dipole moment and $\rho_\mu(\mathbf{r}, \omega_{eg})$ is the *local density of states* at $\mathbf{r}$, the position of the QE, and ω_{eg}, the QE natural frequency. This magnitude encodes the effects of the environment on the decay of the emitter and it can be expressed in terms of the EM dyadic Green's function [72] of the system (see section 1.2) $\mathbf{G}(\mathbf{r}, \mathbf{r}', \omega)$ as

$$\rho_\mu(\mathbf{r}, \omega) = \frac{6\omega}{\pi c^2}\mathrm{Im}\{\hat{\mathbf{n}}_\mu \mathbf{G}(\mathbf{r}, \mathbf{r}, \omega)\hat{\mathbf{n}}_\mu\}, \tag{1.37}$$

where $\hat{\mathbf{n}}_\mu$ accounts for the orientation of the dipole moment.

In order to make clear the link between Eqns. (1.33) and (1.36), if we assume a lossless, closed environment, $\mathbf{G}(\mathbf{r}, \mathbf{r}, \omega)$ can be expanded as a sum of the normal modes of the system $\mathbf{u}_{\mathbf{q}}(\mathbf{r}, \omega)$ that satisfy the wave equation $\nabla \times \nabla \times \mathbf{u}_{\mathbf{q}} - (\omega_q^2/c^2)\mathbf{u}_{\mathbf{q}} = 0$ and a normalization $\int \mathbf{u}_{\mathbf{q}}\mathbf{u}^*_{\mathbf{q}'}\mathrm{d}^3\mathbf{r} = \delta_{\mathbf{q},\mathbf{q}'}$ [55]. Then, the density of states reads

$$\rho_\mu(\mathbf{r}, \omega) = 3\sum_{\mathbf{q}} \Big[\hat{\mathbf{n}}_\mu(\mathbf{u}_{\mathbf{q}}(\mathbf{r})\mathbf{u}^*_{\mathbf{q}}(\mathbf{r}))\hat{\mathbf{n}}_\mu\Big]\delta(\omega_q - \omega). \tag{1.38}$$

From this expression it becomes clear that γ will be enhanced in environments in which the field component of the normal modes at the emitter position becomes very large. Since those satisfy the normalization condition, the extremely confined modes typical of plasmonic resonances emerge explicitly as good candidates for the spontaneous decay modification due to the direct dependence of ρ_μ on their local amplitude. The extension of the normal mode decomposition of EM environments to lossy, dispersive, open systems have been an intricate problem during several decades, but recent results have been obtained in the fields of mQED, QNMs and pseudomode descriptions [38, 42]

1.4.4. Regimes of light-matter interaction

In order to distinguish the different regimes of the interaction, we proceed to analyze the dynamics of the excited state of a QE, coupled with a single EM mode, labelled as λ. We write the Hamiltonian that controls the dynamics of such sub-system, which reads

$$\hat{H}_{\mathcal{S}} = \hbar\omega_{eg}\hat{\sigma}^\dagger\hat{\sigma} + \hbar\omega_\lambda\hat{a}_\lambda^\dagger\hat{a}_\lambda + \hbar g_\lambda(\hat{\sigma}^\dagger\hat{a}_\lambda + \hat{a}_\lambda^\dagger\hat{\sigma}), \tag{1.39}$$

where we consider g_λ, the coupling between the QE and the EM mode. This is the well-known Jaynes-Cummings Hamiltonian, obtained from the more general, Rabi one, by performing the Rotating Wave Approximation, that assumes $\omega_{eg}, \omega_\lambda >> g_\lambda$ and no counter-rotating or non-conserving excitations $\hat{a}_\lambda^\dagger\hat{\sigma}^\dagger$ or $\hat{a}_\lambda\hat{\sigma}$ terms appear. This Hamiltonian describes $\mathcal{S}$, consisting of a QE and a single EM mode, as a closed system. Through the cavity mode λ, the system interacts with the environment . As anticipated, this interaction is described in the Markovian limit. The system is no longer described in terms of pure states and the density matrix operator needs to be used (of the form $\hat{\rho}_{\mathcal{S}} = |\psi\rangle\langle\psi|$ for a pure state). The dynamics of the system is described by the Liouville von Neumann master equation [73]

$$\frac{d}{dt}\hat{\rho}_{\mathcal{S}} = \frac{-i}{\hbar}[\hat{H}_{\mathcal{S}}, \hat{\rho}_{\mathcal{S}}] + \frac{\gamma_\lambda}{2}\Big(2\hat{a}_\lambda\hat{\rho}_{\mathcal{S}}\hat{a}_\lambda^\dagger - \{\hat{a}_\lambda^\dagger\hat{a}_\lambda, \hat{\rho}_{\mathcal{S}}\}\Big), \tag{1.40}$$

where the last term (weighted by γ_λ) corresponds to the Lindblad superoperator describing the Markovian coupling between the EM mode λ and the environment as a reservoir[13]. This means that, at any time, $\mathcal{E}$ is not altered by its interaction with $\mathcal{S}$.

The dynamics of the excited state of the emitter in a spontaneous emission configuration (single excitation manifold) given by Eq. (1.40) is equivalent to that obtained from

---

[13] Note that the interaction of the QE with free propagating fields in the environment can also be accounted for in Eq.(1.40), omitted here for simplicity.

the Schrödinger equation for the non-Hermitian Hamiltonian resulting by replacing ω_λ by $\omega_\lambda - i\gamma_\lambda/2$ in Eq. (1.39) [74, 75]. Following this procedure, for $|\psi(0)\rangle = c_e(0)|e\rangle = |e\rangle$, we obtain

$$\frac{d}{dt}c_e(t) = -\int_0^t c_e(\tau)K(\tau - t)d\tau \tag{1.41}$$

where the Kernel $K(\tau - t) = \int_0^\infty J(\omega)e^{i(\omega-\omega_{eg})(\tau-t)}d\omega$ is written in terms of the spectral density $J(\omega)$ that contains information about the light-matter coupling, with dependence on both QE and EM mode parameters[14]. For the case of the Hamiltonian in Eq. (1.39), $J(\omega)$ has the form of the imaginary part of a Lorentzian [74]

$$J(\omega) = \frac{g_\lambda^2}{\pi}\frac{\gamma_\lambda/2}{(\omega - \omega_\lambda)^2 + \frac{\gamma_\lambda^2}{4}}. \tag{1.42}$$

In order to discriminate between the different coupling regimes, we analyze the eigenenergies and the dynamics of the system under the described approach. When the effective coupling between light and excitons is lower than the energies and the frequencies of the loss channels associated to those transitions, interactions between light and matter occur in the weak coupling regime. If we consider that the energy exchange, represented by g_λ is much lower than the losses γ_λ, we can assume the flatness of $J(\omega)$, the structure of the kernel for $\omega_{eg} = \omega_\lambda$ reduces to

$$K(\tau - t) \approx J(\omega_{eg})\int_0^\infty e^{i(\omega-\omega_{eg})(\tau-t)}d\omega, \tag{1.43}$$

and the temporal dynamics, using Eq. (1.42), reduces to

$$\frac{d}{dt}c_e(t) \approx -\frac{2g_\lambda^2}{\gamma_\lambda}c_e(t). \tag{1.44}$$

Eq. (1.44) implies an irreversible exponential decay[15]. In this limit, the interaction can be interpreted as a perturbation that modifies the long-time decay, modifying the spontaneous decay rate of the QE and the population of the excited state that can be written in terms of the density of states linked to that EM environment with $\gamma = 4g_\lambda^2/\gamma_\lambda = 2\pi J(\omega_{eg})$ as the decay rate of the excited state. Invoking Eq. (1.35), $P_f = 2\pi J(\omega_{eg})/\gamma_0$ is the quantification of the effect observed by Purcell [8] for the particular case of a QE coupled to a single EM mode. In arbitrary environments, the spectral density can be written in terms of the Green's function [55]

$$J(\omega_{eg}) = \frac{\omega_{eg}^2\mu^2}{\pi\hbar\epsilon_0 c^2}\mathrm{Im}\{\hat{\mathbf{n}}_\mu\mathbf{G}(\mathbf{r},\mathbf{r},\omega_{eg})\hat{\mathbf{n}}_\mu\}, \tag{1.45}$$

---

[14] Apart from the references given in the main text, we suggest the derivation of this approach in Ref. [76] to the reader.

[15] It becomes clear the meaning of the term *Markovian* as weak limit in the reservoir-mode coupling.

and from the form of γ, it is clear that

$$P_f = \frac{J(\omega)}{J_0(\omega)} \tag{1.46}$$

where $J_0(\omega) = \omega^3\mu^2/(6\pi^2\hbar\epsilon_0 c^3)$ is the free space spectral density, given by the three-dimensional dyadic Green's function $\mathrm{Im}\{\mathbf{G}(\mathbf{r},\mathbf{r},\omega)\} = \omega/(6\pi c)$. The last expression constitutes a central result that we will use in this thesis, since the enhancement of the density of states in a given environment is determined by the Purcell factor, also known in literature as *generalized* Purcell Factor [37, 77].

We can go further and inspact the eigenenergies of the Hamiltonian, including both the cavity and the emitter losses, that we omitted in Eq. (1.40) for simplicity. Then, we define the complex frequencies, $\tilde{\omega}_{eg} = \omega_{eg} - i\gamma_{eg}/2$ and $\tilde{\omega}_\lambda = \omega_\lambda - i\gamma_\lambda/2$. The eigenfrequencies for the 2×2 matrix read

$$E_\pm = \frac{\tilde{\omega}_{eg} + \tilde{\omega}_\lambda}{2} \pm \frac{1}{2}\sqrt{(\tilde{\omega}_{eg} - \tilde{\omega}_\lambda)^2 + 4g_\lambda^2}. \tag{1.47}$$

In Figure 1.4(a), we represent the dynamics of the population of the excited state for different values of the coupling g_λ, as indicated in the legend, with $\omega_{eg} = \omega_\lambda$, $\gamma_{eg}/\omega_{eg} = 0.02$ and $\gamma_\lambda/\omega_{eg} = 0.1$. When the cavity coupling is zero, the decay is governed by the loss rate, γ_{eg}, following an exponential law (blue line), as it follows from the dynamics in the Markovian case. When the strength of the interaction increases, the dynamics of the exciton cannot be characterized by an exponential decay (red line). We enter in the so called intermediate coupling regime, that can be explained through higher order perturbation theory applied to the system. The Markovian approximation for the exciton dynamics breaks and the decay is monotonic but not exponential [78, 79]. Finally, when the coupling overcomes losses, the dynamics of the excited state population is not a decay anymore, but reproduces several oscillations, indicating the new hybrid nature of the system. In Figure 1.4(b), we plot the real part of the eigenfrequencies of the system as a function of the detuning for a fixed coupling ($g_\lambda/\omega_{eg} = 0.1$). Dashed lines are the frequencies of each excitation. When the QE is off-resonance with respect the cavity mode, the eigenfrequencies are similar to that of the constituents, but an anticrossing between the energy lines appear in resonance, characteristic of the *strong coupling* regime. The separation between the energies gives Ω_R, the Rabi frequency of the population oscillations. The states of the system within the so called strong coupling regime are hybrid light-matter states called polaritons. Whereas an isolated emitter has a frequency that determines its absorption or emission spectra, when both light and matter excitation components are in resonance, the spectra presents two maxima,

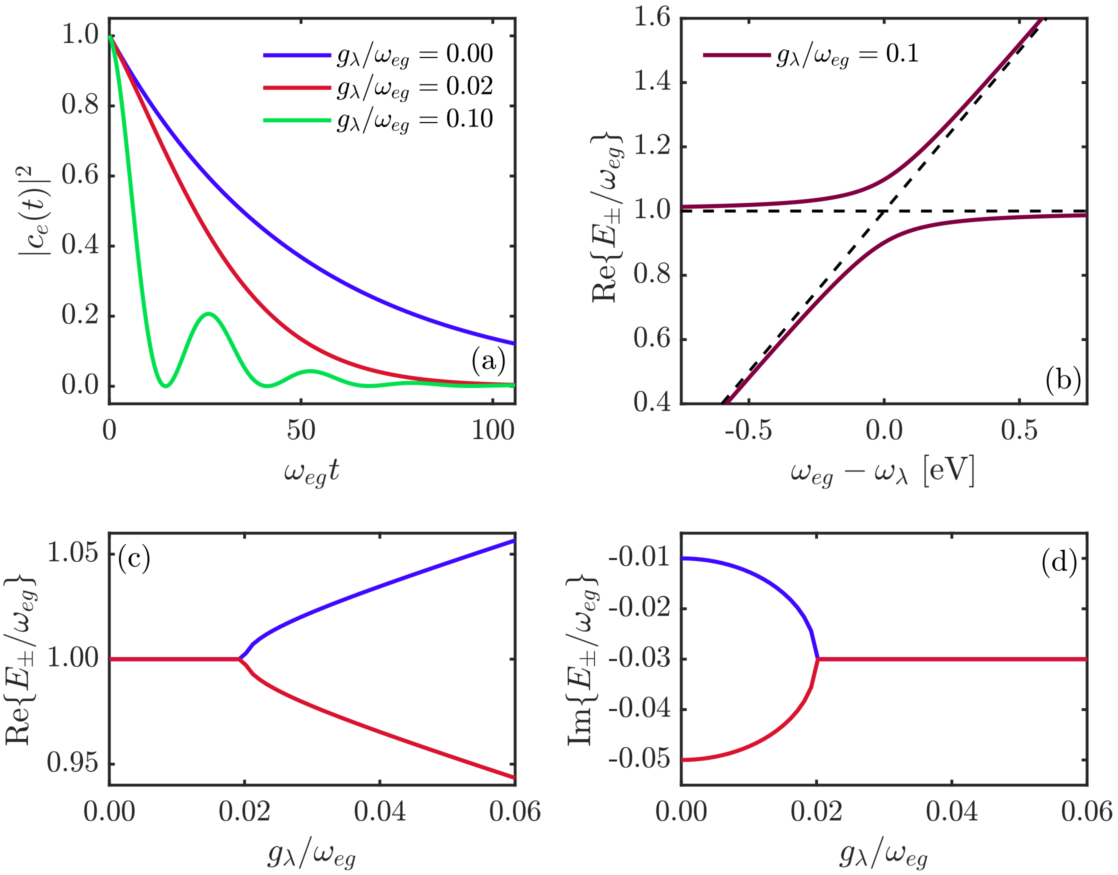

Figure 1.4: Regimes of light-matter coupling. (a) Population dynamics of the excited state for different coupling strengths. (b) Real part of eigenfrequencies $E_\pm$ as a function of the detuning between ω_{eg} and ω_λ. (c,d) Real and imaginary parts of $E_\pm$ as a function of the coupling strength for the zero-detuning case.

corresponding to the upper and lower polaritons, whose energies are given by the curves in Figure 1.4(b). As we can anticipate, we will deal with hybrid states with different excitonic and plasmonic components, plexcitons or plasmon-exciton polaritons [80, 81]. Panels (c) and (d) in Figure 1.4 show how the eigenfrequencies depend on the coupling for the resonant case. It is clear that below a certain value, the real part of $E_\pm$ does not change while the imaginary part is modified starting from $\gamma_\lambda/2$ and $\gamma_{eg}/2$ for the $g_\lambda/\omega_{eg} = 0$ case. This corresponds to the regime of weak coupling. When the coupling exceeds the losses, the system enters in the strong coupling regime where the splitting arises and increases linearly for large values of g_λ.

1.4.5. Platforms for the study of light-matter interactions

Up to this point, we have referred to how the environment modifies the emission properties of QEs, and, specifically, plasmonic environments provide a large field enhancement that support the modification of the density of states. Not surprisingly, there are more scenarios in which the lifetime of excited states of QEs can be changed. In this final section to the introductory chapter, we are going to overview different platforms widely used during the last decades in the research of spontaneous emission modification, as well as on the type of emitters used.

The field of cQED relies on the manipulation of matter excitations through the interaction with EM modes of a *cavity*. The concept cavity is tremendously general, but it sets a tag: the modes will not be the free-space ones. As we already commented, the imposition of boundary conditions on the set of Maxwell's equations grounds the emergence of new modes, as we have seen in metallodielectric interfaces. Although our treatment of light-matter interactions throughout this thesis does not properly rely on cQED concepts, the large scope of this field invite us to provide a brief summary about those and their link to our results.

The easiest route to engineer new EM modes is to bring face to face two mirrors, separated by a distance L_{cav} on the order of the wavelength, λ, associated to the excitonic transition of interest. This system constitutes an optical Fabry-Perot cavity and it contains the set of parameters that determine the properties of any cavity. Modes are characterized by their frequency, ω_n, the quality factor, Q_n, and the mode volume V_n. Resonances are given by the condition in which standing waves appear in the cavity, so $\lambda_n/2 = \pi c/\omega_n \propto L_{\text{cav}}$. Q_n is defined as ω_n/γ_n, where γ_n are the losses of the cavity. The boundaries in this type of system impose the discretization of modes in a three-dimensional system, so the modes are quite similar to those of the bulk material, or light-like, with an spatial extension related to λ_n, and consequently the mode volume $V_n \propto \lambda_n^3$. The cavity mode is said to bounce back and forth between the mirrors, leading to a enhancement of the interaction with the emitter placed inside the cavity. We highlight the particular interest on both Q_n and V_n since they characterize the cavity mode. The central target of cavity-based modifications of SE has been creating cavities with the highest Q_n/V_n, since the Purcell factor, $P_f \propto Q_n/V_n$ [82]. The spatial extension of the mode, described by V_n, is linked to the amplitude of the electric field as $V_n = \max(\epsilon_0 E^2)^{-1} \int_V \epsilon E^2 dV$[16], relating the small mode volumes of highly confined fields

---

[16] The dispersive and lossy nature of plasmonic resonances makes difficult the proper characterization of the mode volume, giving rise to detailed discussions [82, 83], as well as its definition in the context

to the enhancement of emission. Fabry-Perot cavities made of a pair of mirrors have been widely used in the research of cQED and quantum optics fields, where the nature of matter and radiation interaction has been examined in detail with atoms and quasiperfect cavities that allow the determination of coupling and decay channels [13, 85].

Mirror-mirror systems typically operate in very specific regimes of microwave length scales and cryogenic temperatures so those difficulties to manipulate and extent their applicability turned the interest to solid state cavities in the context of nanophotonics. Plasmonic systems, already discussed, are widely used in the study of emission enhancement, even when their lossy character prevent in general the achievement of very large quality factors, with typical values $Q \sim 10-100$, compensated by their ultrasmall mode volumes [86, 87] on the order of nanometer and picometer scales. On the other hand, the use of periodicity in the dielectric constant on non-lossy materials gives place to the emergence of photonic crystals [19], which can create photonic bandgaps in the same way as electrons travelling in a periodic potential. In order to take advantage of the periodic environment, the wavelength of the light has to be comparable to the periodicity of the lattice. The use of 1D periodically-structured semiconductor media in the optical regime makes possible to design Bragg gratings with large reflectances that can be used as effective mirrors. This is the procedure used in planar semiconductors cavities, where the photon is confined in one direction while extended in the other two, usually in the infrared regime for the study of polariton formation [88] and emission characteristics [89]. Micropillar configurations made of cylindrical Bragg reflectors provide larger confinement of the cavity mode preventing propagation in the radial direction through total internal reflection [90], presenting large quality factors, ranging from $Q \sim 10^3$ to ultrahigh $Q \sim 10^{10}$ in spherically designed nanoresonators [91]. Furthermore, three-dimensional material engineering of the material allow the presence of defects in the structure that lead to light confinement. Arrays of defects permit the propagation of light along an effective waveguide of holes [92, 93] whereas localized defects are able to trap light [94]. The capabilities of photonic crystals can be exploited to the study the modification of SE, since emission from QEs whose resonance frequency lies within the band gap can be enhanced or suppressed when those are placed in the defect or in the bulk crystal, respectively.

The last component of the study of light-matter interaction is the matter component. The election of the optimal emitter depends on the desired final performance. The exploitation of light-matter interactions for the obtention of quantum light would rely

---

of quasinormal mode theory [84].

on QEs whose de-excitation is mainly followed by the emission of a photon. Therefore, since the dissipation mechanisms can be characterized as radiative or non-radiative, non-radiative losses should be overwhelmed by radiative ones. The more complex energy and state structure, the more dissipation channels. On the other hand, if the final goal is to achieve the entrance into the strong coupling regime, large transition moments are desired. Finally, another feature to be considered is the integration of the QE in the nanostructure. As a simple summary, atoms constitute a very suitable system in quantum optics, with a strongly antibunched output of light while, due to their simplicity, they do not show large decoherence effects and present narrow linewidths ($\sim \mu$eV). They usually operate at low temperatures and presents difficulties to be integrated in solid state cavities, been widely used in microwave (rubidium) and optical (cesium) mirror-mirror cavities. On the other hand, the more complex structure of molecules and quantum dots reveal larger decoherence mechanisms (couplings between the different energy structures present in the system) and therefore, larger linewidths with respect to atoms ($\sim$ meV) and lower quantum yields $\varphi = \gamma_{\mathrm{r}}/(\gamma_{\mathrm{r}} + \gamma_{\mathrm{nr}})$, due to the importance of non-radiative mechanisms. At the same time, their characteristics make them suitable for isolation and manipulation in photonic and plasmonic optical cavities. Organic molecules, despite their relatively large non-radiative dissipation rates, have remarkable properties as QEs, with large transitions moments (a few Debye) and operability at room temperature. Quantum dots also present large dipole moments and their main benefit is the possibility of tuning their properties through design. The complexity of their energy structure makes them more predisposed to suffer of non-radiative mechanisms, that can be compensated through their operation at low temperatures.

2

Single excitons in a plasmonic cavity

In this chapter, we investigate the interaction between the surface plasmons (SPs) supported by a nanoparticle-on-mirror (NPoM) cavity and single quantum emitters (QEs) of two types: those sustaining dipolar, and those supporting quadrupolar excitons. We present a Transformation Optics (TO) approach which allows us to obtain analytical expressions for all the physical magnitudes characterizing the hybrid QE-SP system. In this context, TO allows the quantization of the plasmonic modes supported by the NPoM cavity and the parametrization of the QE-SP interaction Hamiltonian, in a similar way as other recently proposed methods [38, 41, 95]. Our approach sheds deep insights into two different plasmon-exciton phenomena: the near-field population dynamics in a spontaneous decay configuration and the far-field scattering spectra under dark-field laser illumination. Our model also accounts for finite-size effects associated with both excitonic charge distributions. Throughout the chapter, the differences and similarities in the light-matter coupling phenomenology for dipolar and quadrupolar transitions are discussed and analyzed. Despite the fact that a full three-dimensional (3D) TO framework for dipolar point-like sources is available [96], we employ here its two-dimensional (2D) version [64]. There are three reasons justifying this choice. First, only the latter is fully analytical, which is instrumental for the description of quadrupolar transitions [97] and finite-sized QEs. Second, the 2D theory can be pushed beyond purely quasistatic approximation [98], which allows computing the SP dipole moments and therefore, far-field spectra for the QE-SP system. Finally, as we also show, the comparison between 2D and 3D results reveals that the 2D treatment reproduces all the phenomenology reported in 3D [81].

2.1. The approach: Transformation Optics

The invariance of Maxwell's equations under coordinate transformations is the root of the TO approach to control and manipulate electromagnetic (EM) fields. This fact opened the road to the inverse design of the EM response of a material, exchanging the material and spatial properties of the system. Then, TO provides the link between the desired EM phenomenon and the material response which is required for its realization [99, 100]. The form-invariance of Maxwell's equations satisfies that, for any arbitrary system with coordinates $\mathbf{r}' = (x', y', z')$ and characterized by the material parameters $\boldsymbol{\epsilon}', \boldsymbol{\mu}'$, the curl equations read

$$\nabla' \times \mathbf{E}' = -i\omega\boldsymbol{\mu}'\mathbf{H}' \tag{2.1}$$

$$\nabla' \times \mathbf{H}' = i\omega\boldsymbol{\epsilon}'\mathbf{E}'. \tag{2.2}$$

This primed geometry can be transformed in the form $\mathbf{r} = f(\mathbf{r}')$, and the form-invariance provides

$$\nabla \times \mathbf{E} = -i\omega\boldsymbol{\mu}\mathbf{H} \tag{2.3}$$

$$\nabla \times \mathbf{H} = i\omega\boldsymbol{\epsilon}\mathbf{E}. \tag{2.4}$$

Then, the fields are spatially shaped in the same way as the material parameters, yielding the form for $\boldsymbol{\epsilon}, \boldsymbol{\mu}$ [101, 102]

$$\boldsymbol{\epsilon} = \frac{\mathbf{T}_f\boldsymbol{\epsilon}'\mathbf{T}_f^T}{\det \mathbf{T}_f}; \quad \boldsymbol{\mu} = \frac{\mathbf{T}_f\boldsymbol{\mu}'\mathbf{T}_f^T}{\det \mathbf{T}_f} \tag{2.5}$$

where $(\mathbf{T}_f)_{ij} = \partial x_i/\partial x_j'$ is the Jacobian matrix of the transformation.

The advent of TO came together with that of optical metamaterials, devised with the objective of moulding EM phenomena beyond the constraints of natural material features. Those are artificial materials whose properties are determined by their structure, where the collective response of their sub-wavelength constituents yields a variety of effective permittivities and permeabilities, and a route for such design is provided by TO. The use of TO has been focused in many fields, not only in the context of optics with examples as cloaks [103] and field concentrators [65] but also beyond electromagnetics, where TO has been revealed as a tool in the conception of mechanical metamaterials and seismic cloaking [104–106]. TO and, particularly, conformal mapping (see below), has been also used to obtain analytical solutions of Maxwell's equations in different nanophotonic systems, such as crescents [66, 107], rods [108], dimers [64, 109], bow-ties [110] or tripods [111]. The spirit of this method was already considered in the initial proposal of the approach, which suggested that coordinate transformations would result in easing the numerical solution of Maxwell equations in problems with very different length scales [101].

2.1.1. Conformal mapping

The fundamentals of TO are also related to conformal mapping techniques. The nature of two-dimensional systems makes available the theory of complex variable functions, widely used in the context of solving not only Maxwell's equations, but many types of differential equations with boundary conditions [112]. Following this route, the behavior of fields in complex geometries have been tackled spanning electromagnetics, heat, hydrodynamics or elasticity. Conformal transformations are two-dimensional analytical maps that preserve the angles between the original and transformed geometries, which in the complex plane refers to analytic functions $f(\varrho) = u(x,z) + iv(x,z)$, with $\varrho = x + iz$. We anticipate here the notation that we will use in the following sections. Instead of referring to the complex number with the usual convention z, we denote the Cartesian space in our reference system as (x,z). The conditions that enclose the analyticity are the Cauchy-Riemann equations

$$\frac{\partial u(x,z)}{\partial x} = \frac{\partial v(x,z)}{\partial z} \quad \text{and} \quad \frac{\partial u(x,z)}{\partial z} = -\frac{\partial v(x,z)}{\partial x}. \tag{2.6}$$

An important consequence in terms of simplicity arises from the fulfillment of Cauchy-Riemann equations. Considering the in-plane transformation $T(\varrho) = \varrho' = x' + iz'$, the electric permittivity (and thus the magnetic permeability) can be written

$$\boldsymbol{\epsilon}' = \epsilon'\mathbf{I} = \frac{\epsilon}{\det \hat{T}(\varrho)} \begin{pmatrix} \frac{\partial x'}{\partial x} & \frac{\partial x'}{\partial z} \\ \frac{\partial z'}{\partial x} & \frac{\partial z'}{\partial z} \end{pmatrix} \mathbf{I} \begin{pmatrix} \frac{\partial x'}{\partial x} & \frac{\partial z'}{\partial x} \\ \frac{\partial x'}{\partial z} & \frac{\partial z'}{\partial z} \end{pmatrix} = \frac{\boldsymbol{\epsilon}}{\det \hat{T}(\varrho)} \det \hat{T}(\varrho)\mathbf{I} \tag{2.7}$$

where $\mathbf{I}$ is the identity matrix. From Eq. (2.7), $\epsilon' = \epsilon$, offering the advantage that the in-plane permittivities (and permeabilities) remain unchanged after the transformation.

Furthermore, the differentiation of the Cauchy-Riemann equations yields the Laplace equation

$$\nabla^2 u(x,z) = 0, \quad \text{and} \quad \nabla^2 v(x,z) = 0, \tag{2.8}$$

so the real and imaginary parts of an analytic function $f(\varrho) = u(x,z) + iv(x,z)$ are harmonic. The importance of this equation is well known since many physical problems are described under its form. In particular, when considering nanometric length scales and optical frequencies, the quasistatic approximation applies and then the electric field can be written in terms of a potential that satisfies the Laplace's equation (see Section 1.4), which contains an intimate relation with the properties of conformal mapping. Suppose we are able to map conformally from the ϱ-plane to the ϱ'-plane, via $\varrho' = T(\varrho)$. Then, consider the electrostatic potential that satisfies $\nabla^2\phi(x,z) = 0$, which can be thought as an analytic function $g(\rho)$. We can define an analytic function $G(\varrho') = g(T^{-1}(\varrho')) = (g \circ T^{-1})(\varrho')$, where the composition of two analytic functions is also analytic. Then, a function $\Phi(x', z') = G(\varrho')$ can be written as

$$\Phi(x', z') = G(\varrho') = g(\varrho) = \phi(x, z). \tag{2.9}$$

Thus, if we know $\Phi(x', z')$ (that satisfies Laplace's equation in ϱ'-plane), and the conformal map taking ϱ' to ϱ, we have solved the problem for $\phi(x, z)$. This is the well known condition that ensures the preservation of the electrostatic potential under the transformation.

Now, we present the geometry that stimulated our interest. Metallic nanostructures with nanometric gaps support plasmonic resonances that provide large field enhancements, such as plasmonic dimers as well as nanoparticles on top of metal films [113, 114]. In particular, NPoM cavities have emerged as suitable platforms for the study of strong light-matter interactions. Those present an extreme confinement of the fields down to a few nanometers, ease of fabrication through both lithographic and self-assembly approaches as well as the ability of acting as nanoantennas, coupling free space into these modes and vice versa [115, 116]. These characteristics justify their utilization as plasmonic platforms for the enhancement of light-matter interactions in the quantum regime. Nanocubes on top of metal films have been demonstrated to realize ultrafast spontaneous emission [117] while nanospherical-film structures have revealed single-molecule strong coupling at room temperature [118] and single-molecule optomechanics [87]. Several theoretical works have analyzed the nature of the plasmonic resonances of this type of structures, that can be interpreted as resulting from the hybridization between bright and dark modes (the so called antenna and gap modes) [119, 120]. Furthermore, these resonances show a strong dependence on the morphology and symmetries of the cavity, where facets and atomic protrusions are crucial in the determination of their spectral positions, couplings to far-field illumination and field enhancements [87, 121–123].

From now on, we will refer to the spherical NPoM. A TO approach for this system has been proposed [81, 96] but it presents some limitations. The nature of the field decomposition relies on the symmetry of the problem so only dipolar sources placed at the axis of the cavity can be handled. Furthermore, higher order terms in the multipolar expansion of the potentials cannot be treated analytically. Finally, even when the quasistatic limit has been completed with the inclusions of spatial dispersion [124], there is

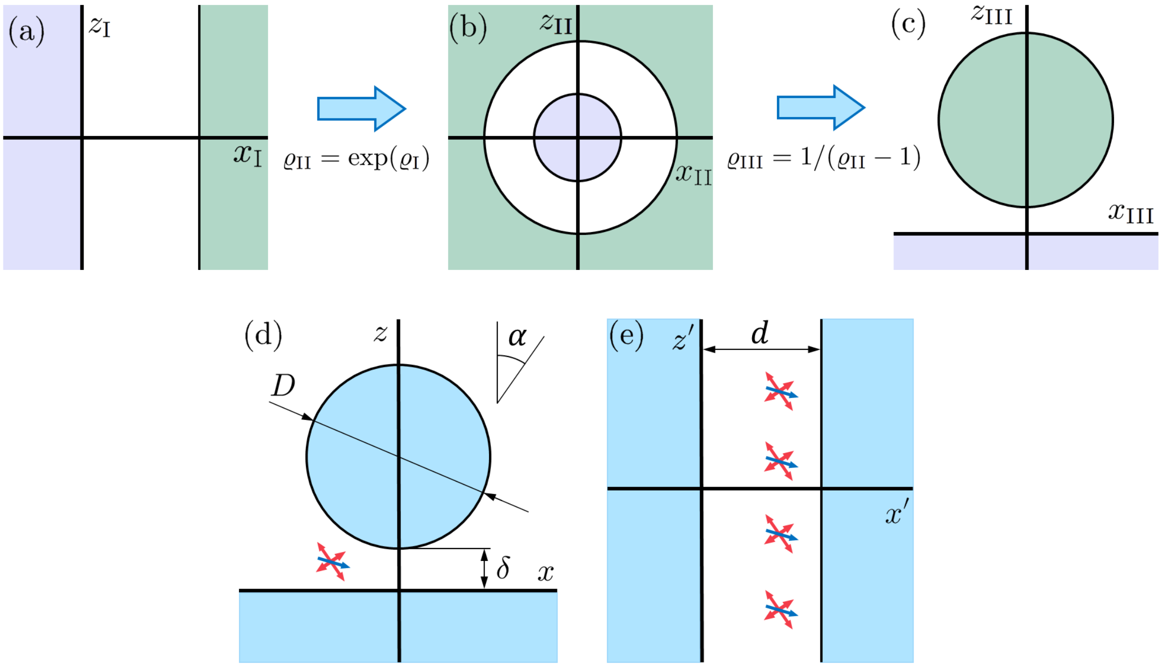

Figure 2.1: Transformation Optics approach. (a-c) Illustration of cascaded transformations. After the first conformal mapping ($\exp(\varrho_{\mathrm{I}})$), the slab geometry maps into a concentric annulus enclosed in the green region. A displaced inversion applied onto the second stage ($1/(\varrho_{\mathrm{II}} - 1)$) provides the two-dimensional version of the NPoM cavity. (d) A microscopic dipolar (blue) or quadrupolar (red) light source in the vicinity of a NPoM cavity with gap δ and diameter D. (e) Geometry obtained under the mapping given by Equation (2.10): a metal-dielectric-metal structure excited by a periodic array of transformed dipole and quadrupole sources. Note the unprimed and primed coordinates used for original (d) and transformed (e) geometries.

not a phenomenological approach for the inclusion of radiative losses that would provide insight into far-field magnitudes. The 2D model of the cavity brings several solutions to those restraints. This approximation lacks of the exact description of the plasmonic frequencies and spatial profiles of 3D cavities but it is justified by the resemblance of near-field phenomenology in 2D and 3D geometries (see Section 2.3).

As already stated, the two-dimensional version of the geometry (presenting translational invariance along the out-of-plane y-direction) allows the use of TO techniques. We start presenting the mapping as a cascaded conformal transformation. The double slab problem (sketched in Figure 2.1(a)) is an ideal starting point, because the solution for Laplace's equation in this geometry is known. Green and violet shadows refer to each domain in order to show the explicit changes after each transformation. From the slab configuration defined in the plane $\varrho_{\mathrm{I}} = x_{\mathrm{I}} + iz_{\mathrm{I}}$, the first step is given by the analytic function $\varrho_{\mathrm{II}} = \exp(\varrho_{\mathrm{I}})$. The left semiplane is transformed into the central unit circle, and the central slab into the intermediate shell. The right semiplane corresponds to the external region. Next, we apply the displaced inverse transformation, given by $\varrho_{\mathrm{III}} = 1/(\varrho_{\mathrm{II}} - 1)$. An inversion maps circles into circles, obtaining the desired form of the 2D NPoM.

Once we know that there exists a transformation linking the 2D NPoM (unprimed coordinates) and the slab (primed ones) geometries, we apply the following transformation

$$\varrho' = T(\varrho) = \log\left(\frac{2iD\sqrt{\rho(1+\rho)}}{\varrho - is} + 1\right), \tag{2.10}$$

to map solutions between both frames. Note that Eq. (2.10) is the inverse version of the cascaded transformations mentioned above. We have introduced two constants, the ratio $\rho = \delta/D$ and $s = \delta + D\sqrt{\rho}/(\sqrt{1+\rho} + \sqrt{\rho})$, where δ and D are the gap and the nanoparticle diameter that define the NPoM cavity (depicted in Figure 2.1(d)). Thus, under Eq. (2.10), the cavity maps into a metal-dielectric-metal waveguide of adimensional width $d = 2\ln(\sqrt{\rho} + \sqrt{1+\rho})$, as sketched in Figure 2.1(e).

2.1.2. Dipolar and quadrupolar fields

The QE, which can be located anywhere in the surroundings of the nanostructure, is generally a system with a complex microscopic structure (i.e., a molecule). The interaction of such a system with light is determined by the electric (and magnetic) transition moments characterizing the quantum transitions that the emitter can undergo in the presence of a EM environment. Even when the size of such emitter is of the order of the nanometric gap of a NPoM [118], it is well known that treating it as a point-like EM source, characterized by its multipolar expansion, provides an accurate understanding of the problem [125]. Then, in a first approximation to the problem, we use the Poisson's equation $\nabla^2\phi_{2\mathrm{D}}(x,z) = -\rho(x,z)/\epsilon_0$ and its free space Green's function $G_0^{2\mathrm{D}}(\mathbf{r},\mathbf{r}')$, with the Cartesian notation for the in-plane vectors $\mathbf{r} = (x,z)$

$$\phi_{2\mathrm{D}}(x,z) = -\frac{1}{\epsilon_0}\int \rho(\mathbf{r}')G_0^{2\mathrm{D}}(\mathbf{r},\mathbf{r}')d^2\mathbf{r}' = -\frac{1}{2\pi\epsilon_0}\int \rho(\mathbf{r}')\log(|\mathbf{r}-\mathbf{r}'|)d^2\mathbf{r}', \tag{2.11}$$

to get the successive orders of the multipolar expansion. As usual, $\mathbf{r}'$ refers to the volume occupied by the distribution of charges. The Taylor expansion of $\log|\mathbf{r}-\mathbf{r}'|$ provides the following terms

$$\phi_{2\mathrm{D}}^{(1)}(x,z) = \frac{-1}{2\pi\epsilon_0}\int \rho(\mathbf{r}')(-\mathbf{r}'\nabla)\log r\, d^2\mathbf{r}' = \frac{1}{2\pi\epsilon_0}\frac{\boldsymbol{\mu}\cdot\mathbf{r}}{r^2}, \tag{2.12}$$

$$\phi^{(2)}_{\mathrm{2D}}(x,z) = \frac{-1}{2\pi\epsilon_0}\int \rho(\mathbf{r}')\frac{1}{2}(-\mathbf{r}'\nabla)^2 \log r \; d^2\mathbf{r}' = \frac{1}{2\pi\epsilon_0}\sum_{ij} Q_{ij}\frac{x_i x_j}{r^4}, \tag{2.13}$$

for the first and second orders in the expansion, respectively[1]. We have already introduced the dipolar moment $\boldsymbol{\mu} = \int \rho(\mathbf{r}')\mathbf{r}' \, d^2\mathbf{r}'$, which can be understood in terms of the vector that connects the effective negative and positive charge distributions. Thus, we can write $\boldsymbol{\mu} = (\mu_x, \mu_z) = \mu(\sin\alpha, \cos\alpha)$, where angle α is defined with respect to the z-axis. On the other hand, the quadrupolar moment is defined by the components of the traceless tensor, $\mathbf{Q}$, with $Q_{ij} = \frac{1}{2}\int \rho(\mathbf{r}')(2x'_i x'_j - r'^2)\delta_{ij} \, d^2\mathbf{r}'$. By symmetry, there are only two independent entries, Q_{xx} and Q_{xz}, which can be expressed in terms of the modulus $Q = \sqrt{\sum_{i,j} Q_{ij}^2}$ and the angle α as

$$\mathbf{Q} = \begin{pmatrix} Q_{xx} & Q_{xz} \\ Q_{zx} & Q_{zz} \end{pmatrix} = \frac{Q}{\sqrt{2}}\begin{pmatrix} \sin 2\alpha & \cos 2\alpha \\ \cos 2\alpha & -\sin 2\alpha \end{pmatrix}. \tag{2.14}$$

Under the conformal mapping, the multivalued character of the transformation (inherited from the logarithmic function) maps the point-like sources in the original frame into a periodic array of sources at the transformed system. They are distributed along the z'-axis and separated by 2π. Thanks to the conformal character of the mapping and the nanometric nature of the cavity, the potential is transformed (see appendix A)

$$\phi_\mu(x,z) = \frac{1}{2\pi\epsilon_0}\mathrm{Re}\left\{\frac{\mu_x + i\mu_z}{\varrho - \varrho_{\mathrm{E}}}\right\} \longrightarrow \phi'_\mu(x',z') = \frac{1}{2\pi\epsilon_0}\mathrm{Re}\left\{\frac{\mu'_{x'} + i\mu_{z'}}{\varrho' - \varrho'_{\mathrm{E}}}\right\}, \tag{2.15}$$

$$\phi_Q(x,z) = \frac{1}{2\pi\epsilon_0}\mathrm{Re}\left\{\frac{Q_{xx} + iQ_{zz}}{(\varrho - \varrho_{\mathrm{E}})^2}\right\} \longrightarrow \phi'_Q(x',z') = \frac{1}{2\pi\epsilon_0}\mathrm{Re}\left\{\frac{Q'_{x'x'} + iQ_{z'z'}}{(\varrho' - \varrho'_{\mathrm{E}})^2}\right\}, \tag{2.16}$$

where we define the position of the QE in the NPoM system as $\varrho_{\mathrm{E}} = x_{\mathrm{E}} + iz_{\mathrm{E}}$. The position of the transformed sources is given by $T(\varrho_{\mathrm{E}}) = \varrho'_{\mathrm{E}} + i\;2\pi n$. The index n, ranging from $-\infty$ to ∞, labels the different sources in the transformed frame resulting from multivaluation. The primed electric moments read

$$\mu'_{x'} + i\mu'_{z'} = \frac{\mu_x + i\mu_z}{(\varrho_{\mathrm{E}} - is)\left(\frac{i(\varrho_{\mathrm{E}} - is)}{2D\sqrt{\rho(1+\rho)}} - 1\right)}, \tag{2.17}$$

$$Q'_{x'x'} + iQ'_{x'z'} = \frac{Q_{xx} + iQ_{xz}}{(\varrho_{\mathrm{E}} - is)^2\left(\frac{i(\varrho_{\mathrm{E}} - is)}{2D\sqrt{\rho(1+\rho)}} - 1\right)^2}. \tag{2.18}$$

Thus, the conformal nature of the mapping in Eq. (2.10) preserves the character of the original source potential: a single dipole (quadrupole) source transforms into a periodic array of dipoles (quadrupoles) distributed along the z'-direction.

---

[1] The different spatial dependence of both potentials and moments (see below) with respect to the 3D case is given by the different form of the Green's function in two- and three-dimensional systems.

2.2. Coupling between QEs and electric fields: Purcell Factor

The interaction between dipolar QEs and electric fields is described through the Green's function formalism. As a classical dipole oscillates, it radiates energy into the medium in its surroundings. The time-averaged power radiated by the dipole, W, is equal to the energy dissipation [55], that reads

$$W = -\frac{1}{2}\int \mathrm{Re}\{\mathbf{J}^*(\mathbf{r}')\mathbf{E}(\mathbf{r}')\}d^3\mathbf{r}'. \tag{2.19}$$

The Taylor expansion of the current density associated to a charge distribution provides the point-like dipole's current density term as $\mathbf{J}(\mathbf{r}) = -i\omega\boldsymbol{\mu}\delta(\mathbf{r}-\mathbf{r}_\mathrm{E})$ [55]. Thus, we find the usual expression for the radiated power

$$W = \frac{\omega}{2}\mathrm{Im}\{\boldsymbol{\mu}^*\mathbf{E}(\mathbf{r}_\mathrm{E})\}, \tag{2.20}$$

given by the imaginary part of the field at the location of the source. The importance of this result specially manifests when we deal with inhomogeneous environments, where energy dissipation can be calculated by means of the electric field at the position of the source instead of integrating the Poynting vector over a surface enclosing the emitter [55].

Equation (2.20) leads to the normalized rate of energy dissipation

$$\frac{W}{W_0} = \frac{\frac{\omega}{2}\mathrm{Im}\{\boldsymbol{\mu}^*\mathbf{E}(\mathbf{r}_\mathrm{E})\}}{W_0} = 1 + \frac{\frac{\omega}{2}\mathrm{Im}\{\boldsymbol{\mu}^*\mathbf{E}_\mathrm{S}(\mathbf{r}_\mathrm{E})\}}{W_0}, \tag{2.21}$$

where in the last step of the equation we have used the convenient separation of the total field into two contributions, the free space one, $\mathbf{E}_0$, and the scattering contribution due to the environment, $\mathbf{E}_\mathrm{S}$. The result in Eq. (2.21) is equivalent to the normalized spontaneous emission rate, so the Purcell factor $P_f = W/W_0$ can be determined through the computation of the scattered field effects on a classical source. The free space contribution, W_0, can be calculated both through the evaluation of the free space electric field at the dipole position, $W_0 = \frac{\omega}{2}\mathrm{Im}\{\boldsymbol{\mu}^*\mathbf{E}_0(\mathbf{r}_\mathrm{E})\}$, or by the integration of the Poyting vector through a surface enclosing the dipole. At the nanoscale regime, the confined character of the scattered fields, $\mathbf{E}_\mathrm{S}$, can be described in the quasistatic limit. Nevertheless, W_0 has to be calculated taking account the electrodynamic character of the source (see below).

Equation (2.21) shows explicitly that P_f is given by the ratio between two energy terms, the free space one and the one given by the interaction with the environment. As we are working in the quasistatic limit, this interactions can be described in terms of the electric potential energy. Then, we examine the form of the interaction energy

$$V_E = \int \rho(\mathbf{r}')\phi(\mathbf{r}')d^3\mathbf{r}', \tag{2.22}$$

where the potential is the external stimuli and the integral runs over the charge distribution volume. We are allowed to write Eq. (2.22) since, in the quasistatic limit, $\phi(\mathbf{r})$ and $\rho(\mathbf{r})$ have the same time dependence, mediated just by the same phase. If the potential slowly varies over the volume of the charge distribution (point-like approximation), we can expand $\phi(\mathbf{r})$ as a Taylor series and the two first orders of the expansion read[2]

$$V_E^{(\mu)} = -\boldsymbol{\mu}\mathbf{E}(\mathbf{r}_\mathrm{E}), \tag{2.23}$$

$$V_E^{(Q)} = -\frac{1}{2}(\mathbf{Q}\nabla)\mathbf{E}|_{\mathbf{r}_\mathrm{E}}. \tag{2.24}$$

Note that we do not consider the zeroth-order term in the expansion of Eq. (2.22), $V_E^{(0)} = q\phi(\mathbf{r}_\mathrm{E})$, as there are not free charges involved in our system. Therefore, the Purcell factor is equivalent to the normalization of the interaction energy in a certain EM environment to the free space case. The calculation reduces to solve Laplace's equation in the geometry sketched in Fig. 2.1(d)

$$P_f^\mu(\omega) = 1 + \frac{V_{E,\mathrm{S}}^{(\mu)}}{V_{E,0}^{(\mu)}} = -\frac{\mathrm{Im}\{\boldsymbol{\mu}\nabla\phi_\mathrm{S}^\mu(\mathbf{r},\omega)|_{\mathbf{r}_\mathrm{E}}\}}{\mathrm{Im}\{\boldsymbol{\mu}\mathbf{E}_0^\mu(\mathbf{r}_\mathrm{E})\}}, \tag{2.25}$$

$$P_f^Q(\omega) = 1 + \frac{V_{E,\mathrm{S}}^{(Q)}}{V_{E,0}^{(Q)}} = -\frac{\mathrm{Im}\{(\mathbf{Q}\nabla)\nabla\phi_\mathrm{S}^Q(\mathbf{r},\omega)|_{\mathbf{r}_\mathrm{E}}\}}{\mathrm{Im}\{(\mathbf{Q}\nabla)\mathbf{E}_0^Q(\mathbf{r}_\mathrm{E})\}}, \tag{2.26}$$

where $\mathbf{r} = (x, z)$ and $\mathbf{r}_\mathrm{E} = (x_\mathrm{E}, z_\mathrm{E})$ are the Cartesian vectors in the xz-plane. Note that on the right side of Eqs. (2.25) and (2.26), we have introduced the expression of the scattered electric field as the gradient of the quasistatic scattered potential, ϕ_S^i. We have also disregarded the constant term in front of the ratio between scattered and free space V_E interaction terms as typically $\frac{V_{E,\mathrm{S}}^{(i)}}{V_{E,0}^{(i)}} \gg 1$.

The free space terms for normalization, given by $\mathbf{E}_0$, are obtained through the computation of the electric field at the position of the source. The purely electrostatic calculation does not provide any meaningful result, since electrostatic potentials, which are real, diverge at $\mathbf{r}_\mathrm{E}$. To get the correct answer, the electric field has to be obtained by means of an electrodynamic approach. As we are working in the 2D version of the NPoM cavity, we

---

[2] Naturally, the quadrupolar tensor in the expansion is defined in the form $\mathbf{Q} = \int \rho(\mathbf{r})\mathbf{r} \otimes \mathbf{r}$, which is not traceless. Due to the condition of external field, $\nabla\mathbf{E} = 0$, we can add any gauge in the form $((\mathbf{Q} - f\mathbf{I})\nabla)\mathbf{E}$. Subtracting $1/2r^2\mathbf{I}$, the quadrupole tensor acquires a traceless form.

use the scalar Green's function for the Helmholtz equation, $G_0^{\mathrm{2D}}(\mathbf{r},\mathbf{r}') = \frac{-i}{4} H_0^{(1)}(k|\mathbf{r}-\mathbf{r}'|)$, given by the Hankel function of the first kind, $H_0^{(1)}$. The electric field can be calculated by means of the vector potential as [55]

$$\mathbf{E}(\mathbf{r}) = i\omega[\mathbf{I} + \frac{1}{k^2}\nabla\nabla]\mathbf{A}(\mathbf{r}), \tag{2.27}$$

where $\mathbf{A}(\mathbf{r}) = \int_V \mu_0 \mathbf{J}(\mathbf{r}') G_0^{\mathrm{2D}}(\mathbf{r},\mathbf{r}') d^3\mathbf{r}'$. The Green's function can be expanded into a multipolar series (see appendix A), yielding the dipolar and quadrupolar contributions to the vector potential, which result in

$$\mathrm{Im}\{\boldsymbol{\mu}\mathbf{E}_0^{\mu}(\mathbf{r}_{\mathrm{E}})\} = \frac{\omega^2\mu^2}{8\epsilon_0 c^2}, \tag{2.28}$$

$$\mathrm{Im}\{(\mathbf{Q}\nabla)\mathbf{E}_0^{Q}(\mathbf{r}_{\mathrm{E}})\} = \frac{\omega^4 Q^2}{32\epsilon_0 c^4}. \tag{2.29}$$

As already mentioned, the problem is analytically solved in the slab-system and, after the inverse transformation (provided by the preservation of the potential), the solution is obtained for the NPoM system (see appendix A for the detailed derivation). The potentials for both sources ($i = \mu, Q$), given by Eqs. (2.15) and (2.16), are written in the transformed slab-frame (see Fig. 2.1(e)) as

$$\phi^i(x,z) \longrightarrow \phi^i(x',z') = \sum_{n=-\infty}^{\infty} \zeta\Big(x' - x'_{\mathrm{E}}, z' - (z'_{\mathrm{E}} + i2\pi n)\Big), \tag{2.30}$$

where the index n accounts for the multivalued character of the log function in the transformation, which yields a periodic array of sources in the transformed frame along z'-direction. In order to solve the Laplace's equation, the primed quasistatic potentials are Fourier transformed

$$\phi^i(k) = \int \phi^i(x',z') e^{-ikz'} dz' = \begin{cases} a_-^i(k) e^{+|k|(x'-x'_{\mathrm{E}})} \text{ if } x' < x'_{\mathrm{E}} \\ a_+^i(k) e^{-|k|(x'-x'_{\mathrm{E}})} \text{ if } x' > x'_{\mathrm{E}} \end{cases} \tag{2.31}$$

where the coefficients, which depend on the dipolar or quadrupolar character of the source, read $a_\pm^i = \sum_{n=-\infty}^{\infty} \tilde{a}^i(k)\delta(k-n)$. Then, we impose that the scattered potentials have the same spatial dependence as the propagating SPs sustained by the metal-dielectric-metal geometry.

$$\phi_{\mathrm{S}}^i(k) = \begin{cases} x' < 0 \rightarrow c_-(k) e^{+|k|(x'-x'_{\mathrm{E}})} \\ x' \in [0,d] \rightarrow b_-(k) e^{+|k|(x'-x'_{\mathrm{E}}))} + b_+(k) e^{-|k|(x'-x'_{\mathrm{E}})} \\ x' > d \rightarrow c_+(k) e^{-|k|(x'-x'_{\mathrm{E}})} \end{cases} \tag{2.32}$$

Applying continuity conditions at the metal-dielectric interfaces, the four coefficients, $c_\pm(k), b_\pm(k)$ are found. Performing an inverse Fourier transform, we obtain the scattered potential in the central slab, $x' \in [0, d]$, which, after the inverse transformation given by Eq. (2.10), corresponds to the scattered potential in the dielectric of the NPoM cavity, written as

$$\phi_{\mathrm{S}}^{\mu}(x,z) = \frac{1}{2\pi\epsilon_0\epsilon_d}\frac{\epsilon_m-\epsilon_d}{\epsilon_m+\epsilon_d}\sum_{n=1}^{\infty}\frac{1}{(\sqrt{\rho}+\sqrt{1+\rho})^{4n}-\left(\frac{\epsilon_m-\epsilon_d}{\epsilon_m+\epsilon_d}\right)^2}\times$$
$$\left[\frac{\epsilon_m-\epsilon_d}{\epsilon_m+\epsilon_d}\mathrm{Re}\Big\{(\mu'_{x'}+i\mu'_{z'})\mathrm{A}_n^-(\varrho,\varrho_{\mathrm{E}})\Big\} + (\sqrt{\rho}+\sqrt{1+\rho})^{2n}\mathrm{Re}\Big\{(\mu'_{x'}-i\mu'_{z'})\mathrm{B}_n^-(\varrho,\varrho_{\mathrm{E}})\Big\}\right]$$

$$\phi_{\mathrm{S}}^{Q}(x,z) = \frac{1}{2\pi\epsilon_0\epsilon_d}\frac{\epsilon_m-\epsilon_d}{\epsilon_m+\epsilon_d}\sum_{n=1}^{\infty}\frac{n}{(\sqrt{\rho}+\sqrt{1+\rho})^{4n}-\left(\frac{\epsilon_m-\epsilon_d}{\epsilon_m+\epsilon_d}\right)^2}\times$$
$$\left[\frac{\epsilon_m-\epsilon_d}{\epsilon_m+\epsilon_d}\mathrm{Re}\{(Q'_{x'x'}+iQ'_{z'z'})\mathrm{A}_n^+(\varrho,\varrho_{\mathrm{E}})\} - (\sqrt{\rho}+\sqrt{1+\rho})^{2n}\mathrm{Re}\{(Q'_{x'x'}-iQ'_{z'z'})\mathrm{B}_n^+(\varrho,\varrho_{\mathrm{E}})\}\right]$$

where the expressions for $\mathrm{A}_n^{\pm}(\varrho,\varrho_{\mathrm{E}})$ and $\mathrm{B}_n^{\pm}(\varrho,\varrho_{\mathrm{E}})$ are given in appendix A. Inserting the above solutions for the scattered potentials into Eqs. (2.25) and (2.26), we obtain the Purcell factor spectra, P_f^i for $i = \mu, Q$ sources, given by the derivatives of $\mathrm{A}_n^{\pm}(\varrho,\varrho_{\mathrm{E}})$ and $\mathrm{B}_n^{\pm}(\varrho,\varrho_{\mathrm{E}})$ evaluated at $\varrho = \varrho_{\mathrm{E}}$.

From the above equations, scattered fields (and so on Purcell factors) can be interpreted as an discrete sum of modes. The index n is indeed the one labelling the periodic transformed sources introduced in Eq. (2.30). Each mode gives rise to a resonance satisfying the condition

$$(\sqrt{\rho}+\sqrt{1+\rho})^{4n} = \mathrm{Re}\left\{\left(\frac{\epsilon_m(\omega)-\epsilon_d}{\epsilon_m(\omega)+\epsilon_d}\right)^2\right\}, \tag{2.33}$$

which reproduces the quasistatic condition for absorption maxima obtained under plane-wave illumination [64].

The description of the spectra as a discrete sum of resonances can be understood as an effect derived from the presence of the finite nanoparticle. In order to get some insight, the SP resonances are obtained in the slab geometry, which resembles the typical metal-insulator-metal (MIM) waveguides, widely studied in the field of nanoplasmonics [126, 127]. The dispersion relation of the *even* plasmonic modes (with even field component along the x'-direction) in a MIM configuration (with m, d subindices denoting metallic and dielectric media) is given by [56]

$$\tanh\left(\frac{k_d w}{2}\right) = -\frac{k_m\epsilon_d}{k_d\epsilon_m}, \tag{2.34}$$

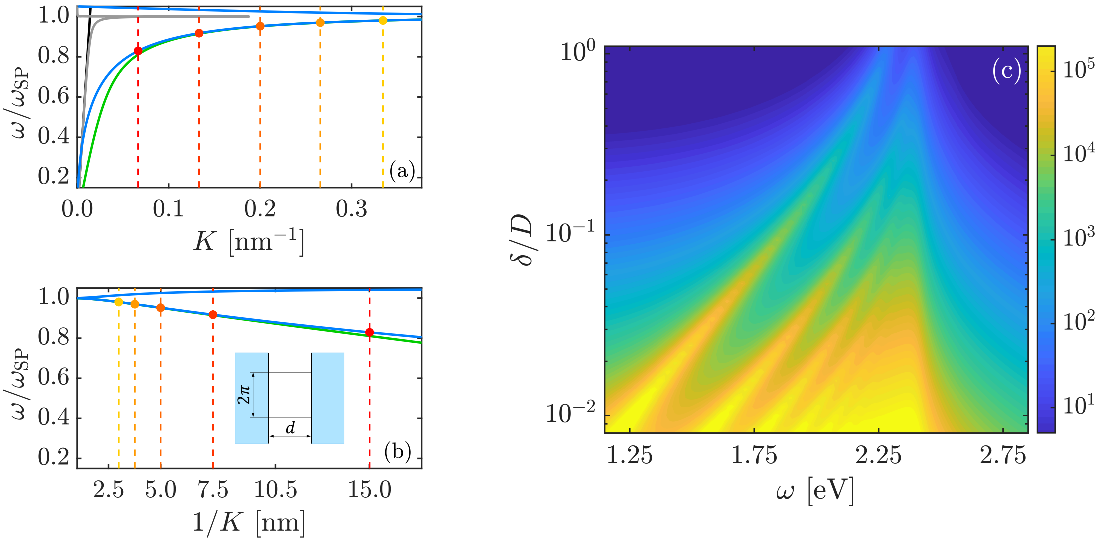

Figure 2.2: Plasmonic modes of NPoM cavities. (a) Free space (black), planar SP (grey) and MIM SP dispersion relation (green) for vacuum-silver systems. Blue line renders the quasistatic result for the MIM configuration equivalent to the NPoM system ($D, \delta = 30.0, 0.9$ nm). Orange-to-yellow dashed lines and points mark the pairs (ω, K) for the lowest four NPoM resonances. (b) Inverse of the wavectors associated to panel (a). (c) Purcell factor for a dipolar QE in a NPoM cavity, oriented along z-direction at $\mathbf{r}_{\mathrm{E}} = (0, \delta/2)$, as a function of frequency and normalized gap size.

where $k_i^2 = K^2 - (\frac{\omega}{c})^2\epsilon_i$ is the component of the wavevector perpendicular to the metal-dielectric interfaces and w is the width of the dielectric layer. K is the propagating component of the wavevector. In the quasistatic limit, the dispersion relation simplifies to

$$K_{\mathrm{QS}} = \frac{1}{w}\log\left(\frac{\epsilon_m - \epsilon_d}{\epsilon_m + \epsilon_d}\right). \tag{2.35}$$

In Figure 2.2, we present the dispersion relation of the low-frequency surface plasmon supported by a MIM waveguide for an almost lossless Drude metal ($\gamma_m = 10^{-4}\omega_p$) and air ($\epsilon_d = 1$). In general throughout this chapter, figure plots will present frequencies in energy units, with the convention $\hbar = 1$, whereas we keep SI units for the equations the main text. In black and grey, the light-line $k = \omega/c$ and the single surface SP dispersion relation, k_{SP} (given by Eq. (1.27)), respectively. The green line sets the full electrodynamic dispersion relation of even modes for the MIM configuration that corresponds with our slab system, given by the NPoM parameters, $(D, \delta) = (30.0, 0.9)$ nm. We have to considerate the form of the conformal transformation to find w. Due to the multi-valued transformation, the transformed frame, which resembles MIM structure, can be understood as a periodic system, determined by unit cells with width d and $\Delta_z = 2\pi$ in the z'-direction, as sketched in the inset of Figure 2.2(b). Periodicity is given by the transformation acting on the circumference of the nanoparticle in the NPoM system, where one period corresponds to $2\pi D/2$, so the effective MIM configuration equivalent to the NPoM cavity is given by a factor $D/2$, with width $w = dD/2 = 5.2\,\text{nm}$. Blue line plots the quasistatic result, which overlaps with the green line at high frequencies but whose crossing with the light-line reflects the failure of the quasistatic approximation. Our resonance condition, given by Eq. (2.33) for the first four modes supported by the NPoM is plotted in orange-like points. Fig. 2.2(b) plots frequency versus $1/K$ in order to show more clearly the wavelength of each mode. As expected, $1/K$ reflects an scaling with the n-th mode as $D/(2n)$. Indeed, the allowed modes are those with an integer number of effective SP wavelengths along the perimeter of the nanoparticle, with their effective wavelength given by $\pi D/n$, revealing n as the azimuthal order of the plasmonic mode. Then, the finite nanoparticle sets an spatial condition for the formation of standing waves which correspond to the plasmonic resonances of the NPoM system.

In what follows, the metal permittivity is given by a Drude fitting to silver, $\epsilon_m(\omega) = \epsilon_\infty - \omega_p^2/(\omega(\omega + i\gamma_m))$ with $\epsilon_\infty = 9.7$, $\hbar\omega_p = 8.91\,\text{eV}$ and $\hbar\gamma_m = 0.06\,\text{eV}$, and the cavity is embedded in a dielectric medium with permittivity $\epsilon_d = 4$, which models a DNA origami scaffolding [128]. We explore the spectral position of resonances of such a system in Figure 2.2(c). We plot the Purcell spectra for a dipolar emitter, P_f^μ, at the center of the gap $\mathbf{r}_\text{E} = (0, \delta/2)$ as a function of frequency and δ/D for a fixed $D = 30.0\,\text{nm}$. As the gap is smaller, larger values for the Purcell factor are obtained due to the strong light confinement. Furthermore, lowest order modes redshift more and more, reflecting the strong hybridization between the nanoparticle and plane eigenmodes. On the contrary, large separations provide a merging of the whole set of modes around the frequency satisfying the resonance condition for the MIM (the same as the single surface), given by Eq. (2.35)

$$\epsilon_m(\omega_\text{SP}) + \epsilon_d = 0 \rightarrow \omega_\text{SP} = \frac{\omega_p}{\sqrt{\epsilon_\infty + \epsilon_d}}, \tag{2.36}$$

forming an effective pseudomode [40, 96].

Now, we turn to study the different Purcell spectra for dipolar and quadrupolar illumination. Figure 2.3 shows the Purcell spectra for NPoM cavities of $D = 30.0\,\text{nm}$ diameter and different gap sizes: $0.9\,\text{nm}$ (blue), $1.8\,\text{nm}$ (red) and $2.7\,\text{nm}$ (green). Two different QEs, placed at the gap center, $z_\text{E} = \delta/2$, are considered: (a) a dipolar source oriented along z-direction ($\boldsymbol{\mu} = \mu\hat{\mathbf{z}} = (0, \mu)$) and (b) a quadrupolar source with a purely non-diagonal moment ($Q_{xz} = Q_{zx} = Q/\sqrt{2}$). In our parametrization, $\alpha = 0$ for both QEs. As

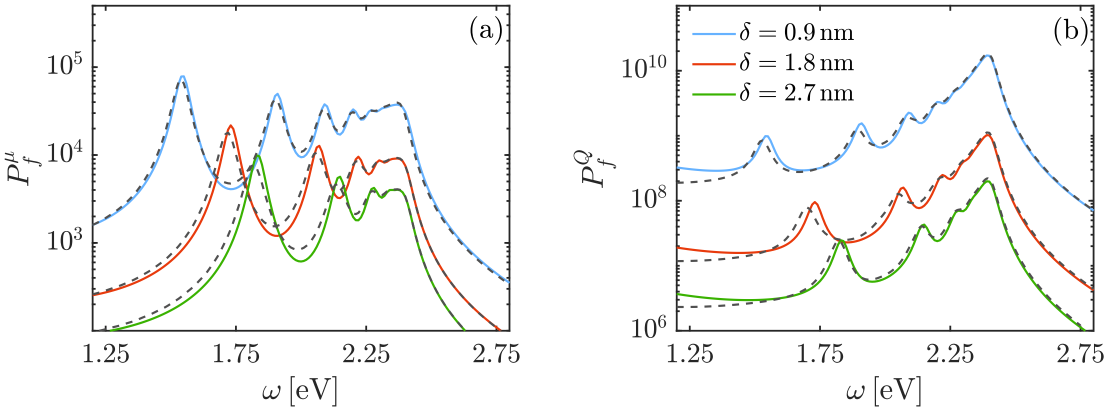

Figure 2.3: Purcell factor at gap center ($z_\mathrm{E} = \delta/2$) of NPoM cavities with $D = 30.0\,\mathrm{nm}$ and three different gap sizes, δ, as indicated in legend. (a) Dipolar source oriented along z-direction. (b) Quadrupolar source with vanishing diagonal terms in $\mathbf{Q}$. In both panels, analytical (solid lines) and numerical (dashed lines) spectra are compared.

retardation effects are neglected, our quasistatic results scale with the size of the system, L, as L^{-2}, with no change of the resonant frequencies of the plasmonic modes supported by the NPoM structure. Analytical predictions obtained from our TO approach (color solid lines) are compared against full numerical 2D calculations (black dashed lines). Those were obtained using COMSOL Multiphysics exploring the size scaling of the quasistatic regime. Both set of quasistatic spectra are in excellent agreement. We observe that $P_f^Q(\omega)$ is several orders of magnitude larger than $P_f^\mu(\omega)$ throughout the spectral window considered, since plasmonic fields can interact largely with higher multipolar emitters due to the dependence on the spatial field derivatives. However, the ratio between both magnitudes is largest around $\hbar\omega \simeq 2.40\,\mathrm{eV}$, corresponding to the plasmonic pseudomode formed by the spectral overlapping of high-order dark SP modes [40, 96].

2.3. Comparison between 2D and 3D results

In the previous sections, we have briefly commented the principal reason that justifies our election of the 2D model of the NPoM cavity instead of its 3D counterpart, the possibility of obtaining analytical results for the system response under illumination of generic point-like sources. In this section, we address the direct comparison between the numerical results obtained in 2D and 3D simulations and our analytical results derived from the TO approach.

We start considering the comparison between 2D and 3D numerical Purcell factors of a single nanoparticle. Simulations were performed in the solver implemented in COMSOL Multiphysics, integrating the total flux of power in a box enclosing the point-like source, in presence/absence of the metal, described through a Drude-like permittivity, ϵ_m, for silver embedded in vacuum ($\epsilon_d = 1$). The system was defined by the diameter of the particle, $D = 40\,\mathrm{nm}$ (cylindrical or spherical depending on the dimensionality) and the separation between the emitter and the metal surface, 0.5 nm. The ratio between the Purcell factors, $P_f^i(3\mathrm{D})/P_f^i(2\mathrm{D})$ is represented in Fig. 2.4, in panels (a) and (d) for the dipolar and quadrupolar sources, respectively. As expected, the $P_f^i(3\mathrm{D})/P_f^i(2\mathrm{D})$ is larger than one, with more remarkable differences for the dipolar source than for the quadrupolar one. The spectral form of the ratio makes clear the different position of the dipolar plasmon in the sphere ($\epsilon_m + 2\epsilon_d \simeq 0$) with respect to the cylinder ($\epsilon_m + \epsilon_d \simeq 0$).

Panels (b) and (e) in Fig. 2.4 show the direct comparison between 2D calculations of the Purcell factor for a Ag dimer, with the emitter placed at the center of the gap, as sketched in panels (c) and (f). The analytical results, labelled as 2DQS and plotted in red lines are obtained within the TO framework whereas numerical ones are calculated by means of COMSOL. The system parameters are $D = 40\,\mathrm{nm}$ and $\delta = 1\,\mathrm{nm}$. The main differences between the numerical and analytical solutions occur at the lowest order plasmons for the dipolar source (Fig. 2.4(b)), where radiative effects take part, both enlarging the width and redshifting the spectral position of the plasmonic resonance, with perfect agreement at high frequencies around the pseudomode, both in the dipolar and quadrupolar cases.

Finally, in Fig. 2.4 (c) and (f), we show the direct comparison between 2D and 3D results in the Ag dimer, same configuration as in previous panels. Green lines represent the 3D simulations, with spherical particles. Red and blue lines correspond to the 2D calculations, given by TO (2DQS) and numerical simulations (2D) in panels (b) and (e), multiplied by the factor $P_f^i(3\mathrm{D})/P_f^i(2\mathrm{D})$ for each case (see again panels (a,d)). Firstly, we highlight that the phenomenology in 2D and 3D is quite similar. The dipolar emitter couples to a set of different plasmonic modes that converge at the pseudomode. This is the dominant mode in the case of the quadrupolar coupling, where discrepancies between 3D and 2D after introducing the correction factor given by the ratio $P_f^i(3\mathrm{D})/P_f^i(2\mathrm{D})$ are negligible. Secondly, the discrepancies between the numerical results for the 3D case and the 2D case are similar to those between the 2D solutions, purely quasistatic and the full electrodynamical one. Then, we conclude that besides a factor, the TO analytical approach captures the main features of the plasmon-emitter coupling at these nanometric systems.

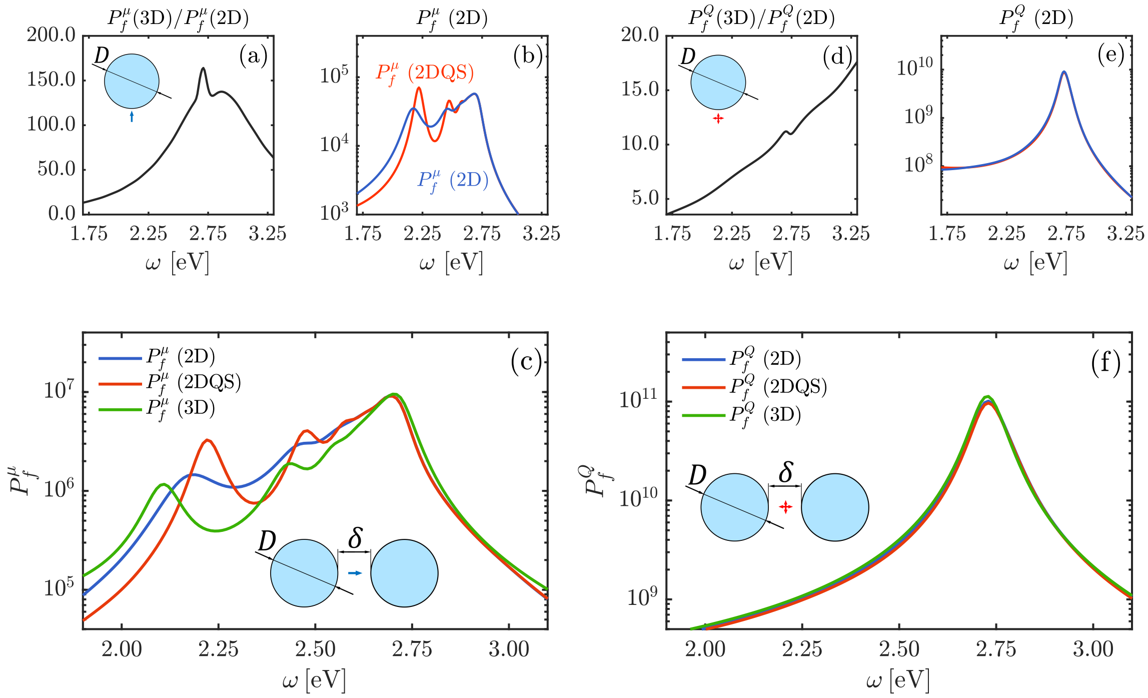

Figure 2.4: Comparison between 2D and 3D results for metallic nanocavities. Panels (a) and (d) show the ratio between 3D and 2D Purcell factors, obtained through numerical simulations, for a dipole and a quadrupole as sketched in the inset, separated 0.5 nm from the surface of a single Ag nanoparticle ($D = 40.0$ nm). Panels (b) and (e) render the numerical-electrodynamic (blue) and analytical-quasistatic (red) solutions for the Purcell factor in a 2D system, formed by a Ag dimer and a single dipolar or quadrupolar emitter placed at the gap center. Panels (c) and (f) show the comparison between 2D quasistatic (red), 2D full electrodynamic (blue) and 3D full electrodynamic (green) results, where the 2D solutions have been multiplied by the ratio in panels (a) and (d). The system sketched as an inset in (c) and (f) applies for calculations with the Ag dimer in panels (b-c-e-f).

2.4. Spectral Density and Coupling Strengths

The Purcell factor, $P_f^i(\omega)$, as a normalized ratio, contains exclusively the effects of the cavity on the emitter without considering its own magnitude. We have shown that it can be written in terms of the classical electric fields, and it is equivalent to the spontaneous decay rate normalized by its value in free space. Then, the Purcell factor can be understood as the local density of states (LDOS) or the spectral density $J(\omega)$ normalized to their free space counterpart. The latter can be expressed in terms of the Purcell factor as

$$J_i(\omega) = \frac{\gamma_i}{2\pi} P_f^i(\omega), \tag{2.37}$$

where $i = \mu, Q$ and γ_i is the QE decay rate in free space that provides the free space spectral density $J_i^0(\omega) = \gamma_i/(2\pi)$. The calculation of $J(\omega)$ through the spontaneous decay rate in free space makes customary the introduction of the transition moments, which appear in the expression of the spontaneous decay rates. The multipolar expansion of the quantum light-matter interaction Hamiltonian has the same form as the classical one introduced in Eq. (2.22) but in terms of momenta and field operators, yielding the transitions between different states of the hybrid light-matter system. From now on, we will refer to those dipolar or quadrupolar transition momenta, understood as the expectation values of the dipolar or quadrupolar operators, $\hat{\boldsymbol{\mu}}$ and $\hat{\mathbf{Q}}$, respectively, between the ground and the excited state of the two-level system, in the form

$$\mu^2 = |\langle g|\, \hat{\boldsymbol{\mu}}\, |e\rangle|^2. \tag{2.38}$$

$$Q^2 = |\langle g|\, \hat{\mathbf{Q}}\, |e\rangle|^2. \tag{2.39}$$

We specially focus on $J(\omega)$ since it is the magnitude that encodes the strength of the light-matter interaction. It is a local quantity that contains information about the electromagnetic modes supported by the cavity as well as the coupling strength between each of them and the QE. Thus, it depends on the cavity geometry (diameter and gap size) and permittivity, the exciton characteristics (natural frequency and dipolar/quadrupolar moment) and its position and orientation. In order to calculate the spectral density experienced by dipolar and quadrupolar excitons in the vicinity of the NPoM cavity, we use the 2D Purcell spectra obtained in the previous section. The decay rates in free space are taken from 3D calculations [129],

$$\gamma_\mu = \frac{\omega^3 \mu^2}{3\pi\epsilon_0 \hbar c^3}, \tag{2.40}$$

$$\gamma_Q = \frac{\omega^5 Q^2}{360\pi\epsilon_0 \hbar c^5}. \tag{2.41}$$

As the fields, the spectral density for both dipolar and quadrupolar excitons are composed by a number of SP contributions. From the solutions of the potentials, we can write

$$\phi_\mathrm{S}^i = \frac{1}{2\pi\epsilon_0\epsilon_d} \sum_{n=1}^{\infty} \frac{e^\alpha}{e^{2nd} - e^{2\alpha}} \left[e^\alpha K_1^i + e^{nd} K_2^i \right] \tag{2.42}$$

where we have defined the exponentials $e^\alpha = \frac{\epsilon_m - \epsilon_d}{\epsilon_m - \epsilon_d}$ and rewritten $e^{nd} = (\sqrt{\rho} + \sqrt{1+\rho})^{2n}$. K_1^i, K_2^i refer to the functions which accompany the exponentials in each case ($i = \mu, Q$).

The summation in Eq. (2.42) can be rewritten as

$$\frac{e^{\alpha}\left[e^{\alpha}K_1^i + e^{nd}K_2^i\right]}{e^{2nd} - e^{2\alpha}} = \frac{1}{2}\left(\frac{K_1^i + K_2^i}{e^{nd} - 1}\frac{\epsilon_m - \epsilon_d}{\epsilon_m + \epsilon_d\frac{e^{nd}+1}{e^{nd}-1}} - \frac{K_1^i - K_2^i}{e^{nd} + 1}\frac{\epsilon_m - \epsilon_d}{\epsilon_m + \epsilon_d\frac{e^{nd}-1}{e^{nd}+1}}\right). \qquad (2.43)$$

Exploiting the Drude form of the metal permittivity ($\epsilon_m = \epsilon_\infty - \omega_p^2/(\omega(\omega + i\gamma_m))$), and using the high quality resonator limit [39] ($\gamma_m \ll \omega$), we can write

$$\frac{\epsilon_m - \epsilon_d}{\epsilon_m + \epsilon_d\xi_{n,\sigma}} \approx \frac{-\omega_{n,\sigma}\frac{\epsilon_d(1+\xi_{n,\sigma})}{\epsilon_\infty + \epsilon_d\xi_{n,\sigma}}}{2((\omega - \omega_{n,\sigma}) + i\frac{\gamma_m}{2})} \qquad (2.44)$$

where we have introduced

$$\xi_{n,\sigma} = \frac{e^{nd} + \sigma}{e^{nd} - \sigma} = \frac{(\sqrt{\rho} + \sqrt{1+\rho})^{2n} + \sigma}{(\sqrt{\rho} + \sqrt{1+\rho})^{2n} - \sigma} \qquad (2.45)$$

and

$$\omega_{n,\sigma} = \frac{\omega_p}{\sqrt{\epsilon_\infty + \epsilon_d\xi_{n,\sigma}}}. \qquad (2.46)$$

as the SP frequencies. As the Purcell factors are given by the imaginary part of the spatial derivatives of ϕ_{S}^i, contained in the coefficients $K_{1,2}^i$, the spectral densities can be expanded as a sum of Lorentzian SP terms of the form

$$J_i(\omega) = \sum_{n=1}^{\infty}\sum_{\sigma=\pm 1}\frac{(g_i^{n,\sigma})^2}{\pi}\frac{\gamma_m/2}{(\omega - \omega_{n,\sigma})^2 + (\gamma_m/2)^2}, \qquad (2.47)$$

where the imaginary part of the Lorentzian is apparent, defined by the SP frequency, $\omega_{n,\sigma}$ and the width γ_m, given by the Drude damping rate (note that SP radiative damping is neglected in the quasistatic limit).

The Lorentzian decomposition shows that for each n, $J(\omega)$ is given by two contributions, denoted by σ. This double contribution can be directly related to the quadratic condition of Eq. (2.33), which means that we can identify two different solutions for a given n. The index σ labels SP modes with different parity, i.e., different parity of the z-component of the electric field across the gap of the NPoM cavity. Even modes are labeled as $\sigma = 1$ while odd ones correspond to $\sigma = -1$. SPs with increasing n approach the pseudomode frequency, $\omega_{\mathrm{PS}} = \frac{\omega_p}{\sqrt{\epsilon_\infty + \epsilon_d}}$. Large ρ provides faster convergence of the SPs frequencies to ω_{SP}. It also reveals that the frequency of even modes increase towards this value, whereas it decreases for the odd ones. The labelling is directly linked to the MIM waveguide modes [56]. In Fig. 2.2(a), we plotted the dispersion relation for the low-frequency SPs supported by this type of system, which corresponds to the

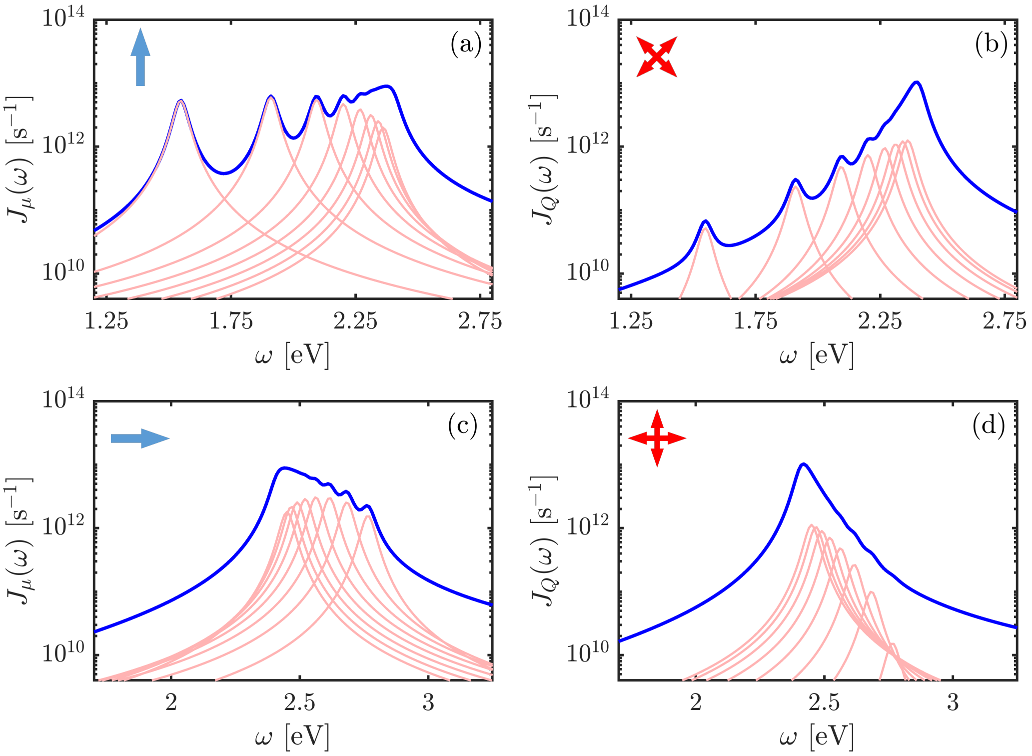

Figure 2.5: Spectral density (blue line) at the gap center $(x_{\mathrm{E}}, z_{\mathrm{E}}) = (0, \delta/2)$ of the NPoM cavity with $D = 30.0\,\mathrm{nm}$ and $\delta = 0.9\,\mathrm{nm}$. Dipolar and quadrupolar QEs are defined through their moments with $\mu = 0.55\,\mathrm{e{\cdot}nm}$ $Q = 0.75\,\mathrm{e{\cdot}nm}^2$. The orientation in (a) and (b) panels is $\alpha = 0$, the same as in Fig. 2.3. Panels (c) and (d) render the spectral densities of dipolar and quadrupolar exciton with $\alpha = \pi/2$ and $\alpha = \pi/4$, respectively. In all panels, orange lines plot the first few terms ($n \leq 10$) in the decomposition in Eq. (2.47). By symmetry, the QEs are coupled only to SP modes with $\sigma = 1$ in the top panels whereas only $\sigma = -1$ modes are apparent in bottom ones.

MIM even modes. Those modes approach asymptotically the frequency for the single metal-dielectric interface (given by ω_{PS} above).

The weight of each term in Equation (2.47) is given by $g_i^{n,\sigma}$, the QE-SP coupling strength between the dipolar or quadrupolar exciton ($i = \mu, Q$) and the SP mode of azimuthal order n and parity σ. These constants contain all the information about the QEs and the SP mode spatial profile. Appendix A presents the analytical expressions for $g_i^{n,\sigma}$ that we obtain from our TO approach.

The blue lines in Figure 2.5 show the spectral densities for a dipolar (a, c) and a quadrupolar (b, d) exciton, with cavity defined by $(D, \delta) = (30.0, 0.9)\,\mathrm{nm}$ (light blue line in Figure 2.3). The QEs are placed at the gap center. In agreement with experimental values [118], we set $\mu = 0.55\,\mathrm{e{\cdot}nm}$. We take $Q = 0.75\,\mathrm{e{\cdot}nm^2}$ for the quadrupole moment, which yields a ratio between free space decay rates $\gamma_Q/\gamma_\mu \simeq 1 \cdot 10^{-6}$ at the center of the frequency window considered, $\hbar\omega = 2.0\,\mathrm{eV}$. Despite this inherent difference between both QEs, the spectral densities are equivalent at the pseudomode position, $J_\mu(\omega_{\mathrm{PS}}) = J_Q(\omega_{\mathrm{PS}}) \simeq 10^{-13}\,\mathrm{s}^{-1}$. Therefore, the interaction strength between the NPoM cavity and both QEs at $\hbar\omega_{\mathrm{PS}} \simeq 2.4\,\mathrm{eV}$ is very similar. Depending on the emitter orientation, sketched in the insets of each panel, we clearly find differences in the modes that contribute to the plasmon-exciton interaction. In Figure 2.5 panels (a) and (b), the orientation of both emitters is $\alpha = 0$, yielding the configuration in the inset which provides coupling with even modes ($\omega_{n,\sigma=+1} < \omega_{\mathrm{PS}}$). On the other hand, panels (c) and (d) render the opposite orientation, $\alpha = \pi/2$ (dipole) and $\alpha = \pi/4$ (quadrupole). For these configurations, the coupling between the QE and the cavity is given by odd-symmetry modes, with resonant frequencies beyond the pseudomode. Both configurations show that $J_\mu(\omega) \gg J_Q(\omega)$ for frequencies $\omega \simeq \omega_{1,\sigma}$, which indicates that the quadrupole exciton couples more weakly than the dipolar one to low-order SPs (with small n), with large contrast at the bright, dipolar SP, $J_\mu(\omega_{1,+1}) \simeq 10^2 J_Q(\omega_{1,+1})$. In fact, the maximum at $\omega_{1,+1}$ barely stands out of the low-frequency tail of the pseudomode maximum in the quadrupolar spectral density (Fig. 2.5(b)). In the odd case, the dominance of the pseudomode with respect the lowest-order modes is apparent for both excitons (see Fig. 2.5(c) and (d)).

In Figure 2.6, we study the dependence of the light-matter coupling strengths on the QE orientation for the different SPs supported by the NPoM cavity. Both dipolar ($\mu = 0.55\,\mathrm{e{\cdot}nm}$) and quadrupolar ($Q = 0.75\,\mathrm{e{\cdot}nm^2}$) excitons are placed at the gap center $(x_{\mathrm{E}}, z_{\mathrm{E}}) = (0, \delta/2)$. Fig. 2.6(a) and (b) display $g_\mu^{n,+1}$ and $g_\mu^{n,-1}$, respectively, versus n and α. These contourplots show that the maximum coupling takes place at $n < 5$ for both σ, and that vertical (horizontal) dipolar QEs couple more efficiently to even (odd) SPs. This can be clearly seen in Fig. 2.6(c) which plots $g_\mu^{n,\sigma}$ for the three orientations indicated by arrows in the previous panels. Only for $\alpha = \pi/4$ (blue lines), the coupling strengths to even (solid) and odd (dashed) SPs are comparable. Note that $g_\mu^{n,+1} > g_\mu^{n,-1}$ for very low azimuthal order, n, in this case. Fig. 2.6(d) and (e) display coupling strength maps for $g_Q^{n,+1}$ and $g_Q^{n,-1}$. They exhibit a similar dependence on n and α as their dipolar counterparts. However, two main differences can be observed. First, although $g_\mu \simeq g_Q$ for large n, the maximum coupling is always lower for quadrupolar QEs, within our considered set of emitter strengths and system parameters. Second, the peak in $g_i^{n,\sigma}$ always takes place at lower n for the dipolar excitons. These two circumstances are

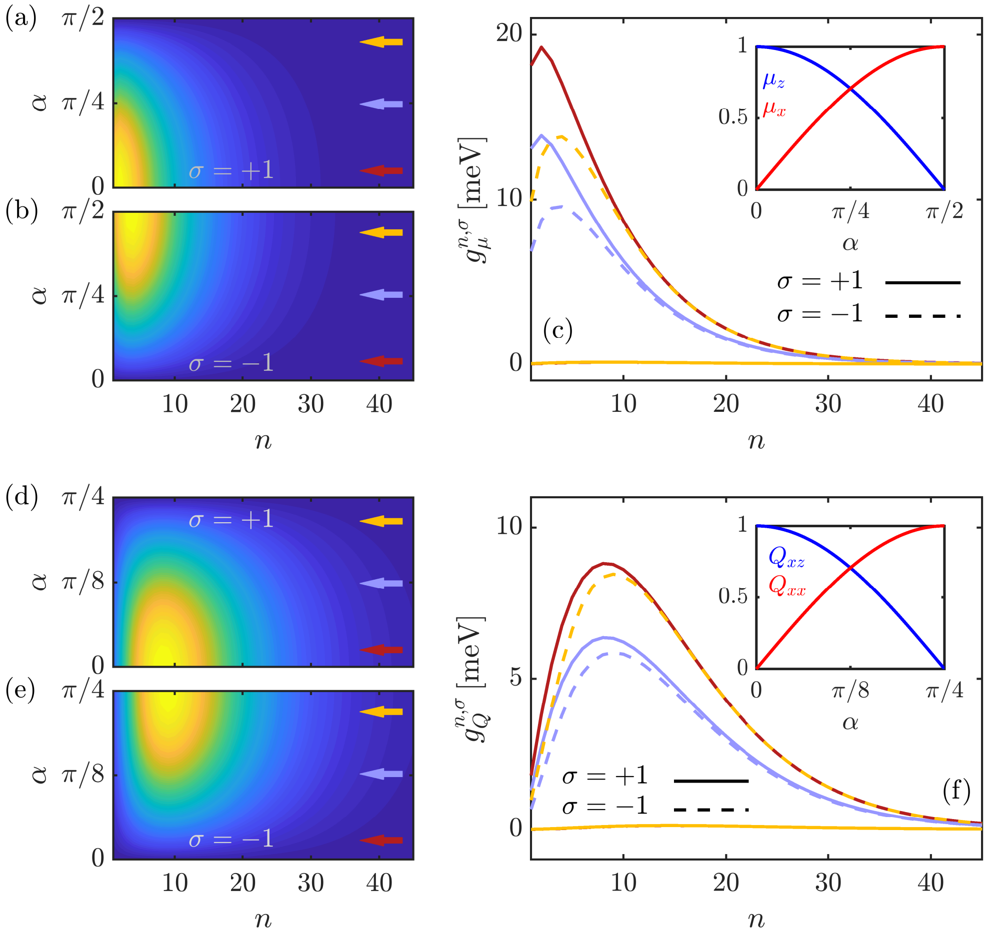

Figure 2.6: Dependence of the coupling strength, $g_i^{n,\sigma}$ on n and α for dipolar (a-c) and quadrupolar (d-f) excitons at the gap center. Panels (a) and (b) [(d) and (e)] display $g_\mu^{n,\sigma}$ [$g_Q^{n,\sigma}$] contourplots for $\sigma = +1$ and $\sigma = -1$, respectively. Panels (c) and (f) show cuts for even (solid lines) and odd (dashed lines) modes and three different values of α (indicated by colored horizontal arrows in the contourplots). The insets render the dipole and quadrupole components as a function of α.

apparent in Fig. 2.6(f), which also shows that for a given n, $g_Q^{n,+1} \simeq g_Q^{n,-1}$ at $\alpha = \pi/8$ (blue lines).

Once we have studied the orientation-dependence of QE-SP couplings, we investigate next the impact of the emitter position. We restrict our attention first to the symmetry axis of the cavity ($x_{\mathrm{E}} = 0$) and the orientations for which emitters placed at the gap center are only coupled with the plasmonic even modes, $\alpha = 0$. Figure 2.7(a) and (b) display $g_\mu^{n,\sigma}$ maps as a function of n and z_{E}/δ between the gap center and the vicinity of the nanoparticle surface for both plasmonic parities. We can see that, in accordance with

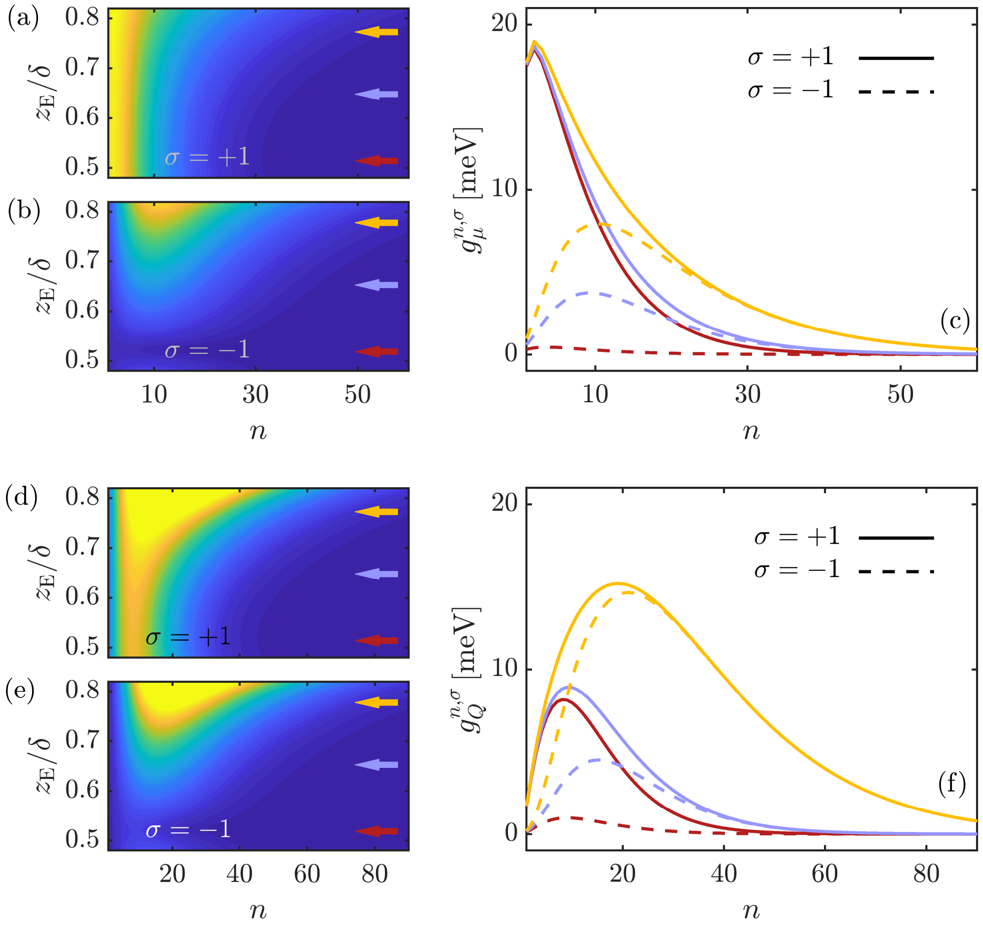

Figure 2.7: Dependence of the coupling strength on n and z_E along the symmetry axis of the cavity ($x_E = 0$) for dipolar (a-c) and quadrupolar (d-f) excitons with $\alpha = 0$. Panels (a) and (b) [(d) and (e)] display $g_\mu^{n,\sigma}$ [$g_Q^{n,\sigma}$] contourplots for $\sigma = +1$ and $\sigma = -1$, respectively. Panels (c) and (f) show cuts for even (solid lines) and odd (dashed lines) modes at three different values of z_E/δ (indicated by colored horizontal arrows in the contourplots).

Fig. 2.6, the light-matter interaction is governed by low-order ($n < 5$) even SPs. Note that the QE coupling to these modes barely depends on the emitter position. The associated electric field profile is constant along the NPoM gap. On the contrary, in accordance with the phenomenology reported for full 3D models [96], $g_\mu^{n,\sigma}$ for both even and odd modes of higher n increases as the QE approach the nanoparticle surface. This trend is visible in Fig. 2.7(c), which evaluates $g_\mu^{n,\sigma}$ for three z_E values. A similar analysis is presented in Fig. 2.7(d)-(f) for quadrupolar excitons. The $g_Q^{n,\sigma}$ maps reveal that, in contrast to dipolar QEs, the coupling vanishes for SPs with very low n, and the maximum takes place for $n > 10$. As we have already discussed, the QE only interacts with $\sigma = +1$ modes at the gap center. The emitter displacement towards the nanoparticle surface increases both $g_Q^{n,+1}$ and $g_Q^{n,-1}$. The light-matter interaction is then fully governed by the plasmonic pseudomode. Indeed, the cuts at fixed QE positions in Fig. 2.7(f) show that the coupling to even and odd SPs for large n is maximum, and very similar, at $z_\mathrm{E} \approx 0.8\delta$. Importantly, the maximum coupling in this panel is higher than in Fig. 2.7(c). This indicates that, by displacing the emitter from the gap center, the plasmonic interaction for quadrupolar QEs becomes larger than for dipolar ones. Furthermore, we can conclude that there is a trade-off in the maximum n^th-plasmon-exciton coupling, since the metal supports modes that are more and more confined to the surface, satisfying a direct relation between order, field confinement and spatial decay.

We exploit the analytical power of our TO approach further and explore fully the spatial distribution of the QE-SP coupling, $g_i^{n,\sigma}(\mathbf{r}_\mathrm{E})$, in the vicinity of the NPoM geometry. Figure 2.8 displays strength maps (in log scale) involving the dipolar (a,c) and quadrupolar (b,d) excitons as well as the lowest-frequency SP ($\omega_{1,+1}$) (a,b) and the plasmonic pseudomode (ω_PS) (c,d). We set all the parameters as in previous figures. The former mode corresponds to $n = 1, \sigma = +1$, the coupling constant for the latter is calculated as [40]

$$g_i^\mathrm{PS} = \sqrt{\sum_{\sigma=\pm1} \sum_{n=n_\mathrm{min}}^{\infty} (g_i^{n,\sigma})^2}, \tag{2.48}$$

where the minimum order for even/odd parity is set by the condition $|\omega_\mathrm{PS} - \omega_{n_\mathrm{min},\sigma}| \leq \gamma_m/2$. Notice that $n_\mathrm{min} = 7$ in Fig. 2.8(c)-(d) for both parities, which is in accordance with Fig. 2.5. This figure only shows five distinguishable peaks in $J_i(\omega)$ below ω_PS. Figure 2.8(a) and (b) evidence that the coupling-strength maps associated to the lowest (dipolar) SP are focused within the gap of the NPoM geometry. However, the localization at the gap is significantly larger for the quadrupole QE ($\alpha = 0$ for both excitons). Whereas the region of high g_μ spreads over the flat metal surface and the perimeter of the nanoparticle, g_Q decays abruptly within a few nanometer range from the gap center. Let us remark again that all contourplots are in logarithmic scale. In contrast, Fig. 2.8(c) and (d) demonstrate that the pseudomode yields coupling maps insensitive to the cavity geometry. These are much more tightly bounded to the metal boundaries, within a sub-nm length scale, both at the nanoparticle and substrate surface. The gap does not seem to play any role in the spatial distribution of g_μ and g_Q, except for the overlapping of their tails across it. In accordance with the top panels, the plasmon-exciton coupling spatial distribution is also more confined in the case of the quadrupole than the dipolar one.

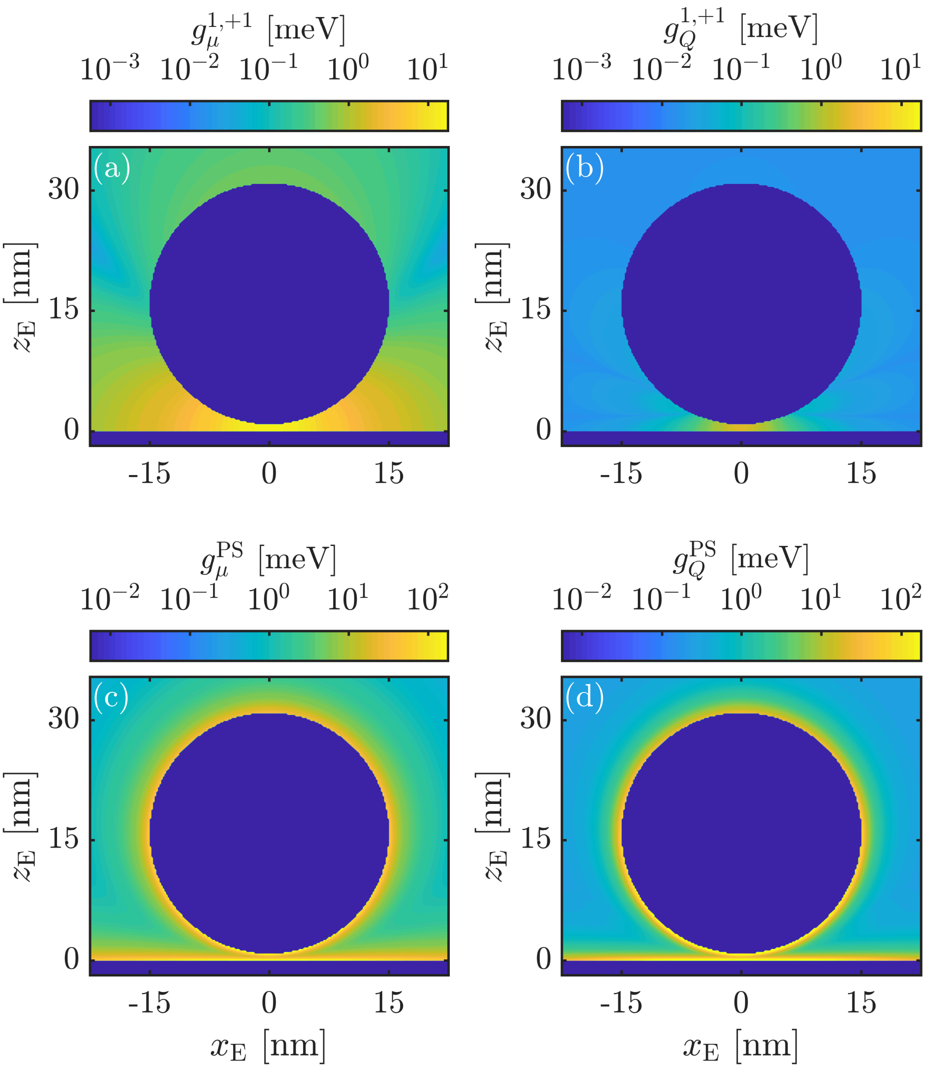

Figure 2.8: Spatial dependence of QE-SP coupling strengths (in log scale) within the xz-plane ($D = 30.0\,\mathrm{nm}$, $\delta = 0.9\,\mathrm{nm}$). Panels (a) and (b) show the dipolar and quadrupolar exciton coupling strength to the lowest order, even SP mode ($n = 1$, $\sigma = +1$). Bottom panels correspond to the (c) dipolar and (d) quadrupolar coupling to the plasmonic pseudomode.

We focus next in the NPoM gap and explore the spatial form of the QE-SP coupling strength specifically this region. As a complement to Figure 2.8, we present in Figure 2.9 the scanning of the $g_i^{n,\sigma}(\mathbf{r}_\mathrm{E})$ for different modes. Panels (a) and (b) render $g_i^{1,+1}$, corresponding to the same configuration as Figure 2.8 panels (a) and (b), making clear the homogeneity of the coupling across the gap for the lowest-order even mode, $\hbar\omega_{1,+1} = 1.55\,\mathrm{eV}$. Fig. 2.9(b) shows the less homogeneous character of the plasmon-quadrupole coupling, as a result of the sensitivity of $g_Q^{n,\sigma}$ to field spatial derivatives.

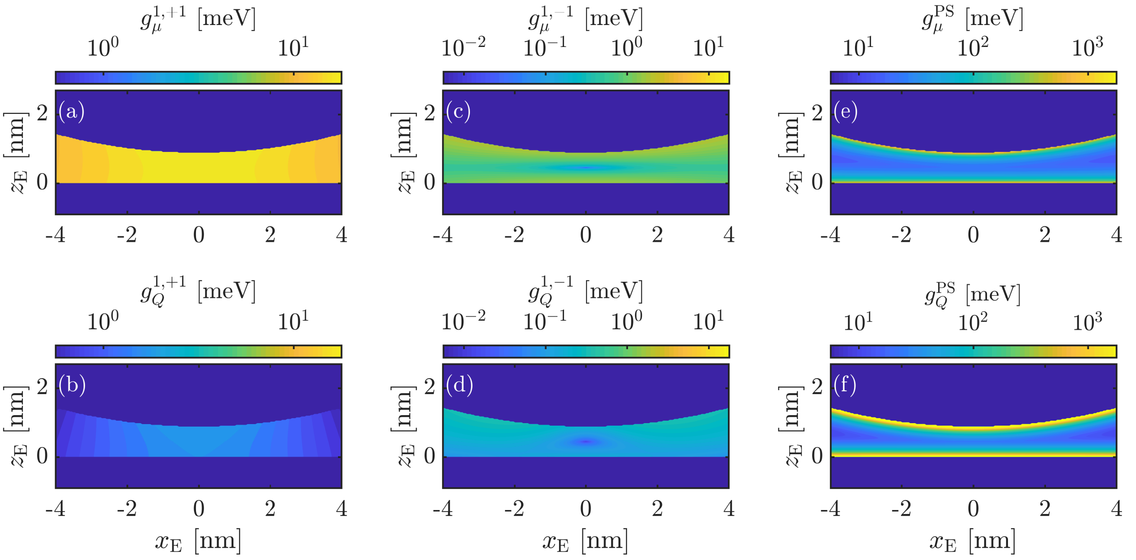

Figure 2.9: Spatial dependence of QE-SP coupling strengths (in log scale) across the NPoM gap ($D = 30.0\,\mathrm{nm}$, $\delta = 0.9\,\mathrm{nm}$). Panels (a-b) show the plasmon-emitter coupling for the lowest even mode $g_i^{1,+1}$ for the dipole and quadrupole exciton, respectively. Panels (c) and (d) render the coupling for the lowest odd mode $g_i^{1,-1}$. Finally, in panels (e) and (f), we plot the dipolar and quadrupolar coupling strength to the plasmonic pseudomode, g_i^{PS}. All calculations consider $\alpha = 0$ for both dipole and quadrupole orientations.

Panels (c) and (d) in Fig. 2.9 show the map of the coupling strength associated to the lowest odd mode, $g_i^{1,-1}$. As it was shown in Figure 2.7, odd modes become more important as the QE is closer to the metal surface, but also as it is displaced from the symmetric position $\mathbf{r}_\mathrm{E} = (0, \delta/2)$. Finally, in panels (e) and (f), we plot the pseudomode spatial profile, as zoomed versions of Figure 2.8(c) and (d). We can see that the region of largest coupling is tightly confined to the metallic surfaces, with higher strength for the quadrupolar exciton. Those panels reveal that through the exploitation of higher order SP modes and multipolar excitons, spatial resolutions in the light-matter coupling well below the nanometer can be achieved [87].

2.5. Finite-size Effects

In this section, we extend our TO approach in order to address the emergence of mesoscopic effects [130] in the light-matter interactions due to the finite size of the QE [131]. The extreme confinement of the plasmonic coupling strength maps shown in Fig. 2.8

suggests that our NPoM cavity is an ideal platform to explore excitonic charge distributions beyond the point-like description of the EM source. As the spatial variation of g_μ or g_Q approaches length-scales comparable to the QE dimensions, we can expect that this approximation breaks down. By inspection of Fig. 2.9, we can anticipate that these finite-size effects would be higher for the plasmonic pseudomode than for SPs with low n.

A dipole EM source can be depicted as a pair of point-like charges of opposite sign and magnitude $|q|$. The vector between both charge positions is $\boldsymbol{\ell} = \mu/|q|(\sin\alpha, \cos\alpha)$ (note that we assume $\mu = |q|\ell$). As we did with both the dipole and quadrupole, we can solve the problem of scattered fields in the presence of the nanoparticle in the double slab frame. The free space potential of a single charge at a position $\mathbf{r}_q = (x_q, z_q)$, reads

$$\phi_q(x,z) = \frac{-q}{4\pi\epsilon_0}\log((x-x_q)^2 + (z-z_q)^2). \tag{2.49}$$

In the transformed frame, the wire source becomes an array of wire sources, whose potential, after being Fourier-transformed in order to solve the Laplace's equation, can be written as

$$\phi_q(k) = \frac{q}{2\pi\epsilon_0}\sum_{n=-\infty}^{\infty}\frac{\delta(k-n)}{|k|}e^{-|k||x'-x'_q|}e^{-ikz'_q}, \tag{2.50}$$

used to impose the continuity conditions at the metal-dielectric interfaces as we did in Eq. (2.32). Performing the inverse Fourier transform and the inverse conformal transformation, the scattered potential for a single charge in the NPoM system reads

$$\begin{aligned}\phi_{\mathrm{S}}^{q}(x,z) = \frac{1}{2\pi\epsilon_0\epsilon_d}\frac{\epsilon_m-\epsilon_d}{\epsilon_m+\epsilon_d}\sum_{n=1}^{\infty}\frac{q/n}{(\sqrt{\rho}+\sqrt{1+\rho})^{4n}-\left(\frac{\epsilon_m-\epsilon_d}{\epsilon_m+\epsilon_d}\right)^2}\times \\ \left[\frac{\epsilon_m-\epsilon_d}{\epsilon_m+\epsilon_d}\mathrm{Re}\{\mathrm{A}_n^+(\varrho,\varrho_q)\} - (\sqrt{\rho}+\sqrt{1+\rho})^{2n}\mathrm{Re}\{\mathrm{B}_n^+(\varrho,\varrho_q)\}\right],\end{aligned} \tag{2.51}$$

where we have used the definition of the complex vector position $\varrho_q = x_q + iz_q$. The Purcell factor will no longer be given by Eq. (2.25). Instead, it reads now

$$\begin{aligned}P_\mu^{\mathrm{ext}}(\omega) &= \frac{-\mu/\ell}{\mathrm{Im}\{\boldsymbol{\mu}\mathbf{E}_0^\mu(\mathbf{r}_\mathrm{E})\}}\left|\int_{\mathbf{r}_E-\frac{\boldsymbol{\ell}}{2}}^{\mathbf{r}_E+\frac{\boldsymbol{\ell}}{2}}\mathrm{Im}\left\{\nabla\phi_\ell^{(2)}(\mathbf{r})d\mathbf{r}\right\}\right| \\ &= \frac{\mu/\ell}{\mathrm{Im}\{\boldsymbol{\mu}\mathbf{E}_0^\mu(\mathbf{r}_\mathrm{E})\}}\left|\mathrm{Im}\left\{\phi_\ell^{(2)}\left(\mathbf{r}_\mathrm{E}-\frac{\boldsymbol{\ell}}{2}\right)-\phi_\ell^{(2)}\left(\mathbf{r}_\mathrm{E}+\frac{\boldsymbol{\ell}}{2}\right)\right\}\right|\end{aligned} \tag{2.52}$$

where, as the QE dimensions are much smaller than optical wavelengths ($\ell \ll 2\pi c/\omega$), we normalize with the expression given by Eq. (2.28) for the power radiated by a pure

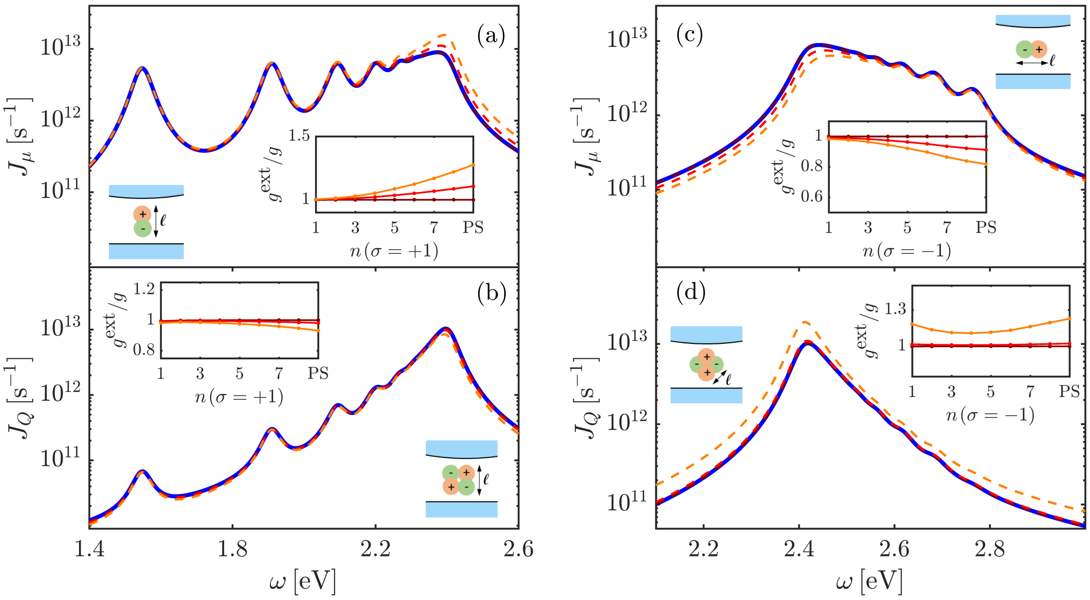

Figure 2.10: Size effects in the spectral density (main panels) and coupling strengths (insets) for the same NPoM cavity and QE parameters as in Fig. 2.5. (a) Dipolar and (b) quadrupolar QEs with $\alpha = 0$. (c) Dipolar and (d) quadrupolar QEs with $\alpha = \pi/2$ and $\alpha = \pi/4$, respectively. The exciton charge distributions are sketched in all panels. The point-source approximation (blue) and finite-size calculations for three different ℓ are shown: 0.05 nm (brown), 0.4 nm (red) and 0.6 nm (orange).

dipole in free space. The quasistatic potential $\phi_\ell^{(2)}(\mathbf{r})$ describes the EM fields scattered by the NPoM cavity excited by the two opposite charges separated by distance ℓ, given by the sum of the contributions in Eq. (2.51) (note that, for simplicity, we have dropped its frequency dependence above). For a generic discrete distribution of N charges, this potential reads

$$\phi_\ell^{(N)}(\mathbf{r}) = \frac{|q|}{2\pi\epsilon_0\epsilon_d}\frac{\epsilon_m-\epsilon_d}{\epsilon_m+\epsilon_d}\sum_{n=1}^{\infty}\frac{1/n}{(\sqrt{\rho}+\sqrt{1+\rho})^{4n}-\left(\frac{\epsilon_m-\epsilon_d}{\epsilon_m+\epsilon_d}\right)^2}\times$$
$$\left[\frac{\epsilon_m-\epsilon_d}{\epsilon_m+\epsilon_d}\mathrm{Re}\left\{\sum_{\nu}^{N}\mathrm{sign}(q_\nu)\mathrm{A}_n^+(\varrho,\varrho_\nu)\right\} - (\sqrt{\rho}+\sqrt{1+\rho})^{2n}\mathrm{Re}\left\{\sum_{\nu}^{N}\mathrm{sign}(q_\nu)\mathrm{B}_n^+(\varrho,\varrho_\nu)\right\}\right], \tag{2.53}$$

where we have labeled the charges through the greek index ν.

As we have done with the dipolar source, an extended quadrupole source corresponds to a square-shaped distribution of four point-like charges with side vectors

$\boldsymbol{\ell} = (Q/\sqrt{2}|q|)^{1/2}(\sin\alpha, \cos\alpha)$ and $\boldsymbol{\ell}_\perp = (Q/\sqrt{2}|q|)^{1/2}(\cos\alpha, -\sin\alpha)$ ($Q = \sqrt{2}|q|\ell^2$). The Purcell factor in this case is given by

$$P_Q^{\mathrm{ext}}(\omega) = \frac{Q/\ell^2}{\mathrm{Im}\{(\mathbf{Q}\nabla)\mathbf{E}_0^Q(\mathbf{r}_\mathrm{E})\}}\Big|\mathrm{Im}\Big\{\phi_\ell^{(4)}\Big(\mathbf{r}_\mathrm{E}+\tfrac{\boldsymbol{\ell}_+}{2}\Big)+\phi_\ell^{(4)}\Big(\mathbf{r}_\mathrm{E}-\tfrac{\boldsymbol{\ell}_+}{2}\Big) - \phi_\ell^{(4)}\Big(\mathbf{r}_\mathrm{E}+\tfrac{\boldsymbol{\ell}_-}{2}\Big)-\phi_\ell^{(4)}\Big(\mathbf{r}_\mathrm{E}-\tfrac{\boldsymbol{\ell}_-}{2}\Big)\Big\}\Big|, \quad (2.54)$$

where $\boldsymbol{\ell}_\pm = \boldsymbol{\ell} \pm \boldsymbol{\ell}_\perp$, with the corresponding normalization for a pure quadrupolar source in free space given by Eq. (2.29).

Figure 2.10 reveals the complex phenomenology behind mesoscopic effects in QE-SP coupling, which depends very much on the emitter orientation (see sketches in all panels). Dipolar QEs with $\alpha = 0$ (a) and $\alpha = \pi/2$ (c) are displayed in the top panels, whereas quadrupolar excitons with $\alpha = 0$ (b) and $\alpha = \pi/4$ (d) are shown in the bottom ones. The geometric and material parameters are the same as in previous figures and the emitter is placed at the gap center. Spectral densities calculated using the point-source approximation (blue) are compared against finite-size charge distributions for different ℓ: 0.05 nm (brown), 0.40 nm (red) and 0.60 nm (orange). As expected, the former coincides with the point-source spectra in all cases, which proves the validity of Eqs. (2.52) and (2.54) in the limit $\ell \to 0$.

Spectral densities for vertical and horizontal dipoles in Fig. 2.10(a) and (c) show the opposite dependence on ℓ, whereas $J_\mu(\omega)$ increases for $\alpha = 0$, it decreases for $\alpha = \pi/2$. These deviations occur mainly at the pseudomode spectral position, $\hbar\omega_{\mathrm{PS}} \simeq 2.40\,\mathrm{eV}$, whereas peaks in $J_\mu(\omega)$ at lower (a) and higher (c) frequencies, which are associated to low-order SPs with $\sigma = +1$ and $\sigma = -1$, respectively, are rather insensitive to ℓ. This is evident in the insets of both panels, which plot the coupling strengths obtained from extended calculations normalized to the point-dipole predictions, with the latter computed following the same procedure as described in Sec. 2.4. We can observe that $g^{\mathrm{ext}}/g \simeq 1$ for $n < 6$, whereas the ratio increases (a) or decreases (c) significantly with ℓ for larger n. The contrast between both descriptions is maximum at the pseudomode, which allows us to gain insight into our findings through the maps in Fig. 2.9 (evaluated for $\alpha = 0$). Indeed, we can infer that the coupling enhancement in Fig. 2.10(a) is due to the fact that the exciton charges approach the metal boundaries as ℓ increases for $\alpha = 0$, where g_μ^{PS} is maximum. On the contrary, they displace laterally, away from the gap center and towards regions of lower g_μ^{PS} for $\alpha = \pi/2$, yielding the coupling reduction observed in Fig. 2.9(e).

The bottom panels of Fig. 2.10 show that, for QEs located at the gap center, the impact of finite-size effects is smaller for quadrupolar excitons than for dipolar ones. Fig. 2.9(f) shows that g_Q^{PS} is more localized than its dipolar counterpart at the metal boundaries, which explains the insensitivity of both $J_Q(\omega)$ and $g^{\mathrm{ext}}/g \simeq 1$ to QE dimensions up to $\ell = 0.4$ nm for both orientations. Only for $\ell = 0.6$ nm (orange lines) deviations from the point-quadrupole approximation become apparent, which again, they take place mainly at the pseudomode frequency. The spectral density and pseudomode coupling are only slightly lower than the point-quadrupole prediction for $\alpha = 0$, while they are significantly higher for $\alpha = \pi/4$. This higher impact of size effects in Fig. 2.10(d) can be attributed to two factors. First, the distance between the nearest point charges in the quadrupole distribution and the metal boundaries is smaller than in Fig. 2.10(c). Second, by increasing ℓ, these charges (located along the vertical axis) interact more strongly with the odd ($\sigma = -1$) SPs supported by the cavity, while their counterparts remain along the $z = \delta/2$ axis, where g_Q^{PS} is minimum. Let us also stress that the coupling strength calculations, specially in Fig. 2.10(d), must be taken carefully. The fact that the pseudomode peak governs completely the spectral density means that the high quality resonator limit [39], inherent to the modal decomposition of $J_i(\omega)$ in our approach, is not a valid formal assumption in this case.

2.6. Exciton Population Dynamics

Once we have analyzed the dependence of the spectral density and coupling strengths on the various parameters of the system, we explore next the onset of strong coupling between dipolar/quadrupolar excitons and NPoM cavities. Our TO approach has allowed us to write the spectral density in terms of the Purcell factor, related to the classical description of the electric fields in the cavity [72]. As we reviewed in chapter 1, the population dynamics of the QE-EM field combined system can be derived my means of the Wigner-Weisskopf formalism

$$\dot{c}_i(t) = -\int_0^t \int_0^\infty J_i(\omega) e^{i(\omega_i-\omega)(t-t')} c_i(t') d\omega dt', \tag{2.55}$$

where $J_i(\omega)$ for $i = \mu, Q$ appears explicitly and $n_e(t) = |c_i(t)|^2$ is the population of the excited state. The above equation is usually expressed in terms of a kernel that accounts for the frequency dispersion

$$K(t-t') = \int_0^\infty J_i(\omega) e^{i(\omega_i-\omega)(t-t')} d\omega. \tag{2.56}$$

The use of the Wigner-Weisskopf formalism, that we solve numerically (see below), does not need of any decomposition of the spectral density. Nevertheless, the Lorentzian decomposition of $J(\omega)$ allows to write an effective Hamiltonian. Single mode Hamiltonians as the one in the Jaynes-Cummings model associate the density of states to a single Lorentzian, weighted by the light-matter coupling, g. Using this interpretation, we perform an heuristic parametrization of the Hamiltonian, and so on, of the master equation, in terms of discrete set of bosonic lossy modes [96, 132]

$$\hat{H} = \hbar\omega_i \hat{\sigma}_i^\dagger \hat{\sigma}_i + \sum_{n,\sigma} \hbar\omega_{n,\sigma} \hat{a}_{n,\sigma}^\dagger \hat{a}_{n,\sigma} + + \sum_{n,\sigma} \hbar g_i^{n,\sigma} [\hat{\sigma}_i^\dagger \hat{a}_{n,\sigma} + \hat{\sigma}_i \hat{a}_{n,\sigma}^\dagger], \tag{2.57}$$

where $\hat{\sigma}_i$ and $\hat{a}_{n,\sigma}$ are the QE ($i = \mu, Q$) and SP annihilation operators. The full density matrix of the system is then given by the master equation,

$$\frac{\partial \hat{\rho}}{\partial t} = -\frac{i}{\hbar}[\hat{H}, \hat{\rho}] + \sum_{n,\sigma} \frac{\gamma_m}{2} L_{\hat{a}_{n,\sigma}}[\hat{\rho}], \tag{2.58}$$

where γ_m is the Drude damping rate, and $L_{\hat{a}_{n,\sigma}}[\hat{\rho}] = 2\hat{a}_{n,\sigma}\hat{\rho}\hat{a}_{n,\sigma}^\dagger - \{\hat{a}_{n,\sigma}^\dagger \hat{a}_{n,\sigma}, \hat{\rho}\}$ is the Lindblad term that accounts for the absorption losses experienced by the SP mode with indices n and σ[3]. In our further analysis, we prove that Eq. (2.58) yields the same exciton population dynamics as the Wigner-Weisskopf solution of the problem given by Eq. (2.55). Let us also stress that, more recently, a formal correspondence between spectral densities and master equations have been established [42], in agreement with this parametrization. We study the temporal evolution of the exciton population, $n_e(t) = \langle e, \{0\}_{n\sigma} | \hat{\rho}(t) | e, \{0\}_{n\sigma} \rangle = \hat{\rho}_{ee}(t)$, in a spontaneous emission configuration. Note that $|e, \{0\}_{n\sigma}\rangle$ stands for the product of the QE excited state and the ground state of all SP modes. Thus, we set the initial density matrix for the system to $\hat{\rho}(t = 0) = |e, \{0\}_{n\sigma}\rangle \langle e, \{0\}_{n\sigma}|$ and investigate the population dynamics.

In the following, we will pay special attention to the occurrence of non-monotonic, reversible dynamics in $n_e(t)$, which we can relate to the onset of QE-SP strong coupling. In this regime, light and matter excitations mix together, giving rise to hybrid states known as plasmon-exciton polaritons (PEPs) [133]. PEP characteristics can be controlled through the weight of their two constituents. For quantum nanophotonics applications, this phenomenon makes it possible to tune the balance between the high coherence of SPs, and the high nonlinearities of optical transitions in QEs [118, 134, 135].

Figure 2.11 analyzes $n_e(t)$ for a vertically-oriented dipolar QE ($\mu = 0.55\,\mathrm{e{\cdot}nm}$) placed at the gap of a NPoM cavity with $\delta = 0.9\,\mathrm{nm}$ and $D = 30.0\,\mathrm{nm}$. Fig. 2.11(a) plots the spectral density at two different positions along the symmetry axis of the structure, $z_\mathrm{E} = \delta/2$ (solid line) and $z_\mathrm{E} = 7\delta/8$ (dashed line). It shows a significant enhancement in

---

[3] The inclusion of radiative losses in the plasmonic modes does not change significantly the following discussion about population dynamics.

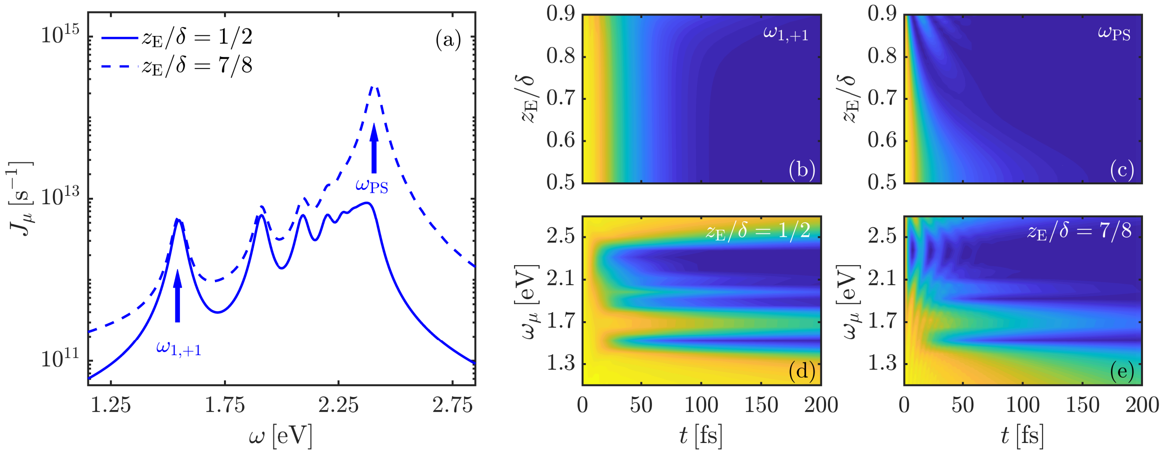

Figure 2.11: (a) Spectral density for a dipolar QE at two different positions within the NPoM cavity in Fig. 2.8 ($\mu = 0.55$ e·nm, $\alpha = 0$). QE population versus time and position for (b) $\omega_\mu = \omega_{1,+1} = 1.55\,$eV and (c) $\omega_\mu = \omega_{\rm PS} = 2.40\,$eV, see vertical arrows in panel (a). QE population versus time and frequency for (d) $z_{\rm E} = \delta/2$ and (e) $z_{\rm E} = 7\delta/8$. The linear color scale in all contourplots ranges from $n_e = 1$ (yellow) to $n_e = 0$ (dark blue).

$J_\mu(\omega)$ as the emitter approaches the metal boundaries. Fig. 2.11(b) and (c) display the exciton population as a function of time and $z_{\rm E}$ for two different QE frequencies (indicated by vertical arrows in panel (a)): $\hbar\omega_\mu = \hbar\omega_{1,+1} = 1.55\,$eV and $\hbar\omega_\mu = \hbar\omega_{\rm PS} = 2.40\,$eV, respectively. If the QE is at resonance with the lowest-frequency SP, $n_e(t)$ undergoes a smooth monotonic decay, as shown in panel (b). Importantly, this trend barely depends on the QE position. Taking into account the uniform $g_\mu^{1,+1}$ map in Fig. 2.9(a), we can conclude that the QE-SP interaction is governed by this mode in this case. On the contrary, when the QE is resonant with the plasmonic pseudomode, $n_e(t)$ varies significantly, see Figure 2.11(c). As expected from $g_\mu^{\rm PS}$ distribution in Fig. 2.9(e), displacing the QE away from the gap center translates into a faster decay initially, and in the occurrence of Rabi oscillations in $n_e(t)$ for $z_{\rm E} > 0.7\delta$. Note that their pitch, the Rabi frequency, diminishes as $z_{\rm E}$ increases further. They reveal the occurrence of QE-SP strong-coupling, and the formation of PEPs, the new eigenstates of the system. Fig. 2.11(d) and (e) explore in a comprehensive manner the dependence of $n_e(t)$ on the QE natural frequency. Panel (d) corresponds to $z_{\rm E} = \delta/2$, and shows that reversible dynamics does not take place at any ω_μ in this configuration. Notice though that the decay rate increases abruptly when the emitter is at resonance with a SP mode. This is particularly evident at frequencies approaching $\omega_{\rm PS}$. Panel (e) is evaluated at $z_{\rm E} = 7\delta/8$ and unveils the emergence of re-

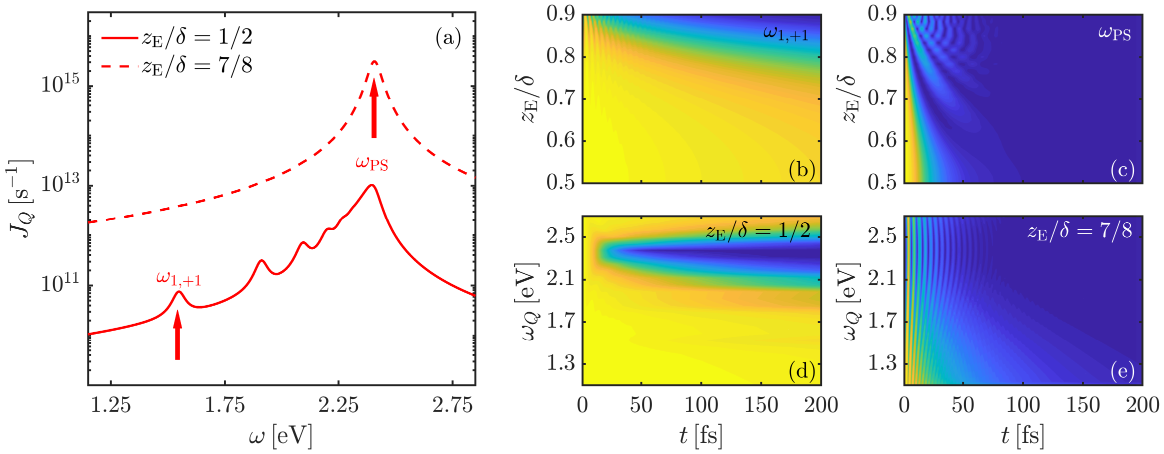

Figure 2.12: (a) Spectral density for a quadrupolar QE at two different positions within the NPoM cavity in Fig. 2.8 ($Q = 0.75$ e·nm^2, $\alpha = 0$). QE population versus time and position for (b) $\omega_Q = \omega_{1,+1} = 1.55\,$eV and (c) $\omega_Q = \omega_{\mathrm{PS}} = 2.40\,$eV, see vertical arrows in panel (a). QE population versus time and frequency for (d) $z_{\mathrm{E}} = \delta/2$ and (e) $z_{\mathrm{E}} = 7\delta/8$. The linear color scale in all contourplots ranges from $n_e = 1$ (yellow) to $n_e = 0$ (dark blue).

versible dynamics in the QE population. The Rabi oscillations become specially apparent in the vicinity of the plasmonic pseudomode, where the evolution of the QE population within the first 50 fs exhibits 5 well-defined maxima ($n_e > 0.6$) and minima ($n_e \simeq 0$).

Figure 2.12 reproduces the study in Fig. 2.11 but for quadrupolar QEs ($Q = 0.75$ e·nm^2, $\alpha = 0$). Fig. 2.12(a) evidences the higher sensitivity of the quadrupole spectral density on the emitter position. Whereas several SP maxima are apparent at the gap center (solid line), $J_Q(\omega)$ is completely governed by the pseudomode at $z_{\mathrm{E}} = 7\delta/8$ (dashed line). Fig. 2.12(b) and (c) reveal that, in agreement with the $g_Q^{n,\sigma}$ contourplots in Fig. 2.9(b)-(f), $n_e(t)$ depends more strongly on z_{E} than it does for dipolar QEs. As shown in Fig. 2.12(b), the QE-SP interaction remains in the weak-coupling regime for $\omega_Q = \omega_{1,+1}$, although the decay rate experiences a strong reduction as z_{E} increases. On the contrary, oscillations in $n_e(t)$ take place when the QE is only slightly displaced from $z_{\mathrm{E}} = \delta/2$ for $\omega_Q = \omega_{\mathrm{PS}}$ (see Fig. 2.12(c)). The system enters the strong-coupling regime in this case, yielding a clear enlargement in the Rabi frequency as the emitter position approaches the metal surface. Fig. 2.12(d) shows that, regardless of ω_Q, the quadrupolar QE at the gap of the cavity always experience a monotonic decay (highly Purcell enhanced at the pseudomode). In contrast, Fig. 2.12(e) proves that $n_e(t)$ develops Rabi oscillations for all QE frequencies when placed at the gap boundaries. As expected, their pitch depends only moderately

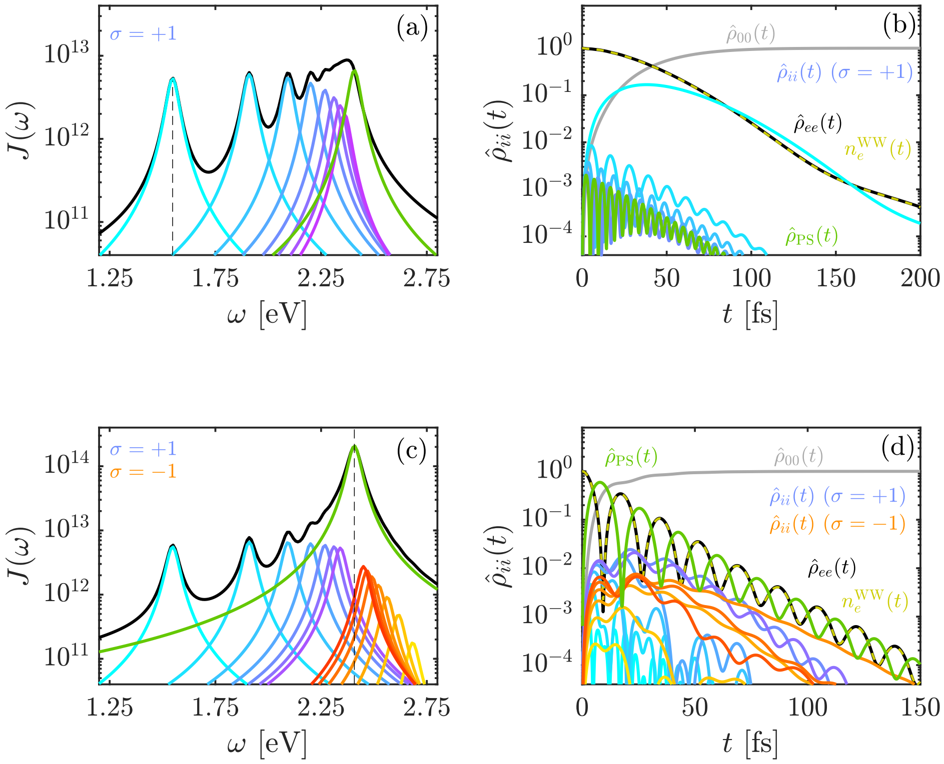

Figure 2.13: Population dynamics in a NPoM cavity. Spectral densities at two different positions of the dipolar QE, $z_{\mathrm{E}} = \delta/2$ (a) and $z_{\mathrm{E}} = 7\delta/8$ (c), with the first even and odd Lorentzian contributions in blue-to-violet and yellow-to-red colorscales, respectively. For each case, the QE natural frequency is chosen to be $\omega_\mu = \omega_{1,+1}$ and $\omega_\mu = \omega_{\mathrm{PS}}$, marked by the vertical dashed lines. Panels (b) and (d) plot the different calculations of the population dynamics, both through the Wigner-Weisskopf and the Lindblad master equation approaches. Colorscales follow the same code as panels (a) and (c). The QE has been chosen $\boldsymbol{\mu} = \mu\hat{\mathbf{z}}$ with $\mu = 0.55\,\mathrm{e}\cdot\mathrm{nm}$.

on ω_Q, as the QE-SP interaction is fully determined by the plasmonic pseudomode.

Our master equation formulation of the problem allows us to go further and investigate not only the excitonic population but also the plasmonic ones. In the following discussion, we focus on the dipolar exciton and two of the most paradigmatic configurations considered above. Left panels in Figure 2.13 plot spectral density as well as modal Lorentzian contributions for $z_{\mathrm{E}} = \delta/2$ (a) and $z_{\mathrm{E}} = 7\delta/8$ (c), where the dominance of the pseudomode is clear. In both panels, the dashed black line marks the QE transition frequency, in resonance with $\omega_{1,+1}$ and ω_{PS}, respectively. Blue-to-purple lines show the increasing azimuthal order for even ($\sigma = +1$) modes, while orange-like lines render the odd ones, only apparent in panel (c). Green line plots the contribution of the pseudomode, $\hbar\omega_{\rm PS} = 2.40\,{\rm eV}$, with $g_\mu^{\rm PS}$ calculated from Eq. (2.48), and $n_{\rm min} = 10$. Right panels show the population dynamics. Black and yellow solid lines plot the exciton population calculated through the Wigner-Weisskopf approach and the master equation, $\hat{\rho}_{ee}(t)$. They overlap exactly, which proves the validity of our TO parametrization of Eqs. (2.57) and (2.58). Grey solid lines render the population of the ground state. The rest of the lines plot the population of different plasmonic modes, following the same color code as panels (a) and (c). As expected from previous panels, in Fig. 2.13(b), the large coupling between the QE and the $\omega_{1,+1}$ plasmonic mode makes this mode the initial receiver of excitation, even yielding a small feeding of population back into the dipolar exciton. For larger n, the smaller coupling and the detuning between ω_μ and $\omega_{n,+1}$ yields faster oscillations and much lower plasmon populations. The pseudomode does not play a relevant role in the dynamics. This is not the case in Fig. 2.13(d), since both even and odd modes have comparable contributions to $J_\mu(\omega)$, specially around the pseudomode (Fig. 2.13(c), green line), whose contribution is dominant. We can observe that the excited state undergoes a series of oscillations. The richer phenomenology now involves the whole set of even and odd modes, where those with $\omega_n \sim \omega_{\rm PS}$ play a role. Note that the principal population exchange is assisted by the pseudomode (green line). Those results prove that the NPoM cavity cannot be pictured as a single mode, not even a single mode and the pseudomode.

2.7. Scattering Spectrum

After exploring QE-SP strong-coupling through the temporal evolution of the exciton population, we turn our attention into the emergence of polariton signatures in far-field magnitudes, which are accessible experimentally. Specifically, we model a dark-field spectroscopy setup [136, 137], sketched in Figure 2.14(a). The system is pumped coherently by a laser field with amplitude E_L and frequency ω_L. The grazing laser provides no direct reflection from the mirror within the numerical aperture of the confocal microscope, that detects the fields scattered by the NPoM cavity along the vertical direction. Without any emitter in the cavity, the different plasmonic modes sustained by the nanoparticle couple to the laser field, through their modal effective dipole moment. The pure quasistatic character of the TO results does not provide access to those radiative effects. Nevertheless, several efforts have been made into the extension of the approach beyond the quasistatic limit. Radiative losses can be included in the response by accounting for the power absorbed by a fictive particle in the transformed frame [64, 67, 98]. Radiative reaction effects accounting for the self-interaction between the nanostructure and its own scattered field can be also related to the field scattered by those fictive absorbers.

As we are interested in the interplay between plasmonic and emitter dipoles, we use a procedure following Ref. [98], where the nanostructure is illuminated by a field perpendicularly polarized with respect the structure axis. This way, we introduce the radiative corrections, obtaining $\gamma_{n,\sigma} = \gamma_m + \gamma^{\mathrm{r}}_{n,\sigma}$, where the non-radiative losses are given by the Drude metal absorption. The starting point is given by the resonance condition of the modes, given by Eq. (2.33). The radiative-corrected resonance conditions [98] read

$$(\sqrt{\rho}+\sqrt{1+\rho})^{2n} = \frac{\epsilon_m-\epsilon_d}{\epsilon_m+\epsilon_d}\left(1+i\frac{2n\pi\omega^2}{c^2}(\delta+\sqrt{\delta(\delta+D)})^2\right), \tag{2.59}$$

$$(\sqrt{\rho}+\sqrt{1+\rho})^{2n} = -\frac{\epsilon_m-\epsilon_d}{\epsilon_m+\epsilon_d}, \tag{2.60}$$

for $\sigma=+1$ (even) and $\sigma=-1$ (odd) modes, respectively

Then, we require the fulfillment of the above conditions for a general complex frequency for each mode, $\tilde{\omega}_{n,\sigma} = \omega_{n,\sigma} + i\gamma_{n,\sigma}$. The expression for odd modes yields $\tilde{\omega}_{n,-1} = \omega_{n,-1} + i\gamma_m$, where the only loss mechanism is given by the Drude losses ($\gamma^{\mathrm{r}}_{n,-1} = 0$). In terms of the spatial profile of the electric fields, the cancellation of the induced dipolar moment along the z-direction originates from the odd character of E_z across the gap. On the other hand, for even modes, we find the radiative decay rates associated to SPs, which read

$$\begin{aligned}\gamma^{\mathrm{r}}_{n,+1} \quad = \quad & \frac{n\pi D^2\omega_{n,+1}}{c^2}\left(\rho+\sqrt{\rho(\rho+1)}\right)^2 \times \\ & \times\frac{\omega_p^2-\omega_{n,1}^2(\epsilon_\infty-\epsilon_d)}{(\epsilon_\infty+\epsilon_d)(\sqrt{\rho}+\sqrt{1+\rho})^{2n}-(\epsilon_\infty-\epsilon_d)},\end{aligned} \tag{2.61}$$

in agreement with an induced dipole moment in the nanostructure.

Once $\gamma^{\mathrm{r}}_{n,+1}$ are known, the even SP dipole moments can be obtained. $\gamma^{\mathrm{r}}_{n,+1}$ have been obtained for a NPoM cavity in which the metallic substrate (mirror) is effectively infinite. The total induced dipole moment can be written as the contribution of the nanoparticle dipole moment and its reflection in the mirror by means of the method of images [64]. In a first order approximation, we can write the total dipole, μ_{NPoM}, in terms of the dipole induced in the nanoparticle, μ_n, as

$$\mu_{\mathrm{NPoM}} = \mu_n\left(1+\frac{\epsilon_m-\epsilon_d}{\epsilon_m+\epsilon_d}\right) \tag{2.62}$$

where the second term in brackets represents the image contribution. Therefore, we write

$$\mu_n = \mathrm{Re}\left\{\frac{\epsilon_m(\omega_{n,+1})+\epsilon_d}{2\epsilon_m(\omega_{n,1})}\right\}\sqrt{\frac{3\pi\epsilon_0\hbar\gamma^{\mathrm{r}}_{n,+1}c^3}{\sqrt{\epsilon_d}\,\omega^3_{n,+1}}}. \tag{2.63}$$

where the correction due to the subtraction of the image in the substrate is apparent. Note that this dipole moment is the one relevant in dark-field experiments, where illumination and detection are designed to minimize the effect of substrate reflection. We account for the effect of the embedding dielectric, having $\gamma_i^{\mathrm{r}} = \sqrt{\epsilon_d}\gamma_i$ $(i = \mu, Q)$, where γ_i are the decay rates in vacuum. Figure 2.14(b) and (c) plot the radiative decay rates and the dipole moments associated to the even plasmonic modes of the system, $\omega_{n,+1}$. Blue-to-yellow lines render the results for different NPoM cavities, with fixed $D = 30.0\,\mathrm{nm}$ and increasing δ from 0.9 to 5.4 nm in steps of 0.9 nm. The larger overall size of the cavity translates into larger radiative losses, but the frequency-dependent character of the image correction, $\mathrm{Re}\{\frac{\epsilon_m(\omega_{1,+1})+\epsilon_d}{2\epsilon_m(\omega_{1,+1})}\}$ provides an almost constant μ_1. Furthermore, increasing δ supplies the predominance of the lowest order modes in the scattering contributions.

The Hamiltonian description for the dark-field experiment reads $\hat{H}_{\mathrm{exp}} = \hat{H}_0 + \hat{H}_L$. The first term is the Hamiltonian given by Eq. (2.57), whereas the second term represents the Hamiltonian for the coherent driving part [138, 139], representing the laser pumping of the system,

$$\hat{H}_L = \sum_{n,+1}(\boldsymbol{\mu}_n\mathbf{E}_L)\left(e^{-i\omega_L t}\hat{a}^\dagger_{n,+1} + e^{+i\omega_L t}\hat{a}_{n,+1}\right) + (\boldsymbol{\mu}_i\mathbf{E}_L)\left(e^{-i\omega_L t}\hat{\sigma}_i^\dagger + e^{+i\omega_L t}\hat{\sigma}_i\right). \tag{2.64}$$

Note that the pumping can couple both the emitter and the plasmonic modes. For the case of the pure quadrupolar emitter, $\mu_Q = 0$, so $\hat{H}_L$ only couples light with the plasmonic dipolar momenta of the even modes. Both the laser field and plasmonic momenta are vertical, so in the following we assume that the dipolar exciton is also vertically oriented, enabling us to replace the scalar products in Eq. (2.64) by the product of the modulus of the incident field and dipole momenta.

The introduction of the coherent driving introduces time-dependences in our Hamiltonian, which can be removed by operating in the rotating frame. Under the use of unitary transformations given by operator $\hat{\mathcal{U}}(t) = e^{-i\hbar\hat{\mathbf{A}}t}$, with

$$\hat{\mathbf{A}} = \hbar\omega_L\left(\hat{\sigma}_i\hat{\sigma}_i + \sum_{n,\sigma}\hat{a}^\dagger_{n,\sigma}\hat{a}_{n,\sigma}\right), \tag{2.65}$$

the Hamiltonian operator in the rotating frame, $\hat{H}'_{i,\mathrm{exp}} = \hat{\mathcal{U}}^\dagger(t)\hat{H}_{\mathrm{exp}}\hat{\mathcal{U}}(t) - \hat{\mathbf{A}}$ reads

$$\begin{aligned}\hat{H}'_{i,\mathrm{exp}} = \hbar(\omega_i - \omega_L)\hat{\sigma}_i^\dagger\hat{\sigma}_i + \sum_{n,\sigma}\hbar(\omega_{n,\sigma} - \omega_L)\hat{a}^\dagger_{n,\sigma}\hat{a}_{n,\sigma} + \sum_{n,\sigma}\hbar g_i^{n,\sigma}(\hat{a}^\dagger_{n,\sigma}\hat{\sigma}_i + \mathrm{h.c.})\\ + (\mu_i E_L)(\hat{\sigma}_i^\dagger + \hat{\sigma}_i) + \sum_n(\mu_n E_L)(\hat{a}^\dagger_{n,+1} + \hat{a}_{n,+1}).\end{aligned} \tag{2.66}$$

In order to compute the dark-field scattering signal, we account for the radiative losses

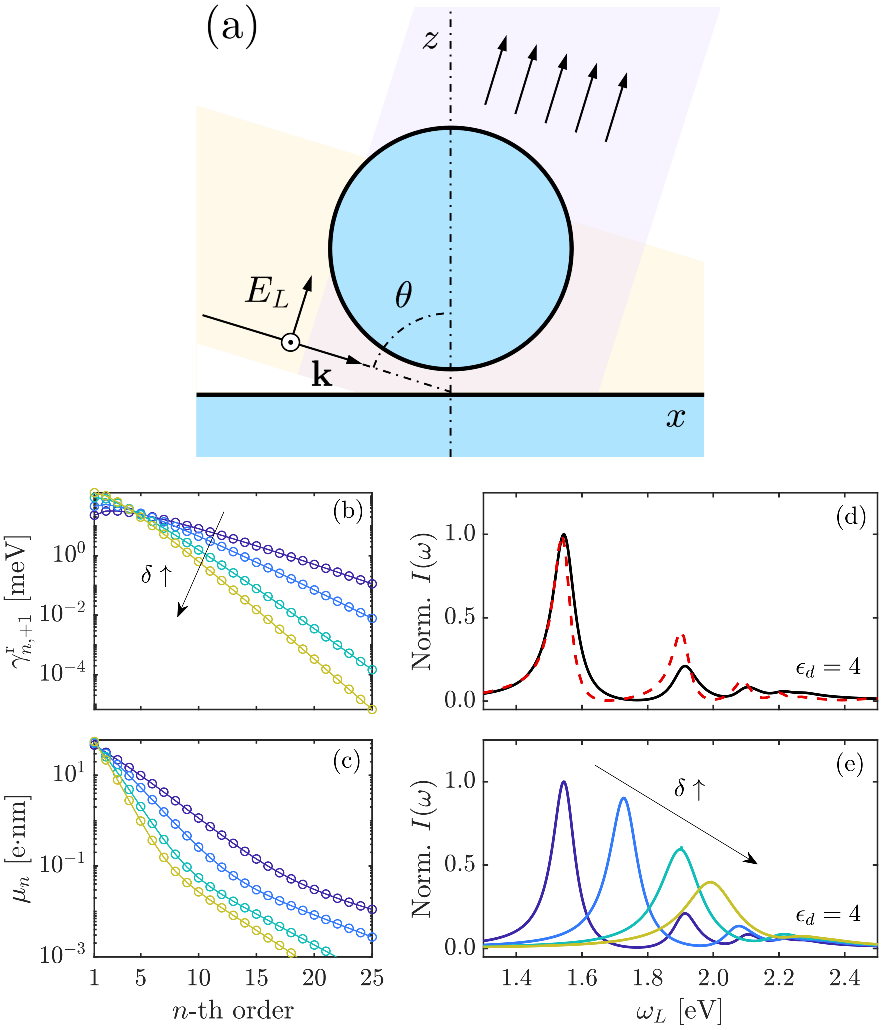

Figure 2.14: Scattering spectrum. (a) Schematics of the side-illumination dark-field setup. (b-c) Plasmonic radiative decay rates and dipolar momenta as a function of the mode order n. Blue-to-yellow colors set the different values for $D = 30.0$ nm and $\delta \in [0.9, 5.4]$ nm. (d) Normalized scattering spectrum for the bare NPoM, $(D, \delta) = (30.0, 0.9)$ nm. Black solid line plots the TO result while red dashed line renders the numerical solution of Maxwell's equations. (e) Different scattering spectra associated to NPoM cavities ($D = 30.0$ nm and $\delta \in [0.9, 5.4]$ nm in 0.9 nm steps, with same color code as panels (b-c).)

associated to both SPs and QEs in the master equation describing the dark-field setup,

$$\frac{\partial \hat{\rho}'}{\partial t} = -\frac{i}{\hbar}[\hat{H}'_{i,\mathrm{exp}}, \hat{\rho}'] + \sum_{n,\sigma} \frac{\gamma_{n,\sigma}}{2} L_{\hat{a}_{n,\sigma}}[\hat{\rho}'] + \frac{\gamma_i^{\mathrm{r}}}{2} L_{\hat{\sigma}_i}[\hat{\rho}'], \tag{2.67}$$

where $\hat{\rho}'$ is the density matrix in the rotating frame. Under continuous pumping, the scattering spectrum is obtained from the steady-state solution of Eq. (2.67), where temporal derivatives vanish. Furthermore, in the limit of low intensity in the driving, several simplifications can be done [138, 140]. Firstly, as most of the population remains in the ground state, the refilling terms in the Lindblad superoperators ($2\hat{\mathcal{O}}^\dagger \hat{\rho} \hat{\mathcal{O}}$ in $L_{\hat{\mathcal{O}}}[\hat{\rho}]$) are negligible. The master equation becomes equivalent to a Schrödinger equation with an effective non-Hermitian Hamiltonian (for each case $i = \mu, Q$)

$$\begin{aligned} \hat{H}'_{i,\mathrm{eff}} = \hbar(\tilde{\omega}_i - \omega_L)\hat{\sigma}_i^\dagger \hat{\sigma}_i + \sum_{n,\sigma} \hbar(\tilde{\omega}_{n,\sigma} - \omega_L)\hat{a}^\dagger_{n,\sigma}\hat{a}_{n,\sigma} \\ + \sum_{n,\sigma} \hbar g_\mu^{n,\sigma}(\hat{a}^\dagger_{n,\sigma}\hat{\sigma}_i + \mathrm{h.c.}) + E_L(\hat{M}_i + \hat{M}_i^\dagger). \end{aligned} \tag{2.68}$$

As desired, the Hamiltonian given by Eq. (2.68) does not depend on time, and the laser frequency introduces a detuning in the first two terms of the Hamiltonian. The operator $\hat{M}_i = \mu_i \hat{\sigma}_i \delta_{i\mu} + \sum_n \mu_n \hat{a}_{n,+1}$ excludes the quadrupolar excitation under the coherent pumping. The frequencies $\tilde{\omega}$ are defined as complex magnitudes, i.e. $\tilde{\omega} = \omega + i\frac{\gamma}{2}$, with the corresponding losses of each case. Due to the low intensity, the Schrödinger equation can be solved within perturbation theory and the steady state can be expanded in a power series of the incident field E_L. Subsequently, as the electric field in the far-field is proportional to the collective dipole moment of the hybrid cavity-QE system [138] , the scattering spectrum, given by the expectation value of the far-field intensity, can be written as

$$\sigma_{\mathrm{sca}}(\omega_L) = \langle \psi_{\mathrm{SS}} | \hat{M}\hat{M}^\dagger | \psi_{\mathrm{SS}} \rangle \,. \tag{2.69}$$

In Figure 2.14(d), we show that Eq. (2.69), restricted to the first excitation manifold and in the limit of low pumping ($E_L \to 0$), reproduces σ_{sca} for bare NPoM cavities, obtained through full electrodynamic calculations[4] (black solid and red dashed lines, respectively), normalized to the scattering maximum. Several peaks can be distinguished, as well as the invisibility dips in between them. Those, which are a characteristic of the scattering spectra which do not appears in the Purcell factor, are due to the destructive interference between the bright modes [64]. Finally, Figure 2.14(e) plots the normalized

---

[4] Performed using the Maxwell's Equation solver implemented in COMSOL Multiphysics.

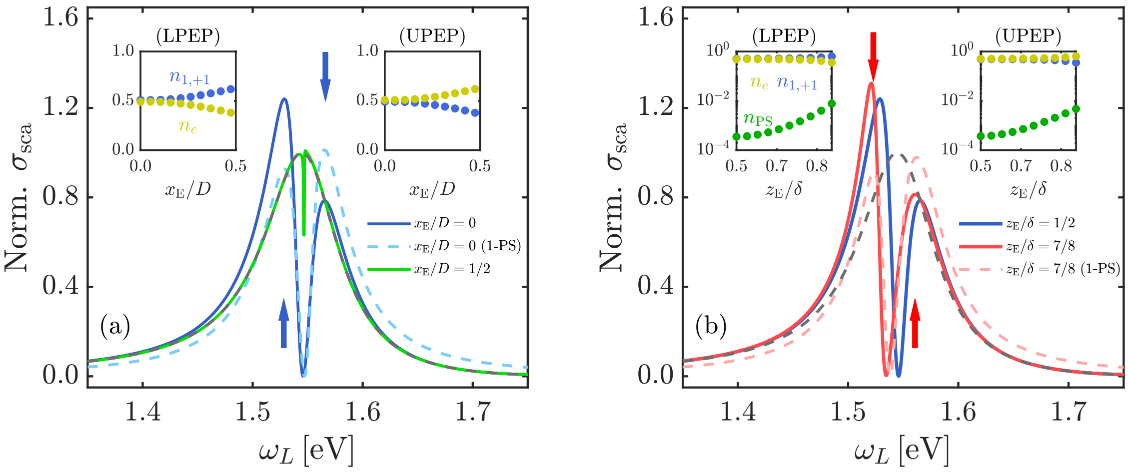

Figure 2.15: Far-field scattering spectra for a dipolar QE placed at a NPoM cavity. All parameters are the same as in Fig. 2.9 and $\omega_\mu = \omega_{1,+1}$. The QE is displaced away from the gap center along (a) x and (b) z-directions. In both panels, grey dashed and blue solid lines render the bare cavity cross section and the spectrum for the QE at the gap center, respectively. Vertical arrows indicate the PEP frequencies for the spectrum in the corresponding color. Right (left) insets plot the square of the Hopfield coefficients, n_e, $n_{1,+1}$ and $n_{\rm PS}$, for the upper (lower) PEP as a function of the QE position.

scattering spectra for different gap sizes, showing the blueshifting of the maximum as δ increases [141].

After a brief description of our calculation of far-field spectra, we investigate next the scattering properties of the QE-SP hybrid systems considered in sec. 2.6. Mimicking the experimental configuration, we fix the QE frequency at resonance with the lowest, brightest SP mode, for which $\omega_{1,+1} = 1.55\,\text{eV}$ and $\mu_1 = 46\,\text{e}\cdot\text{nm}$, and focus in a narrow spectral window around it. As we have notice in Figure 2.14, radiative features occur mainly at the lowest order modes. The normalization of the cross section is defined so that $\sigma_{\rm sca}(\omega_{1,+1}) = 1$ for the bare NPoM structure (in absence of QEs).

Figure 2.15 shows normalized scattering spectra for a vertically-oriented dipolar QE. Grey dashed lines correspond to the bare cavity, and blue solid ones plot $\sigma_{\rm sca}(\omega_L)$ when the QE is at the gap center (the spectra are the same in both panels). The former present a symmetric Lorentzian maximum centered at the SP frequency. The latter exhibit a well-defined Rabi doublet structure, with a central minimum at $\omega_L = \omega_{1,+1}$ and two maxima at the upper (U) and lower (L) PEP frequencies [80, 138, 142]. This splitting is considered the fingerprint of QE-SP strong-coupling regime, and has been thoroughly analyzed in recent experimental reports on gap plasmonic cavities [118, 143, 144].

The gap-center spectrum (blue solid line) in Fig. 2.15 is clearly asymmetric, as the maximum below the SP frequency (lower PEP) is significantly higher than the one above it (upper PEP). In order to analyze the origin of this asymmetry [131], we use a reduced Hamiltonian where the exciton is just coupled with the lowest even plasmon $\omega_{1,+1}$ and with an effective pseudomode ω_{PS}, obtaining the spectrum $\sigma_{\mathrm{sca}}(\omega_L)$ given by the cyan dashed line plots. We can observe that the doublet is symmetric in this case, which allows us to conclude that the height difference of the peaks in the full calculation originates from the interaction between the QEs and even SP modes with azimuthal indices between 2 and $n_{\min} = 7$ (see Eq. (2.48)). The green solid line corresponds to a QE displaced away from the gap center by $D/2 = 15\,\mathrm{nm}$ along x-direction. Fig. 2.8(a) shows that $g_\mu^{1,+1}$ is much lower in this position. The spectrum overlaps with the bare cavity, except in the vicinity of $\omega_{1,+1}$, where it develops a Fano-like profile [145], characteristic of the weak or intermediate coupling regimes [146]. The width of this feature is of the order of $\hbar\gamma_\mu^{\mathrm{r}} \simeq 10\,\mu\mathrm{eV}$, radiative losses of the dipolar QE in free space, and the sharp dip in the spectrum is a consequence of the weak, coherent interaction between QE and cavity [145]. The insets plot the square of the Hopfield coefficients for the lower (left) and the upper (right) PEP as a function of x_{E}/D. These give the PEP content on the dipolar QE, $n_e = |\langle e, \{0\}_{n,\sigma}|\psi_{\mathrm{SS}}\rangle|^2$, (blue dots) and lowest SP mode, $n_{1,+1} = |\langle g, 1_{1,+1}|\psi_{\mathrm{SS}}\rangle|^2$ (yellow dots). They show that, as x_{E}/D increases, the lower PEP becomes more QE-like while the upper acquires a SP-character, due to the reduction of the QE-SP coupling,

Figure 2.15(b) explores the effect that moving the dipolar QE vertically has on the far-field spectrum. Red solid line plots $\sigma_{\mathrm{sca}}(\omega_L)$ for emitter positions very close to the metal surface ($z_{\mathrm{E}} = 7\delta/8$). We can observe that both the Rabi splitting and the difference between lower and upper PEP scattering maxima remain very similar to the ones at the gap center. On the contrary, the whole doublet structure has shifted slightly to lower frequencies (note that the scattering minima is no longer at $\omega_{1,+1}$). The orange dashed line plots the same spectrum but considering only the lowest SP and the pseudomode in the evaluation of Eq. (2.69). The position of the doublet is the same as in the full calculation but, once again, the asymmetry in the peaks height has vanished. This fact agrees with our interpretation, which links the differences in the scattering maxima with intermediate even SP modes. This approximate spectrum exhibits the same redshift as the exact one. Taking Fig. 2.9 into account, we can attribute this shifting of the Rabi doublet to the stronger coupling between the QE and the plasmonic pseudomode caused by the vertical displacement. The squared Hopfield coefficients in the insets of this panel show that, similarly to Fig. 2.15(a), the balance between n_e and $n_{1,+1}$ in both PEPs is

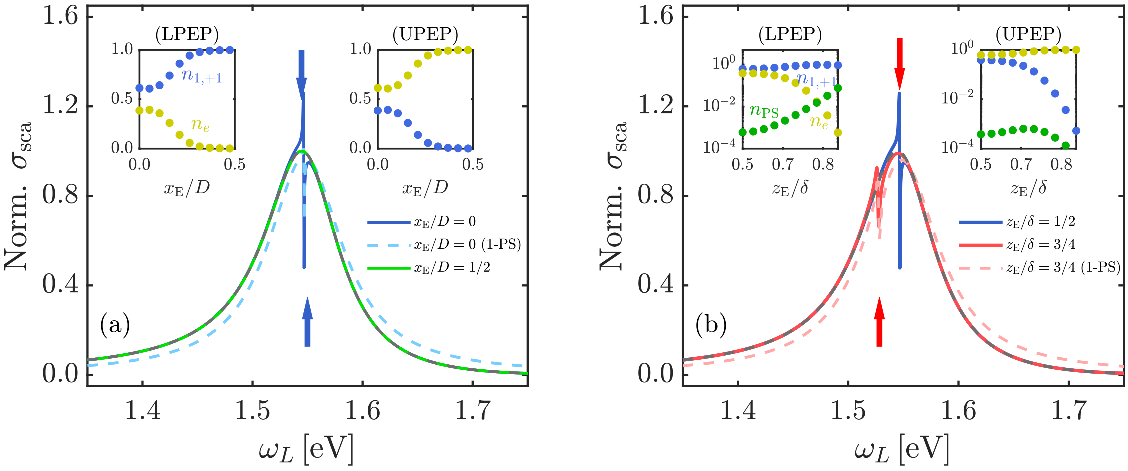

Figure 2.16: Far-field scattering spectra for a quadrupolar QE placed at a NPoM cavity. All parameters are the same as in Fig. 2.9 and $\omega_Q = \omega_{1,+1}$. The QE is displaced away from the gap center along (a) x and (b) z-directions. In both panels, grey dashed and blue solid lines render the bare cavity cross section and the spectrum for the QE at the gap center, respectively. Vertical arrows indicate the PEP frequencies for the spectrum in the corresponding color. Right (left) insets plot the square of the Hopfield coefficients, n_e, $n_{1,+1}$ and n_{PS}, for the upper (lower) PEP as a function of the QE position.

lost as z_{E} increases. Importantly, in contrast to the lateral displacement, this unbalance is accompanied here by an exponential growth of $n_{\text{PS}} = |\langle g, 1_{\text{PS}}|\psi_{\text{SS}}\rangle|^2$ (green dots). This verifies that, indeed, the redshift experienced by the scattering features originates from the stronger interaction between the QE and the plasmonic pseudomode. In fact, it can be interpreted as a result of the anticrossing between the upper PEP and another, even higher frequency, PEP (not analyzed here) that is located around ω_{PS} which emerges due to the QE-pseudomode coupling [97].

Figure 2.16 presents an analysis similar to the one in Fig. 2.15 but for quadrupolar QEs. Grey dashed and blue solid lines in both panels plot the bare cavity cross section and the spectrum for $(x_{\text{E}}, z_{\text{E}}) = (0, \delta/2)$ (all system parameters are the same as in Fig. 2.15 except $Q = 0.75\,\text{e}\cdot\text{nm}^2$). In contrast to its dipolar counterpart, the gap-center spectrum does not exhibit a Rabi doublet, but a sharp Fano profile at $\omega_L = \omega_{1,+1}$. This is due to the fact that $g_Q^{1,+1} \ll g_\mu^{1,+1}$ at the gap center, as shown in Fig. 2.9. As a result of the weaker coupling, the PEP energies (see vertical arrows) are close together in this case. Note that we use the term PEP to designate the state of the hybrid cavity-QE system at the two laser frequencies given by the vertical arrow, although the system may not be in the strong coupling regime. Lighter blue dashed lines in Fig. 2.16(a) render $\sigma_{\text{sca}}(\omega_L)$ for the same configuration, but including only the lowest SP and the pseudomode in the calculation. The deviations from the exact result are apparent mainly at the scattering minimum, which reveals that intermediate SPs play a more minor role than in dipolar QEs. Green solid line plots the $\sigma_{\text{sca}}(\omega_L)$ for $x_{\text{E}} = D/2 = 15\,\text{nm}$. As expected from the tight localization of $g_Q^{1,+1}$ at the NPoM gap in Fig. 2.8(b), this spectrum coincides with the scattering cross section of the bare cavity, as QE-SP interactions vanish in this position. The square of the PEP Hopfield coefficients in the insets shows that the system remains in the weak-coupling regime for all x_{E}/D values. They demonstrate that the lower PEP (upper PEP) collapses into the quadrupole exciton (lowest SP mode) as the emitter moves away from the center of the gap.

The sensitivity of the scattering cross section to variations in the vertical position of the quadrupolar QE is analyzed in Fig. 2.16(b). Red solid and orange dashed lines plot $\sigma_{\text{sca}}(\omega_L)$ at $z_{\text{E}} = 3\delta/4$ obtained from the full NPoM plasmonic spectrum and including only the lowest SP and pseudomode contributions in the calculation, respectively. The differences between them are even smaller than at the gap center, see Fig. 2.16(a). We can observe that, by approaching the emitter to the metal surface, the Fano-like profile in the blue solid line shifts to lower frequencies, but no Rabi doublet structure emerges in the spectrum. This means that the interaction between the QE and the lowest SP remains in the weak-coupling regime, despite the enhancement experienced by their coupling strength. Fig. 2.8(b)-(f) reveal that g_Q^{PS} grows much faster than $g_Q^{1,+1}$ with z_{E}, which explains why the main effect observed in $\sigma_{\text{sca}}(\omega_L)$ is the red-shift of the Fano feature. Again, this occurs due to the anticrossing with another PEP, whose initial content is mainly pseudomode [97]. The square of the lower PEP Hopfield coefficients in the left inset shows that for larger z_{E}/δ, $n_{1,+1}$ decreases, while n_{PS} increases, modifying the inherent character of this hybrid state, which now emerges from the hybridization of the QE exciton and the plasmonic pseudomode. The right panel shows that the upper PEP collapses into the lowest, bright SP in this process, decoupling completely from the quadrupolar QE.

2.8. Conclusions

In this chapter, we have presented a Transformation Optics approach that exploits two-dimensional conformal mapping to obtain a full analytical, insightful description of plasmon-exciton interactions in a nanoparticle-on-a-mirror cavity. Two different quantum emitters, supporting only dipolar or only quadrupolar transitions, have been thoroughly analyzed and compared. We have firstly computed the nanocavity spectral densities for both emitter families, which can be decomposed in terms of Lorentzian contributions. This enables us to identify the plasmon-exciton coupling strengths for the full nanocavity electromagnetic spectrum, which becomes naturally quantized. Next, we have characterized in detail the dependence of plasmon-exciton coupling strengths on the emitter position and orientation. Special attention has been paid to mesoscopic effects taking place when the dimensions of the exciton charge distribution are comparable to the gap of the structure. Finally, the onset of the strong-coupling regime and the formation of plasmon-exciton polaritons has been investigated in two different, complementary, studies. First, we have revealed the occurrence of Rabi oscillations in the temporal evolution of the exciton population in a spontaneous emission configuration. Second, we have shown the emergence of a Rabi doublet structure in the dark-field scattering spectrum of the nanocavity-emitter system under laser illumination.

3

Two excitons in a plasmonic cavity

In the previous chapter, we tackled the complete analysis of the light-matter coupling for a single emitter in nanoparticle-on-mirror (NPoM) cavities. In this chapter, we proceed to present our results on two different studies involving the presence of more than a single excitonic level in the cavity. We remark that in our investigation, we will restrict ourselves to electronic transitions, which couple directly to the EM modes of the cavity, without any consideration about the complexity associated to the vibrational structure of the emitter.

In the first part of the chapter, we focus on the case when two different dipolar quantum emitters (QEs) are present in the system. We study two plasmonic cavities where the presence of a QE as a distorter can alter the local density of states (LDOS) (experienced by a probing QE). In section 3.1, we present our investigation, quantifying the distortion in terms of the Purcell factor and the spectral density, calculated by means of first-order scattering theory through the electromagnetic Green's function. Our theory reveals that $J(\omega)$ presents a series of non-Lorentzian resonances that arise from the interaction between plasmonic fields and the distorting emitter, contrary to the symmetric Lorentzian spectra of the bare plasmonic cavity even in the sub-wavelength regime of our interest.

Additionally, plasmonic systems constitute an incomparable frame to examinate the limits of the point-dipole approximation for QEs. Under the influence of free space plane waves, the interaction of an emitter with the electric field is dominated by its dipolar contribution. Nevertheless, the spatial confinement of plasmonic fields not only causes a large field enhancement but also provides a very abrupt variation of the electromagnetic fields over minimal spatial scales. Then, along a given direction, the electric field associated to plasmonic resonances presents wavevector components much larger than free space waves, $k \gg \omega/c$ contributing to the quadrupolar coupling with an enhancement $|\mathbf{kE}|^2$, where $\mathbf{E}$ is the electric field amplitude. This boost, vaster than the experienced by dipolar momenta [147, 148] leads to the question if dipolar and quadrupolar transitions coexist in the same time scales, making posible their interaction. In section 3.2, we present our results about the inclusion of a second excited state (quadrupolar-like) in a three-level-system QE. We study the phenomenology associated to the dynamics of the excited state and scattering far-field spectrum in a NPoM cavity, finding the interplay of light-allowed and light-forbidden states through plasmonic resonances.

3.1. Presence of a distorting emitter in the nanocavity

In this section, we focus our attention on the study of two QEs interacting with a nanocavity that sustains plasmonic resonances. The general form of the system is presented in Figure 3.1(a). The first QE, $\boldsymbol{\mu}$, probes the LDOS of the hybrid system, composed by the metallic nanostructure and the second QE, $\boldsymbol{\mu}_{\mathrm{E}}$. Our attention will be in analyzing how this emitter distorts the spectral density of the bare cavity. In order to describe the effect of the distorting QE in the system, we introduce the topic of macroscopic light-matter interaction in terms of an scattering description following Ref. [55]. The primary field, $\mathbf{E}_{\mathrm{I}}(\mathbf{r})$, which corresponds to the bare cavity solution, is written as

$$\mathbf{E}_{\mathrm{I}}(\mathbf{r},\omega) = \frac{\omega^2}{\epsilon_0 c^2}\mathbf{G}_{\mathrm{I}}(\mathbf{r},\mathbf{r}',\omega)\boldsymbol{\mu}, \tag{3.1}$$

in terms of the Green's function $\mathbf{G}_{\mathrm{I}}(\mathbf{r},\mathbf{r}',\omega)$ and the dipolar source, $\boldsymbol{\mu}$, placed at position $\mathbf{r}'$. At this point, we consider the presence of the second emitter, which modifies the response of the system as a correction to $\mathbf{E}_{\mathrm{I}}(\mathbf{r})$, and we model this second emitter through an effective permittivity, $\epsilon(\mathbf{r},\omega)$. After the electric field $\mathbf{E}_{\mathrm{I}}(\mathbf{r},\omega)$ spans the region of interest, the inhomogeneity described by $\epsilon(\mathbf{r},\omega)$ induces an scattered field, $\mathbf{E}_{\mathrm{S}}(\mathbf{r},\omega)$. The absence of charges provides the validity of the Helmholtz equation $(\nabla^2 + \epsilon(\mathbf{r},\omega)\left(\frac{\omega}{c}\right)^2)\mathbf{E}_{\mathrm{II}}(\mathbf{r},\omega) = 0$ for the total field $\mathbf{E}_{\mathrm{II}}(\mathbf{r},\omega) = \mathbf{E}_{\mathrm{I}}(\mathbf{r},\omega) + \mathbf{E}_{\mathrm{S}}(\mathbf{r},\omega)$, which implies

$$\left(\nabla^2 + \left(\frac{\omega}{c}\right)^2\right)\mathbf{E}_{\mathrm{S}}(\mathbf{r},\omega) = -\left(\frac{\omega}{c}\right)^2\Big(\epsilon(\mathbf{r},\omega) - 1\Big)\mathbf{E}_{\mathrm{II}}(\mathbf{r},\omega). \tag{3.2}$$

Equation (3.2) is an inhomogeneous Helmholtz equation for the scattered field where the source term is given by $\epsilon(\mathbf{r},\omega)$ and $\mathbf{E}_{\mathrm{II}}(\mathbf{r},\omega)$ that can be solved formally in terms of the Green's function

$$\mathbf{E}_{\mathrm{S}}(\mathbf{r},\omega) = \left(\frac{\omega}{c}\right)^2 \int d^3\mathbf{r}'\mathbf{G}_{\mathrm{I}}(\mathbf{r},\mathbf{r}',\omega)\Big(\epsilon(\mathbf{r}',\omega)-1\Big)\mathbf{E}_{\mathrm{II}}(\mathbf{r}',\omega), \tag{3.3}$$

whose first order solution for the scattered field is then given by[1]

$$\mathbf{E}_{\mathrm{S}}(\mathbf{r},\omega) = \frac{\omega^2}{\epsilon_0 c^2} \int d^3\mathbf{r}'\mathbf{G}_{\mathrm{I}}(\mathbf{r},\mathbf{r}',\omega)\mathbf{P}(\mathbf{r}',\omega), \tag{3.4}$$

where we have used $\mathbf{D} = \epsilon_0\mathbf{E} + \mathbf{P}$. In the limit where the scatterer is small compared to the spatial scales of the fields, this is equivalent to

$$\mathbf{E}_{\mathrm{S}}(\mathbf{r},\omega) = \frac{\omega^2}{\epsilon_0 c^2}\mathbf{G}_{\mathrm{I}}(\mathbf{r},\mathbf{r}_{\mathrm{E}},\omega)\mathbf{p}_{\mathrm{E}}(\omega), \tag{3.5}$$

where $\mathbf{p}_{\mathrm{E}}(\omega)$ is the electric dipole induced in the inhomogeneity (distorting emitter). It is written as a linear expression $\mathbf{p}_{\mathrm{E}}(\omega) = \tilde{\boldsymbol{\alpha}}_{\mathrm{E}}(\omega)\mathbf{E}_{\mathrm{I}}(\mathbf{r}_{\mathrm{E}},\omega)$ in terms of the polarizability tensor $\tilde{\boldsymbol{\alpha}}_{\mathrm{E}}(\omega) = \tilde{\alpha}_{\mathrm{E}}(\omega)\mathbf{T}(\hat{\mathbf{n}}_{\mathrm{E}})$, where $[\mathbf{T}(\hat{\mathbf{n}}_{\mathrm{E}})]_{ij} = [\hat{\mathbf{n}}_{\mathrm{E}}]_i\delta_{ij}$ accounts for the orientation of the distorting QE (δ_{ij} is the Kronecker delta). Thus, we are able to write the electric field $\mathbf{E}_{\mathrm{II}}(\mathbf{r},\omega)$ as

$$\mathbf{E}_{\mathrm{II}}(\mathbf{r},\omega) = \frac{\omega^2}{\epsilon_0 c^2}\mathbf{G}_{\mathrm{I}}(\mathbf{r},\mathbf{r}',\omega)\boldsymbol{\mu} + \frac{\omega^2}{\epsilon_0 c^2}\mathbf{G}_{\mathrm{I}}(\mathbf{r},\mathbf{r}_{\mathrm{E}},\omega)\tilde{\boldsymbol{\alpha}}_{\mathrm{E}}(\omega)\mathbf{E}_{\mathrm{I}}(\mathbf{r}_{\mathrm{E}},\omega). \tag{3.6}$$

By means of the relation between the primary field and the probing QE given by Eq. (3.1) we can rewrite Eq. (3.6) as

$$\mathbf{E}_{\mathrm{II}}(\mathbf{r},\omega) = \frac{\omega^2}{\epsilon_0 c^2}\mathbf{G}_{\mathrm{II}}(\mathbf{r},\mathbf{r}',\omega)\boldsymbol{\mu}, \tag{3.7}$$

where we have used $\mathbf{G}_{\mathrm{II}}(\mathbf{r},\mathbf{r}',\omega)$, the Green's function tensor for the hybrid cavity-QE system, written in terms of its counterpart for the bare cavity as [55, 149],

$$\mathbf{G}_{\mathrm{II}}(\mathbf{r},\mathbf{r}',\omega) = \mathbf{G}_{\mathrm{I}}(\mathbf{r},\mathbf{r}',\omega) + \Psi_0\mathbf{G}_{\mathrm{I}}(\mathbf{r},\mathbf{r}_{\mathrm{E}},\omega)\tilde{\boldsymbol{\alpha}}_{\mathrm{E}}(\omega)\mathbf{G}_{\mathrm{I}}(\mathbf{r}_{\mathrm{E}},\mathbf{r}',\omega). \tag{3.8}$$

Equation (3.8) presents the two different terms marked by arrows in Fig. 3.1(a). As in previous chapters, we evaluate the impact of the environment on the probing emitter at its own position, $\mathbf{G}_{\mathrm{II}}(\mathbf{r},\mathbf{r},\omega)$, as indicated in the figure. The metallic resonator, embedded in a surrounding medium ($\epsilon_d = 1$), is described through a Drude-fitting to Ag permittivity of the form $\epsilon(\omega) = \epsilon_\infty - \omega_p^2/(\omega(\omega + i\gamma_m))$ with parameters $\epsilon_\infty = 9.7$, $\hbar\omega_p = 8.91\,\mathrm{eV}$ and $\hbar\gamma_m = 0.06\,\mathrm{eV}$, equivalent to the permittivity used in the previous chapter. In the figures in this chapter, we use the convention $\hbar = 1$ and parameters related to frequency will have energy dimensions. The probing and distorting QEs are

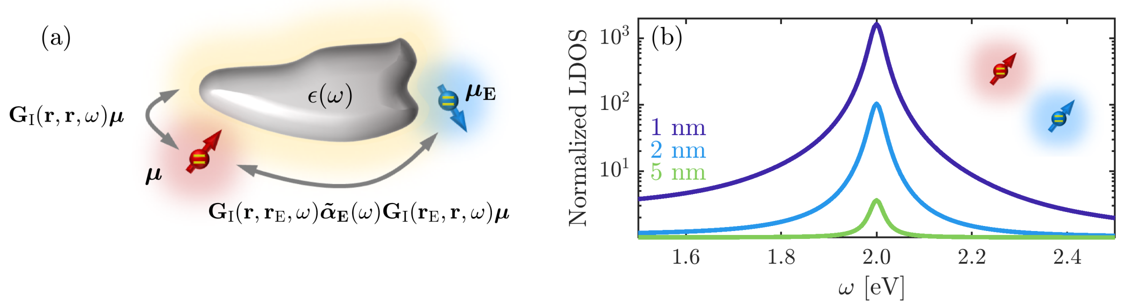

Figure 3.1: Two QEs in a plasmonic cavity. (a) Sketch of the system under study. A QE, $\boldsymbol{\mu}$, probes the LDOS of a plasmonic cavity, with metal permittivity $\epsilon(\omega)$, modified by the presence of a second emitter, $\boldsymbol{\mu}_{\mathrm{E}}$. Grey arrows sketch the two terms in the first-order scattering theory description of the total Green's function. (b) Normalized LDOS experienced by an emitter in free space when a second, parallel one, is placed in its surroundings. Color code (indicated in the legend) corresponds to different separations between emitters ($\mathbf{d} = (\mathbf{r}_{\mathrm{E}} - \mathbf{r}) \perp \boldsymbol{\mu}$).

characterized by their transition dipole momenta ($\boldsymbol{\mu} = \mu\hat{\mathbf{n}}_{\mu}, \boldsymbol{\mu}_{\mathrm{E}} = \mu_{\mathrm{E}}\hat{\mathbf{n}}_{\mathrm{E}}$), their respective transition frequencies $(\omega, \omega_{\mathrm{E}})$ and their positions $(\mathbf{r}, \mathbf{r}_{\mathrm{E}})$.

The distorting emitter is described by a quasistatic atom-like polarizability can be written in the form $\alpha_{\mathrm{E}}(\omega) = \frac{\mu_{\mathrm{E}}^2}{\hbar}\mathcal{L}_{\mathrm{E}}(\omega)$, where $\mathcal{L}_{\mathrm{E}}(\omega) = \frac{1}{(\omega_{\mathrm{E}} - i\gamma_{\mathrm{E}}/2) - \omega}$ is the complex Lorentzian function defined by ω_{E} and γ_{E}, the absorption linewidth [68]. This expression does not satisfy the optical theorem, since the associated extinction cross-section only assesses absorption but not scattering. Nevertheless, it can be refined through a correction to the free space QE polarizability [67] in order to take into consideration the effects of depolarization under the cavity field. It is expressed in terms of the bare cavity Green's function, and therefore does not only account for far-field radiation losses but mainly for near-field plasmonic absorption. This correction is introduced in the theory as the contribution of the associated self-induced field at the position of the induced dipole, contained in $\mathrm{Im}\{\mathbf{G}_{\mathrm{I}}(\mathbf{r}_{\mathrm{E}}, \mathbf{r}_{\mathrm{E}}, \omega)\}$, leading to

$$\tilde{\alpha}_{\mathrm{E}}(\omega) = \frac{\alpha_{\mathrm{E}}(\omega)}{1 - i\beta_{\mathrm{I}}(\mathbf{r}_{\mathrm{E}}, \mathbf{r}_{\mathrm{E}}, \omega)\alpha_{\mathrm{E}}(\omega)}, \tag{3.9}$$

which is equivalent to the condition that emerges from the fulfillment of the optical theorem in the case of a small particle [150]. We have defined the function $\beta_{\mathrm{I}}(\mathbf{r}_{\mathrm{E}}, \mathbf{r}_{\mathrm{E}}, \omega) = \Psi_0 \mathrm{Im}\{\hat{\mathbf{n}}_{\mathrm{E}}\mathbf{G}_{\mathrm{I}}(\mathbf{r}_{\mathrm{E}}, \mathbf{r}_{\mathrm{E}}, \omega)\hat{\mathbf{n}}_{\mathrm{E}}\}$, that accounts for the projection of the Green's function along

---

[1] Equation (3.3) presents a recursive integral form, found in other typical scattering expressions as Lippmann-Schwinger equation, that can be solved iteratively [55].

the orientation of the distorting QE. In addition, we have introduced the frequency dependent factor Ψ_0, which depends on the problem dimensionality and it takes the values $\Psi_0 = \frac{\omega^2}{\epsilon_0 c^2}$ for three-dimensional (3D) calculations or $\Psi_0 = \frac{4\omega^3}{3\pi\epsilon_0 c^3}$ if we consider two-dimensional (2D) systems. Although the electric field in both 2D and 3D systems is correctly defined, the difference in Ψ_0 for each case relies on the different spatial dependence of the dipole moment and the Green's function depending on the dimensionality of the problem $[\mathbf{G}_{3\mathrm{D}}(\mathbf{r},\mathbf{r},\omega)] \neq [\mathbf{G}_{2\mathrm{D}}(\mathbf{r},\mathbf{r},\omega)]$.

As it has been already explained in previous chapters, the Purcell factor, P_f, corresponds to the normalized LDOS. This is defined as

$$P_i^f(\omega) = \frac{\mathrm{Im}\{\hat{\mathbf{n}}_\mu \mathbf{G}_i(\mathbf{r},\mathbf{r},\omega)\hat{\mathbf{n}}_\mu\}}{\mathrm{Im}\{\hat{\mathbf{n}}_\mu \mathbf{G}_0(\mathbf{r},\mathbf{r},\omega)\hat{\mathbf{n}}_\mu\}}, \tag{3.10}$$

where $\mathbf{G}_0(\mathbf{r},\mathbf{r},\omega) = [\mathbf{I} + \frac{c^2}{\omega^2}\nabla\nabla]G_0(\mathbf{r},\mathbf{r},\omega)$ is the Green's function tensor in free space and $G_0(\mathbf{r},\mathbf{r},\omega)$ is the scalar Helmholtz Green's function [151]. Index $i = \mathrm{I,II}$ refers to the bare and QE-distorted cavity, respectively. Figure 3.1(b) shows the modification of the free space LDOS by a single QE, i.e. $\mathbf{G}_\mathrm{I}(\mathbf{r},\mathbf{r}_\mathrm{E},\omega) = \mathbf{G}_0(\mathbf{r},\mathbf{r}_\mathrm{E},\omega)$ in Eq. (3.8). A Purcell factor peak emerges in the spectrum, that inherits its Lorentzian-like shape from the QE absorption lineshape. Throughout this chapter, the QE parameters ($\mu_\mathrm{E} = 0.4\,\mathrm{e{\cdot}nm}$, $\hbar\gamma_\mathrm{E} = 0.03\,\mathrm{eV}$) are set in agreement with recent experimental characterization of dye molecules [152]. In Fig. 3.1(b), the dipole moments of both QEs are parallel to each other ($\hat{\mathbf{n}}_\mu \parallel \hat{\mathbf{n}}_\mathrm{E}$) and $\mathbf{d} = (\mathbf{r}_\mathrm{E} - \mathbf{r}) \perp \hat{\mathbf{n}}_\mu$. The height of the LDOS maximum is set by the dipole moment strength of the distorting QE and $|\mathbf{d}|$, the distance between the emitters, for which we chose three different values. We can observe Purcell enhancements as large as 10^3 for QE-QE distances as small as 1 nm.

3.1.1. Emitter distortion of Purcell factor: NPoM case

We use the scattering formalism above to study the Purcell factor experienced by the emitter $\boldsymbol{\mu}$ in a NPoM cavity hosting the emitter $\boldsymbol{\mu}_\mathrm{E}$. The system is characterized by the following geometrical parameters: D, diameter of the particle, δ, gap size between the particle and the mirror plane, and the positions of the probing and distorting QEs, $\mathbf{r}$ and $\mathbf{r}_\mathrm{E}$, respectively.

Figure 3.2(a) shows the variety of effects that the presence of the distorting QE in the vicinity of the NPoM cavity can produce in the near-field emission spectrum (mainly into non-radiative channels) of the probing one. The inset presents a sketch of the cavity and the emitters. Black to grey dotted lines correspond to $P_\mathrm{I}^f(\omega)$, the normalized LDOS

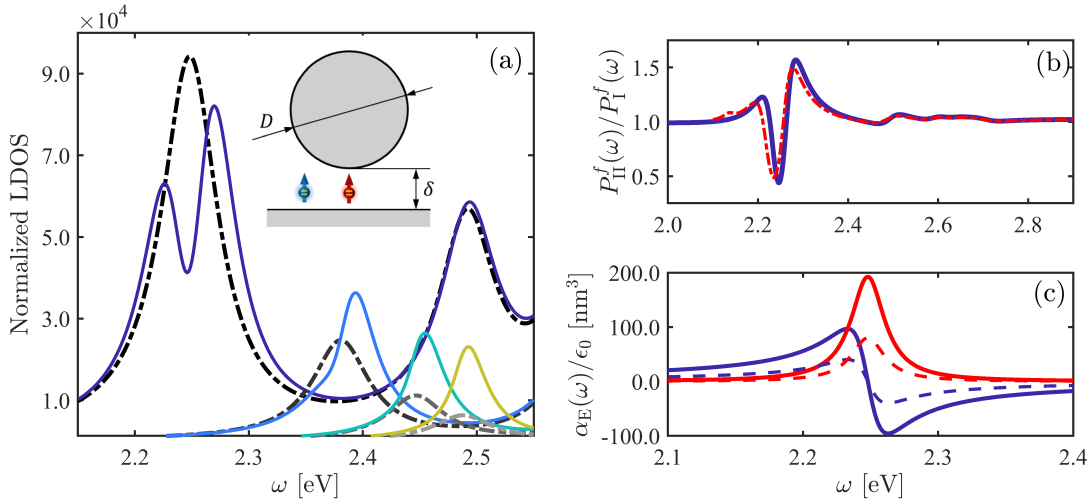

Figure 3.2: Distortion of the LDOS in NPoM cavities by a QE. (a) Normalized LDOS spectra for NPoM cavities with $D = 35\,$nm and different gap sizes ($\delta \in [1, 4]\,$nm from dark blue to yellow in 1 nm steps) for a vertical QE at the gap center. Black to grey dotted lines represent $P_{\rm I}^f(\omega)$. Blue to yellow solid lines show $P_{\rm II}^f(\omega)$, corresponding to the distorted spectra due to a QE, displaced 0.5 nm horizontally from the probing one. (b) $P_{\rm II}^f(\omega)/P_{\rm I}^f(\omega)$ for $D = 35\,$nm and $\delta = 1\,$nm. The blue solid line corresponds to full electrodynamic calculations whereas red dotted one is the scattering theory calculation in the quasistatic limit. (c) Red and blue solid lines plot the real and imaginary parts of the polarizability $\alpha_{\rm E}(\omega)$ for the case $\omega_{\rm E} = \omega_1 = 2.25\,$eV. Dashed lines show the same components of $\tilde{\alpha}_{\rm E}(\omega)$, corrected due to the depolarization field induced in the cavity.

spectrum, for a single emitter in different cavities, $D = 35\,$nm and increasing δ, from 1 to 4 nm in 1 nm steps, placed at the center of the gap and oriented along the vertical direction (see red marker in the inset). The LDOS of the bare cavity is composed by a set of plasmonic modes characterized by their azymuthal order n and their frequency ω_n as shown in chapter 2. In this chapter, we are going to focus on the red side of the pseudomode, (i.e frequencies below $\omega_{\rm PS} = \frac{\omega_p}{\sqrt{\epsilon_\infty+1}}$), where only even modes ($\sigma = +1$) are apparent, so, for the sake of simplicity, we omit index σ. The lowest energy peak corresponds to the dipolar plasmon (ω_1). As ${\rm Re}\{\epsilon(\omega)\}$ diverges for low frequencies, the shrinking of the gap provides that the contribution of the lowest order mode ω_1 increases and redshifts with respect $\omega_{\rm PS}$, the pseudomode frequency at which high-order modes converge.

Dark blue to yellow lines represent the Purcell spectra for the same cavities but considering the hybrid scenario, with the presence of $\boldsymbol{\mu}_{\rm E}$ at a horizontal distance $|\mathbf{d}| = 0.5\,$nm.

The distorting QE is vertically oriented and characterized by the same parameters as in Fig. 3.1(b) with $\omega_{\mathrm{E}} = \omega_1$, i.e. it is always at resonance with the lowest order even plasmon mode. For small gaps, comparable to those realized experimentally to achieve plasmon-exciton strong coupling [87, 118], the presence of $\boldsymbol{\mu}_{\mathrm{E}}$ causes a clear dip in the spectra. As the gap size increases, the dip disappears and the $\boldsymbol{\mu}_{\mathrm{E}}$ causes both an enhancement and blueshifting with respect to the bare cavity LDOS maximum at ω_1. This result demonstrates that the presence of more than one emitter interacting with gap plasmons can enrich the light-matter coupling phenomenology, effectively increasing or decreasing the LDOS depending on the cavity configuration.

In order to check the validity of our scattering approach, we perform finite-element simulations using COMSOL Multiphysics. In our numerical calculations, the probing QE, $\boldsymbol{\mu}$, is treated as a dipolar EM source in the presence of the bare metal cavity. Then, we add an spherical particle with radius a as the object that effectively simulates the absorbing character of the distorting QE, $\boldsymbol{\mu}_{\mathrm{E}}$. Its effective permittivity is chosen to match the atom-like polarizability. Using the quasistatic scattering of a dielectric sphere under plane-wave illumination, we can write $\alpha_{\mathrm{E}}(\omega) = 4\pi\epsilon_0 a^3 \frac{\epsilon_{\mathrm{eff}}(\omega)-1}{\epsilon_{\mathrm{eff}}(\omega)+2}$, or $\epsilon_{\mathrm{eff}}(\omega) = \frac{1+2\eta_{3\mathrm{D}}(\omega)}{1-\eta_{3\mathrm{D}}(\omega)}$, where $\eta_{3\mathrm{D}}(\omega) = \frac{\alpha_{\mathrm{E}}(\omega)}{4\pi\epsilon_0 a^3}$. The value of the free parameter a is set by means of free space calculations similar to those in Fig. 3.1(b). The radius of the distorting QE is made small enough to reach convergence in the Purcell factor spectrum. Note that the effective permittivity used for simulations does not require the introduction of radiative reaction corrections, since those emerge naturally in the numerical solution. Our model is similar to others, applied for phenomena such as plasmon-QE strong coupling [153], plasmon-assisted Förster resonance energy transfer [154], near-field exciton harvesting [155] and energy transfer in nanocrystals [156]. We employ this modelling scheme also to test our 2D analytical calculations for the NPoM cavity, discussed in section 2.3. In this case, the relationship between the polarizability and the permittivity of the distorting QE is $\frac{4\omega}{3\pi c}\alpha_{\mathrm{E}}(\omega) = 2\pi\epsilon_0 a^2 \frac{\epsilon_{\mathrm{eff}}(\omega)-1}{\epsilon_{\mathrm{eff}}(\omega)+1}$, where $\frac{4\omega}{3\pi c}$ is the value of the ratio between 2D and 3D Ψ_0 factors, needed for dimensionality correctness. In this case, the effective permittivity has the form $\epsilon_{\mathrm{eff}}(\omega) = \frac{1+\eta_{2\mathrm{D}}(\omega)}{1-\eta_{2\mathrm{D}}(\omega)}$ with $\eta_{2\mathrm{D}}(\omega) = \frac{4\omega}{3\pi c}\frac{\alpha_{\mathrm{E}}(\omega)}{2\pi\epsilon_0 a^2}$. Figure 3.2(b) shows the distorted LDOS normalized to the bare cavity one, equivalent to the ratio $P_{\mathrm{II}}^{f}(\omega)/P_{\mathrm{I}}^{f}(\omega)$ between the Purcell factors for the hybrid cavity-QE and bare cavity systems for the case $\delta = 1\,\mathrm{nm}$. Blue solid line corresponds to the numerical calculation and red dotted one to our scattering theory approach. They are in almost perfect agreement. In Figure 3.2(c) we plot both real and imaginary parts of $\alpha_{\mathrm{E}}(\omega)$ in solid blue and red, respectively. Dashed lines display $\tilde{\alpha}_{\mathrm{E}}(\omega)$ for $\delta = 1\,\mathrm{nm}$ ($\hbar\omega_1 = 2.25\,\mathrm{eV}$) when considering the correction $1 + \beta_{\mathrm{I}}(\mathbf{r}_{\mathrm{E}}, \mathbf{r}_{\mathrm{E}}, \omega_{\mathrm{E}})\mathrm{Im}\{\alpha_{\mathrm{E}}(\omega_{\mathrm{E}})\}$. In this configuration, the radiative correction is the strongest,

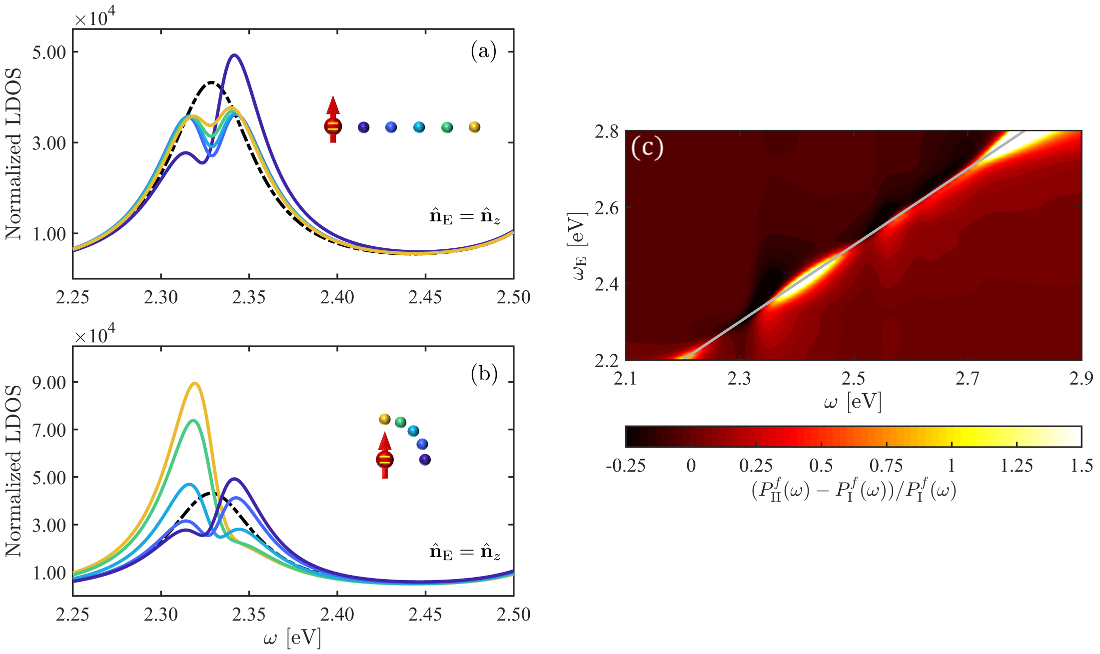

Figure 3.3: LDOS dependence on the QEs relative position. (a) Normalized LDOS dependence on the separation, $|\mathbf{d}|$, between the emitters. Blue to yellow lines show $P^f_\mathrm{II}(\omega)$ for $\boldsymbol{\mu}_\mathrm{E}$ displaced horizontally (see coloured dots plotted in the inset). (b) Normalized LDOS dependence on the orientation of the relative position $\mathbf{d}$ between the QEs for a fixed separation $|\mathbf{d}| = 0.5\,\mathrm{nm}$. In both panels (a) and (b), black dotted line plots the bare cavity spectrum and the probing QE, $\boldsymbol{\mu}$ is placed at $\mathbf{r} = (0, \delta/2)$. (c) Weighted difference $(P^f_\mathrm{II}(\omega) - P^f_\mathrm{I}(\omega))/P^f_\mathrm{I}(\omega)$ as a function of both ω and ω_E for the case where the distorting QE is displaced $|\mathbf{d}| = 0.5\,\mathrm{nm}$ horizontally. (Darkest blue point in insets (a) and (b)). Grey solid line sets $\omega = \omega_\mathrm{E}$. In all panels, the NPoM is defined by $(D, \delta) = (35.0, 1.5)\,\mathrm{nm}$.

but the polarizability keeps its Lorentzian functional form. It is clear that the action of the depolarization field is relevant in the nanometric gaps in Figure 3.2 panels (a) and (b).

The analytical character of the our approach permits us to explore the full set of parameters that define the LDOS. Inspired by the experimental setups in which plasmon-emitter strong coupling has been reported [118, 146], we focus on cavity configurations where the probing QE is placed at the gap center. In Figure 3.3, we explore NPoMs (with fixed $(D, \delta) = (35.0, 1.5)$ nm) in which the distorting QE is around this symmetric position. It presents an exhaustive scan of the effects of the distorting emitter on the Purcell factor. As in Figure 3.2, we center our attention on the case $\omega_\mathrm{E} = \omega_1$ and both $\boldsymbol{\mu}$ and $\boldsymbol{\mu}_\mathrm{E}$ oriented along the vertical direction. , The bare cavity spectrum, $P^f_\mathrm{I}(\omega)$, is plotted in black dotted line in Fig. 3.3(a) and (b). The solid blue-to-yellow lines in Fig. 3.3(a) represent the different Purcell spectra $P^f_{\mathrm{II}}(\omega)$ as $\boldsymbol{\mu}_{\mathrm{E}}$ is displaced horizontally in 0.5 nm steps (see the relative positions in the inset). The dip produced by the emitter changes its character (from asymmetric to symmetric) and finally disappears as the QE-QE separation increases. The interplay between the free space (dominant for the smallest separations) and plasmonic contribution to $\mathbf{G}_{\mathrm{I}}(\mathbf{r}_{\mathrm{E}}, \mathbf{r}, \omega)$ provides the difference in the spectral features. When both emitters are far from each other (not shown here), $\boldsymbol{\mu}_{\mathrm{E}}$ becomes decoupled from the cavity fields and $\mathbf{G}_{\mathrm{I}}(\mathbf{r}_{\mathrm{E}}, \mathbf{r}, \omega)$ is negligible.

Figure 3.3(b) shows how the LDOS is modified depending on the orientation of the relative position vector $\mathbf{d}$ ($|\mathbf{d}| = 0.5$ nm). We consider five different orientations, with angular steps of $\pi/8$. As in Figure 3.3(a), the color code relates each spectrum with the distorting QE position as indicated in the inset. The apparent differences in the Purcell spectra originate from the spatial dependence of $\mathbf{G}_{\mathrm{I}}(\mathbf{r}_{\mathrm{E}}, \mathbf{r}, \omega)$ across the gap. While the vertical component of the plasmonic field at ω_1 is mainly uniform within the gap, the free space contribution changes its sign around its center. This gives rise to LDOS maxima at the low and high frequency sides of the bare cavity resonance, for horizontal and vertical QE-QE relative positions, respectively. In between these two configurations, around the position of the distorting QE that vanishes the free space contribution to $\mathbf{G}_{\mathrm{I}}(\mathbf{r}_{\mathrm{E}}, \mathbf{r}, \omega)$, a symmetric dip emerges in the spectrum. Figure 3.3(c) analyzes the dependence of the Purcell factor on both ω and ω_{E} in terms of the weighted difference $(P^f_{\mathrm{II}}(\omega) - P^f_{\mathrm{I}}(\omega))/P^f_{\mathrm{I}}(\omega)$ for the horizontal configuration with $|\mathbf{d}| = 0.5$ nm (see dark markers in panels (a) and (b)). This magnitude quantifies the effect of the distorting QE beyond the dipolar plasmon and within a broader frequency window. The map shows clearly that the distorting QE affects significantly the Purcell factor even when it is not at resonance with any plasmonic mode of the cavity. Differences between distorted and bare cavity LDOS are apparent at all frequencies, mainly, but not only, when the natural frequencies of both QEs overlap ($\omega = \omega_{\mathrm{E}}$, grey line). Furthermore, as already commented above, the distorting QE can induce an increase or decrease in the Purcell factor depending on the system configuration.

3.1.2. Spectral density and mode decomposition

In order to elucidate the nature of the changes induced by the distorting QE into the cavity LDOS, we focus next into disentangling the different modal contributions to the spectral density, $J_{\mathrm{II}}(\omega)$, that encodes the interaction strength between the probing QE and its electromagnetic environment, written in terms of the Purcell factor $P^f_i(\omega)$ as

$J_{\mathrm{i}}(\omega) = \frac{\gamma_0}{2\pi} P_i^f(\omega)$, where $\gamma_0 = \omega^3\mu^2/(3\pi\epsilon_0\hbar c^3)$ is the decay rate of the probing QE in free space. As shown in sec. 2.4, the Drude-like form of the metal permittivity and the high-quality resonator approximation allow us to express the Dyadic Green's function for the bare cavity as

$$\mathbf{G}_{\mathrm{I}}(\mathbf{r},\mathbf{r}',\omega) = \mathbf{G}_0(\mathbf{r},\mathbf{r}',\omega) + \sum_n \boldsymbol{\mathcal{G}}_n(\mathbf{r},\mathbf{r}')\mathcal{L}_n(\omega), \tag{3.11}$$

where the first term in Eq. (3.11) is the free space dyadic Green's function. The second (scattering) one is decomposed into complex Lorentzian functions, $\mathcal{L}_n(\omega) = \frac{1}{(\omega_n - i\gamma_m/2)-\omega}$, centered at ω_n, the resonant frequency of plasmon mode n, and whose width is given by the metal damping frequency, γ_m [157]. $\boldsymbol{\mathcal{G}}_n(\mathbf{r},\mathbf{r}')$ is the light-matter coupling tensor that weights the contribution of mode n and contains all the spatial information on the modal fields. Crucially, this term is mainly real. Thus, in bare nanocavities, where the second term in Eq. (3.11) dominates, the spectral density acquires the form of a sum of perfectly symmetric Lorentzian profiles, $J_{\mathrm{I}}(\omega) = \sum_n \frac{g_n^2}{\pi}\frac{\gamma_m/2}{(\omega-\omega_n)^2+\gamma_m^2/4}$ with $g_n^2 \propto \hat{\mathbf{n}}_\mu \boldsymbol{\mathcal{G}}_n(\mathbf{r},\mathbf{r},\omega)\hat{\mathbf{n}}_\mu$ [157].

By introducing Eq. (3.11) into Eq. (3.8), we can obtain the spectral density experienced by the probing QE in the distorted cavity as $J_{\mathrm{II}}(\omega) = \frac{\gamma_0}{2\pi}P_{\mathrm{II}}^f = J_{\mathrm{I}}(\omega) + J_{\text{I-II}}(\omega)$, where the second term accounts for the effect of the second QE in the bare cavity LDOS. In general, we can write

$$J_{\text{I-II}}(\omega) = \frac{1}{\pi}\mathrm{Im}\Big\{\sum_n \chi_{1,n}\mathcal{L}_n(\omega) + \sum_n \chi_{2,n}(\mathcal{L}_n(\omega))^2 + \chi_{\mathrm{E}}\mathcal{L}_{\mathrm{E}}(\omega)\Big\}, \tag{3.12}$$

Eq. (3.12) shows clearly that $J_{\mathrm{II}}(\omega)$ does not have the same spectral form as $J_{\mathrm{I}}(\omega)$. The presence of $\boldsymbol{\mu}_{\mathrm{E}}$ in the bare cavity modifies the spectral density through three different physical mechanisms. Firstly, it alters the original plasmonic coupling strength constants, g_n, which are no longer real. Second, it induces modal-like plasmon interactions, yielding quadratic, $(\mathcal{L}_n(\omega))^2$, terms in the LDOS. Finally, the polarizability lineshape of the distorting QE, $\mathcal{L}_{\mathrm{E}}(\omega)$, also emerges naturally in the spectral density, as it does in the free space configuration in Fig. 3.1(b). The different weights of the Lorentzians, χ_i can be written as

$$\chi_i = \frac{\gamma_0\Psi_0}{2\mathrm{Im}\{\hat{\mathbf{n}}_\mu \mathbf{G}_0(\mathbf{r},\mathbf{r},\omega_i)\hat{\mathbf{n}}_\mu\}}\hat{\mathbf{n}}_\mu \mathbf{Q}_i \hat{\mathbf{n}}_\mu, \tag{3.13}$$

where the matrices $\mathbf{Q}_i$ reflect the spatial and spectral characteristics of the plasmonic modes and the QE polarizability. They are labeled as $i = 1, n$ for the n-th plasmonic linear term, $i = 2, n$ for the quadratic term and $i = \mathrm{E}$ accounting for the distorting emitter absorption. They read

$$\mathbf{Q}_{1,n} = \frac{\mu_{\mathrm{E}}^2/\hbar}{1+\beta_{\mathrm{I}}(\mathbf{r}_{\mathrm{E}},\mathbf{r}_{\mathrm{E}},\omega_{\mathrm{E}})\mathrm{Im}\{\alpha_{\mathrm{E}}(\omega_{\mathrm{E}})\}}\times \left(\boldsymbol{\mathcal{M}}_{n0}+\boldsymbol{\mathcal{M}}_{n0}^{\mathrm{T}}-\boldsymbol{\mathcal{M}}_{nn}+\sum_{m\neq n}\boldsymbol{\mathcal{M}}_{nm}+\boldsymbol{\mathcal{M}}_{nm}^{\mathrm{T}}\right),$$

$$\mathbf{Q}_{2,n} = \frac{(\mu_{\mathrm{E}}^2/\hbar)(\tilde{\omega}_{\mathrm{E}}-\tilde{\omega}_n)}{1+\beta_{\mathrm{I}}(\mathbf{r}_{\mathrm{E}},\mathbf{r}_{\mathrm{E}},\omega_{\mathrm{E}})\mathrm{Im}\{\alpha_{\mathrm{E}}(\omega_{\mathrm{E}})\}}\boldsymbol{\mathcal{M}}_{nn},$$

$$\mathbf{Q}_{\mathrm{E}} = \frac{(\mu_{\mathrm{E}}^2/\hbar)}{1+\beta_{\mathrm{I}}(\mathbf{r}_{\mathrm{E}},\mathbf{r}_{\mathrm{E}},\omega_{\mathrm{E}})\mathrm{Im}\{\alpha_{\mathrm{E}}(\omega_{\mathrm{E}})\}}\left(\boldsymbol{\mathcal{M}}_{00}-\sum_n \mathbf{Q}_{1,n}\right),$$

where we have used $\tilde{\omega}_{\mathrm{E}}=\omega_{\mathrm{E}}-i\gamma_{\mathrm{E}}/2$, $\tilde{\omega}_n=\omega_n-i\gamma_m/2$ and the definition of the matrices $\boldsymbol{\mathcal{M}}_{nm}$

$$\boldsymbol{\mathcal{M}}_{00} = \mathbf{G}_0(\mathbf{r},\mathbf{r}_{\mathrm{E}})\mathbf{T}(\hat{\mathbf{n}}_{\mathrm{E}})\mathbf{G}_0^{\mathrm{T}}(\mathbf{r},\mathbf{r}_{\mathrm{E}}),$$

$$\boldsymbol{\mathcal{M}}_{n0} = \frac{\boldsymbol{\mathcal{G}}_n(\mathbf{r},\mathbf{r}_{\mathrm{E}})\mathbf{T}(\hat{\mathbf{n}}_{\mathrm{E}})\mathbf{G}_0^{\mathrm{T}}(\mathbf{r},\mathbf{r}_{\mathrm{E}})}{\tilde{\omega}_{\mathrm{E}}-\tilde{\omega}_n},$$

$$\boldsymbol{\mathcal{M}}_{nn} = \frac{\boldsymbol{\mathcal{G}}_n(\mathbf{r},\mathbf{r}_{\mathrm{E}})\mathbf{T}(\hat{\mathbf{n}}_{\mathrm{E}})\boldsymbol{\mathcal{G}}_n^{\mathrm{T}}(\mathbf{r},\mathbf{r}_{\mathrm{E}})}{(\tilde{\omega}_{\mathrm{E}}-\tilde{\omega}_n)^2},$$

$$\boldsymbol{\mathcal{M}}_{nm} = \frac{\boldsymbol{\mathcal{G}}_n(\mathbf{r},\mathbf{r}_{\mathrm{E}})\mathbf{T}(\hat{\mathbf{n}}_{\mathrm{E}})\boldsymbol{\mathcal{G}}_m^{\mathrm{T}}(\mathbf{r},\mathbf{r}_{\mathrm{E}}),}{(\omega_m-\omega_n)(\tilde{\omega}_{\mathrm{E}}-\tilde{\omega}_n)}.$$

In the following subsections, we investigate how these different terms contribute to the phenomenology presented in Figures 3.2 and 3.3 for a NPoM geometry and for a three-dimensional system.

3.1.3. NPoM cavity

We commence examinating the different spectral features of the LDOS in NPoM cavities, specifically around the frequency of the lowest-frequency plasmon mode, ω_1. Figure 3.4 panels (a) and (b) show the different contributions to $J_{\mathrm{II}}(\omega)$ at the gap center of a NPoM cavity with $D = 35.0$ nm and $\delta = 1.5$ nm (red lines). The distorting QE is displaced 0.5 nm horizontally (a) and vertically (b) from the probing one. The dipole moment of both emitters is oriented vertically. The spectral parameters are the same as in Fig. 3.3. The black solid line plots the spectrum for the bare cavity, $J_{\mathrm{I}}(\omega)$. The components of $J_{\text{I-II}}(\omega)$ (cyan line) in Eq. (3.12) are plotted in dotted lines. The quadratic plasmonic Lorentzian contribution presents the same symmetric Lorentzian-like profile in both panels (orange). On the contrary, the terms altering the coupling strength of the bare cavity (blue) and the QE polarizability (green) are clearly asymmetric. This allows

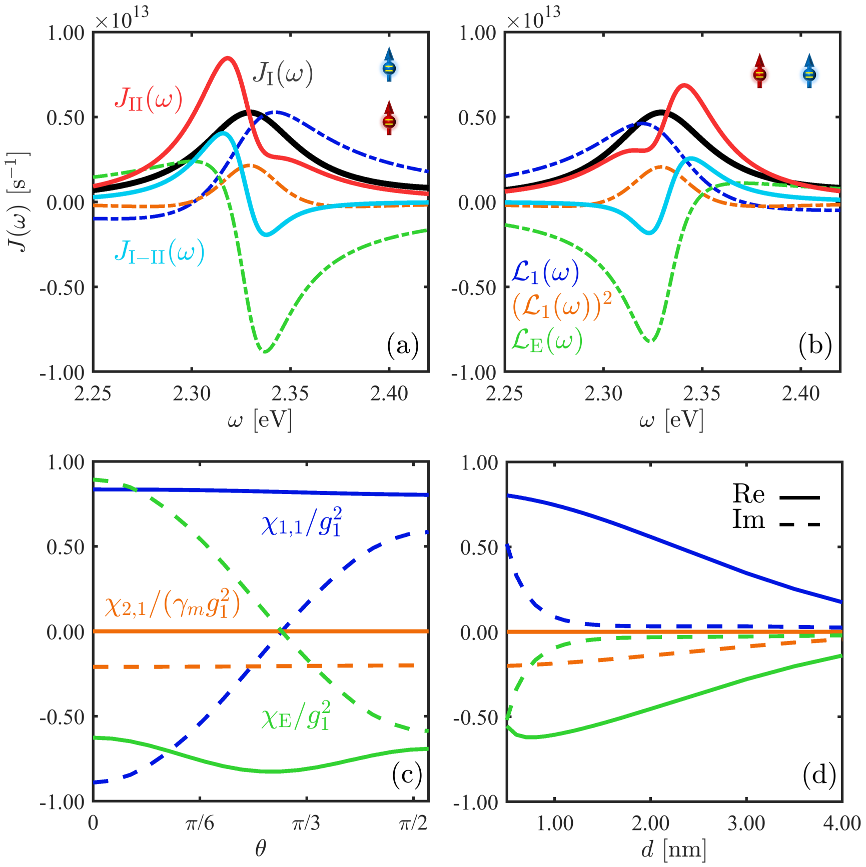

Figure 3.4: Modal decomposition of $J(\omega)$ at the gap center of a distorted NPoM cavity ($D = 35.0\,\mathrm{nm}$, $\delta = 1.5\,\mathrm{nm}$) around $\omega = \omega_1$. (a,b) Bare and distorted spectral densities (solid lines) for vertical and horizontal QE-QE displacement ($|\mathbf{d}| = 0.5\,\mathrm{nm}$), respectively (both QEs are oriented vertically). Dotted lines plot the different contributions in $J_{\text{I-II}}(\omega)$. (c) Modal weights of the different contributions in Eq. (3.12) versus the orientation of the QE-QE relative position ($\theta = 0$ corresponds to the vertical configuration). (d) Same as panel (c) but versus distance $|\mathbf{d}|$ for the horizontal case ($\theta = \pi/2$). In panels (c) and (d), solid (dashed) lines correspond to the real (imaginary) the part of the modal amplitudes, normalized to g_1^2, the coupling strength for the bare cavity.

us to anticipate complex $\chi_{1,1}$ and χ_{E} amplitudes, as the asymmetries originate from the real part of the complex Lorentzian functions in Eq. (3.12). Note as well that these two mechanisms oppose each other in both panels, and present maxima (minima) that are slightly redshifted (blueshifted) with respect to $\omega = \omega_1$. This gives rise to the qualitative differences in the asymmetry of $J_{\mathrm{II}}(\omega)$ (red solid line) in both panels.

To explore the spatial dependence of the three contributions in $J_{\text{I-II}}(\omega)$, we plot in

Fig. 3.4 panels (c) and (d) their weights. $\chi_{1,1}$ and χ_{E}, normalized to g_1^2, the lowest-order plasmon-emitter coupling strength for the bare cavity, while $\chi_{2,1}$ (note its different dimensionality), is normalized to $\gamma_m g_1^2$. In Fig. 3.4(c), similarly to Fig. 3.3(b), these amplitudes are evaluated at a fixed distance, $|\mathbf{d}| = 0.5\,\mathrm{nm}$, and different QE-QE relative position orientations from vertical ($\theta = 0$) to horizontal ($\theta = \pi/2$) alignments. We plot real parts in solid lines and imaginary parts in dashed ones. We can observe that the real parts are rather insensitive to the orientation of $\mathbf{d}$ within the gap. As anticipated, $\chi_{2,1}$ is isotropic and purely imaginary, as a consequence of the uniform character of the resonant near-fields ($\boldsymbol{\mathcal{M}}_{11}$) for the underlying capacitor-like plasmonic mode. Moreover, it is smaller than g_1^2 even at distances significantly shorter than the gap size ($|\mathbf{d}| = \delta/3$). On the contrary, not only the uniform fields, $\boldsymbol{\mathcal{M}}_{11}$, but also the inhomogeneous off-resonant modes in $\boldsymbol{\mathcal{M}}_{1m}$ and the product of plasmon and free space field components given by $\boldsymbol{\mathcal{M}}_{10}$ contribute to $\mathrm{Im}\{\chi_{1,1}\}$ and $\mathrm{Im}\{\chi_{\mathrm{E}}\}$. Note that the QE contribution also presents a dipole-like free space field part given by $\boldsymbol{\mathcal{M}}_{00}$. The weights $\mathrm{Im}\{\chi_{1,1}\}$ and $\mathrm{Im}\{\chi_{\mathrm{E}}\}$ are much larger and flip sign with θ, which gives rise to the qualitative differences in $J_{\mathrm{II}}(\omega)$ shown in Fig. 3.3(a) and (b). The $\boldsymbol{\mathcal{M}}_{10}$ term is the origin of the change of sign in the imaginary part of the amplitudes. At resonance, $\tilde{\omega}_{\mathrm{E}} - \tilde{\omega}_1 = i/2(\gamma_m - \gamma_{\mathrm{E}})$ is purely imaginary. The term $\boldsymbol{\mathcal{M}}_{11}$ provides an almost constant background, as noticed in $\chi_{2,1}$, whose slightly larger absolute value for $\theta \approx 0$ is due to the interplay between the fields at the gap center and close to the metallic surface.

Figure 3.4(d) plots normalized $\chi_{1,1}, \chi_{2,1}/\gamma_m$ and χ_{E} as a function of the QE-QE distance for $\theta = \pi/2$ (horizontal displacement of the distorting QE). Both real and imaginary parts decay with increasing $|\mathbf{d}|$. The faster decay of the imaginary parts of $\chi_{1,1}$ and χ_{E}, dominantly given by the dipole-like free space field $\boldsymbol{\mathcal{M}}_{00}$, reflects the more homogeneous character of the plasmonic fields. As a result, at distances around $2-3\,\mathrm{nm}$ the three terms in Eq. (3.12) acquire a purely symmetric Lorentzian spectral shape. At such distances $\chi_{\mathrm{E}} \approx -\chi_{1,1}$, but the negative sign of χ_{E} together with the narrower character of the $\mathcal{L}_{\mathrm{E}}$ translates into a symmetric dip superimposed on $J_{\mathrm{I}}(\omega)$, as it was shown in Fig. 3.3(a).

3.1.4. Bow-tie-like antenna

To show the general character and validity of our analysis, we apply the Green's function scattering formalism to a full three-dimensional system. The cavity of choice is sketched in Figure 3.5(a). It is composed by two free-standing metallic (same Drude permittivity as before) rounded cones with 15 nm diameter and 15 nm height. One of the cones is

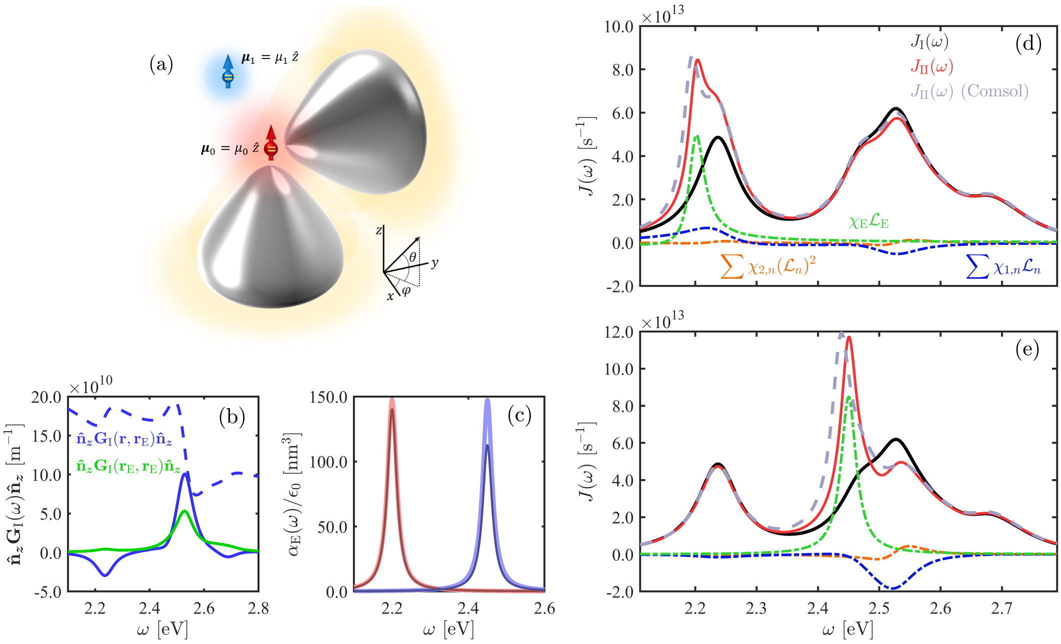

Figure 3.5: $J(\omega)$ distortion in a bow-tie cavity. (a) Sketch of the cavity formed by two rounded cones (15 nm height and diameter) and the position of the probing (red) and distorting (blue) QEs (both are oriented along z-direction). (b) Dyadic Green's function components involved in the calculation of $J_{\text{I-II}}(\omega)$ in Eq. (3.12). (c) Imaginary part of $\alpha_E(\omega)$ (bright) and $\tilde{\alpha}_E(\omega)$ (dark) of QEs with $\omega_E = 2.20$ (red) and 2.45 eV (blue). (d) Spectral density decomposition for $\omega_E = 2.20$ eV. Solid lines correspond to $J_I(\omega)$ (black) and $J_{\text{I-II}}(\omega)$ (red), and dotted lines show the three contributions to $J_{\text{I-II}}(\omega)$. Dashed light grey line sets the spectra obtained from numerical simulations using an effective permittivity modelling of the distorting QE. (e) Same as panel (d) but for $\omega_E = 2.45$ eV.

oriented vertically (z-axis), the other horizontally (y-axis), in a bow-tie-like arrangement. Again, the dipole momenta of both QEs are oriented vertically. The probing emitter is placed 1 nm away from the vertices of both cones. The distorting one is displaced $|\mathbf{d}| = 2$ nm away along the positive z-direction. The dyadic Green's functions of the bare structure, the only input required for the calculation of $J_{\text{II}}(\omega)$ in our approach, are computed by means of numerical simulations performed using the finite-element solver of Maxwell's Equations in COMSOL Multiphysics.

Figure 3.5(b) shows the Green's tensor components involved in the second term of Eq. (3.8), where the real and imaginary parts of $\hat{\mathbf{n}}_z \mathbf{G}_I(\mathbf{r}, \mathbf{r}_E, \omega)\hat{\mathbf{n}}_z$ are plotted in dashed and solid blue lines, respectively. The green solid line renders $\text{Im}\{\hat{\mathbf{n}}_z \mathbf{G}_I(\mathbf{r}_E, \mathbf{r}_E, \omega)\hat{\mathbf{n}}_z\}$, which yields the depolarization correction to the free space polarizability of the distorting

QE. By direct inspection, several symmetric Lorentzian contributions can be identified in the imaginary spectra of Fig. 3.5(b), whereas a free space background is apparent in $\mathrm{Re}\{\hat{\mathbf{n}}_z\mathbf{G}_\mathrm{I}(\mathbf{r},\mathbf{r}_\mathrm{E},\omega)\hat{\mathbf{n}}_z\}$. Both Green's functions were fitted using the form of Eq. (3.11), with the need of only five plasmonic modes. This fitting allows us to obtain $J_\text{I-II}(\omega)$ and identify the contribution of the three terms in Eq. (3.12). Fig. 3.5(c) shows the comparison between $\mathrm{Im}\{\tilde{\alpha}_\mathrm{E}(\omega)\}$ (dark lines) and $\mathrm{Im}\{\alpha_\mathrm{E}(\omega)\}$ (bright lines) for $\hbar\omega_\mathrm{E} = 2.20$ (red) and 2.45 eV (blue), where the depolarization effects by the plasmonic fields become clear.

Figure 3.5(d) and (e) show the spectral densities for two distorting QE frequencies, $\hbar\omega_\mathrm{E} = 2.20$ and 2.45 eV, respectively. In each panel, the bare cavity spectrum, $J_\mathrm{I}(\omega)$, is presented in black solid lines. It is calculated from $\mathrm{Im}\{\hat{\mathbf{n}}_z\mathbf{G}_\mathrm{I}(\mathbf{r},\mathbf{r},\omega)\hat{\mathbf{n}}_z\}$, obtained from full electrodynamic solutions for Maxwell's equations. The different contributions to $J_\text{I-II}(\omega)$ are plotted by colored dotted lines, and $J_\mathrm{II}(\omega)$ is shown in red solid line. For comparison, $J_\mathrm{II}(\omega)$ computed by means of COMSOL Multiphysics in which simulations modelling the distorting QE as dielectric sphere of permittivity $\epsilon_\mathrm{eff}(\omega)$ (see section 3.1.1) are rendered in light grey dashed line. We can observe that they are in very good agreement with the prediction from our approach. In both panels, the absorption lineshape of the distorting QE is clearly imprinted in the cavity LDOS. Therefore, the Lorentzian contribution of the QE, $\mathcal{L}_\mathrm{E}(\omega)$, with (mainly) real χ_E, dominates $J_\text{I-II}(\omega)$. However, the plasmonic contributions $\mathcal{L}_n(\omega)$ (blue) and $(\mathcal{L}_n(\omega))^2$ (orange) are not negligible either. Both yield asymmetric profiles with maxima and minima not (only) at the QE natural frequency, but in the vicinities of the resonant plasmonic frequencies, $\hbar\omega_1 = 2.25$ eV and $\hbar\omega_4 = 2.56$ eV, which correspond to the dominant modes. Remarkably, panel (d) in Fig. 3.5 reveals that the coupling of the probing QE to the mode $\hbar\omega_4 = 2.56$ eV is significantly reduced by the distorting QE, even in situations with considerable detuning, as rendered in Fig. 3.5(d), where $\omega_4 - \omega_\mathrm{E} \gg \gamma_m, \gamma_\mathrm{E}$.

3.1.5. Hamiltonian picture

In order to gain insight into Eq. (3.12) and the physical interpretation of the three terms contributing to $J_\text{I-II}(\omega)$, we revisit here the hybrid QE-cavity system under a quantum description. This could be done taking into account the full richness of the plasmonic spectrum of the bare cavity, but, for simplicity, we will focus here on its single-mode version. The Hamiltonian for this simplified system reads

$$\begin{aligned}\hat{H} &= \hat{H}_\sigma + \hat{H}_{\text{cav}} + \hat{H}_{\text{int}} \\ &= \Big(\hbar\omega\hat{\sigma}^\dagger\hat{\sigma}\Big) + \Big(\hbar\omega_n\hat{a}_n^\dagger\hat{a}_n + \hbar\omega_{\text{E}}\hat{b}^\dagger\hat{b} + \hbar g_{n,\text{E}}\hat{a}_n^\dagger\hat{b} + \text{h.c.}\Big) + \big(\hbar g_n\hat{a}_n^\dagger\hat{\sigma} + \text{h.c.}\Big), \end{aligned} \tag{3.14}$$

where the first, second and third terms correspond to the probing QE (modelled as a two-level system), its photonic environment (which involves the plasmon resonance, labelled as n, and the distorting QE) and their interaction, respectively. Thus, $\hat{a}_n$, $\hat{\sigma}$, and $\hat{b}$ are the annihilation operators for the cavity mode and the two QEs. Note that the distorting emitter has been bosonized, in agreement with our scattering theory description, in which it is treated as part of the LDOS. The plasmon mode is coupled to both QEs, with strengths g_n and $g_{n,\text{E}}$, but the emitters are not interacting with each other.

Recently, a general approach has been proposed that sets the link between the Hamiltonian describing the interaction between a single QE and its photonic environment and the spectral density for the system, $J(\omega)$ [42, 158]. This framework, based on Fano diagonalization theory [159], is valid for Hamiltonians involving interacting modes, like Eq. (3.14). Applying this formalism to our system, we can obtain the spectral density for our system from the resolvent of the non-hermitian Hamiltonian for the photonic environment, $\hat{H}'_{\text{cav}} = \hat{H}_{\text{cav}} - i\frac{\hbar\gamma_m}{2}\hat{a}_n^\dagger\hat{a}_n - i\frac{\hbar\gamma_{\text{E}}}{2}\hat{b}^\dagger\hat{b}$. The origin of the complex frequencies in the Hamiltonian above resides in the master equation description of the system. This includes Lindblad operators, $L_{n,E}[\hat{\rho}]$, accounting for the dissipation experienced by the cavity (with rate γ_m) and the distorting QE (with rate γ_{E}), $\partial_t\hat{\rho} = -\frac{i}{\hbar}[\hat{H},\hat{\rho}] + \frac{\gamma_m}{2}L_n[\hat{\rho}] + \frac{\gamma_{\text{E}}}{2}L_{\text{E}}[\hat{\rho}]$. We can now express the spectral density in terms of the resolvent matrix as [42, 158]

$$J_{\text{II}}(\omega) = \frac{1}{\pi}\text{Im}\Big\{\mathbf{g}^{\text{T}}\Big(\mathbf{H}' - \mathbf{I}\omega\Big)^{-1}\mathbf{g}\Big\} = \frac{1}{\pi}\text{Im}\left\{\frac{g_n^2(\tilde{\omega}_{\text{E}} - \omega)}{(\tilde{\omega}_n - \omega)(\tilde{\omega}_{\text{E}} - \omega) - g_{n,\text{E}}^2}\right\}, \tag{3.15}$$

where we have used

$$\mathbf{H}' = \begin{pmatrix} \omega_n - i\gamma_m/2 & g_{n,\text{E}} \\ g_{n,\text{E}} & \omega_{\text{E}} - i\gamma_{\text{E}}/2 \end{pmatrix}, \quad \mathbf{g} = \begin{pmatrix} g_n \\ 0 \end{pmatrix}.$$

By keeping only the first-order correction in the Taylor expansion at $g_{n,\text{E}}^2 = 0$ of the spectral density above, we obtain $J_{\text{II}}(\omega) = J_{\text{I}}(\omega) + J_{\text{I-II}}(\omega)$ with

$$J_{\text{I}}(\omega) = \frac{1}{\pi}g_n^2\text{Im}\{\mathcal{L}_n(\omega)\}, \tag{3.16}$$

and

$$J_{\text{I-II}}(\omega) = \frac{1}{\pi}\text{Im}\left\{\frac{g_n^2 g_{n,\text{E}}^2}{(\tilde{\omega}_{\text{E}} - \tilde{\omega}_n)^2}\mathcal{L}_{\text{E}}(\omega) - \frac{g_n^2 g_{n,\text{E}}^2}{(\tilde{\omega}_{\text{E}} - \tilde{\omega}_n)^2}\mathcal{L}_n(\omega) + \frac{g_n^2 g_{n,\text{E}}^2}{\tilde{\omega}_{\text{E}} - \tilde{\omega}_n}(\mathcal{L}_n(\omega))^2\right\}. \tag{3.17}$$

Thus, in the regime of weak interaction between cavity and distorting QE ($g_{n,\mathrm{E}} \ll \omega_n, \omega_\mathrm{E}$), in which Eq. (3.8) is valid, we obtain an spectral density in which the effect of the distorting QE acquires exactly the same for as $J_{\text{I-II}}(\omega)$ in Eq. (3.12). Thus, we can now express the modal amplitudes in this expression in terms of the parameters of the Hamiltonian as

$$\chi_\mathrm{E} = -\chi_{1,n} = \frac{g_n^2 g_{n,\mathrm{E}}^2}{(\tilde{\omega}_\mathrm{E} - \tilde{\omega}_n)^2}, \; \chi_{2,n} = \frac{g_n^2 g_{n,\mathrm{E}}^2}{\tilde{\omega}_\mathrm{E} - \tilde{\omega}_n}, \tag{3.18}$$

where $\tilde{\omega}_n = \omega_n - i\gamma_m/2$ and $\tilde{\omega}_\mathrm{E} = \omega_\mathrm{E} - i\gamma_\mathrm{E}/2$ are the complex cavity and QE frequencies that emerge naturally in $\hat{H}'_\mathrm{cav}$.

Let us stress that Eq. (3.18) sheds light into the results presented above for distorted NPoM and bow-tie cavities. Firstly, they show that all modal amplitudes are proportional to $g_n^2 g_{n,\mathrm{E}}^2$, the square of the product of the plasmon-QE coupling constants. More importantly, they are complex, in general. As we already discussed, this yields a non-vanishing contribution of the real part of the complex Lorentzian functions in Eq. (3.12) to the LDOS of distorted cavities. Particulary, when plasmon resonance and QE natural frequency are at resonance, $\omega_n = \omega_\mathrm{E}$, $\mathrm{Re}\{\chi_{2,n}\} = 0$, which explains the imaginary character of this amplitude in Fig. 3.4(c) and (d) for all relative QE-QE positions. Furthermore, as predicted by Eq. (3.18), both the real and imaginary parts of $\chi_{1,1}$ and χ_E are, despite deviations contained in the QE dipole-like free space component, opposite in sign in these two panels.

Finally, these single-mode amplitudes also help us interpret the findings in Fig. 3.5. Note that the plasmonic mode components to the various $J_{\text{I-II}}(\omega)$ contributions cannot be disentangled in this case. However, focusing only on the distorting QE spectra, we can observe that it presents a slight asymmetry in panel (d), where the QE is close to resonance with the cavity mode at 2.22 eV, but it is fully symmetric in panel (e), where the QE is further from resonance with the mode at 2.52 eV. We can link this observation to the effect of cavity-QE detuning on χ_E in Eqs. (3.18). Note that, near the resonance condition, this is complex, with similar real and imaginary parts if $|\omega_n - \omega_\mathrm{E}| \sim (\gamma_m - \gamma_\mathrm{E})/2$, and becomes effectively real for $|\omega_n - \omega_\mathrm{E}| \gg (\gamma_m - \gamma_\mathrm{E})/2$. Thus, we can conclude that the off-resonant character of the distorting QE in Fig. 3.5(e) is behind its fully symmetric contribution to the LDOS. We finalize remarking that the condition $\tilde{\omega}_\mathrm{E} = \tilde{\omega}_n$ is not considered in our analysis since it does not allow the Lorentzian decomposition perfomed. Nevertheless, even when in the described conditions non-Lorentzian effects are quite related to the effects of different losses ratios for the plasmon-distorting QE mechanisms, pure non-Lorentzian effects would arise even in the total resonance case, where cubic Lorentzian terms become apparent.

3.2. Light-allowed and light-forbidden transitions in a plasmonic cavity

After presenting our results on how the presence of a second emitter can modify the LDOS in a deeply sub-wavelength plasmonic cavity, we turn our attention to the issue of considering a more complex structure in a single emitter, described as a three-level system, including two different excited states, characterized by their dipolar and quadrupolar nature.

Figure 3.6(a) sketches a NPoM cavity with diameter $D = 30.0\,\mathrm{nm}$ and gap size $\delta = 0.9\,\mathrm{nm}$. In the same fashion as already shown, the metal permittivity $\epsilon_m(\omega)$ is given by low-frequency Drude-fitting to Ag. In this case, we consider the whole plasmonic structure embedded in $\epsilon_d = 4$. We treat the QE as a point-like three-level system, placed at $\mathbf{r}_\mathrm{E} = (x_\mathrm{E}, z_\mathrm{E})$, with the origin of coordinates is located at the bottom of the gap. We assume that the QE presents two transitions of interest, with energies in the visible, each of them with different character. The light-allowed transition between the ground $|g\rangle$ and the $|e_\mu\rangle$ state presents a transition dipole moment $\boldsymbol{\mu}$, with natural frequency ω_μ, and radiative decay rate in vacuum $\gamma_\mu = \gamma_\mu(\omega_\mu) = \omega_\mu^3\mu^2/3\pi\epsilon_0\hbar c^3$. On the other hand, the state $|e_Q\rangle$ is assumed to have only quadrupolar component with zero net transition dipole moment. Then, the transition from $|g\rangle$ to $|e_Q\rangle$ is distinguished by a net transition quadrupole moment Q and a frequency ω_Q, giving a free space decay rate $\gamma_Q = \gamma_Q(\omega_Q) = \omega_Q^5 Q^2/360\pi\epsilon_0\hbar c^5$. The comparison between the free space decay rates, with $\gamma_Q/\gamma_\mu \sim 10^{-5}, 10^{-6}$ provides the difference in time scales between the $|e_\mu\rangle, |e_Q\rangle$ states, which are completely decoupled each other. For this reason, it is usually assumed that quadrupolar transitions are very unlikely to interact with free space fields, acquiring a light-forbidden character. In our study, internal nonradiative decay channels in the QE are neglected, and the orientation of both excitonic moments is chosen to maximize plasmon-emitter coupling. Based on the results already shown in chapter 2, this is given by the vertical electric dipole $\boldsymbol{\mu} = \mu\hat{\mathbf{n}}_z$ and the antidiagonal electric quadrupole defined by the crossed outer product $\mathbf{Q} = \frac{Q}{\sqrt{2}}[\hat{\mathbf{n}}_x \otimes \hat{\mathbf{n}}_z + \hat{\mathbf{n}}_z \otimes \hat{\mathbf{n}}_x]$. Within the Transformation Optics approach, we can calculate the electric field scattered by the nanostructure for the cavity in Fig. 3.6(a). In order to account for the radiative losses experienced by surface plasmon (SP) modes and keep our calculations fully analytical for all system configurations, we model the cavity geometry through its 2D counterpart [64], as we did in chapter 2.

In Figure 3.6(b), we render the ratio between quadrupolar and dipolar Purcell factors $P_f^Q(\omega)/P_f^\mu(\omega)$ versus frequency and δ/D, for the QE at the gap center, $\mathbf{r}_\mathrm{E} = (0, \delta/2)$.

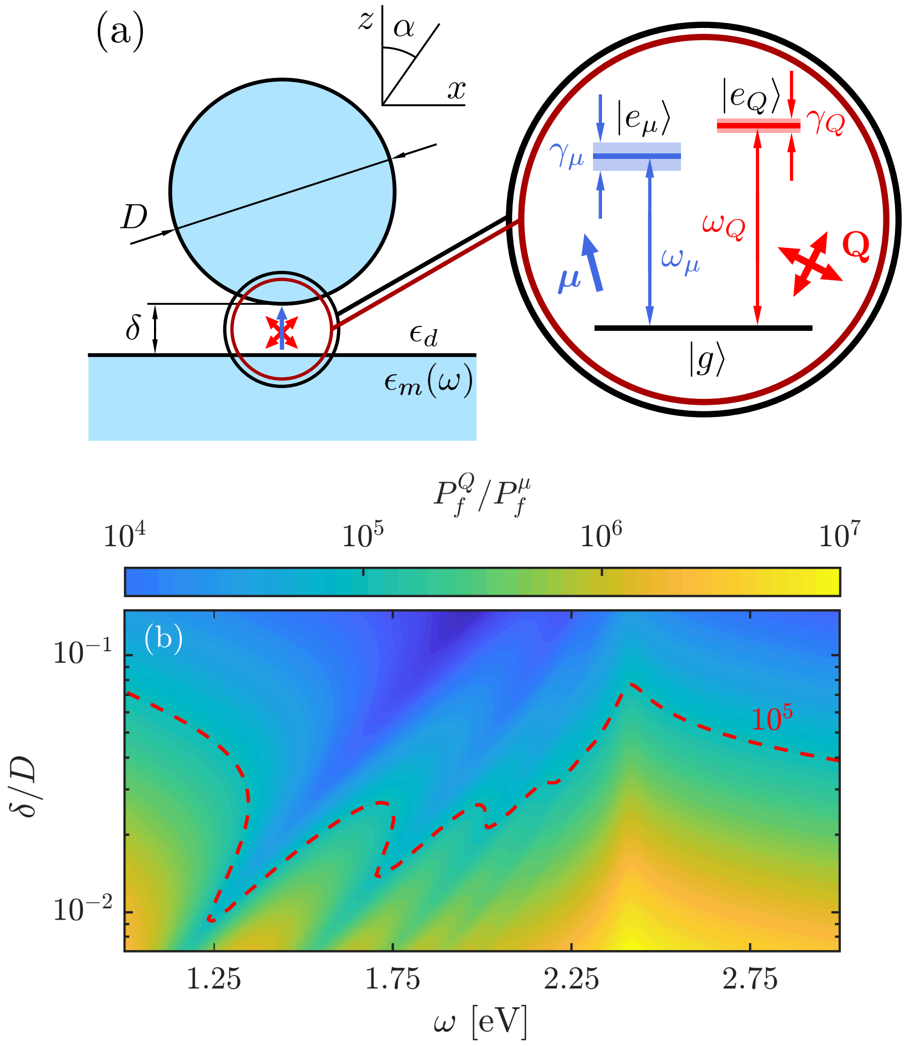

Figure 3.6: (a) Sketch of a QE placed at the gap of a metallic NPoM cavity. The QE is modelled as a three-level system with one dipolar (μ) and one quadrupolar (Q) exciton transitions. (b) Ratio between the quadrupolar and dipolar Purcell factors at the gap center as a function of frequency and normalized gap size.

The red dashed line plots the contour $P_f^Q(\omega)/P_f^\mu(\omega) = 10^5$ and sets the parameter region for which the time scales of light-forbidden and light-allowed exciton dynamics become comparable, mediated by the impact of the cavity fields. We can observe that this condition can only be satisfied for gap sizes in the sub-nanometric regime, much smaller than the nanoparticle dimensions. For the geometry in Figure 3.6(a), we can identify two spectral regions where this is the case ($\delta/D = 0.03$): below the lowest-frequency SP ($\hbar\omega_{1,+1} = 1.55\,\mathrm{eV}$) and at the pseudomode which emerges at $\hbar\omega_{\mathrm{PS}} = 2.40\,\mathrm{eV}$ from the

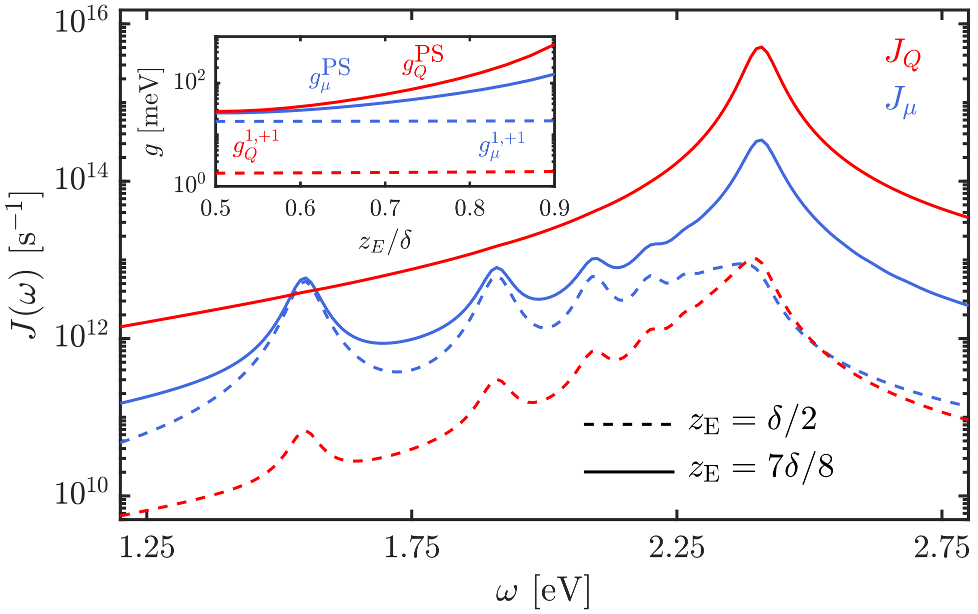

Figure 3.7: (a) Spectral densities for the dipole and quadrupole excitons($\mu = 0.55$ e·nm, $Q = 0.75$ e·nm^2), in blue and red lines, respectively, evaluated at $z_{\mathrm{E}} = \delta/2$ (dashed lines) and $7\delta/8$ (solid lines). Inset: Coupling strengths for the lowest-frequency mode, $g_i^{1,+1}$, and the pseudomode, g_i^{PS}, as a function of z_{E} in dashed and solid lines, respectively.

spectral overlapping of high-frequency SPs [96].

3.2.1. Spectral densities: Wigner-Weisskopf theory

We proceed to study the spectral features experienced by the emitter. Figure 3.7 shows the spectral density, $J_i(\omega) = \frac{\gamma_i(\omega)}{2\pi} P_f^i(\omega)$, for dipolar ($i = \mu$) and quadrupolar ($i = Q$) excitonic transitions within the cavity in Figure 3.6(a) with $\mu = 0.55$ e·nm and $Q = 0.75$ e·nm^2. This value is chosen so that the spectral density at the pseudomode is the same for both excitons at $z_{\mathrm{E}} = \delta/2$, although $J_Q(\omega)$ decays much faster with decreasing frequency. By displacing the emitter position to $z_{\mathrm{E}} = 7\delta/8$, both spectral densities increase. This enhancement is more pronounced in $J_Q(\omega)$, which is fully governed by the pseudomode and whose maximum is almost two orders of magnitude larger than $J_\mu(\omega_{\mathrm{PS}})$. As we have already discussed in chapter 2, the analytical expressions obtained for the spectral densities can be reshaped into a sum of Lorentzian terms of the form $J_i(\omega) = \sum_{n=1}^{\infty} \sum_{\sigma=\pm 1} \frac{\left(g_i^{n,\sigma}\right)^2}{\pi} \mathrm{Im}\{\mathcal{L}_{n,\sigma}\}$ where n is the SP azimuthal order, and σ the parity (even/odd) of the electric field in the z-direction with respect to the gap center. The QE-SP coupling constants, $g_i^{n,\sigma}$, weighting the different Lorentzian contributions are plotted in the inset of Figure 3.7 for both dipole and quadrupole transitions and for the lowest-frequency SP and for the pseudomode, $g_i^{\rm PS} = \sqrt{\sum_{n\geq 7,\sigma}(g_i^{n,\sigma})^2}$. Whereas $g_\mu^{1,+1}$ and $g_Q^{1,+1}$ do not depend on $z_{\rm E}$, $g_\mu^{\rm PS}$ and $g_Q^{\rm PS}$ grow exponentially as the QE approaches the metal surface, being this enhancement significantly larger for the quadrupole exciton.

We use our approach to analyze first the influence that light-forbidden transitions have in the exciton population dynamics. Specifically, we assume that initially ($t = 0$) only the light-allowed state is occupied, this is $n_\mu(0) = |c_\mu(0)|^2 = 1$ and $n_Q(0) = |c_Q(0)|^2 = 0$, and investigate how the excited state populations evolve in time. The Wigner-Weisskopf problem for our system (see appendix B) consists in two coupled integro-differential equations of the form

$$\begin{aligned}\dot{c}_i(t) = &-\int_0^t\int_0^\infty J_i(\omega)e^{i(\omega_i-\omega)(t-t')}c_i(t')d\omega dt' \\ &-\int_0^t J_{ij}(\omega)e^{i(\omega_i-\omega)(t-t')}e^{i(\omega_i-\omega_j)t'}c_j(t')d\omega dt' \end{aligned} \tag{3.19}$$

where $i, j = \mu, Q, \forall i \neq j$, and $J_{ij}(\omega) = J_{ji}(\omega)$ is given by the Lorentzian decompsition with the corresponding $g_{ij}^{n,\sigma} = \sqrt{g_\mu^{n,\sigma} g_Q^{n,\sigma}}$. This spectral density feeds the second term in Eq. (3.19), which couples the dipolar and quadrupolar excitonic populations through the full plasmonic spectrum supported by the NPoM. We proceed to study two different system configurations, already introduced in Figure 3.7 and indicated in the top sketch of Figure 3.8. In Fig. 3.8(a), the QE is placed at the gap center and the dipole and quadrupole transition frequencies are at resonance with the lowest SP mode, $\omega_Q = \omega_\mu = \omega_{1,+1}$. In Figure 3.8(b), the QE is in the vicinity of the nanoparticle surface, $z_{\rm E} = 7\delta/8$, $\omega_\mu = \omega_{1,+1}$ but the quadrupole transition is shifted to $\omega_{\rm PS}$.

In the first case, where the QE is at the gap center and $\omega_\mu = \omega_Q = \omega_{1,+1}$, the quadrupolar exciton is very detuned from the dominant peak of $J_Q(\omega_{\rm PS})$. The left panel in Figure 3.8(a) shows the dependence of the total population dynamics $n_\mu(t) + n_Q(t)$ ($n_i(t) = |c_i(t)|^2$) with the ratio between the spontaneous decay rates in free space, γ_Q/γ_μ, calculated fixing μ and varying Q. It is clear that for small values of the quadrupole moment, the interplay will be negligible and the QE population will show the trend of a common decay, determined by the plasmon-dipolar exciton coupling. Nevertheless, in an intermediate region, we find a suppression of the downfall. We plot in the right panel the net populations evaluated at $Q/\mu = 3.2\,\text{nm}$, which corresponds to $\gamma_Q/\gamma_\mu = 6 \cdot 10^{-6}$, marked by the orange arrow in the contour map. The population of the light-allowed, $n_\mu(t)$, and light-forbidden, $n_Q(t)$, states are shown in blue and red lines, respectively, and

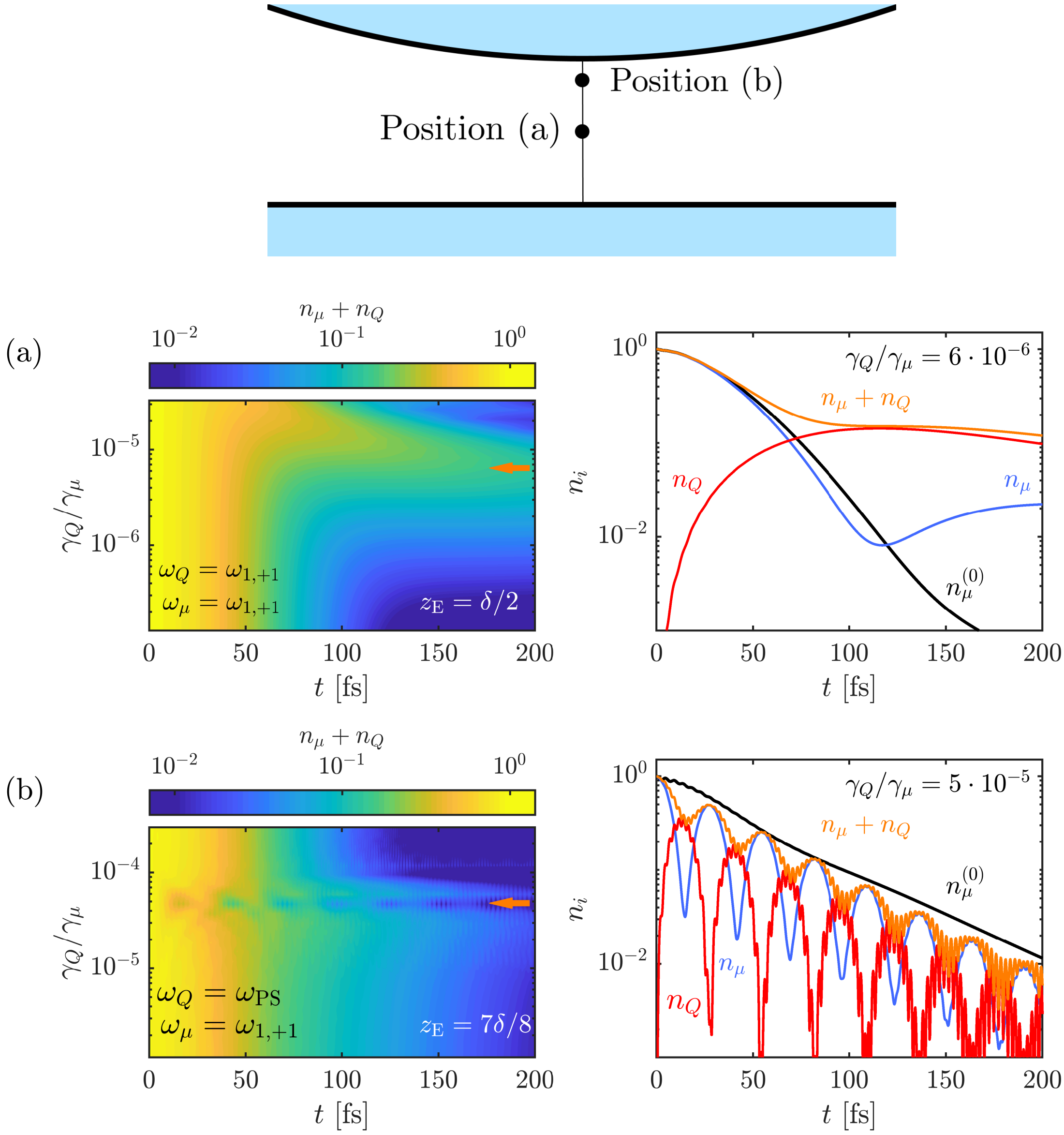

Figure 3.8: Population dynamics. In the top panel, we represent the sketch of the QE positions analyzed in panels (a) and (b), with the QE at the gap center and displaced towards the nanoparticle, respectively. (a,b) Right panel renders the temporal evolution of the total, $n_\mu + n_Q$, exciton population as a function of the free space spontaneous decay ratio, γ_Q/γ_μ, that we change varying the strength of the transition moment Q. As indicated, (a) panels correspond to $\omega_\mu = \omega_Q = \omega_{1,+1}$ and $z_{\mathrm{E}} = \delta/2$, whereas (b) represents $\omega_\mu = \omega_{1,+1}$, $\omega_Q = \omega_{\mathrm{PS}}$ and $z_{\mathrm{E}} = 7\delta/8$. Right panels show the cuts of the contour map, marked by the orange arrows, that correspond to (a) $\gamma_Q/\gamma_\mu = 6 \cdot 10^{-6}$ and (b) $\gamma_Q/\gamma_\mu = 5 \cdot 10^{-5}$ besides each of the contributions, $n_\mu(t)$ and $n_Q(t)$. The dipole population in absence of the light-forbidden transition, $n_\mu^{(0)}$, is also shown.

the orange line plots $n_\mu(t)+n_Q(t)$. For comparison, the dipole state population in absence of the quadrupole exciton, $n_\mu^{(0)}(t)$, is shown in black line. The right panel displays that the effective decay of the total population is related to the feeding of population into $n_Q(t)$. This grows initially, up to crossing n_μ. At longer times, the quadrupole exciton feeds population back into the dipole state, and induces a decay in the total QE population, which is significantly slower than $n_\mu^{(0)}(t)$. Both show a rather monotonic decay decorated by very shallow oscillations, which can be linked to the onset of the plasmonic strong coupling, within the two-level description of the QE.

The fingerprint of the quadrupole exciton is even more remarkable in Fig. 3.8(b). The contour map in the left panel shows that small values of the Q transition moment do no change significantly the decay of the dipolar state. Nevertheless, in a certain region around $\gamma_Q/\gamma_\mu \simeq 5 \cdot 10^{-5}$, a shortening fo the decay is observed. Right panel shows the corresponding cuts for this value of the ratio, marked by an orange arrow in the contour map. The panel shows the emergence of fast Rabi oscillations in $n_Q(t)$, which originate from its strong coupling to the pseudomode, are quickly transferred to $n_\mu(t)$. The resulting total population profile oscillates and decays much faster than $n_\mu^{(0)}(t)$. The fast oscillations superimposed to the main oscillation can be understood from the examination of the Wigner-Weisskopf expression, Eq. (3.19). Whereas for the previous configuration $\omega_\mu = \omega_Q$, now the difference in frequencies provides the emergence of oscillations due to the exponential term $e^{i(\omega_\mu-\omega_Q)t'}$ in the integration kernel. We remark that we vary the Q moment within the same interval of values in (a) and (b) panels, being the different ω_Q the responsible of the change by an order of magnitude in the spontaneous decay ratio. Both configurations show that the strong modification of QE lifetimes takes place only within a certain range of Q-values. We can conclude that depending on the emitter position and exciton detuning, light-forbidden transitions can effectively reduce or enlarge the QE lifetime, altering significantly the Purcell effect obtained within the two-level system model.

3.2.2. Far-field effects: Scattering spectrum

In order to evaluate the impact that the quadrupole exciton has in the performance of the QE-SP system as a photonic device, we study next its far-field scattering spectrum. We recover the model introduced in chapter 2 for a dark-field spectroscopy set-up [118] in which the NPoM is illuminated by a grazing laser field, E_L, with frequency ω_L and polarization along z-direction. Due to its inherent open and lossy nature, describing the scattering properties of the hybrid system would require, in principle, the computation of its steady-state density matrix out of a Liovillian formulation of the problem. As we did in the previous chapter, we can use a non-hermitian Hamiltonian of the form

$$\begin{aligned}\hat{H}_{\text{eff}} = \sum_i \hbar\Delta_i \hat{\sigma}_i^\dagger \hat{\sigma}_i + \sum_{n,\sigma} \hbar\Delta_{n,\sigma} \hat{a}_{n,\sigma}^\dagger \hat{a}_{n,\sigma} \\ + \sum_i \sum_{n,\sigma} \hbar g_i^{n,\sigma} (\hat{a}_{n,\sigma}^\dagger \hat{\sigma}_i + \text{h.c.}) + E_L(\hat{M} + \hat{M}^\dagger)\end{aligned} \tag{3.20}$$

where $\hat{a}_{n,\sigma}^\dagger$ ($\hat{a}_{n,\sigma}$) and $\hat{\sigma}_i^\dagger$ ($\hat{\sigma}_i$) are the creation (annihilation) operators for SP and QE excitations, and $\Delta_{n,\sigma} = \omega_{n,\sigma} - \omega_L - i\frac{\gamma_{n,\sigma}}{2}$ and $\Delta_i = \omega_i - \omega_L - i\frac{\gamma_i}{2}$ are the complex detuned frequencies for the SPs and the QE dipole transition, respectively, given in terms of ω_i and laser frequency, ω_L. The only difference with respect to Eq. (2.68) is the consideration of both excitons.

The Hamiltonian in Eq. (3.20) is given by applying the same transformation procedure the one behind the Wigner-Weisskopf approach after adding the external pumping, where it is assumed that the only coupling between the far-field and the system is mediated by the dipole moments of the various plasmon modes, $\hat{M} = \mu\hat{\sigma}_\mu + \sum_n \mu_n \hat{a}_{n,+1}$. As we did in chapter 2, the SP dipole moments for the even modes ($\sigma = +1$) can be expressed in terms of their radiative decay rates and we solve perturbatively the Schrödinger equation in the rotating frame to obtain the steady-state wavefunction for the QE-SP system, $|\psi_{\text{SS}}\rangle$. The scattering cross section is then calculated as Eq. (2.69), the expectation value of the $\hat{M}$ operator, $\sigma_{\text{sca}} = \langle\psi_{\text{SS}}| \hat{M}M^\dagger |\psi_{\text{SS}}\rangle$.

We start our analysis considering the configuration with the emitter at the gap center. Figure 3.9(a) panel renders the normalized scattering cross section versus laser frequency, ω_L and the free space spontaneous decay ratio γ_Q/γ_μ. The configuration is the same as the considered in Figure 3.8(a), with both excitonic levels in resonance with the lowest order plasmonic mode, $\omega_\mu = \omega_Q = \omega_{1,+1}$. We choose this mode since its contribution to the far-field signal is the largest. We plot σ_{sca} within a wider spectral window, spanning beyond the scattering peak at $\omega_{2,+1}$, where it is apparent the presence of an invisibility dip [64] at $\hbar\omega_L = 1.77\,\text{eV}$, which originates from superposition effects among the coherent emission from different SPs. For low values of Q, which translate in negligible quadrupole-plasmon coupling compared the dipolar counterpart, Figure 3.9(a) shows the Rabi splitting of the bare NPoM scattering peak, an indication of the formation of plasmon-exciton polaritons (PEPs) in the system due to the strong coupling between the lowest SP and the dipolar exciton [118]. As the Q-coupling increases, the fingerprint of the QE quadrupole transition becomes apparent only at larger γ_Q/γ_μ, giving rise to a third peak in $\sigma_{\text{sca}}(\omega)$ at $\omega = \omega_{1,+1}$. This maximum grows and broadens, and its position redshifts. Fig. 3.9(b) plots the cuts of this map, marked by the color arrows, for

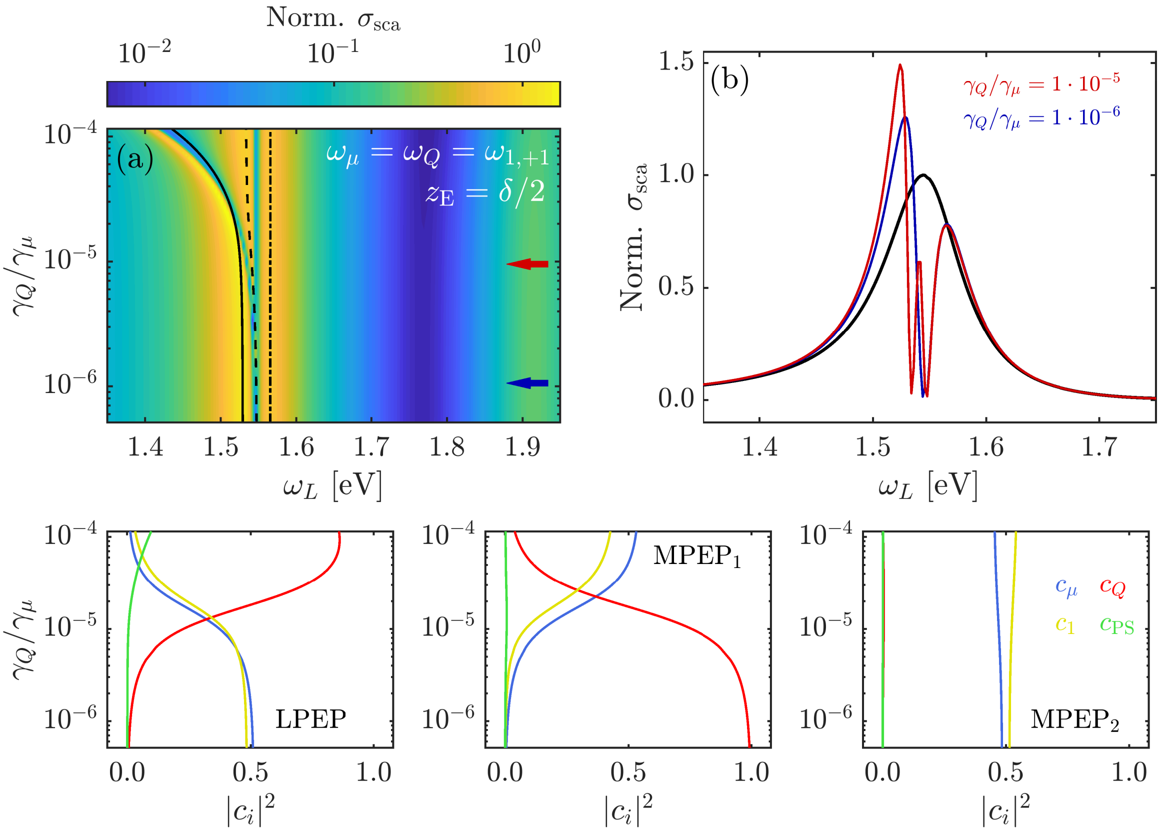

Figure 3.9: Scattering spectra for QE-SP systems with $\omega_\mu = \omega_Q = \omega_{1,+1}$, $z_{\text{E}} = \delta/2$. (a) Normalized scattering cross-section σ_{sca} vs laser frequency and free space spontaneous decay ratio, γ_Q/γ_μ. Black lines represent the eigenenergies of a reduced Hamiltonian with four states: LPEP (solid), MPEP$_1$ (dashed) and MPEP$_2$ (dotted). (b) Normalized σ_{sca} spectra for the values indicated by arrows in panel (a) and for the bare cavity (black solid line). Bottom panels: Squared absolute values of the PEP Hopfield coefficients as a function of γ_Q/γ_μ for dipole (blue) and quadrupole (red) excitons, lowest-frequency SP (yellow) and pseudomode (green).

$\gamma_Q/\gamma_\mu = 1 \cdot 10^{-6}$ (blue) and $\gamma_Q/\gamma_\mu = 1 \cdot 10^{-5}$ (red), showing the two-peak splitting and three-peak spectra cases. As a comparison, the bare NPoM spectrum is plotted in black solid line.

As in chapter 2, we study the eigenstates and eigenvalues of a reduced Hamiltonian, just considering the excitons and two plasmonic modes, $\omega_{1,+1}$ and ω_{PS}. The energies of those hybrid states, termed as PEPs[2], are shown in panel (a), labelled as lower PEP

---

[2] As in chapter 2, we refer to the hybrid states as PEPs even when their nature is purely plasmonic or excitonic to highlight their general hybrid character.

(solid lines), first middle PEP, MPEP$_1$ (dashed lines) and second middle PEP, MPEP$_2$ (connected-dotted lines). A fourth (upper) polariton (not shown) emerges at ω_{PS}. The Hopfield coefficients in the bottom panels of Figure 3.9 shed light into this strong modification of the Rabi doublet profile, obtained from the projection of the reduced hamiltonian eigenstates onto the bare exciton-plasmon basis. Those reveal that the peak at $\omega_{1,+1}$ develops when MPEP$_1$ losses its light-forbidden exciton character (see red line in central panel). This is in turn transferred to LPEP, whose associated peak becomes narrower. In contrast, MPEP$_2$ is barely affected in this process, and the corresponding scattering maximum remains the same as in the two-level system model for the QE. Importantly, the modification of the Rabi doublet spectrum takes place within the same parametric region in which the QE lifetime is longest, see Figure 3.8(a).

Figure 3.10 evidences that the Rabi splitting phenomenology is modified even at lower γ_Q/γ_μ in the second QE-SP configuration, with $z_{\text{E}} = 7\delta/8$ and $\omega_Q = \omega_{\text{PS}}$. As before, we study the variation of σ_{sca} as Q increases. This higher sensitivity to the quadrupole exciton is a consequence of the large enhancement that g_Q^{PS} experiences as the QE is displaced across the cavity gap, see Fig. 3.7. For negligible plasmon-Q-exciton coupling, dipolar exciton defines the spectrum. Due to the large detuning and coupling between the dipolar level and the pseudomode, the scattering minima between the Rabi doublet is no longer at $\omega = \omega_{1,+1}$ but a bit redshifted in the spectrum, as discussed in section 2.7. Remarkably, by increasing the quadrupole moment, the lowest frequency peak vanishes, and the spectrum for the hybrid system resembles very much the one of the bare NPoM (see red and black lines in Fig. 3.10(b)). This profile can be observed only within a narrow range of Q-values, beyond which a symmetric Rabi doublet spectrum, very similar to the one observed at $Q \simeq 0$ is recovered (blue line). The eigenenergies of the polaritons in the reduced model and the Hopfield coefficients in the bottom panels clarify this evolution of $\sigma_{\text{sca}}(\omega)$. In this case, MPEP$_2$, which initially originates from the strong coupling between the quadrupole exciton and the pseudomode (see red and green lines in MPEP$_2$), becomes strongly Rabi-shifted towards $\omega_{1,+1}$. For large enough Q, anti-crossing among PEP bands takes place. As a result, LPEP and MPEP$_2$ present a vanishing content on the lowest SP mode (see yellow lines in PEP panels) at $\gamma_Q/\gamma_\mu = 5 \cdot 10^{-5}$, which is fully transferred to MPEP$_1$ (central bottom panel in Fig 3.10). In these particular conditions, light-allowed and light-forbidden QE states interact only through the pseudomode and become completely dark. As a result, the Rabi doublet in $\sigma_{\text{sca}}(\omega)$ vanishes and, as shown in Fig 3.8(b), the large excitonic couplings to the pseudomode lead to a fast oscillations in the QE population and an effective shortening of its lifetime.

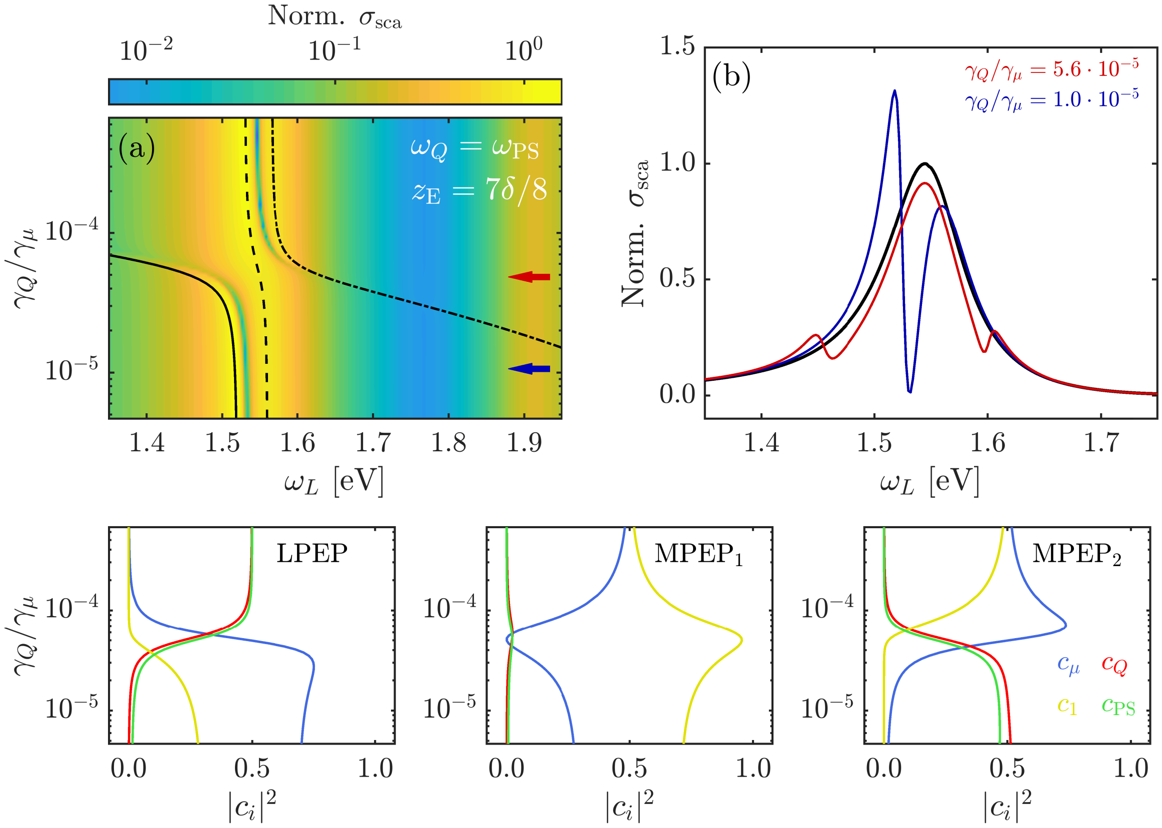

Figure 3.10: Scattering spectra for QE-SP systems with $\omega_\mu = \omega_{1,+1}$, $\omega_Q = \omega_{\text{PS}}$ and $z_{\text{E}} = 7\delta/8$. (a) Normalized scattering cross-section σ_{sca} vs laser frequency and free space spontaneous decay ratio, γ_Q/γ_μ. Black lines represent the eigenenergies of a reduced Hamiltonian with four states: LPEP (solid), MPEP$_1$ (dashed) and MPEP$_2$ (dotted). (b) Normalized σ_{sca} spectra for the values indicated by arrows in panel (a) and for the bare cavity (black solid line). Bottom panels: Square absolute values of the PEP Hopfield coefficients as a function of γ_Q/γ_μ for dipole (blue) and quadrupole (red) excitons, lowest-frequency SP (yellow) and pseudomode (green).

3.3. Conclusions

To conclude this chapter, we have investigated plasmonic cavities hosting more than one exciton, revealing that the near field enhancement associated to plasmonic resonances can lead to a rich and complex light-matter interaction phenomenology. In the first section, we have presented an insightful approach based on first-order electromagnetic scattering theory to investigate the distortion induced by a quantum emitter in the local density of states of a nanocavity. The presence of the distorting emitter can modify strongly the near-field spectrum, enhancing or suppresing the local density of states even when it is out of resonance with any plasmonic mode. The quasistatic character of the system enables us to perform a complex Lorentzian decomposition of the dyadic Green's function, allowing us to identify and isolate three different mechanisms behind the distortion due to the presence of the second emitter. On the other hand, the extreme light confinement provided by plasmonic resonances leads to large spatial derivatives of the electric field, making possible the interplay between dipolar excitons and higher-order multipolar terms. Using our Transformation Optics approach, we have explored the near-field population dynamics and the far-field scattering spectrum for a three-level quantum emitter, with dipole-active and dipole-inactive (quadrupole) excited states. We have focused on two system configurations in which the quadrupolar excited state leads to opposite modifications of the Purcell effect and Rabi splitting phenomenology.

4

Lattice resonances

During the previous chapters, we have analyzed the form of plasmon-emitter interactions in different plasmonic cavities. In this chapter, we focus our study on plasmonic resonances supported by nanoparticle arrays, exploring the possibilities of arrangements that result in the observation of one or two different resonances, with special emphasis in the broad or narrow character of the mode.

4.1. Introduction

As we have seen in previous chapters, metallic nanostructures are exceptional tools to manipulate the interaction between light and matter at the nanoscale due to their ability to support surface plasmons [56]. Up to this point in the thesis, we have restricted ourselves to the study of the optical behavior of systems much smaller than the wavelength, yielding the regime where radiation is neglected and EM phenomena have a near-field character. At optical frequencies, the validity of the quasistatic approximation where radiative effects are generally negligible with respect to evanescent fields extends up to sizes of the order of 50 nm. In addition to plasmonic resonances, sub-wavelength-sized metallic nanostructures also support collective modes when they form a periodic lattice. The nature of such arrangements, which implies the interplay between the near-field and far-field regimes, show a rich EM phenomenology. When the interparticle distance is small compared to the size and the wavelength, the phenomena can be described in terms of quasistatic concepts. Larger spacings, when the wavelength λ is of the order of the interparticle separation, lead to long-range electrodynamic interactions and diffraction effects. In particular, we will focus on two-dimensional arrays of metallic nanoparticles. These systems support several types of collective resonances, from plasmon-like localized surface plasmons (LSPs) to mixed plasmonic-photonic modes resulting from the coupling between diffractive Rayleigh anomalies and individual LSPs, the so-called lattice resonances.

The lineshape of plasmonic resonances is determined by its lifetime, related to the damping mechanisms. Localized surface plasmons usually display relatively broad lineshapes, with quality factors (*i.e.*, the ratio of the resonance width to the central wavelength of the resonance) in the range $Q \lesssim 10 - 20$ [160, 161]. Resonance broadening can occur through both non-radiative and radiative processes, proportional to the volume of the resonator. Both individual and multiparticle structures can support multipolar plasmon modes. The magnitude of the associated dipole moments provides the distinction between bright and dark modes as well as a characterization of the resonance linewidth. Bright modes are broadened due to radiation associated to the net dipole arising from the sum of the plasmonic dipole moments supported by the individual constituents. On the other hand, the cancellation of the net dipole leads to dark resonances, with narrower lineshapes. Bright and dark plasmons are classical analogues of the superradiant and subradiant quantum optical phenomena, respectively [162, 163]. Surface plasmons with a large bandwidth are useful for certain applications based on field enhancement and absorption [164] while there are many others, such as biosensing [165], that benefit from surface plasmons with large Q factors. By breaking the spatial symmetries in plasmonic composites, bright and dark modes can couple each other, giving rise to asymmetric spectral features and providing new degrees of freedom for the design of the optical spectrum [166–168]. Lattice resonances constitute a promising approach to obtain large field enhancements and narrow modes that display large Q factors [169–171]. Indeed, a recent experimental work has reported quality factors $Q \sim 2400$ in single-particle plasmonic arrays[1] [172]. Thanks to these extraordinary properties, periodic arrays of metallic nanoparticles are being used in applications ranging from the design of different optical elements such as light-emitting devices [173–175] to platforms for exploring new physical phenomena [176, 177].

In this chapter, we focus our study on lattice resonances supported by bipartite nanoparticle arrays, exploring the possibilities of arrangements that result in super- or subradiant modes. We show that the considered bipartite arrays generally support two different lattice resonances, but certain geometrical configurations determine the obser-

---

[1] Throughout the text, we will refer to periodic arrays as those in which the unit cell is formed by one particle (*single-particle arrays*) or two particles (*bipartite arrays*).

vation of an unique lattice resonance. Moreover, for those situations in which a single resonance is found, depending on the relative position of the two particles within the unit cell, it may display a super- or subradiant character. Not surprisingly, each of these two behaviors leads to a very distinct optical response. Specifically, superradiant lattice resonances produce large values of reflectance with broad lineshapes, as expected from their increased radiative losses. On the other hand, the significant reduction of the radiative losses associated with subradiant lattice resonances gives rise to very small linewidths with maximum absorbance.

4.2. Nanoparticle arrays. The coupled dipole model

In this section, we present the theory that we have used to describe lattice resonances in infinite periodic arrays of metallic nanoparticles under plane wave illumination. As a starting point, we consider a square array of spherical particles, structured in single-particle unit cells that pattern infinitely, with lattice constant a. If we illuminate the array with an electromagnetic field $\mathbf{E}_{\text{ext}}$, the particles behave mainly as pure dipoles if the incident wavelength is larger than both their size and the array period. Then, within the linear and non-magnetic response assumptions, each nanosphere is assumed to respond through a polarizability α (for simplicity of notation, we exclude the explicit frequency dependence of the physical magnitudes). In the coupled dipole model approach [169, 178, 179], the induced dipole moment in a particle placed at $\mathbf{r} = \mathbf{r}_i$ is written as

$$\mathbf{p}(\mathbf{r}_i) = \alpha \mathbf{E}_{\text{ext}}(\mathbf{r}_i) + \frac{\alpha}{\epsilon_0} \sum_{j \neq i} [k^2 \mathbf{I} + \nabla\nabla] G_0(\mathbf{r}_i, \mathbf{r}_j) \mathbf{p}(\mathbf{r}_j), \tag{4.1}$$

where $k = 2\pi/\lambda$, with λ being the wavelength of light, $\mathbf{p}(\mathbf{r}_i)$ is the dipole induced in the particle located at $\mathbf{r}_i = (\mathbf{R}_i, 0)$, $G_0(\mathbf{r}_i, \mathbf{r}_j) = G_0(|\mathbf{r}_i - \mathbf{r}_j|) = e^{ik|\mathbf{r}_i - \mathbf{r}_j|}/(4\pi|\mathbf{r}_i - \mathbf{r}_j|)$ is the scalar Helmholtz Green's function in 3D and $\mathbf{I}$ is the 3×3 identity matrix. The summation in the second term indicates the contribution induced by the rest of the particles. As the array is periodic, the solutions can be Fourier-transformed and expanded in periodic functions as $\mathbf{p}(\mathbf{r}_i) = \int d\mathbf{k}_\parallel \mathbf{p}(\mathbf{k}_\parallel) e^{i\mathbf{k}_\parallel \mathbf{r}_i}$.

If we assume plane wave illumination $\mathbf{E}_{\text{ext}}(\mathbf{r}) = \mathbf{E}_0 e^{i\mathbf{k}_\parallel \mathbf{r}}$ and we consider isotropic polarizabilities for the particle description, we can write:

$$\mathbf{p}(\mathbf{k}_\parallel) = \alpha \mathbf{E}_0 + \frac{\alpha}{\epsilon_0} \sum_{j \neq i} [k^2 \mathbf{I} + \nabla\nabla] G_0(|\mathbf{r}_i - \mathbf{r}_j|) \mathbf{p}(\mathbf{k}_\parallel) e^{i\mathbf{k}_\parallel (\mathbf{r}_j - \mathbf{r}_i)}, \tag{4.2}$$

where we have used the fact that the array is placed in the xy plane and $\mathbf{k}_\parallel$ has zero z-component. Then, the solution can be written as

$$\mathbf{p}(k_\parallel) = [\alpha^{-1} \mathbf{I} - \boldsymbol{\mathcal{G}}(\mathbf{k}_\parallel)]^{-1} \mathbf{E}_0, \tag{4.3}$$

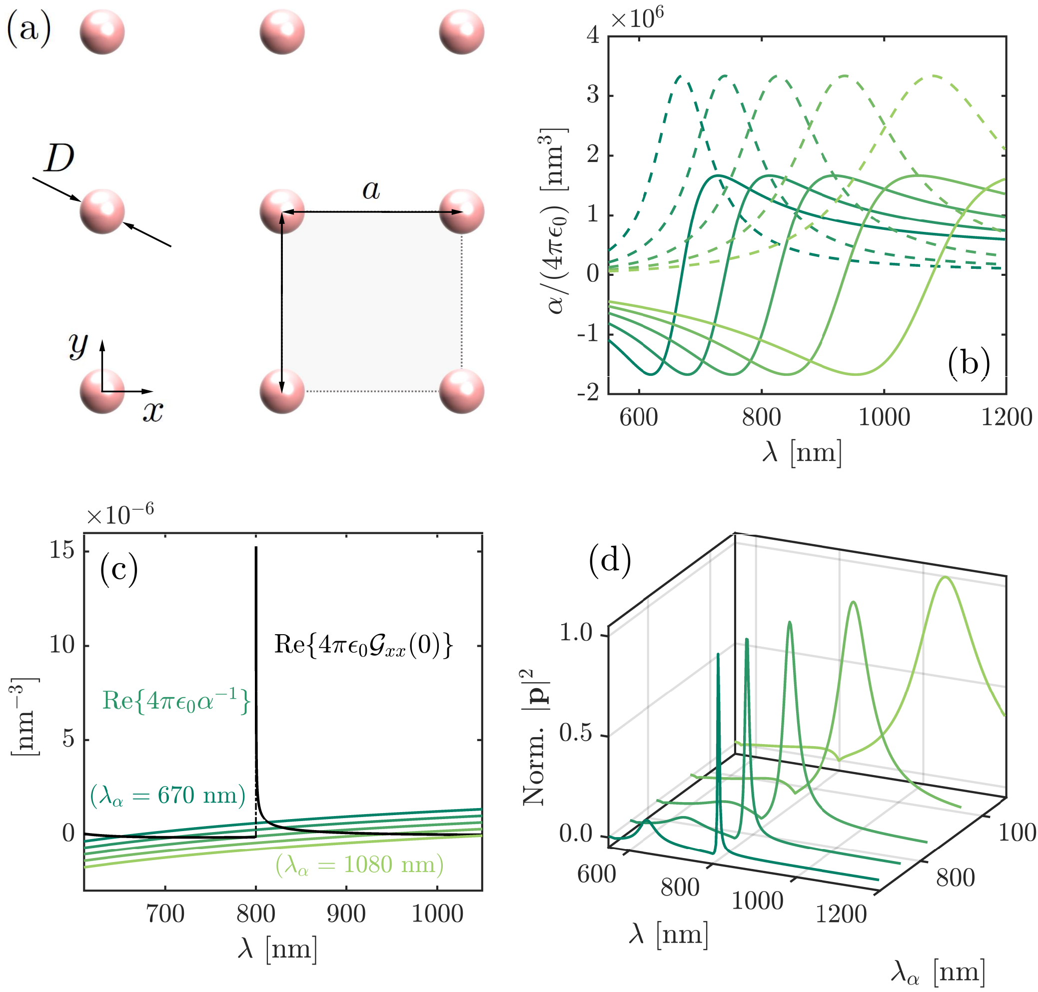

Figure 4.1: A generic approach to single-particle arrays. (a) Sketch of a square array, with lattice parameter a, formed by a periodic pattern of metallic nanoparticles, described by their polarizability, α. (b) Real (solid lines) and imaginary (dashed lines) parts of α as a function of λ, defined through Lorentzian lineshapes, $\mathcal{L}_\alpha(\omega)$. From left to right, the trend observed is similar to vary the size of the nanoparticle out of the quasistatic limit. (c) Real parts of $\mathcal{G}_{xx}(0)$ and α^{-1}. The lattice sum is calculated for an array with $a = 800\,$nm, whereas the polarizabilities are those given in panel (b). (d) Normalized $|\mathbf{p}|^2$ for the cases shown in the previous panels. A similar analysis on nanodisk arrays can be found in Ref. [179].

where we have introduced the term $\boldsymbol{\mathcal{G}}(\mathbf{k}_\parallel) = (1/\epsilon_0)\sum_{j\neq i}[k^2\mathbf{I}+\nabla\nabla]G_0(|\mathbf{r}_i-\mathbf{r}_j|)e^{-i\mathbf{k}_\parallel(\mathbf{r}_i-\mathbf{r}_j)}$, which is known as the lattice sum [178, 180]. This quantity contains the geometrical response of the array[2]. Note that the denominator in Eq. (4.3) separates the properties of the lattice, given by the lattice sum, from those of the particles, contained in the polarizability.

We can gain insight into the form of the $\mathbf{p}(\mathbf{k}_\parallel)$ by inspecting the form of α and $\boldsymbol{\mathcal{G}}(\mathbf{k}_\parallel)$. On the one hand, the lattice sum can be numerically calculated using Ewald's method [178, 182]. However, as the lattice sum is defined by $G_0(|\mathbf{r}_i - \mathbf{r}_j|)$, an analytical approach, shown in [179], consists in making use of the Weyl identity [55],

$$\frac{e^{ikr}}{r} = \frac{i}{2\pi}\int\int \frac{e^{i\mathbf{k}_\parallel \mathbf{R}}e^{ik_z|z|}}{k_z}d\mathbf{k}_\parallel, \tag{4.4}$$

which provides a plane-wave decomposition of the scalar Helmholtz Green's function. Following this route, it is found that

$$\boldsymbol{\mathcal{G}}(\mathbf{k}_\parallel) = \frac{i}{2\epsilon_0 a^2}\sum_{\mathbf{q}}\left(k^2 - \mathbf{k}_q\otimes\mathbf{k}_q\right)\frac{e^{ik_z|z|}}{k_z}, \tag{4.5}$$

with $k_z = \sqrt{k^2 - |\mathbf{k}_\parallel + \mathbf{q}|^2}$ and $\mathbf{k}_q = \mathbf{k}_\parallel + \mathbf{q}$, where $\mathbf{q} = (2\pi m/a, 2\pi n/a)$ are the reciprocal lattice vectors [180]. Then, it is clear that $\boldsymbol{\mathcal{G}}(\mathbf{k}_\parallel)$ diverges for the limit $k_z \to 0$, which can be interpreted as the condition for which the diffracted light becomes grazing to the plane of the array. These divergences of the lattice sum, known as Rayleigh anomalies (RA), occur at specific wavelengths $\lambda_{m,n}$. For the paradigmatic case of normal incidence ($\mathbf{k}_\parallel = 0$), $\lambda_{m,n} = a/\sqrt{m^2+n^2}$ gives the resonant wavelength, resulting in the degeneracy for different diffracting orders [180].

On the other hand, the polarizability of the nanospheres can be calculated through analytical or numerical approaches. Small particles can be described through α written in the quasistatic limit including the damping correction discussed in chapters 1 and 3. Above 50 nm radii, the quasistatic approximation fails and the polarizability must be obtained through numerical approaches. We anticipate that in subsequent sections referring to bipartite arrays, we calculate α using the Mie theory to obtain the dipolar contribution to scattering coefficients [183] (see appendix C). In this section, in order to discuss the emergence of lattice resonances in single-particle arrays, we use a quasistatic version of the polarizability.

The resonances of a square array under normal incidence are discussed in Figure 4.1. Panel (a) renders the geometry of the periodic array, with a single particle per unit cell

---

[2] Lattice sums are widely used in the context of dipole-dipole interactions in extended systems, as those in atomic arrays [181].

with fixed lattice period, a. In order to illustrate the different type of resonances that can be observed, we take the liberty of considering the polarizability of the particles not defined by its corresponding Mie expression, but by a typical Lorentzian profile $\mathcal{L}_\alpha(\omega) \propto (\omega_\alpha - i\gamma_\alpha/2 + \omega)^{-1}$, with the resonant wavelength $\lambda_\alpha = 2\pi c/\omega_\alpha$, associated to a fundamental plasmon [179], and accounting for the radiative correction as we did in sec. 3.1 [55]

$$\alpha(\omega) = \frac{\mathcal{L}_\alpha(\omega)}{1 - i\frac{k^3}{6\pi\epsilon_0}\mathcal{L}_\alpha(\omega)}. \tag{4.6}$$

where the factor in front of $\mathcal{L}_\alpha(\omega)$ in the denominator is given by the Green's function in free-space. This definition of the polarizability allows us to explore how the resonances change through the variation of their spectral position. This can be seen in Figure 4.1(b), where we plot the real and imaginary parts of the polarizabilities (solid and dashed lines) for different values of λ_α (with fixed $\hbar\gamma_\alpha = 0.15\,\mathrm{eV}$), effectively resembling the redshifting of the plasmon resonance frequency as nanoparticle size increases [56, 179] (increasing λ_α from darker to lighter solid green lines). The array is illuminated by an external field polarized along x-direction. For this configuration, by symmetry, the only dipole component excited in the system is p_x, so the interaction is determined by $\boldsymbol{\mathcal{G}}_{xx}(0)$ [170, 179]. Figure 4.1(c) plots the two key magnitudes that define the lattice resonances: the real part of the lattice sum (solid black line), calculated for an array with $a = 800\,\mathrm{nm}$, and the real part of the inverse of the particle polarizabilities α^{-1} for different resonant wavelengths. It is clear that, as the geometry of the lattice is fixed, the lattice sum does not depend on the properties of the particles. It diverges at the Rayleigh anomalies, here shown for the lowest order, $\lambda = a$. Both functions, $\mathrm{Re}\{\boldsymbol{\mathcal{G}}_{xx}(0)\}$ and $\mathrm{Re}\{\alpha^{-1}\}$ cross twice. At those crossings, the bracket term in Eq. (4.3) vanishes, giving rise to the resonances that can be seen in Figure 4.1(d), where we plot $|\mathbf{p}|^2$, given by Eq. (4.3) and normalized to its maximum, which is closely related to the reflectance (see below). The first maximum of $|\mathbf{p}|^2$ occurs near the maximum of $\mathrm{Im}\{\alpha\}$ ($\lambda \sim \lambda_\alpha$), where the lattice sum is small, giving rise to a plasmon-like resonance, with broad character, slightly blueshifted with respect to the single-particle one ($\lambda = \lambda_\alpha$). The second crossing, which happens on the red side of the RA, is associated to the lattice resonance that propagates along the system. This resonance is characterized by a narrow but non-vanishing width, associated to the imaginary part of $[\alpha^{-1} - \boldsymbol{\mathcal{G}}_{xx}(0)]$. It can be seen in both Fig. 4.1(c) and (d) that this second peak only takes place when the LSP resonance is blueshifted with respect to the RA. For $\lambda_\alpha > a$, the lattice mode cannot be excited and only the plasmon-like resonance is apparent in the spectrum. The asymmetries observed in Fig. 4.1 are those of typical Fano effects in the interaction between broad and narrow resonances [166, 168].

4.3. Breaking the symmetry. Bipartite arrays

Inspired by the collective enhancement of plasmonic radiative damping observed in multiparticle systems [184, 185], we turn our attention into bipartite arrays, with two different particles per unit cell. As discussed above, they allow the exploration of symmetry breaking effects that lead to the coupling between dark and bright modes in plasmonic nanostructures [58, 186]. The interaction between bright and dark resonances results in new hybridized modes in the system with some admixture of the bright mode, providing certain visibility of the dark mode in the optical spectrum. When the dark mode is far away from the bright one in the spectra, it would appear as a weak symmetric signature. As the modes become resonant, the Fano interference results in a resonance with a characteristic asymmetric lineshape, even antisymmetric [58].

A nice approach to understand the resonances of multiparticle arrays can be found in Ref. [180]. Multiparticle arrays can be understood as a superposition of several identical single-particle arrays, displaced with respect to each other along the plane where they lie. In terms of a plasmonic hybridization approach [61], the response of the array is determined by the interaction of the lattice resonances supported by the individual lattices in the same way as the bonding and antibonding modes in the near-field plasmonic scheme. Nevertheless, the extended nature of plasmonic resonances leads to a far-field coupling, very different to the studied through the quasistatic limit in nanometric finite structures.

We consider a bipartite square array, formed by two different particles, sketched in Figure 4.2(a). One of the particles (particle 1) is placed at the origin of our coordinate system for the unit cell, $\mathbf{r}_1 = (0, 0)$, whereas the second particle is at a position $\mathbf{r}_2 = (x_2, y_2)$ in the xy plane of the array, with lattice parameter a. We further assume that the array is illuminated with an external field of amplitude E_0, which propagates along the z-axis (*i.e.*, perpendicularly to the array) and is polarized along the x-axis. Under such conditions, and due to the square symmetry of the array, the dipole induced in the nanoparticles is also polarized along the x-axis and it can be written in terms of a Bloch solution. Therefore, the x-component of dipole induced in a given nanoparticle reads

$$p_i = \alpha_i E_0 + \frac{\alpha_i}{\epsilon_0} \sum_{\nu}{}' \sum_{j=1}^{2} G_{ij,\nu 0} p_{j,\nu}, \tag{4.7}$$

where we use greek indices to denote the unit cell to which the particle belongs and latin ones to label each of the two particles within the unit cell. The prime in the first summation indicates that the term $\nu = 0$ is excluded from it when $i = j$, since a dipole does not interact with itself, and $G_{ij,\nu 0}$ is the dipole-dipole interaction tensor exactly of the same form as the dyadic Green's function in Eq. (4.2). It is defined as

$$G_{ij,\nu 0} = [k^2 + \partial_x \partial_x] \frac{e^{ik|\mathbf{r}_i - \mathbf{r}_j - \mathbf{T}_\nu|}}{4\pi|\mathbf{r}_i - \mathbf{r}_j - \mathbf{T}_\nu|}, \tag{4.8}$$

with $\mathbf{T}_\nu$ being the vector connecting the unit cell that we have taken as an origin for the calculation and the corresponding ν unit cell. Thanks to the periodicity of the array, Eq. (4.7) admits a solution in the form of Bloch waves with amplitude

$$\begin{bmatrix} p_1 \\ p_2 \end{bmatrix} = \frac{E_0}{F} \begin{bmatrix} \alpha_2^{-1} - \mathcal{G}_{11} + \mathcal{G}_{12} \\ \alpha_1^{-1} - \mathcal{G}_{11} + \mathcal{G}_{12} \end{bmatrix}. \tag{4.9}$$

Here, $F = (\alpha_1^{-1} - \mathcal{G}_{11})(\alpha_2^{-1} - \mathcal{G}_{11}) - \mathcal{G}_{12}^2$ and $\mathcal{G}_{ij} = (1/\epsilon_0)\sum_\nu G_{ij,\nu 0}$ are the components of the lattice sum, calculated by means of the Ewald's method [178]. As expected (see appendix C), $\mathcal{G}_{11}(\mathbf{k}_\parallel = 0)$ and $\mathcal{G}_{12}(\mathbf{k}_\parallel = 0)$ components have the same dependence on k_z as $\mathcal{G}(\mathbf{k}_\parallel)$ discussed in the previous section for single-particle arrays, so those diverge in the vicinity of Rayleigh anomalies, which for normal incidence, appear at wavelengths $\lambda_{\mathbf{q}} = 2\pi/|\mathbf{q}|$. The vectors $\mathbf{q}$ represent the reciprocal lattice vectors of the array, $\mathbf{q} = (\frac{2\pi m}{a}, \frac{2\pi n}{a})$, with lattice constant a.

The geometry of the bipartite unit cell is just the superposition of two identical single-particle arrays with the same periodicity and displaced in the xy-plane. The diagonal terms, $\mathcal{G}_{11}$, which are equal for both arrays, determine the position of the lattice resonances for the single-particle array. On the other hand, the off-diagonal terms, $\mathcal{G}_{12}$, represent the interaction between the single-particle arrays corresponding to particles 1 and 2. Therefore, the lattice sum determines the existence of the lattice resonances, which emerge on the red side of the Rayleigh anomalies, corresponding to the poles, given by the vanishing condition of F, of the total dipole induced in the unit cell $p = p_1 + p_2$ [179, 180]

$$p = \frac{E_0(\alpha_1^{-1} + \alpha_2^{-1} - 2(\mathcal{G}_{11} + \mathcal{G}_{12}))}{(\alpha_1^{-1} - \mathcal{G}_{11})(\alpha_2^{-1} - \mathcal{G}_{11}) - \mathcal{G}_{12}^2}. \tag{4.10}$$

We are interested in the optical response of the array due to the lowest order lattice resonance, which, under normal incidence illumination, occurs in the spectrum at wavelengths satisfying $\lambda \simeq a$. It can be characterized by analyzing its reflectance, R, and absorbance, A. As shown in appendix C, these two quantities can be written in terms of p as

$$R = |p|^2/(2\Pi_0)^2, \qquad A = \mathrm{Im}\{p\}/\Pi_0 - 2|p|^2/(2\Pi_0)^2, \tag{4.11}$$

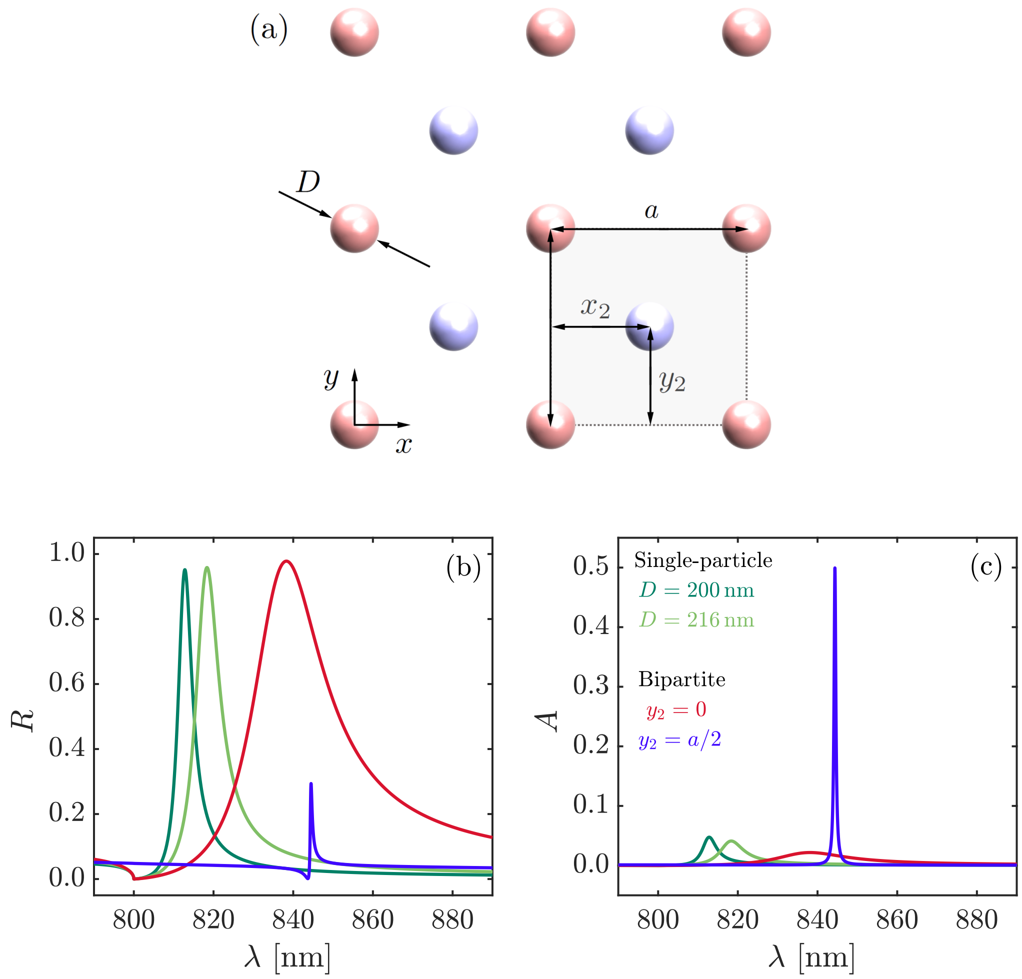

Figure 4.2: Resonances in bipartite nanoparticle arrays. (a) Sketch of the system under study, built from the periodic repetition of a unit cell containing two silver nanospheres (shaded area) over a square lattice with periodicity a. Particle 1 (red), with diameter D_1, is placed at the origin of the unit cell, while particle 2, D_2, is located at a position (x_2, y_2). (b,c) Reflectance, R, and absorbance, A, spectra for a bipartite array with $a = 800\,\text{nm}$, $D_1 = 200\,\text{nm}$ and $D_1 = 216\,\text{nm}$. Red and blue solid lines correspond to $y_2 = 0$ and $y_2 = a/2$, respectively, with $x_2 = a/2$ in both cases. For comparison, we plot R and A of a single-particle array with the same periodicity a, made of particles $D = 200\,\text{nm}$ and $D = 216\,\text{nm}$ (darker and lighter green lines, respectively). In all cases, discussed in this chapter, we assume illumination at normal incidence and polarized along the x-direction.

where $\Pi_0 = \epsilon_0 a^2 E_0/k$. Using these expressions we calculate the reflectance and the absorbance for two different bipartite arrays. Both of them have the same period $a = 800\,\text{nm}$, particle 1 is placed at position $\mathbf{r}_1 = (x_1, y_1) = (0, 0)$ and particle sizes are $D_1 =$

200 nm and $D_2 = 216\,\mathrm{nm}$. However, for one of them, particle 2 is located at $(x_2, y_2) = (a/2, 0)$, while, for the other, it is placed at $(x_2, y_2) = (a/2, a/2)$ (see Figure 4.2(a), which presents the sketch of the bipartite array). In the following, we are going to restrict ourselves to cases in which $x_2 = a/2$. The corresponding results are shown in Figure 4.2(b) and (c), with red curves for $y_2 = 0$ and blue lines for $y_2 = a/2$. Clearly, both bipartite arrays support a single lattice resonance; however, its optical properties are very different. Specifically, the lattice resonance of the array with $y_2 = 0$ gives rise to a very large reflectance, $R \sim 0.98$, and an almost negligible absorbance, $A \sim 0.02$, both with a significantly broad lineshape. On the contrary, the bipartite array with $y_2 = a/2$ supports a very narrow lattice resonance, resulting in a moderate reflectance, $R \sim 0.39$, and an absorbance that almost saturates the theoretical limit for two-dimensional systems, $A = 0.5$ [187]. These characteristics can be linked to the formation of super- and subradiant lattice resonance resulting from the hybridization of the lattice resonances supported by the two single-particle arrays into which these bipartite arrays can be divided. Indeed, analyzing the reflectance and absorbance of a single-particle array with the same periodicity, made of particles with diameter either $D = 200\,\mathrm{nm}$ or $D = 216\,\mathrm{nm}$ (darker and lighter solid green curves, respectively), we observe that the width of the lattice resonances supported by these single-particle arrays is significantly smaller than that of the bipartite array with $y_2 = 0$, but larger than the one of the array with $y_2 = a/2$. This is consistent with the increase and decrease of the radiative losses expected, respectively, for a super- and a subradiant mode.

We can gain further insight into the properties of these lattice resonances by analyzing their dependence with respect to the relative size of the two particles in the unit cell. In Figure 4.3, we plot the reflectance and the absorbance of the two bipartite arrays with $y_2 = 0$ and $y_2 = a/2$, both of which have $a = 800\,\mathrm{nm}$ and $D_1 = 200\,\mathrm{nm}$, as shown schematically in the corresponding insets of bottom panels. Each of the curves in these plots corresponds to a different value of D_2, ranging from 152 nm, for the leftmost curve, to 248 nm, for the rightmost one, increasing in steps of 4 nm (colorscale from cyan to violet). As expected from our previous results, the resonance for the $y_2 = 0$ case displays much broader lineshapes than its $y_2 = a/2$ counterpart. Furthermore, for both arrays, the increase of D_2 produces a redshift of the lattice resonance. However, while the values of the reflectance and absorbance for the $y_2 = 0$ array are not significantly modified with the change of D_2 ($R \approx 0.98$ and $A \approx 0.02$ for all values of D_2 in Fig. 4.3(b) and (d) respectively), the $y_2 = a/2$ lattice resonance undergoes dramatic changes as D_2 approaches to D_1 (see panels (a) and (c)). Interestingly, as shown in Figure 4.3(c), the absorbance of the subradiant lattice resonance is greatly increased on both sides of

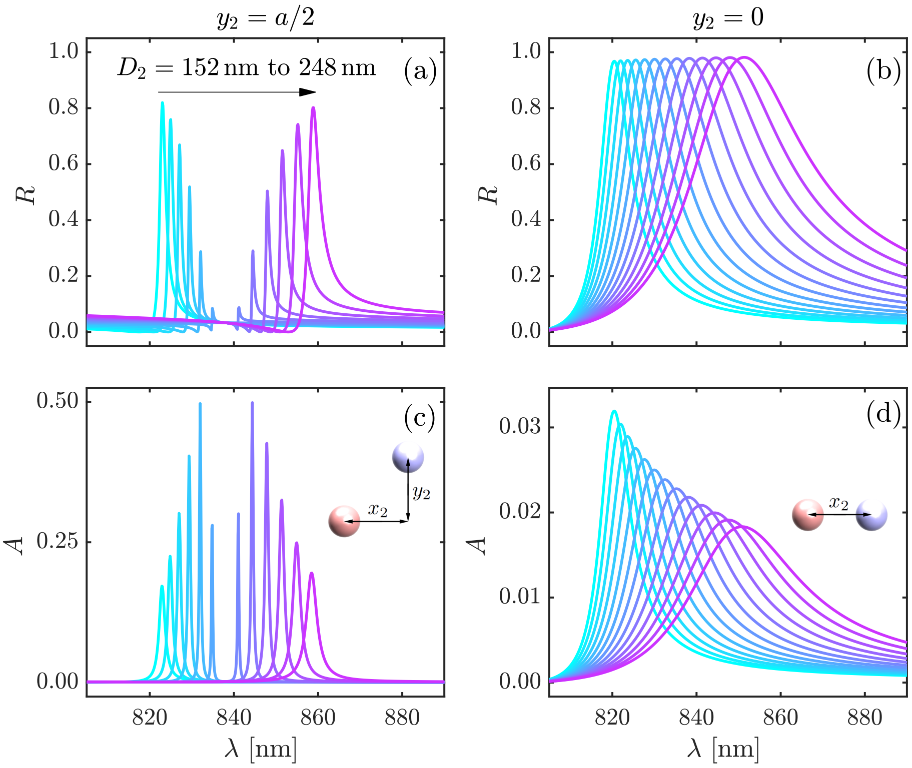

Figure 4.3: Role of particle size on lattice resonances. Spectral dependence of the reflectance (a,b), absorbance (c,d) for the $y_2 = a/2$ and $y_2 = 0$ array configurations. We consider arrays with $a = 800\,\mathrm{nm}$, $D_1 = 200\,\mathrm{nm}$, and D_2 varying from $152\,\mathrm{nm}$ (leftmost curves) to $248\,\mathrm{nm}$ (rightmost curves) in steps of $4\,\mathrm{nm}$.

the critical condition $D_2 = D_1$. In particular, for $D_2 = D_1$, this resonance completely disappears. All of these results are obtained assuming normal incidence and deviations from this condition would result in spectral shifts on the lattice resonances.

4.3.1. Super- and subradiant lattice resonances

In order to confirm the super- and subradiant nature of the lattice resonances supported by the bipartite arrays with $y_2 = 0$ and $y_2 = a/2$, we perform a detailed analysis of the total dipole induced in the unit cell. Specifically, defining $\beta = 2/(\alpha_1^{-1} + \alpha_2^{-1})$ and $\delta = \alpha_1^{-1} - \alpha_2^{-1}$, we can rewrite p as (see appendix C)

$$p = \frac{\zeta_+ E_0}{\beta^{-1} - \Omega_+} + \frac{\zeta_- E_0}{\beta^{-1} - \Omega_-}, \tag{4.12}$$

where $\zeta_\pm = 1 \pm \frac{\mathcal{G}_{12}}{\sqrt{\mathcal{G}_{12}^2+\delta^2/4}}$ and $\Omega_\pm = \mathcal{G}_{11} \pm \sqrt{\mathcal{G}_{12}^2 + \delta^2/4}$. In principle, this expression predicts the existence of two lattice resonances associated with the cancelation of the denominator of each of the two terms but up to this point, for the cases $y_2 = 0, a/2$ we found a single resonance. Figure 4.4(a) renders the real parts of the lattice sums $\mathcal{G}_{11}$ and $\mathcal{G}_{12}$ involved in the two configurations shown in previous figures. It is clear that $\mathrm{Re}\{\mathcal{G}_{12}\} \approx \mathrm{Re}\{\mathcal{G}_{11}\}$ for $y_2 = 0$ and $\mathrm{Re}\{\mathcal{G}_{12}\} \approx -\mathrm{Re}\{\mathcal{G}_{11}\}$ for $y_2 = a/2$. Assuming that the two particles in the unit cell have similar sizes, *i.e.*, $|\beta\delta| \ll 1$ and $|\delta/\mathcal{G}_{12}| \ll 1$, we have that

$$\zeta_\pm \approx 1 \pm \frac{\mathrm{sign}(\mathrm{Re}\{\mathcal{G}_{12}\})}{1 + \delta^2/(8\mathcal{G}_{12}^2)} \qquad\qquad \Omega_\pm \approx \mathcal{G}_{11} \pm |\mathrm{Re}\{\mathcal{G}_{12}\}| \tag{4.13}$$

The above equations in Eq. (4.13) explain that arrays with $y_2 = 0$ and $y_2 = a/2$ support a single lattice resonance associated with the first (Ω_+) term of Eq. (4.12), since, importantly, in these two cases, the vanishing condition of the second term $(\beta^{-1} - \Omega_-)$ is not met $(\beta^{-1} \gg \Omega_-)$. The single resonance appears in the spectrum approximately at wavelengths for which $\mathrm{Re}\{\beta^{-1} - 2\mathcal{G}_{11}\} \approx 0$. As we noticed in Figure 4.3, the lattice resonance redshifts as D_2 increases. This behavior can be understood from the condition $\mathrm{Re}\{\beta^{-1} - 2\mathcal{G}_{11}\} \approx 0$, which shifts to larger wavelengths, for which $\mathrm{Re}\{\mathcal{G}_{11}\}$ takes smaller values (see Figure 4.4(a)) as β^{-1} decreases. Furthermore, the disappearance of the mode for the $y_2 = a/2$ is explained by the value of ζ_+, which vanishes when $\delta = 0$. At that point, the subradiant mode becomes a perfectly dark mode or bound state in the continuum, as recently shown [188].

As the character of the Ω_+ lattice resonance is very different depending on the y_2 values, we turn our attention onto its imaginary part. As shown in the appendix C, for $|\beta\delta| \ll 1$, the imaginary part of the denominator of the first term in Eq. (4.12) can be written as

$$\mathrm{Im}\{\beta^{-1} - \Omega_+\} \approx -\frac{k^3}{12\pi\epsilon_0}(\xi_1 + \xi_2) - \frac{k}{2\epsilon_0 a^2} - \mathrm{Im}\left\{\sqrt{\mathcal{G}_{12}^2 + \frac{\delta^2}{4}}\right\}, \tag{4.14}$$

where $\xi_i = \sigma_i^{\mathrm{abs}}/\sigma_i^{\mathrm{sca}}$ is the ratio between the dipolar absorption, $\sigma_i^{\mathrm{abs}} = (k/\epsilon_0)(\mathrm{Im}\{\alpha_i\} - k^3|\alpha_i|^2/(6\pi\epsilon_0))$, and scattering, $\sigma_i^{\mathrm{sca}} = k^4|\alpha_i|^2/(6\pi\epsilon_0^2)$, cross sections of particle i in isolation (see appendix C). We can distinguish that the first term on the right-hand side of Eq. (4.14) corresponds to the *material* losses of the lattice resonance, determined by the material and geometrical properties of the nanoparticles. The rest of the terms, which depend mostly on the array geometry through the lattice sum and the lattice parameter, a, can be interpreted as the *lattice* losses, and these can be assumed as purely radiative. As a result, the single lattice resonance supported by the bipartite arrays with $y_2 = 0$ and $y_2 = a/2$ has *lattice* losses proportional to $-k/(2\epsilon_0 a^2) - \mathrm{Im}\left\{\sqrt{\mathcal{G}_{12}^2 + \delta^2/4}\right\}$.

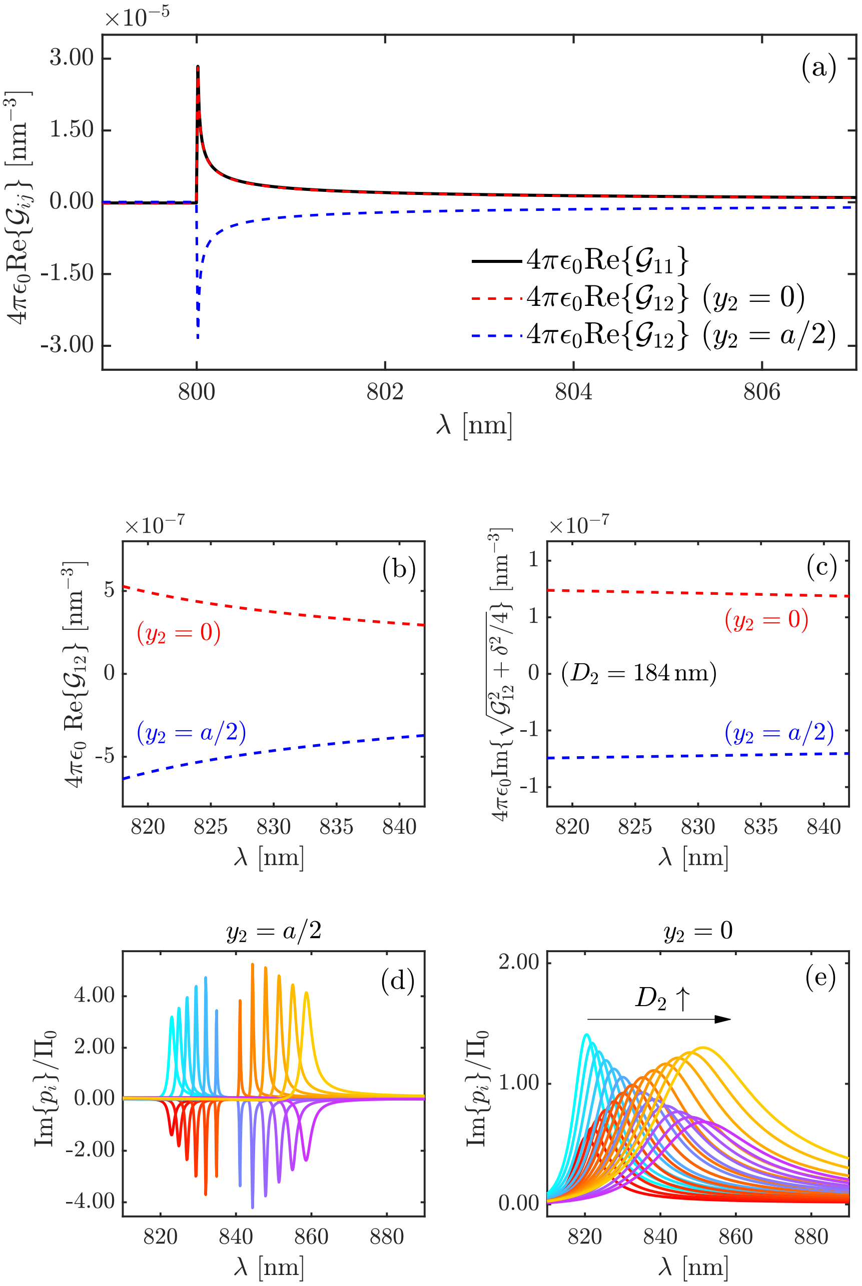

Figure 4.4: Lattice sums and particle size. (a) Wavelength dependence of $\mathrm{Re}\{\mathcal{G}_{ij}\}$ for $y_2 = 0$ and $y_2 = a/2$. (b) Real part of $\mathcal{G}_{12}$ in the region of Ω_+ lattice resonance. Blue and red dashed lines plot the arrays with $y_2 = a/2$ and $y_2 = 0$, respectively. (c) Imaginary part of the $\sqrt{\mathcal{G}_{12} + \delta^2/4}$ for $y_2 = a/2$ and, $y_2 = 0$ with $(D_1, D_2) = (200, 184)\,\mathrm{nm}$. (d,e) Imaginary part of the dipole induced in the array nanoparticles, normalized to Π_0. Cyan-to-violet and red-to-yellow solid lines represent the dipole in particles 1 and 2, respectively. We consider arrays with $a = 800\,\mathrm{nm}$, under normal incidence, with $D_1 = 200\,\mathrm{nm}$ and D_2 varying from 152 nm to 248 nm (from leftmost to rightmost curves) in steps of 8 nm.

Then, comparing these expressions for the lattice losses with the corresponding one for a single-particle array, $-k/(2\epsilon_0 a^2)$ (see appendix C), we conclude that the lattice losses in the bipartite array are totally dominated by both the amplitude and the phase of $\mathcal{G}_{12}$. Depending on the values of this magnitude, these radiative losses can be significantly enlarged or reduced for the array. Then, in Figure 4.4(b), we plot $\mathrm{Re}\{\mathcal{G}_{12}\}$ for $y_2 = 0$ and $y_2 = a/2$, in red and blue dashed lines, respectively, in the region where the Ω_+ mode arises at $\lambda \sim [820, 840]$ nm. We find that for the subradiant case ($y_2 = a/2$, dashed blue line), the slightly larger value of $|\mathrm{Re}\{\mathcal{G}_{12}\}|$ implies a more significant change in lattice losses. Nevertheless, not only the larger absolute value of the lattice sum is responsible for the change in the resonance character, but also the change of sign in $\mathcal{G}_{12}$. Figure 4.4(c) renders $\mathrm{Im}\Big\{\sqrt{\mathcal{G}_{12}^2 + \delta^2/4}\Big\}$ for $y_2 = 0$ and $y_2 = a/2$, providing the negative correction to $k/(2\epsilon_0 a^2)$ that corresponds to the subradiant case ($y_2 = a/2$). δ is calculated for the values $(D_1, D_2) = (200, 184)$ nm. Again, this is the expected behavior for super- and subradiant modes. Therefore, based on this analysis, we conclude that the bipartite arrays with $y_2 = 0$ and $y_2 = a/2$ support a super- and subradiant lattice resonance, respectively.

All of these trends are consistent with the behavior of the dipole moment induced in the nanoparticles. As expected from the hybridization model [180], the change of sign between $\mathcal{G}_{11}$ and $\mathcal{G}_{12}$ depending on the array configuration leads to the different eigensolutions of the system, as shown in Figure 4.4(d) and (e) for the subradiant and superradiant lattice resonance. We plot the imaginary parts of the first, p_1 and p_2 terms in Eq. (4.9), normalized to Π_0, as a function of the incident wavelength, λ. We use cyan-to-violet solid curves to denote the dipole induced in particle 1 in arrays with $a = 800$ nm and $D_1 = 200$ nm under normal incidence. The colorscale indicates the result for D_2 varying from 152 nm (leftmost curve) to 248 nm (rightmost curve) in 8 nm steps. Red-to-yellow lines plot the imaginary components of the dipoles induced in particle 2. In the subradiant case (Fig. 4.4(d)), the induced dipoles have opposite signs, meaning that the two dipoles oscillate in antiphase. In the superradiant counterpart (Fig. 4.4(e)), the two dipoles oscillate in phase, resulting in a stronger combined dipole moment that gives rise to large reflectance values.

So far, we have focused on bipartite arrays in which the second particle in the unit cell is placed at either $y_2 = 0$ or $y_2 = a/2$, which support a sole lattice resonance. However, this is not the expected behavior for arbitrary values of y_2 lying between these two limits. In these cases, Eq. (4.12) predicts the existence of two different lattice resonances whose optical properties are largely determined by the interplay between $\mathcal{G}_{12}$ and δ. This is confirmed in Figure 4.5, where we analyze the spectral position and optical properties of

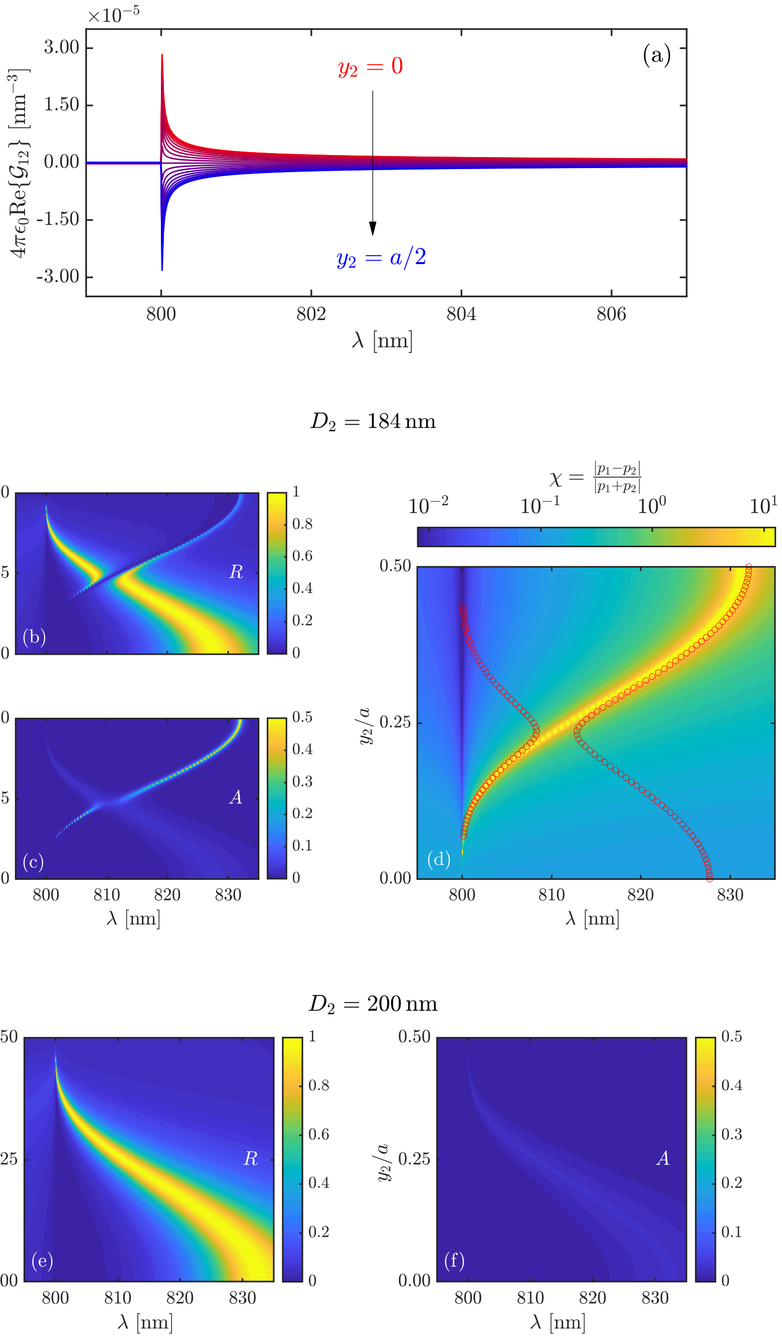

Figure 4.5: Transition from super- to subradiant lattice resonances in bipartite nanoparticle arrays. (a) Real part of $\mathcal{G}_{12}$ for $y_2 \in [0, a/2]$. (b,c) Reflectance, R, and absorbance, A, spectra as a function of λ, the incident wavelength, and the y-position of the second particle in the unit cell, y_2 for $(D_1, D_2) = (200, 184)\,\mathrm{nm}$, which yields $\delta \neq 0$. (d) $\chi = |p_1 - p_2| \,/\, |p_1 + p_2|$, as a function of both wavelength and y_2. Red markers plots the maxima of R in panel (b). (e,f) Reflectance, R, and the absorbance, A, spectra as a function of λ, the incident wavelength, and the y-position of the second particle in the unit cell, y_2 for $(D_1, D_2) = (200, 200)\,\mathrm{nm}$, $(\delta = 0)$. In all cases, we consider arrays with $a = 800\,\mathrm{nm}$.

the lattice resonances supported by arrays as a function of the incident wavelength and the position of the second particle, $\mathbf{r}_2 = (a/2, y_2)$. We consider arrays with $a = 800\,\mathrm{nm}$ and $D_1 = 200\,\mathrm{nm}$. The emergence of the two different resonances can be understood by noticing that, as shown in Figure 4.5(a), in the transition from $y_2/a = 1/2 \rightarrow 0$ (red to blue solid lines), $\mathrm{Re}\{\mathcal{G}_{12}\}$ takes very different values. Fig. 4.5 panels (b) and (c) display, respectively, the reflectance, R, and the absorbance, A, as a function of both λ and y_2, with $D_2 = 184\,\mathrm{nm}$, as indicated. We observe that there are two lattice resonances whose spectral positions merge as the value y_2 approaches $a/4$. This coalescence occurs since the lattice sum components satisfy $\mathrm{Re}\{\mathcal{G}_{12}\} \ll \mathrm{Re}\{\mathcal{G}_{11}\}$ for $y_2 = a/4$ (see Fig. 4.5(a)), which results in Ω_+ and Ω_- having similar values. It is worth mentioning that the wavelengths of the peaks of the absorbance and reflectance spectra do not exactly coincide, which is consistent with the fact that the reflectance is directly proportional to $|p|^2$ while the absorbance depends on the interplay between $\mathrm{Im}\{p\}$ and $|p|^2$, as shown in Eq. (4.11).

Figure 4.5(d) sheds light into the sub- or superradiant character of the resonances observed for the $(D_1, D_2) = (200, 184)\,\mathrm{nm}$ case. The function $\chi = |p_1 - p_2| \,/\, |p_1 + p_2|$ serves to characterize the nature of the lattice resonance since its value ranges from zero, for a perfectly superradiant mode with $p_1 = p_2$, to large values for subradiant modes for which $p_1 \approx -p_2$. The maxima of R, plotted in red markers, show that, for values of y_2 below $a/4$, the lattice resonance located at longer wavelengths has a superradiant character, as inferred from the large R (Fig. 4.5(b)) and the vanishing value of χ. On the other hand, the lattice resonance closer to the Rayleigh anomaly (*i.e.*, $\lambda = a$) exhibits non-negligible values of absorbance and large values of χ, thus corresponding to a subradiant mode. This trend changes completely for the cases where $y_2 \in (a/4, a/2)$. There, the resonance appearing at longer wavelengths displays the subradiant character, while the closer to the Rayleigh anomaly corresponds to the superradiant mode.

When the two particles are identical (*i.e.*, $D_1 = D_2 \rightarrow \delta = 0$), only one resonance is visible in the spectra of R and A (see Fig. 4.5 (e) and (f), respectively). The subradiant mode becomes completely dark and hence disappears. As expected from the analysis of Eq. (4.12), only one resonance is visible, since the weights $\zeta_\pm$ become zero depending on the sign of $\mathcal{G}_{12}$. In this case, not shown, it is clear that $\chi = 0$.

4.3.2. Conditions for maximum absorbance

The results shown in previous figures demonstrate that the single subradiant lattice resonance that takes places in bipartite arrays with $\mathbf{r}_2 = (a/2, a/2)$ is characterized by a very large absorbance. Interestingly, the maximum values are reached on both sides

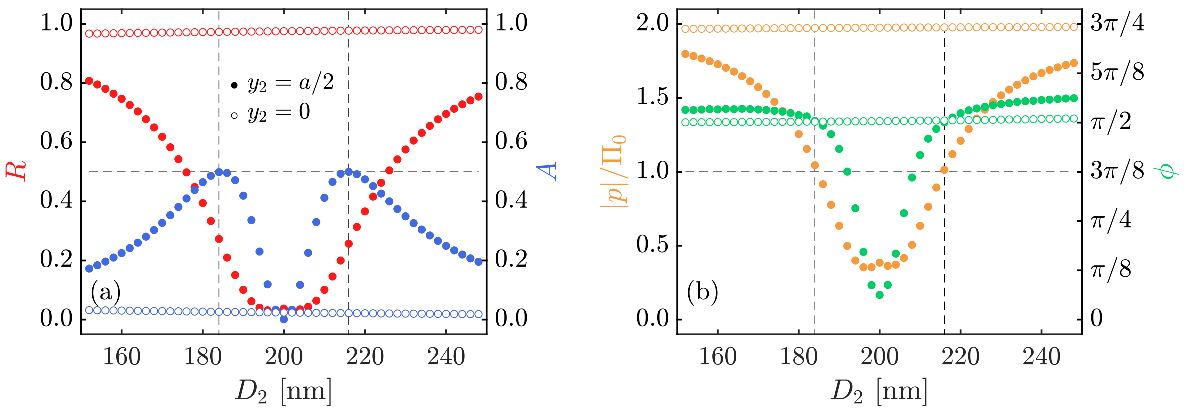

Figure 4.6: Conditions for maximum absorbance in bipartite nanoparticle arrays. (a) Value of the reflectance, R, (red, left scale) and absorbance, A, (blue, right scale) for the lattice resonance of the sub- and superradiant arrays, calculated at the wavelength of the maximum absorbance as function of D_2. (b) Normalized magnitude of the total dipole $|p| = |p_1 + p_2|$, induced in the unit cell (orange, left scale), and its corresponding phase ϕ (green, right scale), calculated in the same conditions as panel (a). We use filled dots to display the subradiant array and empty dots for the superradiant configuration. All the calculations are performed for arrays $a = 800\,\text{nm}$ and $D_1 = 200\,\text{nm}$. The vertical dashed lines mark the values of D_2 at which maximum absorbance is reached, $A = 0.5$ (horizontal dashed line in (a)).

of the critical condition $D_1 = D_2$ (see Figure 4.3(c)). We explore this phenomenon in more detail in this section, where we focus again on configurations which show a single resonance, with super- or subradiant character.

In the spirit of Figure 4.3, we proceed to study, as a function of the size of the second particle, D_2, the value of the reflectance and absorbance at the wavelength for which A is maximum. We plot those values in red and blue, respectively, in Figure 4.6(a). We use empty and filled dots, respectively, for the super- ($y_2 = 0$) and subradiant ($y_2 = a/2$) cases, with $a = 800$ nm and $D_1 = 200\,\text{nm}$. We vary D_2 in steps of 2 nm for increased resolution with respect to Figure 4.3. As discussed before, the reflectance and absorbance for the superradiant case ($y_2 = 0$) remain almost constant as the value of D_2 is varied, whereas, for the subradiant system, we observe significant changes. In particular, the value of reflectance monotonically decreases as D_2 approaches D_1 from either side. However, the absorbance displays two maxima at $D_2 = 184\,\text{nm}$ and $D_2 = 216\,\text{nm}$ (see the crossings between dashed lines that mark the positions of the maxima). At these points, the absorbance reaches 0.5, which is the theoretical maximum value for a two-dimensional system [187].

We can understand this behavior by examining the expression of the absorbance given in Eq. (4.11). We can generally write $p = p_1 + p_2 = |p|e^{i\phi}$. With that expression, and taking the derivative of A with respect to p, we find that its maximum is reached at $p = i\Pi_0$, for which $A = 0.5$. Interestingly, for that value of p, the reflectance becomes $R = 0.25$, in complete agreement with the results of previous works [187]. It is clear that to maximize the absorption, the total induced dipole p must be purely imaginary (dephased $\pi/2$ with respect to the incident field) since any real component only serves to reduce this quantity.

Indeed, noticing that, for a perfectly periodic array, the absorption and scattering efficiencies can be assimilated to A and $2R$, respectively, this condition can be seen as a manifestation of the well-known result that states that the maximum absorption of a dipolar system is reached when its absorption and scattering efficiencies become equal [189, 190]. In order to verify these arguments, in Figure 4.6(b), we plot the magnitude (orange) and the phase (green) of p for the same systems analyzed in panel (a). Again, we use empty and filled dots for the super- and subradiant arrays, respectively. Clearly, the magnitude of p for the subradiant system approaches Π_0 and its phase becomes $\pi/2$ for $D_2 = 184\,\text{nm}$ and $D_2 = 216\,\text{nm}$, in excellent agreement with our predictions. On the other hand, for the superradiant system, the magnitude and phase of p remain at $2\Pi_0$ and $\pi/2$, respectively. Substituting these values in Eq. (4.11), we obtain $R = 1$ and $A = 0$, in complete consistency with the results of Figure 4.6(a).

4.3.3. Quality factors

A distinct feature of the lattice resonance supported by the subradiant bipartite array is its reduced lineshape as compared with its superradiant counterpart. Consequently, the subradiant lattice resonance displays a much larger quality factor Q. We focus then on the comparison of Q between super- and subradiant configurations, as shown in Figure 4.7(a). We use filled and empty blue dots, respectively, to plot Q for the super- ($y_2 = 0$) and subradiant ($y_2 = a/2$) arrays as a function of D_2. We consider systems with $a = 800\,\text{nm}$ and $D_1 = 200\,\text{nm}$, and vary D_2 from 152 nm to 248 nm, in steps of 2 nm, as in Figure 4.6. We will calculate $Q = \frac{\lambda_E}{\Delta\lambda}$ from the spectrum of the extinction efficiency, where λ_E and $\Delta\lambda$ are the central wavelength and the full-width at half maximum (FWHM) of the extinction resonance, respectively. For infinite arrays, within the dipolar approximation, the extinction is defined as

$$E = 2R + A = \frac{\mathrm{Im}\{p\}}{\Pi_0}. \tag{4.15}$$

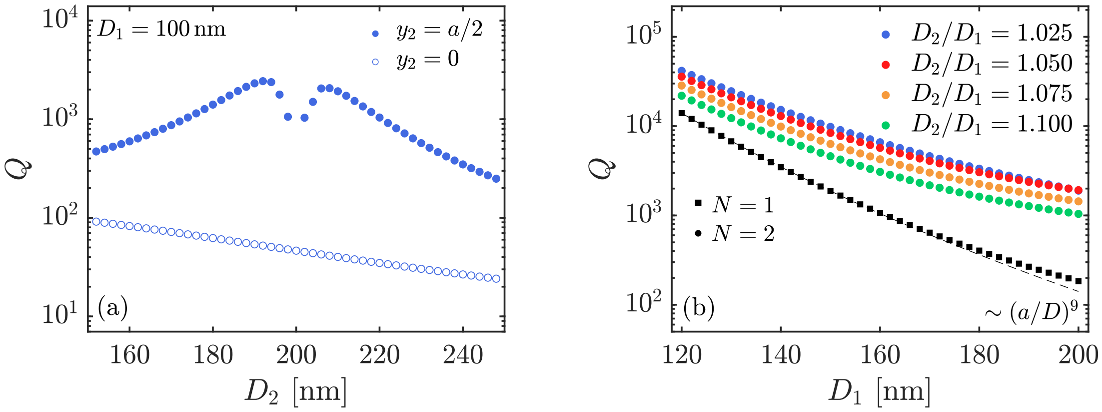

Figure 4.7: Analysis of the quality factor of the lattice resonances. (a) Quality factor for the lattice resonance of the super- and subradiant arrays, plotted as a function of D_2. We assume $D_1 = 200\,\mathrm{nm}$ and use empty (filled) dots to display the results for the array with $y_2 = 0$ ($y_2 = a/2$). (b) Quality factor for the lattice resonance of the subradiant array plotted as a function of D_1 for different ratios D_2/D_1, as indicated in the legend. For comparison, we plot the results for a single-particle array with $D = D_1$ using black dots. The dashed black line indicates a scaling of $\sim (a/D)^9$.

This expression can be understood from the fact that an infinite array, within the coupled dipole model, behaves as a thin layer formed by point-like dipoles. The field scattered by this kind of system has to be symmetric, since not phase is acquired by the field while travelling through the vanishing width of the array [187]. Therefore, we can identify the normalized scattered power with $2R$. The definition of the extinction is then natural, as the sum of scattering and absorption contributions. Examining the results of Figure 4.7(a), we observe that the quality factor of the superradiant lattice resonance is always below 100 for the values of D_2 analyzed. On the contrary, for the subradiant lattice resonance, Q is beyond 1000 for D_2 in the range $174-220\,\mathrm{nm}$, reaching two local maxima of ≈ 2400 for $D_2 = 192\,\mathrm{nm}$ and ≈ 2000 for $D_2 = 208\,\mathrm{nm}$. Interestingly, these values of D_2 are not far from the ones that maximized the absorbance $D_2 = 184\,\mathrm{nm}$ and $D_2 = 216\,\mathrm{nm}$, for which Q is ≈ 1500 and ≈ 1300, respectively.

It is also important to remark that the quality factor of the subradiant bipartite array is also larger than that of a single-particle array with similar period and particle size. It has been recently demonstrated [191] that the quality factor of the lattice resonance of a single-particle array with period a and particle size D scales as $Q \sim (a/D)^9$. Therefore, by using single-particle arrays with increasing a/D, it is possible to obtain lattice resonances with larger quality factors [172]. This can be seen in Figure 4.7(b), where the black dots represent the value of Q for the lattice resonance of a single-particle array with period $a = 800\,\mathrm{nm}$ and particle diameter $D = D_1$. However, for a given value of D_1, it is possible to construct a subradiant bipartite array supporting a lattice resonance with Q larger than that of a single-particle array with the same periodicity. Note that the density of particles is two times larger in the bipartite array, which in principle could reduce Q. However, as it can be seen in Figure 4.7(b), the quality factor for the lattice resonance of a subradiant array can be larger. Coloured filled dots render Q for bipartite arrays satisfying different particle-size ratios D_2/D_1. As shown, by decreasing this ratio, it is possible to further increase the quality factor. Interestingly, for the largest sizes under consideration, all the ratios D_2/D_1 result in a value of Q that is almost one order of magnitude larger than that of the single-particle array. However, as D_1 decreases, it is necessary to use an increasingly smaller D_2/D_1 ratio to achieve the same improvement.

4.4. Conclusions

To conclude this chapter, we have provided a comprehensive analysis of the lattice resonances supported by nanoparticle arrays, inspired by the hybridization of both plasmonic and lattice resonances. Using a rigorous coupled dipole model, we have shown that it is possible to obtain modes with either a super- or subradiant character, depending on the relative position of the two particles within the unit cell of a bipartite array, which result in very different optical responses. In particular, superradiant lattice resonances result in increased radiative losses that lead to large reflectance values and broad lineshapes. In sharp contrast with this phenomenology, subradiant lattice resonances display much narrower lineshapes, and therefore much higher quality factors, as well as large values of the absorbance. The reflectance and absorbance features are well understood in terms of the induced dipoles in the particles and the losses associated to the lattice. We have found that the lattice sum that mediates the interaction becomes crucial, and, for general configurations, the different values taken by the lattice sum lead to the emergence of two different resonances, each one with a different superradiant or subradiant character. Finally, we have found that, while the relative size of the two particles has a minimal impact on the response of the superradiant array, the optical response of the subradiant one undergoes dramatic transformation as the particle size is changed, making it possible to reach perfect absorbance and high quality factors.

5

Plasmon-assisted Purcell effect and Förster resonance energy transfer

In this chapter we are going to explore how plasmonic resonances can affect the photophysical properties of fluorophores. In particular, we are going to present several results that give theoretical support to experiments based on the molecular self-assembly techniques related to the use of DNA complexes. We will briefly review this technique in section 5.2, that provides an accurate control on positioning the building blocks of nanophotonic structures. Subsequently, in section 5.3, we will show our results on how plasmonic resonances can enhance the fluorescence capability of molecules, through exploitation of the competition between radiative and internal photochemical processes. Finally, in section 5.4, we provide an approach to the study of plasmon-assisted energy transfer between a donor-acceptor pair in the vicinities of metallic nanoparticles. Our findings are the result of the collaboration with the group of Prof. Guillermo Acuña, currently at the Université de Fribourg, Switzerland.

5.1. Introduction

In many situations, specially in the context of theoretical electromagnetics, electric and magnetic fields are just God-given magnitudes. We usually place them wherever and study the system response under their influence. Nevertheless, if we go a step back, the roots of any light field are intimately related to photophysical and photochemical processes where energy excitations are converted into photons. Apart from those taking place in nature, the future of many technological applications relies on the phenomena assisted by such processes, specially within the scope of nanotechnology. Photochemical processes present plenty of potential applications, from energy storage to optical memories and switches [192, 193], often inspired by living-like processes. However, they also show detrimental effects (i.e., efficiency reduction) that should be avoided [194, 195]. Photophysical processes are at the basis of the design of fluorescent compounds for a wide set of sensing applications and single-photon sources [196, 197].

In chapter 1, we overviewed the basic concepts of quantum emitters, nanometer (or sub-nanometer) -sized systems, whose interaction with light is described by absorption and emission spectra having a number of well-defined maxima. We recommend the reader Ref. [198], where this topic is treated in detail. Light excitation with a photon promotes the molecule from its ground state, $|g\rangle$, to an excited one, $|e\rangle$. Once in this state, $|e\rangle$, and after no external pumping of energy, several channels provide its spontaneous photophysical deactivation, with processes that can be seen in a typical Jablonski diagram [198]. If the deactivaction occurs without the emission of a photon, it is said radiationless or non-radiative. It occurs between isoenergetic vibrational levels of different excited electronic states, leading to an increase of entropy that makes them essentially irreversible. Non-radiative transitions between states of equal spin multiplicity are called internal conversion [199], whereas intersystem crossing denotes transitions where spin is not conserved (singlet-triplet transitions) [198, 200, 201]. The contrary, a radiative process of deactivation, implies the emission of a photon and it is mainly determined by the light-matter interaction Hamiltonian. The spontaneous emission of light from any substance is known in general as *luminescence* but the importance of the measurements on samples based on molecular spectroscopy, specially in situations dealing with organic dyes provided the use of the term *fluorescence*. In particular, we are going to refer to fluorescent radiative processes, which denote the deactivation of the excited electronic state to the ground state with the same spin multiplicity (typically singlet-singlet states), accompanied by the emission of a photon[1]. As the rate of internal conversion is large, emission can usually be observed only from the lowest excited state (Kasha's rule) [198]. If the excited and ground state potential energy surfaces present different structure, there is a shift between absorption and emission spectra for the same transition (Stokes shift). Furthermore, excited states can achieve deactivation by a variety of chemical processes not shown in the Jablonski diagram.

Because of triplet-state excursions, fluorescence emission shows patterns: high count rates associated to singlet-singlet transitions are interrupted by temporally dark peri-

---

[1] The complexity in the molecule structure can lead to phosphorescence, i.e. radiative deactivation between states with different spin multiplicity, not considered here [202].

ods [55]. This phenomenon, known as blinking, is particularly important in quantum dots more than in organic fluorescent dyes. In addition, molecules eventually cease to fluorescence completely. In this case, the fluorophore undergoes photobleaching, mostly due to photochemical reactions. Photobleaching imposes a fundamental limit to the total of number of photons that can be harvested. The excited state decays with a lifetime that mixes different deactivation processes in the terms of the rates

$$\tau = \left(\sum_i \gamma_i \right)^{-1}.$$

Therefore, the decay from the excited state is usually a competition among several processes with rates γ_i, which usually correspond to the chemical (γ_{b}), radiative (γ_{r}) and non-radiative (γ_{nr}) contributions.

5.2. DNA origami technique

The arrangement of individual photonic blocks is crucial for the creation of systems that present tailored optical properties and functionalities. Top-down approaches for nanophotonics as colloidal techniques or lithographic definition of optical antennas and plasmonic systems have provided much insight into the nature of light-matter interactions [203, 204]. However, these techniques do not offer reproducible control over tiny spaces needed for certain situations involving tightly confined electromagnetic fields. The main limitation is the lack of precision in the positioning of single light sources at the plasmonic hot-spots of the system [205]. Molecular self-assembly offers an alternative that complements the top-down original approach [141, 206]. In particular, DNA origami techniques exploit the design of origami structures with almost any shape, that can serve as templates for assembly with nanometer precision [207–209].

In Figure 5.1 we sketch briefly the procedure of DNA origami fabrication. The basic ingredients are two chains of single-stranded DNA: a long one, called scaffold, and a set of short ones, called staples. Each staple strand has a defined sequence and it can be linked to the scaffold at specific places. The geometry of the structure is pre-designed, see Fig. 5.1(a), and translated into a certain nucleid configuration of the strands, that serves to fold the scaffold into the designed two- or three-dimensional shape after performing a thermal annealing to the scaffold-staples mixture represented in Fig. 5.1(b), with black and color lines for scaffold and staples, respectively. As illustrated in Fig. 5.1(c), it is also possible to add capture strands at certain positions that allow the binding of the nanoscale components, including proteins, nanoparticles and emitters. The purified structure has the symbolic forms sketched in Fig. 5.1 (c) and (d). The structure can

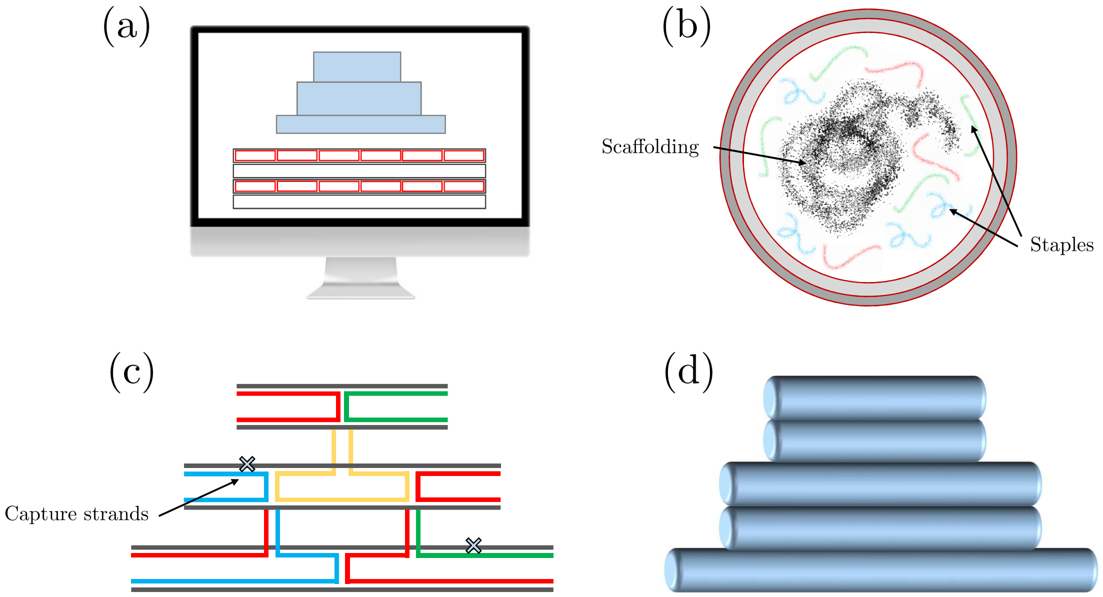

Figure 5.1: DNA origami design and assembly. (a) Computer-aided designing of DNA origami. (b) DNA origami mixture consisting of two different types of single-strand DNA chains: a longer one (black line), the scaffold, and several short ones (colored lines), the staples. (c) Example of the complete scaffolding-staple layout, with coloured staples linking the different parts of the scaffolding. (d) Cylindrical representation of the macroscopic structure corresponding to panel (c).

be also represented in the typical cylindrical geometry that render usual DNA origami structures, denoting the three-dimensional character of the scaffold strand after the origami formation.

The utilization of DNA for assembly of metal nanoparticles was first demonstrated in the mid-90s [210]. About ten years later, DNA origami technique allowed the fabrication of well-defined plasmonic clusters [207]. The possibilities offered by the technique opened the way to construct plasmonic structures with novel optical properties like helical assemblies or reconfigurable plasmonic systems with dynamically controlled optical responses, where dynamic DNA origami templates can be switched by external stimuli [211, 212]. In the context of plasmon-emitter interactions, the origami technique allows unique spatial addressability, ranging from a few to hundreds of nanometers with a nanometric positioning accuracy. This excellent self-assembly capacity provides new degrees of freedom for the design of hybrid systems, combining metallodielectric nanostructures and fluorescent molecules. Currently, much work is focused on achieving control over the emitter orientation, an aspect that, so far, remains elusive. DNA origami arrangements have enabled investigations on FRET between fluorophores, with definitions of energy paths through arrays of molecules [213], as well as detailed studies of the manipulation of luminescence under plasmonic influence [214]. DNA-origami-based antennas have been employed towards fluorescent imaging and Raman scattering, exploiting the unprecedented control over molecule position and detection [215]. Arrays of nanoparticles bound to DNA structures have been shown to work as plasmonic waveguides, yielding reversible energy transfer in chains of nanoparticles and light-harvesting [216, 217].

5.3. Enhancing photostability through plasmonic coupling

Most experimental works on plasmonic optical antennas have focused on their capacity to concentrate propagating radiation into sub-wavelength volumes to enhance fluorescence intensity, mostly through an increment of the excitation rate [72, 204, 218]. Fewer addressed the function of optical antennas in emission, where those can modulate the decay rates and the emission directionality [219, 220].

Perhaps the main reason behind the lack of experimental studies on the effect of nanoantennas on the photostability of single molecules lies in the fact that measurements are intrinsically demanding. The total number of photons emitted by a single fluorophore is in first approximation independent of excitation intensity in the low pumping limit. Photobleaching is a stochastic process, and in ideal cases, the total number of emitted photons by a set of fluorophores follows an probability distribution, so the obtention of the total number of emitter photons, N, requires of the determination of an exponential distribution. Then, the procedure involves the realization of single molecule measurements until the occurrence of a photobleaching event. Furthermore, during this photobleaching time, which can take up to several minutes, the distance between the optical antennas and the single fluorophores has to be adjusted with nanometer accuracy due to the local character of the density of states, as seen in previous chapters.

The plasmonic effect on photobleaching can be modeled within a simplified two-level system approach. The molecule absorbs photons with a rate, γ_{exc} in the excitation process. The evolution in the excited state is determined by the competition between two processes. First, the relaxation, that can be radiative or non-radiative, represented by rates γ_{r} and γ_{nr}. The second process is photobleaching with a rate γ_{b}. Looking at the dynamic equations of the ground and excited states [221], those are not symmetric due to the photobleaching rate present in the excited state dynamics. Usually, working in the low power regime, γ_{b} is assumed to be a constant [222] and the average time that a fluorophore emits photons until it bleaches is approximated as [221]

$$\tau_p = \frac{1}{\varphi}\frac{\gamma_{\mathrm{r}}}{\gamma_{\mathrm{b}}\gamma_{\mathrm{exc}}}, \tag{5.1}$$

where $\varphi = \gamma_{\mathrm{r}}/(\gamma_{\mathrm{r}} + \gamma_{\mathrm{nr}})$ is the quantum yield of the fluorophore.

On the other hand, the total number of photons emitted by the fluorophore until the occurrence of bleaching, N, is known as the photobleaching limit. It is a more appropriate quantity to measure the effect, avoiding the dependence on excitation intensity, which reads [221, 223]

$$N = \frac{\gamma_{\mathrm{r}}}{\gamma_{\mathrm{b}}}. \tag{5.2}$$

Equation (5.2) shows that the total number of photons harvested from a single molecule can be enlarged through the modification of its radiative decay rate. As photobleaching deteriorates the emission capability, many efforts have been devoted to suppress this effect based on chemical approaches [224, 225]. Furthermore, plasmonic platforms manifest as a good candidate to suppress photobleaching. The spontaneous emission from the excited state can be largely altered through the Purcell effect[2]. As the molecules spend shorter periods in the excited state before the emission of a photon, it performs more cycles before losing its fluorescent capability. The effect of increasing photostability of fluorophores by means of the local density of states (LDOS) was firstly predicted in Ref. [227] but it remained unexplored until recently, with approaches to fluorophores incorporated to nanoshells [221], in a ensemble of fluorophore-nanoparticle systems. A clear experimental proof of the LDOS mechanism on photostability was absent due to the highly precise control needed in the positioning on emitters in the plasmonic resonators surroundings.

In the following, we present numerical results of enhancement of radiative decay rates of a fluorophore in a plasmonic environment. By the obtention of numerical solutions of the Maxwell's equations, we can compute the effects of light-matter coupling between a

---

[2] In the context of quantum emitters, the modification of the LDOS has been shown to affect also blinking [226].

fluorescent molecule and the plasmonic resonances of a metallic dimer in terms of the radiative Purcell factor, giving support to experimental results. Those consisted in the obtention of the total number of emitted photons before bleaching, N, by time-resolved fluorescent measurements of single molecule emission in Ag dimers, designed by means of DNA origami technique. The comparison of N for different samples can be linked to the radiative Purcell enhancement mediated by the plasmonic resonances.

5.3.1. Enhancement of the radiative decay rate: Purcell factor

Figure 5.2(a) sketches the optical antenna employed to enhance the photostability of fluorophores and measure the enhancement of the radiative decay rate. It consists of a pillar-shaped three-dimensional (3D) DNA origami structure, thinned at the top to a diameter of approximately 6 nm and immersed in an aqueous solution. Two silver nanospheres with radius $R = 40\,\mathrm{nm}$ are incorporated at the top of the origami structure in order to fabricate dimers by with a set capturing strands attached at each nanoparticle. Within the nanofabrication protocol followed [128], samples can contain a distribution of DNA origami structures with dimers, monomers, and no nanoparticles (reference). In the 12-nm gap between the nanoparticles, a single fluorophore Alexa488 is incorporated within the DNA. This dye presents excitation and emission peaks centered at $\lambda = 490$ and 525 nm, respectively, with a high quantum yield, $\varphi = 0.92$.

Three sets of samples were studied, DNA origami structures with different concentrations of capturing strands in order to have the three described configurations. The reference sample only contained fluorescent dyes but both the monomer and dimer samples did not exclusively contain monomer and dimer structures. References were present in the monomer sample whereas dimers, monomers and references appeared in the dimer sample. Each sample contained a large amount of DNA structures. Figure 5.2(b) shows the typical fluorescence transients that were measured in the laboratory, where only a single step occurs, indicating photobleaching from a single molecule. The sample was scanned sequentially and the time-resolved fluorescence emission was measured until photobleaching occurs. From the fluorescence transients, the total number of emitted photons, N, for each DNA structure in the corresponding sample was extracted. The stochastic character of the photobleaching process provides that N follows a Poissonian probability distribution, and looking at individual cases does not provide meaningful information, since N can acquire arbitrarily high values [223]. Then, many different sys-

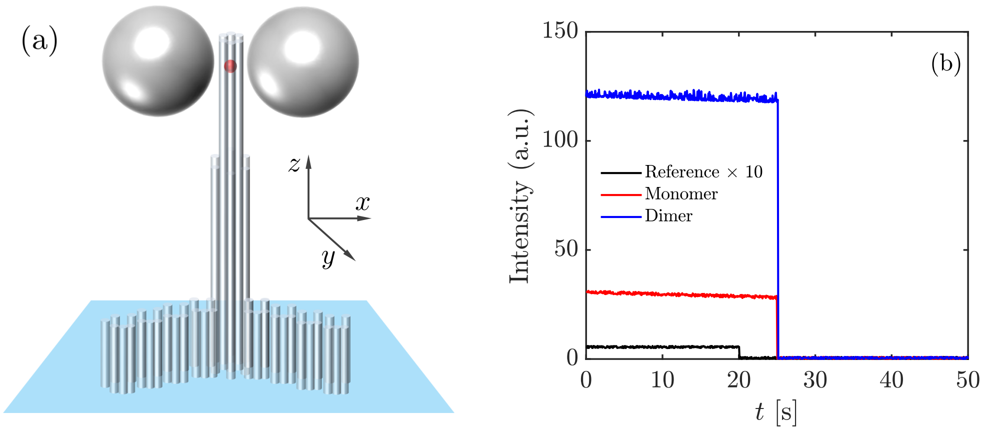

Figure 5.2: Photobleaching reduction through plasmonic coupling. (a) Sketch of the plasmonic system, consisting of two 80-nm-diameter Ag nanoparticles, self-assembled onto a three-dimensional (3D) DNA origami structure. In the 12-nm gap between the particles, a single fluorophore (Alexa488) is positioned. (b) Example of fluorescence transients extracted from dimer, monomer and no-particle (reference) samples, with the single step, signature of single-molecule photobleaching.

tems in the sample were observed to extract the probability distribution of the sample, which was modeled following a exponential trend according to

$$P_i(n) \propto e^{-n/N_i}, \tag{5.3}$$

with n as the number of photons and the sub-index i will denote the reference and the monomer samples. Following this analysis, the average numbers of emitted photons, measured in the large ensemble of samples, before photobleaching for the reference and the monomer are $N_{\mathrm{ref}} = (28 \pm 1) \cdot 10^3$ and $N_{\mathrm{m}} = (110 \pm 10) \cdot 10^3$, respectively, which translate into a factor 4 in radiative enhancement for the monomer structure. On the other hand, the third sample contained both monomers and dimers, whose contribution had to be distinguished. This was done by adjusting the probability distribution of the dimer sample as a sum of two exponential terms, representing the monomer and dimer contribution (given by κ) as

$$P_{\mathrm{d}}(n) \propto e^{-n/N_{\mathrm{m}}} + \kappa e^{-n/N_{\mathrm{d}}}. \tag{5.4}$$

In this case, the average numbers of photons obtained are $N_{\mathrm{m}} = (116 \pm 13) \cdot 10^3$ (in agreement with the only-monomer sample) and $N_{\mathrm{d}} = (840 \pm 210) \cdot 10^3$, for the dimer contribution. Thus, N_{d} reveals a 30× enhancement factor in the average number of emitted photons.

As shown in Equation (5.2), the total number of emitted photons, N, is a direct measure of the radiative rate. Therefore, we can directly compare the changes of the radiative rate with finite element simulations of an emitter next to plasmonic structures. We performed numerical simulations in order to gain insight into the experimental findings. Due to the Purcell effect, γ_r varies from one structure to the other, whereas γ_b is assumed to be inherent to the fluorophore itself. Thus, we can identify the ratio between average photons emitted in different samples with the numerically-calculated ratio between the corresponding radiative decay rates. In the fashion of the experimental measurements, the decay rate in the absence of metal nanoparticles, γ_r^0, is taken as the reference in the simulations. We performed our calculations using the RF Module implemented in COMSOL Multiphysics, based on the finite element method to solve Maxwell's equations in the frequency domain. We computed the power radiated by the source through the calculation of the flow of the time-averaged Poynting vector, $\frac{1}{2}\mathrm{Re}\{\mathbf{E}\times\mathbf{H}^*\}$ across a numerical aperture $\mathrm{NA} = 1.4$ solid angle along the vertical direction, in the presence or absence of the silver dimer. The non-radiative components were calculated by integrating the power dissipated within the metallic regions. The spectra were obtained by averaging the fluorophore orientation as

$$P_f^i = \frac{\gamma_i}{\gamma_i^0} = \frac{W_x^i + 2W_y^i}{3W_0}, \tag{5.5}$$

where x-direction is defined parallel to the dimer axis (see inset in Figure 5.3(b)). Subindex $i = \mathrm{r,nr}$, represents the radiative or non-radiative contribution and W_0 is the power in free space.

Special efforts were devoted to mimicking the experimental set-up and samples as accurately as possible in our theoretical model. The DNA origami and metal nanoparticles were placed on top of a silica substrate $\mathrm{SiO_2}$ (with refractive index $n_{\mathrm{SiO_2}} = 1.5$) [228] and embedded in an aqueous environment ($n_{\mathrm{H_2O}} = 1.33$). The origami was modeled as a 6 nm diameter, 110-nm-height cylinder with homogeneous refractive index $n_{\mathrm{DNA}} = 2.1$ [229]. The frequency-dependent silver permittivity for the $R = 40\,\mathrm{nm}$ radius nanoparticle was fitted to the experimental data in the fashion of a Drude-Lorentz model [230] (see sec. 1.4) and nonlocal effects in the metal permittivity were neglected [231]. The plasmonic monomer and dimer were attached to the DNA origami, 60 nm above the silica substrate in a similar way as sketched in Figure 5.2(a). The refractive index of the DNA strands surrounding the nanoparticles was approximated to the refractive index of water. Our preliminary simulations, as well as previous simulations of Au dimers [232], predicted large enhancements of the radiative rates, so we attributed the mismatch to a

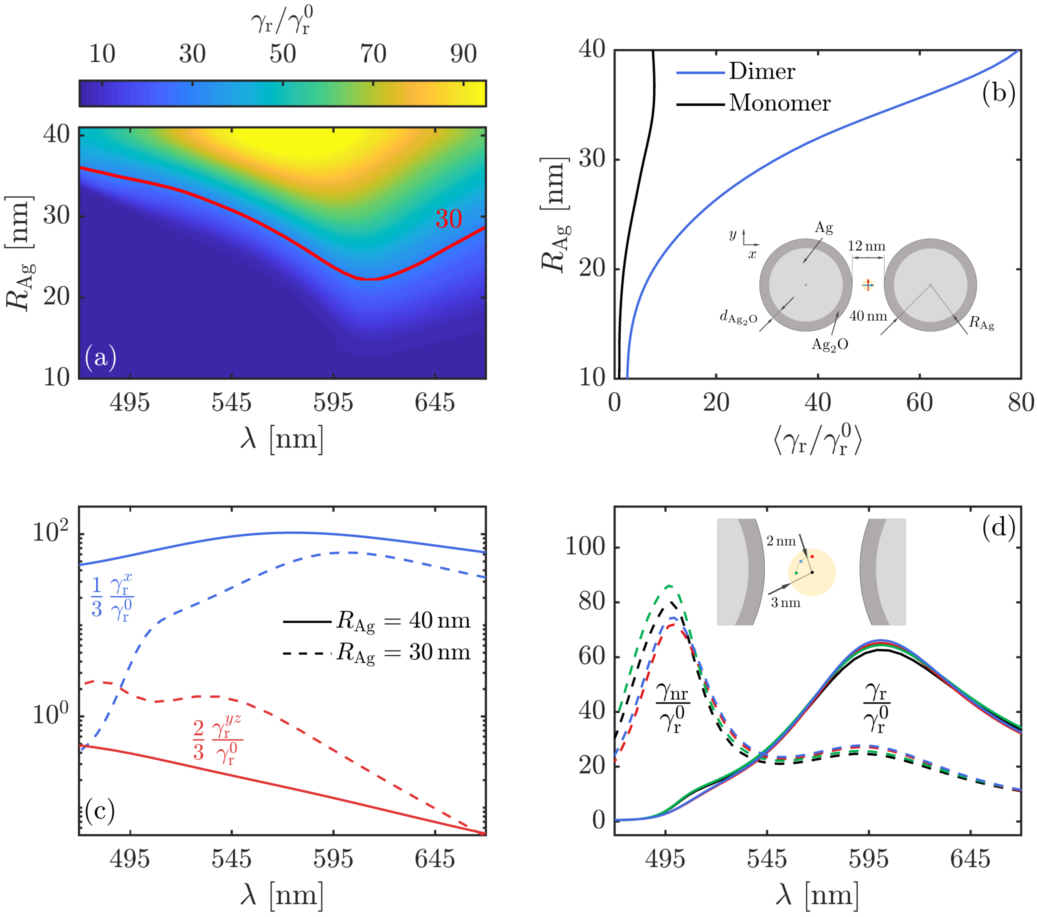

Figure 5.3: Numerical simulations results for normalized rates. (a) Normalized radiative decay rate as a function of the wavelength, λ and nanoparticle oxidation level, expressed in terms of the inner Ag radius, R_{Ag}. Red solid line renders the contour $\gamma_r/\gamma_r^0 = 30$, obtained in the experiments. (b) Spectrally averaged decay rate as a function of oxidation level for monomers and dimers. The inset represents a top-view sketch of the geometry. (c) Radiative decay for both axial (blue) and normal (red) fluorophore orientations. Solid and dashed lines represent non-oxidized and oxidized dimers, respectively. (d) Radiative and non-radiative normalized decay rates for four different positions (see coloured dots in the inset).

possible impact of oxidation. We modeled the oxidized nanoparticles through a core-shell geometry, with a silver inner core of radius R_{Ag} and an outer layer of oxide $\mathrm{Ag_2O}$ with thickness $d_{\mathrm{Ag_2O}}$ and refractive index $n_{\mathrm{Ag_2O}} = 2.5$ [233].

Figure 5.3(a) shows the normalized radiative decay rate, $\gamma_{\mathrm{r}}/\gamma_{\mathrm{r}}^{0}$, or radiative Purcell factor, for the dimer structure within the spectral window $\Delta\lambda$ corresponding to the emission band of Alexa488 as a function of the level of nanoparticles oxidation. In all cases, the decay rate spectra are governed by a broad maximum that originates from the dipolar plasmonic resonance supported by the plasmonic system at $\lambda \approx 550 - 600\,\mathrm{nm}$. Note that this peak lowers, broadens, and redshifts slightly with increasing the external oxide coating. The red solid line renders the contour $\gamma_{\mathrm{r}}/\gamma_{\mathrm{r}}^{0} = 30$ (the measured radiative enhancement factor). Our results indicate that significant oxidation must be introduced in the numerical calculations in order to reproduce the experimental results.

Figure 5.3(b) renders the spectrally averaged radiative enhancement factor

$$\langle \gamma_{\mathrm{r}}/\gamma_{\mathrm{r}}^{0} \rangle = \frac{1}{\Delta\lambda} \int_{\Delta\lambda} \gamma_{\mathrm{r}}/\gamma_{\mathrm{r}}^{0} d\lambda, \tag{5.6}$$

which accounts for the spectral emission range of the fluorophore employed. The scarce variation of γ_{r}^{0} over the spectral window provides the equivalence of Eq. (5.6) with $\langle \gamma_{\mathrm{r}} \rangle / \langle \gamma_{\mathrm{r}}^{0} \rangle$. We find that a 10 nm oxide layer ($R_{\mathrm{Ag}} = 30\,\mathrm{nm}$) leads to values for this averaged magnitude, which are in agreement with experiments for both monomers (5.4) and dimers (30.2). The inset shows the system geometry and fluorophore orientations, parallel (blue) and normal (red) to the dimer axis. Figure 5.3(c) plots the two contributions to the total decay rate for a non-oxidized (solid lines) and an oxidized (dashed lines) dimer. The latter presents a 10-nm-thick oxide layer, the configuration closer to the experimental results in Figure 5.3(a) and (b). We can observe that the parallel contribution completely governs the spectra, although the contribution due to normal orientation increases slightly in the oxidized case.

Finally, Fig. 5.3(d) shows the little dependence of $\gamma_{\mathrm{r}}/\gamma_{\mathrm{r}}^{0}$ on the fluorophore position within the bulk of the DNA origami. The radiative decay rate evaluated at three different positions (green, blue, and red lines) was displaced 2 nm from the origami center (black line) overlap. We have also calculated the corresponding non-radiative decay rates, which vary more significantly in space. These spectra show a narrow peak at shorter wavelengths ($\lambda \sim 490\,\mathrm{nm}$) compared with the radiative ones. This is caused by the excitation of a higher order, quadrupole-like, dark plasmonic resonance in the dimer. We can observe that the non-radiative decay channel becomes faster as the fluorophore approaches one of the metal nanoparticles, as expected from previous theoretical reports on emitter-plasmon strong coupling in dimer geometries [96].

To conclude this section, we have presented our work on giving theoretical support to experiments based on measuring the radiative Purcell effect mediated by plasmon-emitter coupling. Experimental results demonstrated the enhancement of photostability in fluorophores through the plasmon-assisted modification of radiative decay rates, in agreement with our numerical results. Our calculations also made possible to discern the relevant effects of the oxidation of plasmonic resonators in aqueous environments, determining the upper limit of the Purcell enhancement.

5.4. Plasmon-assisted energy transfer

When two or more fluorophores are brought together, interactions among then can occur, leading to new channels of deactivation. Energy transfer occurs when excitations jump from one molecule to another during the lifetime of the excited state. There are different mechanisms that control such hopping. From the electromagnetic point of view, the interaction between quantum emitters can be treated within a Coulombic scheme, assuming that the interaction occurs in a regime where their inner structure remains unchanged and excluding processes as electron transfer [55]. The multipolar expansion leads to the dipole-dipole interaction, that accounts for the Förster resonance energy transfer (FRET). This is a non-radiative process that dominate over short distances.

FRET is a typical near-field process, with large spatial decay, between a pair of dipolar molecular transitions. The energy transfer rate, γ_{FRET}, from the donor to the acceptor is given by [55]

$$\gamma_{\text{FRET}} \propto \frac{1}{\tau_{\text{D}}}\left(\frac{R_0}{R}\right)^6, \tag{5.7}$$

where R and τ_{D} are the donor-acceptor distance and the donor lifetime in free space, respectively. R_0 is known as the Förster distance, defined as the distance at which the efficiency, η_{FRET} is about 1/2 [198]. This quantity is defined as

$$\eta_{\text{FRET}} = \frac{\gamma_{\text{FRET}}}{\gamma_{\text{FRET}} + \gamma_{\text{D}}^0} \tag{5.8}$$

with $\gamma_{\text{D}}^0 = \gamma_{D,\text{r}} + \gamma_{D,\text{nr}}$ given by the radiative and non-radiative contributions to the decay rate. In the donor perspective, its total decay rate is effectively modified by the presence of the acceptor, $\gamma_{\text{D}} = \gamma_{\text{D}}^0 + \gamma_{\text{FRET}}$. This increase is directly linked to non-radiative channels, due to the radiationless character of FRET.

The Förster distance, R_0, encodes the dependence of energy transfer on donor-acceptor spectral and spatial configuration [55]

$$R_0^6 \propto [\hat{\mathbf{n}}_{\text{A}}\hat{\mathbf{n}}_{\text{D}} - 2(\hat{\mathbf{n}}_{\text{r}}\hat{\mathbf{n}}_{\text{D}})(\hat{\mathbf{n}}_{\text{r}}\hat{\mathbf{n}}_{\text{A}})]^2 \int f_{\text{A}}(\omega) f_{\text{D}}(\omega) d\omega, \tag{5.9}$$

where $\hat{\mathbf{n}}_{\mathrm{A}}$,$\hat{\mathbf{n}}_{\mathrm{D}}$ and $\hat{\mathbf{n}}_{\mathrm{r}}$ are the unit vectors for the acceptor orientation, donor orientation and relative position from donor to acceptor. The first term in brackets in Eq. (5.9) accounts for the orientation of the dipolar emitters whereas the integral over frequencies sets the spectral overlap of the acceptor absorption and donor emission.

In the previous section, we showed how plasmonic resonances can affect the photophysical properties of fluorophores through the modification of their decay rates. In recent years, the possibility of manipulating photophysical interactions between molecules, which lead to energy transfer, has attracted much attention due to the implications that FRET phenomenology has in biophysical and light-harvesting processes [234–236]. The effects of the near-field of plasmonic resonances onto the energy transfer phenomena are still controversial [237]. Contradictory phenomena have been reported, ranging from FRET efficiency reduction [237, 238] to enhancement [239], together with different dependences on the FRET rate on the LDOS [237, 240]. From an experimental point of view, the lack of conclusive results can be attributed mainly to two factors. First, the technological challenge behind the positioning of a FRET pair in the near field of a resonator with nanometer precision. Second, the inherent difficulty of isolating the impact of plasmons on FRET efficiency and rate. Therefore, conclusive results can only be drawn if FRET is studied at the single nanoparticle-fluorophore pair level.

DNA scaffolding techniques have been extensively employed to self-assemble FRET pairs with nanometer precision [241]. Several works have exploited this approach to reveal how plasmonic resonances modify the FRET between diffusing donor–acceptor pairs in Refs. [242, 243]. These works were only able to account for the spatially averaged effect of the metallic structures on FRET because the donor–acceptor pair was allowed to freely diffuse across the plasmonic system. Indeed, the photophysics of single donor-acceptor pairs cannot be monitored to determine the FRET efficiency in terms of the donor-acceptor lifetime. In order to overcome those limitations, the group of Prof. Acuña at Université de Fribourg designed a DNA origami scaffolding to position both the metallic nanoparticle and the donor-acceptor pair to perform single-molecule fluorescence measurements. Figure 5.4 includes an sketch of the system, with a rectangular DNA origami structure with thickness 2.0 nm. The FRET pair consists of two molecules: donor (ATTO532) and acceptor (ATTO647N), attached to the DNA structure, with a distance of 3.4 nm between the fluorophores. On the other hand, a single metal Au nanoparticle is bound on the upper side of the DNA origami. Four different particles with diameter $D = 5$ nm to 20 nm (5 nm steps) were employed. The distance between the metal surface and the FRET pair is approximately 10 nm. These particles exhibit an extinction cross section with a resonance at $\lambda \approx 520$ nm that overlaps with the absorption and

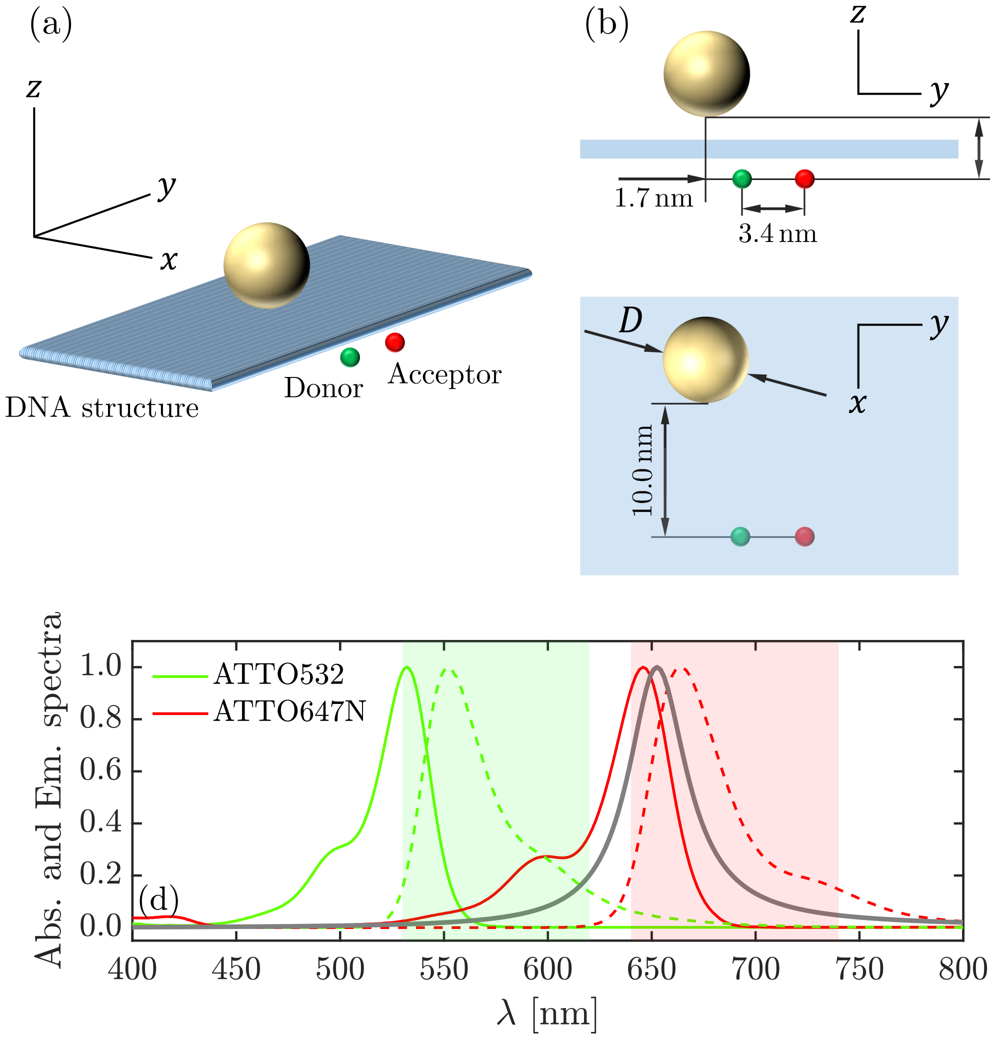

Figure 5.4: DNA origami structure for FRET characterization. (a) General view of the rectangular DNA structure, with the Au nanoparticle bound on the upper side. The FRET pair consists of ATTO532 (donor) and ATTO647N (acceptor) molecules, placed on the lower side of the DNA scaffolding. Panels (b) and (c) correspond to the front and top views of the structure, respectively, with the distances that separate the different components of the system. (d) Normalized emission (dashed) and absorption (solid) spectra for the FRET pair used. Grey solid line plots the Lorentzian spectra used to model the effective permittivity of the acceptor.

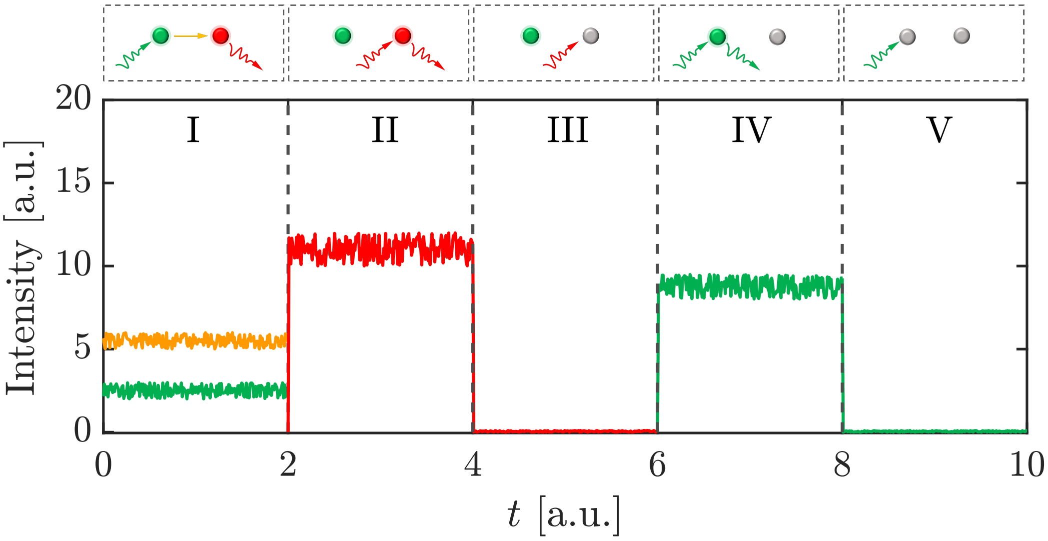

Figure 5.5: Example of a fluorescence transient obtained through laser alternation for single-molecule FRET determination using the *acceptor bleaching* approach. In I, only the green laser is on to monitor the intensities I_{DA} (green excitation–green detection) and I_{AD} (green excitation–red detection). In II and III, only the red laser is switched on to measure I_{A} (red excitation–red detection) until the acceptor bleaches (III). In IV and V, only the green laser is exciting to determine I_{D} until the donor bleaches (V).

emission spectral ranges of the donor (strongly) and acceptor (moderately) fluorophores. Experimental reports indicate that 10 nm is the distance where fluorescence quenching of molecules by metal particles is roughly 50% and therefore this is a very relevant and sensitive distance range, as FRET applications require far-field detection [244, 245]. Figure 5.4(d) renders the emission (dashed) and absorption (solid) spectra of the donor and acceptor molecules (green and red lines), showing the typical Stokes shift. In our simulations, the emission of the donor in the presence of the acceptor was performed modeling a semiclassical scheme for FRET with a Lorentzian profile (see grey line), as explained below.

For each FRET pair, fluorescence transients were recorded in different steps, (see Roman numerals in Fig. 5.5), allowing to extract the intensities and the fluorescence lifetimes, alternating donor and acceptor excitation. In I, donor and acceptor intensity profiles were extracted upon donor excitation at 532 nm, I_{DA} and I_{AD}, in green and orange, respectively. Afterwards, the sample was excited in the red spectral range (II) and the acceptor intensity, I_{A}, is obtained until photobleaching (III). Finally, the donor was excited again until bleaching (IV and V) and I_{D} was measured. Two donor lifetimes,

τ_{DA} and τ_{D}, with and without the presence of the acceptor, respectively, and the acceptor lifetime, τ_{A}, were obtained for both the no-nanoparticle case (reference) and the four considered particle sizes.

Our work consisted in complementing the experimental results on energy transfer. We performed numerical electromagnetic simulations modelling the experimental setup using COMSOL Multiphysics, in a similar way as we explained in the previous section. We used measured values for the geometric parameters as those in Figure 5.4. The refractive index of DNA origami was set to $n_{\mathrm{DNA}} = 2.1$ and the Au permittivity was taken from experimental data [246]. In order to account for the different bounding between the FRET pair and the metal nanoparticle to the rectangular DNA origami, the distances of the FRET pair to the origami were adjusted differently with respect to the used for the nanoparticle ones. We carried out two different sets of simulations. In the first one, we modeled the single molecule (donor or acceptor) as a point-dipole-like electromagnetic source. By averaging over three perpendicular orientations, we computed the total Purcell spectrum as

$$P_f^i = \frac{W_x^i + W_y^i + W_z^i}{3W^0}, \tag{5.10}$$

by means of the total power radiated by the source aligned with the three different directions, (W_x, W_y, W_z) and $\sum_j W_j^i = W^i$, calculated through the integration of the Poynting vector. The superindex i indicates the location of the dipolar source at the donor or acceptor position, with $i = \mathrm{D}, \mathrm{A}$, respectively. The term W^0 represents the total power radiated in vacuum. The procedure was repeated for the four cases with the different Au particles. The results can be seen in Figure 5.6(a) and (b), for the donor (D) and acceptor (A) cases, respectively. The different colors indicate the size of the nanoparticle, as indicated in the legend, from cyan to violet as D increases. Performing the spectral average within the dye emission window, marked in green and red following the widths of the spectra as plotted in Fig. 5.4(d), the normalized lifetime τ_i/τ_i^0 reads

$$\frac{\tau_i}{\tau_i^0} = \frac{1}{\varphi_i P_f^i + (1 - \varphi_i)}, \tag{5.11}$$

including the intrinsic quantum yield of each fluorophore $\varphi_{\mathrm{D}} = 0.8$ and $\varphi_{\mathrm{A}} = 0.6$. The lifetime τ_i^0 is the one in the absence of the Au nanoparticle.

In order to account for the donor-acceptor interaction, we designed a second set of numerical calculations. We modeled again the donor as a point-dipole source but the acceptor as an absorbing dielectric sphere. In the same way as in chapter 3, its permittivity was set to reproduce a two-level system polarizability,

$$\alpha_{\mathrm{A}}(\omega) = \frac{\mu_{\mathrm{A}}^2/\hbar}{(\omega_{\mathrm{A}} - i\gamma_{\mathrm{A}}^{\alpha}/2) - \omega}, \tag{5.12}$$

which results in an effective permittivity, similar to models proposed in the context of plasmon-assisted exciton transport [155]

$$\epsilon_{\mathrm{eff}}(\omega) = \frac{1 + 2\eta_{3\mathrm{D}}(\omega)}{1 - \eta_{3\mathrm{D}}(\omega)} \tag{5.13}$$

where $\eta_{3\mathrm{D}}(\omega) = \frac{\alpha_{\mathrm{A}}(\omega)}{4\pi\epsilon_0 a^3}$. The radius of the distorting QE is made small enough to reach convergence in the Purcell factor spectrum and was finally set to 0.25 nm. The parameters of the acceptor were chosen in accordance with experiments: $\mu_{\mathrm{A}} = 0.3\,\mathrm{e{\cdot}nm}$, $\hbar\omega_{\mathrm{A}} = 1.9\,\mathrm{eV}$ and $\hbar\gamma_A^{\alpha} = 0.1\,\mathrm{eV}$. Our Lorentzian model (see Fig. 5.4(d), grey solid line) for the acceptor spectra is approximated to lie between its emission and absorption spectra. We anticipate that this choice yielded a very good agreement with the experimental results. We calculated the Purcell factor in the fashion of Eq. (5.10) as

$$P_f^{\mathrm{DA}} = \frac{W_x^{\mathrm{DA}} + W_y^{\mathrm{DA}} + W_z^{\mathrm{DA}}}{W_x^{0,\mathrm{A}} + W_y^{0,\mathrm{A}} + W_z^{0,\mathrm{A}}} = \frac{W^{\mathrm{DA}}}{W^{0,\mathrm{A}}}, \tag{5.14}$$

where the numerator terms are calculated for a point-like dipolar source representing the donor in the presence of both the Au nanoparticle and the acceptor, whereas the denominator $W_{0,\mathrm{A}}$ is obtained when considering only the FRET pair. The results are shown in Fig. 5.6(c), where the presence of the acceptor clearly causes a reduction of the values of the averaged Purcell factor with respect to P_f^{D} (see Fig. 5.6(a)).

The intensity profiles obtained in the time-fluorescent measurements allow the determination of the FRET efficiency, η_{FRET}, which reads

$$\eta_{\mathrm{FRET}} = 1 - \frac{I_{\mathrm{DA}}}{I_{\mathrm{D}}} \tag{5.15}$$

where I_{D} and I_{DA} are the fluorescence intensities of the donor fluorophore in the absence and presence of the acceptor respectively, plotted in Fig. 5.5 in green and orange. This result assumes that there is not direct excitation of the acceptor by the external light [247]. Furthermore, far from saturation, the intensities are proportional to the molecular quantum yields [247], which read

$$I_{\mathrm{DA}} \propto \frac{\gamma_{\mathrm{D,r}}}{\gamma_{\mathrm{D,r}} + \gamma_{\mathrm{D,nr}} + \gamma_{\mathrm{FRET}}} \tag{5.16}$$

$$I_{\mathrm{D}} \propto \frac{\gamma_{\mathrm{D,r}}}{\gamma_{\mathrm{D,r}} + \gamma_{\mathrm{D,nr}}} \tag{5.17}$$

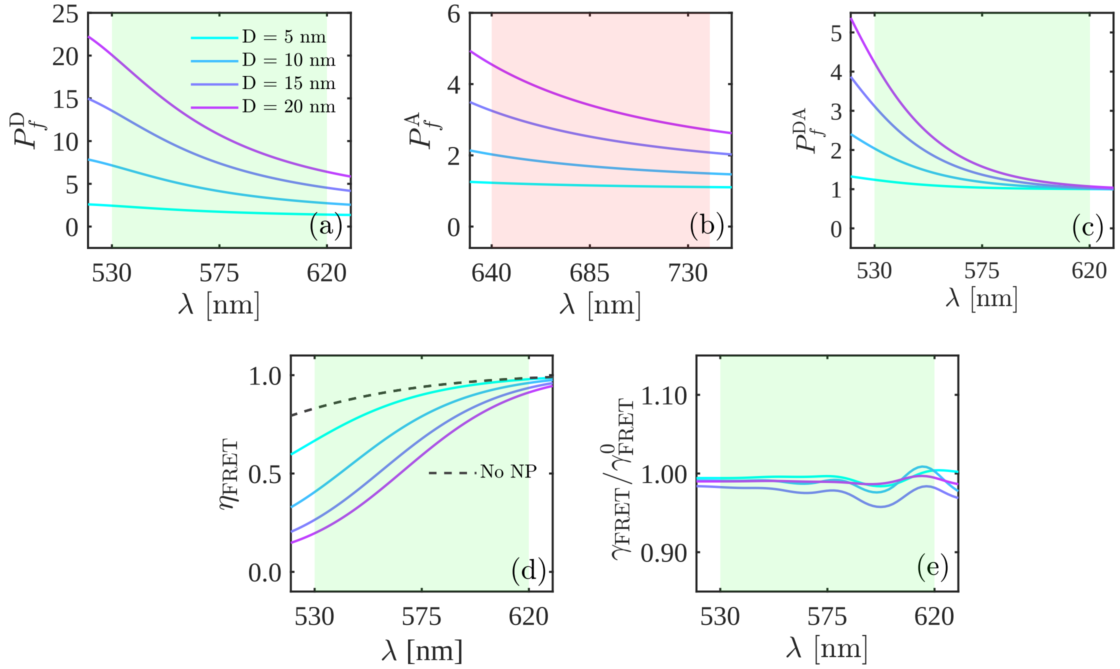

Figure 5.6: Numerical calculations for plasmon assisted FRET. Purcell factor spectra for the (a) donor (D), (b) acceptor (A) and (c) donor in presence of the acceptor (DA). Cyan-to-violet lines represent the spectra for increasing size or the Au nanoparticle. Green and red transparent patches mark the emission window for the donor and acceptor, respectively, as shown in Fig. 5.4. (d) FRET efficiency as a function of the wavelength for different Au nanoparticle sizes. The dashed black line plots the case without nanoparticle. (e) FRET rate spectra, normalized to the no nanoparticle case, $\gamma_{\mathrm{FRET}}/\gamma^0_{\mathrm{FRET}}$, for different nanoparticle sizes.

.

yielding the definition of the FRET efficiency in terms of the lifetimes as

$$\eta_{\mathrm{FRET}} = 1 - \frac{\tau_{\mathrm{DA}}}{\tau_{\mathrm{D}}} = 1 - \frac{\gamma_{\mathrm{D}}}{\gamma_{\mathrm{DA}}} \tag{5.18}$$

where we have used $\tau_i = \left(\sum_i \gamma_i\right)^{-1}$. The last term of Eq. (5.18) allows us the computation of η_{FRET} in terms of the powers, $\gamma_{\mathrm{D}}/\gamma_{\mathrm{DA}} = W^{\mathrm{D}}/W^{\mathrm{DA}}$. This quantity is plotted in Fig. 5.6(d), where we indicate the spectral window of donor emission for averaging. Furthermore, we added η^0_{FRET}, calculated in the absence of nanoparticle (labeled as No NP).

From the definition of the total decay rate, the FRET rate γ_{FRET}, can be estimated from the donor's fluorescence experimental lifetimes in the presence and absence of the

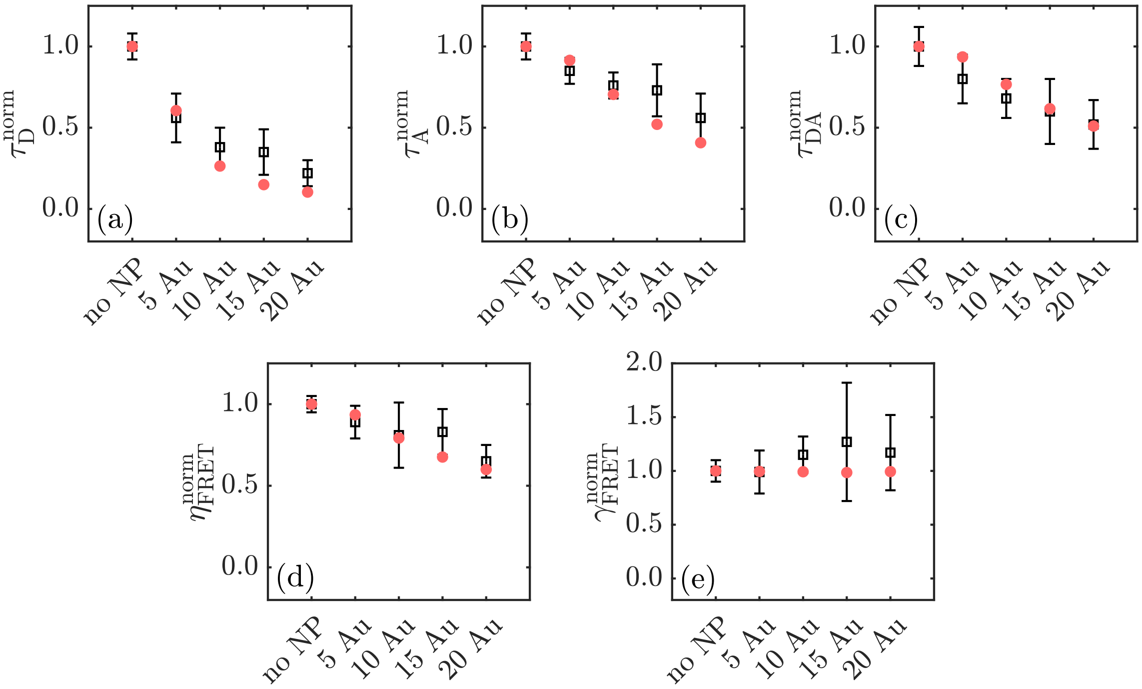

Figure 5.7: Plasmon assisted energy transfer. The averaged and normalized (to the absence of nanoparticle value) fluorescence lifetimes measurements and numerical calculations are rendered in panels (a) $\tau_{\mathrm{D}}^{\mathrm{norm}}$, (b) $\tau_{\mathrm{A}}^{\mathrm{norm}}$ and (c) $\tau_{\mathrm{DA}}^{\mathrm{norm}}$, with experimental data in hollow symbols with error bars. Panels (e) and (f) plot the experimental and numerical results for the FRET efficiency and the FRET rate, respectively.

acceptor as

$$\gamma_{\mathrm{FRET}} = \frac{1}{\tau_{\mathrm{DA}}} - \frac{1}{\tau_{\mathrm{D}}}. \tag{5.19}$$

From the theoretical point of view, we computed the FRET rate spectra through the electromagnetic power absorbed by the dielectric sphere in our model, writing $\gamma_{\mathrm{FRET}} \propto \int_{V_{\mathrm{A}}} |E|^2 dV$ inside the volume of the acceptor scatterer in our simulations [248]. The results of this approach are shown in Figure 5.6(e), normalized to the free space spectrum, γ_{FRET}^0, without significant changes among the different configurations.

The spectral averaging of the results in Figure 5.6 is shown in Figure 5.7. Panels (a), (b) and (c) render the normalized lifetimes to the reference (no NP). The results obtained through numerical calculations are plotted in red circles whereas values obtained from fluorescence measurements are represented in square markers with their corresponding error bars. Remarkably, both are in very good agreement, with theoretical predicitions lying within the experimental error bars in most cases. The plots reveal a 2× and 4×

total plasmon-mediated Purcell enhancement for the acceptor and donor molecules, respectively. The comparison between $\tau_{\mathrm{DA}}^{\mathrm{norm}}$ and $\tau_{\mathrm{D}}^{\mathrm{norm}}$ demonstrates that the presence of the acceptor disminishes the effect of the metal in the donor fluorescence characteristics. The strong modification of $\tau_{\mathrm{D}}^{\mathrm{norm}}$ with respect to $\tau_{\mathrm{A}}^{\mathrm{norm}}$ is mediated by donor's closer spectral character to the plasmonic resonance as the FRET pair distance to the nanoparticle is in practice the same.

Introducing the measured donor lifetimes into Equations (5.18) and (5.19), both γ_{FRET} and η_{FRET} were calculated from experimental results. For the normalized FRET rate, γ_{FRET}, the numerical results were obtained in the direct calculation through the spectral averaging of $\int_{V_{\mathrm{A}}} |E|^2 dV$ within the acceptor volume. Both numerical and experimental results indicate that the presence of the metal nanostructure does not have a significant impact on the FRET rate constant. We can also observe that Au nanoparticles decrease the FRET efficiency, being the reduction in η_{FRET} of 25% for the largest structure (20 nm diameter). Note that, following previous equations, η_{FRET} can be also written as

$$\eta_{\mathrm{FRET}} = \gamma_{\mathrm{FRET}} \tau_{\mathrm{DA}} \tag{5.20}$$

revealing that that the decrease in this quantity is a direct consequence of the reduction of the donor lifetime in the presence of the acceptor, mediated by the nanoparticle plasmons. Eq. (5.20) also clarifies why the FRET efficiency is not significantly modified by the metal nanoparticle, since it is governed by τ_{DA}, whose decay with size in Fig. 5.7(c) indicates its lower sensitivity to plasmon fields with respect to τ_{D} and τ_{A}.

5.5. Conclusions

In this chapter, we have described our theoretical support to two different experiments in the context of plasmon-emitter interactions. In particular, we have focused on plasmonic modification of fluorescence in nanophotonic structures built on a DNA origami scheme, that provides a fundamental and accurate control of positioning of both the emitters and the plasmonic resonators. In the first work, we have studied the Purcell effect of Ag dimers on the emission of single fluorophores, complementing experimental measurements on molecular photostability. Our numerical calculations on radiative and non-radiative components of the Purcell factor showed that dimer structures yielded an enhancement factor of 30, in agreement with the experimental results. Furthermore, our findings helped to determine that the oxidation of the nanoparticles had a relevant impact in the optical measurements. In a second study, we focused on the interaction between single Au nanoparticle and a fluorescent donor–acceptor pair, used to analyze the effect on the FRET induced by different nanoparticles of different size. The measurements allowed the determination of the plasmon-assisted FRET rate and efficiency based solely on the measurement of the donor's fluorescence lifetime in the presence/absence of the acceptor. We implemented two sets of numerical calculations for the calculation of the power radiated by point-like dipolar sources, representing the FRET pair. Moreover, a semiclassical model for FRET was devised, in terms of a Lorentzian model for acceptor absorption, to account for the lifetimes of the donor in the presence of the acceptor. Our theoretical findings, in agreement with experimental results, contradict previous works using colloidal particles and DNA, in which an enhancement of the FRET rate with the LDOS was reported. The single-molecule measurements and calculations presented here reveal that, despite the significant plasmon-assisted fluorescence lifetime reduction and quenching experienced by both donor and acceptor molecules, the Au particles have a minor effect on the FRET rate in the experimental samples.

6

General conclusions

6.1. English

This work consists of a compilation of the research activity carried out during four years focused on the EM phenomena at the nanoscale, with special interest in the study of light-matter interaction between excitons and plasmonic resonances. Chapters 2 and 3 present our approximation to the description of electromagnetic fields in terms of Transformation Optics, in a two-dimensional version, which allows for analytic/quasi-analytic descriptions of light-matter coupling, population dynamics of the excited state and scattering spectrum. We want to highlight that the principal objective of this part of our investigation was the analysis of the interaction between plasmonic fields and quadrupolar excitons, second order in the multipolar expansion of the light-matter Hamiltonian.

Moreover, successive opportunities gave us the chance to go in depth in different aspects of light-matter interaction. Firstly, in chronological order, our collaboration with the experimental group of Prof. Guillermo Acuña (Université de Fribourg) allowed us to address the study of the modification of the fluorescent emission by plasmonic resonances in DNA origami structures where the positioning of single emitters is attained with high precision. In this way, we tackled the theoretical study and analysis of radiative Purcell factors and plasmonic influence in energy transfer processes between a FRET pair in nanoplasmonic structures. We have presented these results in chapter 5.

Finally, in the last part of the doctorate, in collaboration with the group of Prof. Alejandro Manjavacas (University of New Mexico), we investigated the form of plasmonic resonances in periodic structures of metallic nanoparticles, presented in chapter 4.

Plasmon-exciton coupling

One of the essential points in this thesis has been to unveil the spatial and spectral form of the coupling between plasmonic modes and quantum emitters, in particular dipolar and quadrupolar active ones. For the sake of obtaining a complete description, a Transformation Optics approach based on conformal mapping permitted us to obtain the analytical solutions for the scattered electric fields, customary for the computation of Purcell factors. This magnitude quantifies the modification of the local density of states that mediates the radiative and non-radiative decay of a quantum emitter. By means of a modal expansion, we have shown that the density of states can be written as a sum of Lorentzian terms, where the modal coupling strengths appear explicitly. Once these were known, we have analyzed their dependences on the position and orientation of the emitter and determined the order of the plasmonic mode that gives maximum coupling. We have also investigated finite-size effects due to the non point-like character of the emitter.

Our theory allowed us to address the quantization of plasmonic fields and the study of both the population dynamics of the excited state and the scattering spectrum under coherent pumping. On the one hand, the results on the population dynamics allowed us to prove that the heuristic quantization made of our spectral density was correct, since the excited state population calculated by means of the Wigner-Weisskopf formalism and master equation (Hamiltonian) formalisms were exactly the same. On the other hand, the introduction of coherent pumping in the Hamiltonian description enabled us to investigate the far-field spectral properties of hybrid plasmon-exciton systems. Our results show the emergence of Rabi oscillations and Rabi splittings, typical of the strong coupling regime that can be reached in these cavities in the limit of a few or even single emitter [118]. Furthermore, the analysis of the population dynamics and the asymmetries in the scattering spectra took us to the conclusion that it is not always possible to describe the plasmonic environment in terms of a single mode at resonance with the emitter natural frequency. The presence of higher-order plasmonic resonances, and, overall, a pseudomode at high-frequencies, play a role even when they are highly detuned. We have shown that, despite the fact that our description makes use of a two-dimensional mapping of the cavity, our model reproduces the same phenomenology as the three-dimensional geometry. The difference between two- and three-dimensional systems stems from a frequency-dependent scale factor, which translates into the fact that we can renormalize our results through the magnitude of the transition moment that we use for our calculation in order to compare with experimental results. Our exhaustive study serves as a guidance for the design and interpretation of experiments aiming to harness plasmon-exciton strong-coupling at the single emitter level beyond the dipolar approximation.

With the analytical description of nanoparticle-on-mirror cavities under control, we have shown its application to configurations involving more than one excited state. In the first part of chapter 3 we have considered the modification of the density of states in the cavity for a dipolar emitter due to the presence of a second emitter of the same sort. In our approach, we exploit a scattering formalism in terms of the dyadic Green's function tensor and an effective polarizability that accounts for the distorting emitter, whose presence can enhance or suppress the local density of states even when both emitters are out of resonance. As we showed in chapter 2, Green's functions can be written in terms of a Lorentzian sum and the modified spectral density can be understood as a sum of three different contributions: linear and quadratic plasmonic ones, and another one accounting for the absorption by the distorting emitter. Our findings are in concordance with recent studies about the connection between spectral densities and Hamiltonian models [42], as well with reports of exotic photonic environments where quadratic contributions can appear [249, 250]. Our study also reveals that the plasmon mediated coupling between quantum emitters in nanocavities effectively gives rise to non-Lorentzian features in the density of states within the sub-wavelength regime that characterizes our system. Our work offers a new perspective on quantum emitter interactions at the nanoscale, especially in the context of exciton transfer phenomena, quantum optical metamaterials, as well as on picocavity design and engineering, where sub-nanometer features alter greatly the local density of states.

In the second part of chapter 3, we have investigated the presence of a three-level emitter, with a dipolar and a quadrupolar excited states, without internal coupling between different excitons to study the dynamics of the dipolar excited state and the far-field scattering spectrum. The analysis of the phenomenology associated to the plasmonic coupling of the quadrupole exciton, weighted by its transition quadrupole moment, permitted us to find configurations where the emitter decay can be faster or slower that the experienced by the dipolar excited state isolated. We have also found the emergence of Rabi oscillations related to the strong coupling regime between the quadrupolar excitonic component and the plasmonic modes of the system. The shape of the scattering spectra sheds light on the hybrid nature of the eigenstates of the system (plasmon-exciton polaritons). Our findings reveal excitonic degrees of freedom that can be present in the light-matter interaction, beyond the dipolar approximation and usually hidden to propagating fields. Our work presents that the extreme field confinement reveals opportunities to access light-forbidden states, mediating the interplay between different type of excitonic states, bringing together different time scales, yet to be uncovered in polaritonic and optical applications.

Lattice resonances

In addition to our work in the plasmon-exciton interaction in the near field, in chapter 4 we have presented a detailed analysis of plasmonic resonances in periodic arrays of nanoparticles, in collaboration with the group of Prof. Manjavacas. In particular, our results were focused on the study of lattice resonances in bipartite arrays. In the same vein as recent studies, plasmonic resonances of these type of systems can be understood as the result of the hybridization of plasmonic modes of simpler constituents, as the modes of plasmonic cavities in the sub-wavelength regime. We have found that these structures can support the existence of two resonances under plane-wave illumination and, under certain conditions, it is only possible to excite one of them. Each of these resonances shows a totally different character, that we can describe as super- and subradiant in terms of the analysis of both the dipolar momenta induced in the particles and the radiative losses of the array. Our results show that the size of the particles can have a negligible/critical impact depending on whether the resonance is super- or subradiant, respectively. Moreover, we have demonstrated that the quality factor of subradiant resonances in these systems is larger than in single-particle arrays of the same size. Our findings are of interest for the investigation of lattice resonances in metallic nanostructures, since we focus on their design and tailoring through the lattice geometry, complementing other studies where the quality factor is enhanced through the particle characteristics. We highlight the applicability of these type of resonances in the spectroscopy and sensing fields, where minimal changes can drastically modify the response of the system. In this line, lattice resonances in bipartite arrays present a remarkable robustness against finite-size effects, acquiring a relevant advantage over other periodic systems. We also highlight their near-field characteristics, where lattice resonances show remarkable field enhancements and spatial extensions much larger than those of the localized surface plasmons.

Purcell Factor and plasmonic effects in energy transfer

Finally, in chapter 5, we have presented our work in collaboration with the group of Prof. Acuña, complementing with our theoretical investigations their experimental findings on single molecule flourescence next to metallic nanostructures bound by means of DNA origami techniques, described in the initial part of the chapter. Our theoretical analysis of the radiative Purcell factor allowed the interpretation of the experimental results, and revealed the impact of oxidation in the optical properties of plasmonic dimers in aqueous environments. Particularly, we have shown that it can greatly diminish light-matter coupling strength in these systems. Our work also confirmed that plasmonic resonances can improve the photostability of fluorophores through the Purcell effect, demonstrating that the light-matter coupling can increase the total number of photons emitted by a molecule before losing its fluorescence capabilities due to permanent changes in its structure (photobleaching). Additionally, our collaborators designed *ad hoc* a structure to quantify the effects of the plasmon-emitter interaction in a FRET pair. Our theoretical study was focused on understanding how the presence of a metallic nanoparticle can modify the emission of both acceptor and donor, and, in terms of an effective model for the acceptor, how the donor emission changes in the presence of the acceptor. We calculated the total Purcell factors, the efficiency of the energy transfer and the decay rate associated to the mechanism of non-radiative energy transfer between donor and acceptor. In contrast with other works that reported an enhancement of the energy transfer rate proportional to the density of states, our theoretical and experimental results determine that, in the limit of a single FRET pair in the regime of moderate quenching, the effect of plasmon-exciton coupling in the energy transfer process is negligible. On the contrary, the FRET efficiency decreases as the plasmon-emitter strength increases, due to the enhancement of decay rates associated to the plasmonic interaction.

6.2. Castellano

Este trabajo contiene la compilación de nuestra actividad investigadora llevada a cabo durante cuatro años en torno a la fenomenología electromagnética en la nanoescala, con especial énfasis en el estudio de la interacción luz-materia entre excitones y plasmones. Los capítulos 2 y 3 contienen nuestra aproximación a las soluciones de los campos electromagnéticos a través del método de Óptica de transformación, en una versión dos-dimensional, que permite una descripción analítica del acoplamiento luz-materia y cuasi-analítica de las dinámicas de población del estado excitado y del espectro de dispersión. Hemos de destacar que el principal objetivo de esta parte de nuestra investigación fue el estudio de la interacción de los campos plasmónicos con los excitones cuadrupolares, segundo orden de la expansión multipolar del hamiltoniano de interacción luz-materia.

Además de esta rama principal de investigación, sucesivas circunstancias nos dieron la oportunidad de profundizar en otros aspectos de la interacción luz-materia. En primer lugar y de forma cronológica, la colaboración con el grupo experimental del Prof. Guillermo Acuña nos permitió abordar el estudio teórico la influencia de las resonancias plasmónicas en la emisión de fluorescencia en el límite de una sola molécula. Concretamente, abordamos el estudio y análisis teórico del factor de Purcell radiativo y de la influencia de los campos plasmónicos en la transferencia de energía en nanoestructuras plasmónicas, diseñadas y construidas por medio de las técnicas de origamis de ADN, tal y como hemos presentado en el capítulo 5.

Finalmente, en la última parte de la tesis, en colaboración con el grupo del Prof. Alejandro Manjavacas, se desarrolló un estudio sobre la forma de resonancias plasmónicas en redes periódicas de resonadores plasmónicos, cuyos resultados han sido presentados en el capítulo 4.

Acoplamiento entre plasmones y excitones

Uno de los puntos esenciales de esta tesis ha sido desgranar la forma espacial y espectral del acoplamiento entre modos plasmónicos y emisores cuánticos, en particular, de tipo dipolar y cuadrupolar. En aras de obtener una descripción completa de esta, los métodos de mapeo conforme asociados a la óptica de transformación nos ha permitido abordar las soluciones analíticas de los campos electromagnéticos escatereados necesarias para la obtención del factor de Purcell, que mide la modificación de la densidad de estados fotónicos a los que la excitación material puede decaer, y por tanto, la densidad de estados del sistema. A través de una expansión modal, hemos mostrado como la densidad de estados se puede escribir como suma de términos lorentzianos, donde el acoplamiento aparece explícitamente. Una vez obtenidas las expresiones de los acoplamientos, hemos analizado sus dependencias en la posición y orientación del emisor, así como el orden del modo plasmónico que da un acoplamiento mayor y hemos hecho a aproximación a la comprensión de los posibles efectos derivados del carácter no puntual de los emisores. Nuestra teoría nos ha permitido abordar el estudio de la dinámica del excitón y del espectro del sistema bajo iluminación coherente. Del primer estudio extraemos que la cuantización heurística hecha de nuestra densidad espectral es correcta, dado que la dinámica del estado excitado calculada por medio de la densidad espectral y el formalismo del Wigner-Weisskopf sin aproximación Markoviana es igual que la obtenida a través de una master equation con el Hamiltoniano efectivo obtenido. Nuestros resultados de las dinámicas de las poblaciones y de la forma de los espectros muestran tanto la aparición de oscilaciones de Rabi como de Rabi splittings, huellas del régimen de acoplamiento fuerte que se puede dar en estas cavidades en el límite de uno o pocos emisores. Asimismo, las dinámicas de las poblaciones de los modos plasmónicos y la asimetría de los espectros nos llevan a concluir que no es posible describir de forma general este tipo de cavidades plasmónicas en términos de un único modo, ya que la presencia de los modos intermedios y, sobre todo, de un pseudomodo efectivo a altas frecuencias juegan un papel incluso fuera de resonancia. Hemos de puntualizar que aún cuando nuestra descripción hace uso de un mapeado dos-dimensional de la cavidad, hemos mostrado resultados de cómo nuestro modelo reproduce la misma fenomenología que el caso tridimensional. La diferencia entre ambos resultados estriba en un factor de escala dependiente de la frecuencia, lo que se traduce que nuestros resultados renormalizado a la magnitud del dipolo de transición que usamos para nuestro cálculo para una completa comparación con los resultados experimentales. Finalmente, consideramos que nuestros hallazgos pueden servir como guía en el diseño e interpretación de experimentos enfocados en la exploración del régimen de acoplamiento fuerte entre plasmones y excitones, en el límite de un solo emisor más allá de la aproximación dipolar.

Con la descripción analítica del acoplamiento bajo control, hemos explicado su aplicación a sistemas más complejos con presencia de más de un estado excitado. En la primera parte del capítulo 3 hemos considerado la modificación de la densidad de estados de la cavidad plasmónica para un emisor dipolar por parte de un segundo emisor de la misma especie. Hacemos nuestro estudio a través de un formalismo de scattering en términos de la funcion de Green diádica en el que el segundo emisor entra a través de una polarizabilidad efectiva. Nuestros resultados muestran que la presencia de este segundo emisor puede aumentar o disminuir la densidad de estados incluso con los emisores fuera de resonancia mutua. Como hicimos en el capítulo 2, las funciones de Green pueden descomponerse como una suma de Lorentzianas y la densidad espectral modificada se puede entender en términos de tres contribuciones, plasmónica lineal, plasmónica cuadrática y absorción del emisor. Estos resultados están de acuerdo con resultados muy recientes sobre las conexiones entre la densidad espectral y el formalismo Hamiltoniano. Nuestro estudio muestra que el acoplamiento entre emisores, mediado por los plasmones, da lugar a fenomenología no-Lorentziana en la densidad de estados, incluso en el régimen de campo cercano, en distancias mucho menores que la longitud de onda, que nos ocupa. Creemos que este trabajo ofrece una perspectiva nueva en las interacciones luz-materia en la nanoescala y enfatizamos su relevancia especialmente en el contexto de transferencia de energía, metamateriales cuánticos y el diseño de picocavidades, donde variaciones sub-nanométricas pueden modificar drásticamente la densidad de estados.

En la segunda parte del capítulo 3 hemos abordado a partir de nuestros hallazgos en el capítulo 1, la presencia de excitones cuadrupolares en la cavidad plasmónica, en este caso dentro de un emisor cuántico de tres niveles, sin acoplamiento directo interno entre niveles excitados. A través de la descripción hamiltoniana en términos del acoplamiento estudiamos la dinámica del decaimiento del excitón dipolar y el especrtro de dispersión en el campo lejano. El estudio de la fenomenología en términos del acoplamiento plasmón-exciton cuadrupolar, mediado por el transition cuadrupole moment, nos ha permitido encontrar configuraciones donde el decaimiento puede ser más rápido o más lento que el del excitón dipolar en solitario, con emergencia de oscilaciones de Rabi relacionadas con el acoplamiento fuerte entre el excitón cuadrupolar y los modos plasmónicos del sistema. La forma del espectro ayuda a entender esta fenomenología gracias a la naturaleza híbrida de los modos (polaritones plasmón-excitón) del sistema. Remarcamos que tanto estos como los resultados referidos a cuadrupolos del capítulo 1 constituyen un acercamiento teórico al acceso de grados internos de libertad más complejos que los referidos a la aproximación dipolar, a través de los plasmones, y normalmente velados a la interacción con los campos en espacio libre. Nuestro trabajo presenta que el confinamiento plasmónico se presenta no solo como una oportunidad para acceder a estados light-forbidden, sino como un medio para explorar el interplay entre estados excitados de distinto carácter, haciendo solapar sus escalas temporales de desexcitación, aún por desvelar en aplicaciones polaritónicas y óptico-cuánticas.

Resonancias plasmónicas de red

Además de nuestro trabajo en la interacción plasmón-excitón en regímenes de campo cercano, en el capítulo 4 hemos presentado un análisis detallado de las resonancias plasmónicas que pueden aparecer en sistemas extendidos, en colaboración con el grupo del Prof. Manjavacas. En particular, nuestros resultados principales se centran en el estudio de resonancias de red de estructuras periódicas donde la celda unidad del sistema está constituida por dos partículas. En la línea de estudios recientes, las resonancias plasmónicas de este tipo de sistemas extendidos pueden entenderse como resultado de la hibridación de los modos plasmónicos de los constituyentes del sistema, al igual que los modos de cavidades mucho más pequeñas que la longitud de onda. Hemos encontrado que este tipo de estructuras bipartitas pueden soportar la existencia en general de dos resonancias bajo iluminación de campo lejano y que, bajo ciertas condiciones, solo es posible excitar uno de los modos. Cada una de estas resonancias muestra un carácter totalmente distinto, que podemos calificar de superradiante y subradiante a partir del análisis de los dipolos inducidos en el sistema y de las pérdidas radiativas. Nuestros resultados muestran que el tamaño de las partículas puede tener un impacto despreciable o crítico en función de si la resonancia es de carácter superradiante o subradiante, respectivamente. Asismismo, hemos demostrado que el factor de calidad de las resonancias subradiantes de este sistema es mayor que el de estructuras similares basadas en una única partícula. Consideramos que nuestros resultados pueden ser de interés para el estudio resonancias de red en nanoestructuras metálicas, donde aportamos un análisis sobre el diseño de las resonancias a partir de la propia estructura de la red, complementando los estudios donde el factor de calidad puede mejorarse a través de las características de las propias partículas. Destacamos la aplicabilidad es este tipo de resonancias en los campos de espectroscopía y fotodetección, donde cambios mínimos pueden modificar de forma drástica la respuesta del sistema y donde las resonancias de red han sido profusamente utilizadas. En esta línea, este tipo de resonancias también se revelan como más resistentes a efectos de tamaño finito del sistema, generando una ventaja frente a sistemas periódicos que necesitan de un gran número de elementos. Finalmente, apuntamos a su posible impacto en el régimen de campo cercano, donde presentan mejoras de campo notables y al mismo tiempo extensiones espaciales mucho mayores a las de las resonancias plasmónicas localizadas.

Factor de Purcell radiativo y efectos plasmónicos en transferencia de energía

En el capítulo 5 hemos presentado nuestro trabajo en colaboración con el grupo del Prof. Acuña, complementando con nuestro análisis teórico sus resultados experimentales en sistemas en el límite de una sola molécula diseñados por medio de técnicas de origamis de ADN, descritas en la primera parte del capítulo 5. En cuanto a nuestros resultados, nuestro estudio de la componente del Purcell radiativo sirvió tanto como confirmar los resultados experimentales como para determinar la importancia que la oxidación del material puede tener en la eficiencia del acoplamiento, que logramos cuantificar y que para este sistema reduce notablemente el acoplamiento plasmón-excitón. Nuestro trabajo se enmarca en el estudio sobre la modificación de la fotoestabilidad de fluoróforos a través del efecto Purcell, demostrando que el acoplamiento luz-materia puede incrementar el número total de fotones emitidos por una molécula antes de perder su capacidad de emisión debido a cambios permanentes en su estructura (photobleaching). Por otro lado, nuestros colaboradores diseñaron ad hoc un sistema para medir los efectos de la interacción entre plasmones y un par aceptor-donor para el estudio de transferencia de energía no radiativa. Nuestro estudio teórico se basó en analizar cómo la presencia de la nanopartícula cambia la emisión, tanto del aceptor como del donor, y, en términos de un modelo efectivo para el donor, cómo cambia la emisión del aceptor en presencia del donor, permitiéndonos calcular los factores de Purcell radiativos, la eficiencia de la transferencia de energía y la tasa de decaimiento asociada al mecanismo de transferencia no radiativa. Al contrario que otros trabajos que reportaron mejora de la tasa de trasnferencia proporcional a la densidad de estados, nuestros resultados teóricos confirman las medidas experimentales, que determinan, en el límite de una sola molécula, el efecto despreciable que tiene el acoplamiento plasmón-excitón en la transferencia de energía en este sistema. Al contrario, la eficiencia FRET disminuye con el tamaño de las partículas consideradas debido al aumento de las tasas de decaimiento asociadas al acoplamiento plasmón-excitón.

A

Details of the Transformation Optics derivations

In this appendix A, we provide several proofs and derivations used throughout chapters 2 and 3 in our study of light-allowed and light-forbidden transitions in a NPoM cavity by means of conformal mapping approaches. We will start with the preservation of the source character under conformal mapping, that allows us to write the transformed potential as a superposition of potentials. Then, we will give details about the calculations of the scattered potentials in chapter 2.

Transformation Optics: preservation of the source character under conformal mapping

We start considering the form of the potential of a single point charge in a two-dimensional space, which reads

$$\phi^q(x,z) = \frac{-q}{2\pi\epsilon_0}\log(\sqrt{(x-x_q)^2+(z-z_q)^2}). \tag{A.1}$$

Let us introduce the complex notation for the potential just writing the positions in the (x,z) plane as complex numbers, $\varrho = x + iz$

$$\tilde{\phi}^q(\varrho,\varrho_q) = \frac{-q}{2\pi\epsilon_0}\log(\varrho-\varrho_q). \tag{A.2}$$

In order to simulate a dipolar source, we write the potential made of a distribution of two charges with different sign $\pm q$, placed at positions $\varrho_\pm$ respectively. This potential reads

$$\tilde{\phi}^\mu(\varrho,\varrho_+,\varrho_-) = \frac{-q}{2\pi\epsilon_0}\log\left(\frac{\varrho-\varrho_+}{\varrho-\varrho_-}\right) \tag{A.3}$$

which, after imposing the condition $\varrho'_- = \varrho'_+ + \epsilon'$, and applying a Taylor expansion of the logarithm for $\epsilon' \ll \varrho'_\pm$, can be written as

$$\tilde{\phi}^\mu(\varrho, \varrho_+, \varrho_-) = \frac{-q}{2\pi\epsilon_0}\frac{\epsilon'}{\varrho - \varrho_+} \tag{A.4}$$

with the typical inverse dependence on distance. At this point, we proceed to study the form of a similar potential in a transformed frame, which would be defined by the function $(\varrho' - \varrho'_0)^{-1}$, and we apply the conformal mapping from the transformed to the original frame

$$\frac{1}{\varrho' - \varrho'_0} = \frac{1}{\log\left(\frac{ig}{\varrho - is} + 1\right) - \log\left(\frac{ig}{\varrho_0 - is} + 1\right)} = \frac{1}{\log\left(\frac{i(g-s)+\varrho}{i(g-s)+\varrho_0}\frac{\varrho_0 - is}{\varrho - is}\right)}. \tag{A.5}$$

where we used $g = 2D\sqrt{\rho(1+\rho)}$, $s = \delta + D\sqrt{\rho}/(\sqrt{1+\rho} + \sqrt{\rho})$ and $\rho = \delta/D$. In the region of interest, within the gap $\varrho_0 << g - s$, and we can expand the denominator as

$$\log\left(\frac{i(g-s)+\varrho}{i(g-s)+\varrho_0}\frac{\varrho_0 - is}{\varrho - is}\right) \simeq \frac{-ig}{s(g-s)}(\varrho - \varrho_0) \tag{A.6}$$

which results in

$$\frac{1}{\varrho' - \varrho'_0} = \frac{is(1 - s/g)}{\varrho - \varrho_0} \tag{A.7}$$

which demonstrates that, under certain conditions, the potential of a source in the original frame maps to the potential of an effective source (mediated by a geometric factor) with the same character in the transformed frame.

Interaction of a pure point-like dipolar source with a NPoM cavity

It is well known that the three-dimensional derivation of the multipolar expansion is done in terms of the scalar Helmholtz Green's function integration

$$\phi_{3\mathrm{D}}(x,y) = \frac{1}{4\pi\epsilon_0}\int \frac{\rho_q(\boldsymbol{r}')}{|\boldsymbol{r} - \boldsymbol{r}'|}d^3\boldsymbol{r}' = -\frac{1}{\epsilon_0}\int \rho_q(\boldsymbol{r}')G_{3\mathrm{D}}(\boldsymbol{r},\boldsymbol{r}')d^3\boldsymbol{r}' = \\ = -\frac{1}{\epsilon_0}\int \rho_q(\boldsymbol{r}')\frac{-1}{4\pi}\frac{1}{|\boldsymbol{r} - \boldsymbol{r}'|}d^3\boldsymbol{r}', \tag{A.8}$$

which in the two-dimensional case becomes

$$\phi_{2\mathrm{D}}(x,y) = -\frac{1}{\epsilon_0}\int \rho_q(\boldsymbol{r}')G_{2\mathrm{D}}(\boldsymbol{r},\boldsymbol{r}')d^2\boldsymbol{r}' = -\frac{1}{2\pi\epsilon_0}\int \rho_q(\boldsymbol{r}')\log(|\boldsymbol{r} - \boldsymbol{r}'|)d^2\boldsymbol{r}'. \tag{A.9}$$

The multipolar expansion arises just from the direct Taylor series expansion of the $G(r, r')$

$$\frac{1}{|\boldsymbol{r}-\boldsymbol{r}'|} \rightarrow f(\boldsymbol{r}+\boldsymbol{a}) = f(\boldsymbol{r}) + (\boldsymbol{a}\nabla) f(\boldsymbol{r}) + \frac{1}{2}(\boldsymbol{a}\nabla)^2 f(\boldsymbol{r})... \tag{A.10}$$

which reads

$$\log|\boldsymbol{r}-\boldsymbol{r}'| \approx \log(r) - (\boldsymbol{r}'\nabla)\log(r) + \frac{1}{2}(-\boldsymbol{r}'\nabla)^2\log(r) \tag{A.11}$$

and provides the first-order term in the expansion $\phi^{(1)}_{\text{2D}}(x, y)$:

$$\begin{aligned}\phi^{(1)}_{\text{2D}}(x,y) = \frac{-1}{2\pi\epsilon_0}\int \rho_q(\boldsymbol{r}')(-\boldsymbol{r}'\nabla)\log r\; d^2\boldsymbol{r}' = \\ = \frac{1}{2\pi\epsilon_0}\int \rho_q(\boldsymbol{r}')\boldsymbol{r}'\; d^2\boldsymbol{r}'\frac{\boldsymbol{r}}{r^2} = \frac{1}{2\pi\epsilon_0}\frac{\boldsymbol{\mu}\cdot\boldsymbol{r}}{r^2} = \phi^{\mu}(x,z)\end{aligned} \tag{A.12}$$

that represents the potential or a pure point-like dipolar source. Under the conformal transformation, the multivalued character of the mapping results in a periodic array of sources in the z'-direction in the transformed frame

$$\begin{aligned}\phi^{\mu}(x',z') = \frac{1}{2\pi\epsilon_0\epsilon_d}\sum_{n=-\infty}^{\infty}\frac{\mu'_x(x'-x'_{\text{E}}) + \mu'_z(z'-z'_n)}{(x'-x'_{\text{E}})^2 + (z'-z'_n)^2} = \\ = \frac{1}{2\pi\epsilon_0\epsilon_d}\sum_{n=-\infty}^{\infty}\frac{\mu'_x(x'-x'_{\text{E}}) + \mu'_z(z'-(z'_{\text{E}}+2n\pi))}{(x'-x'_{\text{E}})^2 + (z'-(z'_{\text{E}}+2n\pi))^2}\end{aligned} \tag{A.13}$$

The first step is to obtain the Fourier transform $\phi^{\mu}(k)$ from this potential:

$$\begin{aligned}\phi^{\mu}(k) = \int \phi^{\mu}(x',z')e^{-ikz'}dz' = \\ = \int_{-\infty}^{\infty}\frac{1}{2\pi\epsilon_0\epsilon_d}\sum_{n=-\infty}^{\infty}\frac{\mu'_x(x'-x'_{\text{E}}) + \mu'_z(z'-(z'_{\text{E}}+2n\pi))}{(x'-x'_{\text{E}})^2 + (z'-(z'_{\text{E}}+2n\pi))^2}e^{-ikz'}dz' = \\ = \frac{1}{2\epsilon_0\epsilon_d}\sum_{n=-\infty}^{\infty}\Big(\mu'_x\,\text{sign}(x'-x'_{\text{E}}) - i\mu'_z\,\text{sign}(k)\Big)e^{-|k||x'-x'_{\text{E}}|}e^{-ik(z'_{\text{E}}+2n\pi)},\end{aligned} \tag{A.14}$$

so we can write

$$\phi^{\mu}(k) = \begin{cases} a^{\mu}_{-}(k)e^{+|k|(x'-x'_{\text{E}})} \text{ if } x' < x'_{\text{E}} \\ a^{\mu}_{+}(k)e^{-|k|(x'-x'_{\text{E}})} \text{ if } x' > x'_{\text{E}} \end{cases} \tag{A.15}$$

with

$$a^{\mu}_{\pm}(k) = \frac{1}{2\epsilon_0\epsilon_d}\sum_{n=-\infty}^{\infty}\Big(\pm\mu'_x - i\mu'_z\text{sign}(k)\Big)e^{-ikz'_{\text{E}}}\delta(k-n) \tag{A.16}$$

where we have used the identity

$$\sum_{n=-\infty}^{\infty} e^{i2\pi kn} = \sum_{n=-\infty}^{\infty}\delta(k-n) \tag{A.17}$$

Now, we proceed to calculate the field induced by the metal plates under illumination, that is assumed to have the same functional form as the incident field. The dielectric-metal interfaces in the transformed frame are placed at $x' = 0$ and $x' = d$.

$$\phi^{\mu}(k) = \begin{cases} x' < 0 \rightarrow c_{-}e^{+|k|(x'-x'_{\mathrm{E}})} \\ x' \in [0,d] \rightarrow b_{-}e^{+|k|(x'-x'_{\mathrm{E}})} + b_{+}e^{-|k|(x'-x'_{\mathrm{E}})} \\ x' > d \rightarrow c_{+}e^{-|k|(x'-x'_{\mathrm{E}})} \end{cases} \tag{A.18}$$

and the corresponding coefficients are determined by the imposition of Boundary Conditions (BCs) for the fields $(E_{\|}, D_{\perp})$ at $x' = 0$ and $x' = d$, with the corresponding system of equations

$$\mathrm{BCs} = \begin{cases} c_{-}(k) = a^{\mu}_{-}(k) + b_{-}(k) + b_{+}(k)e^{2|k|x'_{\mathrm{E}}} \\ \frac{\epsilon_m}{\epsilon_d}c_{-}(k) = a^{\mu}_{-}(k) + b_{-}(k) - b_{+}(k)e^{2|k|x'_{\mathrm{E}}} \\ c_{+}(k) = a^{\mu}_{+}(k) + b_{+}(k) + b_{-}(k)e^{2|k|(d-x'_{\mathrm{E}})} \\ -\frac{\epsilon_m}{\epsilon_d}c_{+}(k) = -a^{\mu}_{+}(k) - b_{+}(k) + b_{-}(k)e^{2|k|(d-x'_{\mathrm{E}})} \end{cases} \tag{A.19}$$

and the coefficients that determine the scattered field inside the dielectric slab ($x' \in [0,d]$) are written as

$$b_{-}(k) = \frac{R-1}{R+1}\frac{1}{e^{2|k|d} - \left(\frac{R-1}{R+1}\right)^2}\left(a^{\mu}_{-}(k)\frac{R-1}{R+1} - a^{\mu}_{+}e^{2|k|x'_{\mathrm{E}}}\right) \tag{A.20}$$

$$b_{+}(k) = \frac{R-1}{R+1}\frac{1}{e^{2|k|d} - \left(\frac{R-1}{R+1}\right)^2}\left(a^{\mu}_{+}(k)\frac{R-1}{R+1} - a^{\mu}_{-}e^{2|k|(d-x'_{\mathrm{E}})}\right). \tag{A.21}$$

where we have used $R = \epsilon_m/\epsilon_d$. To obtain the expression of the scattered potential in the real space we just apply the inverse Fourier Transform

$$\begin{aligned} \phi^{\mu}(x',z')\;\forall\, x \in [0,d] &= \frac{1}{2\pi}\int \left(b_{-}e^{+|k|(x-x_0)} + b_{+}e^{-|k|(x-x_0)}\right)e^{ikz}dk = \\ &= \frac{1}{2\pi\epsilon_0\epsilon_d}\sum_{n=1}^{\infty}\frac{R-1}{e^{2nd}(R+1)^2 - (R-1)^2}\Big[(R-1)\mathrm{Re}\Big\{(\mu'_x + i\mu'_z)(e^{-n\Delta\varrho'} - e^{n\Delta\varrho'})\Big\} \\ &\quad + e^{nd}(R+1)\mathrm{Re}\Big\{(\mu'_x - i\mu'_z)(e^{-n\Delta\varrho'}e^{-2n(x'_{\mathrm{E}}-d/2)} - e^{n\Delta\varrho'}e^{2n(x'_{\mathrm{E}}-d/2)})\Big\}\Big] \end{aligned} \tag{A.22}$$

where we have used the notation

$$e^{\Delta\varrho'} = e^{\varrho'-\varrho'_{\mathrm{E}}} \text{ with } \varrho' = x' + iz', \varrho'_{\mathrm{E}} = x'_{\mathrm{E}} + iz'_{\mathrm{E}} \tag{A.23}$$

The preservation of the potential under the mapping provides that, after the inverse transformation, the scattered potential in the NPoM (diameter D and gap δ) system reads

$$\phi_{\mathrm{S}}^{\mu}(x,z) = \frac{1}{2\pi\epsilon_0\epsilon_d}\frac{\epsilon_m-\epsilon_d}{\epsilon_m+\epsilon_d}\sum_{n=1}^{\infty}\frac{1}{(\sqrt{\rho}+\sqrt{1+\rho})^{4n}-\left(\frac{\epsilon_m-\epsilon_d}{\epsilon_m+\epsilon_d}\right)^2}$$
$$\left[\frac{\epsilon_m-\epsilon_d}{\epsilon_m+\epsilon_d}\mathrm{Re}\Big\{(\mu'_x+i\mu'_z)\mathrm{A}_n^{-}(\varrho,\varrho_{\mathrm{E}})\Big\}+(\sqrt{\rho}+\sqrt{1+\rho})^{2n}\mathrm{Re}\Big\{(\mu'_x-i\mu'_z)\mathrm{B}_n^{-}(\varrho,\varrho_{\mathrm{E}})\Big\}\right] \tag{A.24}$$

where we have used

$$e^{\varrho'} = \frac{ig}{\varrho-is}+1 \tag{A.25}$$

in terms of the position in the original frame with the complex notation $\varrho = x+iz$. The transformation is defined through $g = 2D\sqrt{\rho(1+\rho)}$, $\rho = \delta/D$ and $s = \delta + D\sqrt{\rho}/(\sqrt{1+\rho}+\sqrt{\rho})$ and we have written

$$\mathrm{A}_n^{-}(\varrho,\varrho_{\mathrm{E}}) = \left[\left(\frac{ig+\varrho-is}{ig+\varrho_{\mathrm{E}}-is}\frac{\varrho_{\mathrm{E}}-is}{\varrho-is}\right)^{-n}-\left(\frac{ig+\varrho-is}{ig+\varrho_{\mathrm{E}}-is}\frac{\varrho_{\mathrm{E}}-is}{\varrho-is}\right)^{n}\right] \tag{A.26}$$

$$\mathrm{B}_n^{-}(\varrho,\varrho_{\mathrm{E}}) = \left[e^{-2n\Delta}\left(\frac{ig+\varrho-is}{ig+\varrho_{\mathrm{E}}-is}\frac{\varrho_{\mathrm{E}}-i\tilde{s}}{\varrho-is}\right)^{-n}-e^{2n\Delta}\left(\frac{ig+\varrho-is}{ig+\varrho_{\mathrm{E}}-is}\frac{\varrho_{\mathrm{E}}-is}{\varrho-is}\right)^{n}\right] \tag{A.27}$$

$$\Delta = \mathrm{Re}\{\log(ig/(\varrho_{\mathrm{E}}-is)+1)\}-\log(\sqrt{\rho}+\sqrt{1+\rho}) \tag{A.28}$$

The electric field along the j-direction is directly obtained from differentiation

$$E_j(x,z) = \frac{-\partial\phi(x,z)}{\partial x_j} = \frac{-1}{2\pi\epsilon_0\epsilon_d}\frac{\epsilon_m-\epsilon_d}{\epsilon_m+\epsilon_d}\sum_{n=1}^{\infty}\frac{1}{e^{2nd}-\left(\frac{\epsilon_m-\epsilon_d}{\epsilon_m+\epsilon_d}\right)^2}$$
$$\left[\frac{\epsilon_m-\epsilon_d}{\epsilon_m+\epsilon_d}\mathrm{Re}\left\{(\mu'_x+i\mu'_z)\frac{\partial\mathrm{A}_n^{-}(\varrho,\varrho_{\mathrm{E}})}{\partial x_j}\right\}+(\sqrt{\rho}+\sqrt{1+\rho})^{2n}\mathrm{Re}\left\{(\mu'_x-i\mu'_z)\frac{\partial\mathrm{B}_n^{-}(\varrho,\varrho_{\mathrm{E}})}{\partial x_j}\right\}\right]. \tag{A.29}$$

Interaction of a pure point-like quadrupolar source with a NPoM cavity

As we already did in the dipolar case, we proceed to analyze the second order of the multipolar expandion of the scalar potential, $\phi_{\mathrm{2D}}^{(2)}(x,y)$:

$$\begin{aligned}\phi_{\mathrm{2D}}^{(2)}(x,y) = \frac{-1}{2\pi\epsilon_0}&\int\rho_q(\boldsymbol{r}')\frac{1}{2}(-\boldsymbol{r}'\nabla)(-\boldsymbol{r}'\nabla)\log r\, d^2\boldsymbol{r}' =\\ &= \frac{-1}{4\pi\epsilon_0}\int\rho_q(\boldsymbol{r}')[x'^2\partial_x^2+2x'y'\partial_x\partial_y+y'^2\partial_y^2]\log r\, d^2\boldsymbol{r}' =\\ &= \frac{1}{2\pi\epsilon_0}\sum_{ij}\left(\int\rho_q(\boldsymbol{r}')\frac{1}{2}(2x'_ix'_j-r'^2\delta_{ij})\, d^2\boldsymbol{r}'\right)\frac{x_ix_j}{r^4} = \frac{1}{2\pi\epsilon_0}\sum_{ij}Q_{ij}\frac{x_ix_j}{r^4}\end{aligned} \tag{A.30}$$

This term is now the illumination in our transformed system $((x', z')$ (slabs at $x' = 0$ and $x' = d$)), as an array of sources:

$$\phi^Q(x', z') = \frac{1}{2\pi\epsilon_0\epsilon_d} \sum_{n=-\infty}^{\infty} \sum_{ij} \frac{Q'_{ij} x'_i x'_j}{\left((x' - x'_{\mathrm{E}})^2 + (z' - (z'_{\mathrm{E}} + 2n\pi))^2\right)^2} \tag{A.31}$$

The first step is to obtain the Fourier transform $\phi_0(k)$ from this potential:

$$\phi^Q(k) = \int \phi^Q(x', z') e^{-ikz'} dz' = \frac{1}{4\epsilon_0\epsilon_d} \sum_{n=-\infty}^{\infty} e^{-|k||x' - x'_{\mathrm{E}}|} e^{+ik(z'_{\mathrm{E}} + 2n\pi)} \times$$
$$\left(Q'_{xx} \frac{1 + |k(x' - x'_{\mathrm{E}})|}{|x' - x'_{\mathrm{E}}|} - i(Q'_{xz} + Q'_{zx}) k \operatorname{sign}(x' - x'_{\mathrm{E}}) + Q_{zz} \frac{1 - |k(x' - x'_{\mathrm{E}})|}{|x' - x'_{\mathrm{E}}|}\right) \tag{A.32}$$

and using the traceless condition

$$\phi^Q(k) = \frac{1}{2\epsilon_0\epsilon_d} \sum_{n=-\infty}^{\infty} e^{-|k||x' - x'_{\mathrm{E}}|} e^{+ik(z'_{\mathrm{E}} + 2n\pi)} \left(Q'_{xx} \frac{|k||x' - x'_{\mathrm{E}}|}{|x' - x'_{\mathrm{E}}|} - iQ'_{xz} k \operatorname{sign}(x' - x'_{\mathrm{E}})\right) \tag{A.33}$$

So:

$$\phi^Q(k) = \begin{cases} a^Q_-(k) \exp(+|k|(x' - x'_{\mathrm{E}})) \text{ if } x' < x'_{\mathrm{E}} \\ a^Q_+(k) \exp(-|k|(x' - x'_{\mathrm{E}})) \text{ if } x' > x'_{\mathrm{E}} \end{cases} \tag{A.34}$$

with:

$$a^Q_\pm(k) = \frac{1}{2\epsilon_0\epsilon_d} \sum_{n=-\infty}^{\infty} e^{-ikz'_{\mathrm{E}}} \delta(k - n) k \left(Q'_{xx} \operatorname{sign}(k) \mp iQ'_{xz}\right) \tag{A.35}$$

where we used the identity between exponential sums and delta distributions. These coefficients are equivalent to those obtained for the dipole case, with an extra dependence on k due to the different spatial dependences in the quadrupolar potential. As we already did, we impose the same functional form to the scattered fields by the metal plates in the transformed system. The coefficients of the expansion are obtained from the same system of equations that in the dipolar case after the imposition of boundary conditions, and the coefficients for the scattered field in the dielectric space are written as

$$b^Q_-(k) = \frac{R-1}{R+1} \frac{1}{e^{2|k|d} - \left(\frac{R-1}{R+1}\right)^2} \left(a^Q_-(k) \frac{R-1}{R+1} - a^Q_+ e^{2|k|x'_{\mathrm{E}}}\right) \tag{A.36}$$

$$b^Q_+(k) = \frac{R-1}{R+1} \frac{1}{e^{2|k|d} - \left(\frac{R-1}{R+1}\right)^2} \left(a^Q_+(k) \frac{R-1}{R+1} - a^Q_- e^{2|k|(d - x'_{\mathrm{E}})}\right) \tag{A.37}$$

where we used $R = \epsilon_m/\epsilon_d$. The potential in the real (transformed frame) space is obtained by performing the inverse Fourier Transform

$$\begin{aligned}\phi_{\mathrm{S}}^{Q}(x',z')\;\forall\, x'\in[0,d] &= \frac{1}{2\pi}\int\Big(b_{-}^{Q}e^{+|k|(x'-x'_{\mathrm{E}})}+b_{+}^{Q}e^{-|k|(x'-x'_{\mathrm{E}})}\Big)e^{ikz'}dk = \\ = \frac{1}{2\pi\epsilon_0\epsilon_d}\left(\frac{R-1}{R+1}\right)\sum_{n=1}^{\infty}\frac{n}{e^{2nd}-\left(\frac{R-1}{R+1}\right)^2}&\Bigg[\left(\frac{R-1}{R+1}\right)\mathrm{Re}\Big\{(Q'_{xx}+iQ'_{xz})(e^{-n\Delta\varrho'}+e^{n\Delta\varrho'})\Big\} \\ &- e^{nd}\mathrm{Re}\Big\{(Q'_{xx}-iQ'_{xz})(e^{-2n(x'_{\mathrm{E}}-d/2)}e^{-n\Delta\varrho'}+e^{2n(x'_{\mathrm{E}}-d/2)}e^{n\Delta\varrho'})\Big\}\Bigg]\end{aligned} \tag{A.38}$$

which after the inverse conformal mapping, can be expressed in terms of the coordinates in the original frame as

$$\begin{gathered}\phi_{S}^{Q}(x,z)=\frac{1}{2\pi\epsilon_0\epsilon_d}\left(\frac{\epsilon_m-\epsilon_d}{\epsilon_m+\epsilon_d}\right)\sum_{n=1}^{\infty}\frac{n}{(\sqrt{\rho}+\sqrt{1+\rho})^{4n}-\left(\frac{\epsilon_m-\epsilon_d}{\epsilon_m+\epsilon_d}\right)^2} \\ \Bigg[\left(\frac{\epsilon_m-\epsilon_d}{\epsilon_m+\epsilon_d}\right)\mathrm{Re}\Big\{(Q'_{xx}+iQ'_{xz})A_n^{+}(\varrho,\varrho_{\mathrm{E}})\Big\}-(\sqrt{\rho}+\sqrt{1+\rho})^{2n}\mathrm{Re}\Big\{(Q'_{xx}-iQ'_{xz})B_n^{+}(\varrho,\varrho_{\mathrm{E}})\Big\}\Bigg]\end{gathered} \tag{A.39}$$

where we have used

$$e^{\varrho'}=\frac{ig}{\varrho-is}+1 \tag{A.40}$$

in terms of the position in the original frame with the complex notation $\varrho = x + iz$. The transformation is defined through $g = 2D\sqrt{\rho(1+\rho)}$, $\rho = \delta/D$, $s = \delta + D\sqrt{\rho}/(\sqrt{1+\rho}+\sqrt{\rho})$ and $d = 2\log(\sqrt{\rho}+\sqrt{1+\rho})$ we have written

$$\mathrm{A}_n^{+}(\varrho,\varrho_{\mathrm{E}})=\left[\left(\frac{ig+\varrho-is}{ig+\varrho_{\mathrm{E}}-is}\frac{\varrho_{\mathrm{E}}-is}{\varrho-is}\right)^{-n}+\left(\frac{ig+\varrho-is}{ig+\varrho_{\mathrm{E}}-is}\frac{\varrho_{\mathrm{E}}-is}{\varrho-is}\right)^{n}\right] \tag{A.41}$$

$$\mathrm{B}_n^{+}(\varrho,\varrho_{\mathrm{E}})=\left[e^{-2n\Delta}\left(\frac{ig+\varrho-is}{ig+\varrho_{\mathrm{E}}-is}\frac{\varrho_{\mathrm{E}}-is}{\varrho-is}\right)^{-n}+e^{2n\Delta}\left(\frac{ig+\varrho-is}{ig+\varrho_{\mathrm{E}}-is}\frac{\varrho_{\mathrm{E}}-is}{\varrho-is}\right)^{n}\right] \tag{A.42}$$

$$\Delta=\mathrm{Re}\{\log(ig/(\varrho_{\mathrm{E}}-is)+1)\}-\log(\sqrt{\rho}+\sqrt{1+\rho}) \tag{A.43}$$

and the fields are obtained straightforwardly from the spatial derivatives of $\mathrm{A}_n^{+}, \mathrm{B}_n^{+}$.

Expressions for light-matter coupling strengths

Our TO approach yields the following analytical expressions for the light-matter coupling strengths that weight the various SP contributions to the spectral density as a sum of

Lorentzians

$$g_\mu^{n,\sigma} = \sqrt{\frac{4\sigma n D^2\rho(1+\rho)\mu^2\omega_{n,\sigma}^2}{3\pi^2\hbar c\epsilon_0}\frac{1+\xi_{n,\sigma}}{\epsilon_\infty+\epsilon_d\xi_{n,\sigma}}\frac{\mathrm{Re}\{\mathrm{K}_n(\alpha)\}+\sigma\mathrm{Re}\{\Lambda_n(\alpha)\}}{(\sqrt{\rho}+\sqrt{1+\rho})^{2n}-\sigma}}, \tag{A.44}$$

$$g_Q^{n,\sigma} = \sqrt{\frac{8\sigma n^3 D^4(\rho(1+\rho))^2 Q^2\omega_{n,\sigma}^2}{45\pi^2\hbar c\epsilon_0}\frac{1+\xi_{n,\sigma}}{\epsilon_\infty+\epsilon_d\xi_{n,\sigma}}\frac{\mathrm{Re}\{\mathrm{K}_n'(\alpha)\}+\sigma\mathrm{Re}\{\Lambda_n'(\alpha)\}}{(\sqrt{\rho}+\sqrt{1+\rho})^{2n}-\sigma}} \tag{A.45}$$

where α is the angle defining the QE orientation and

$$\mathrm{K}_n(\alpha) = -\frac{(\sin\alpha+i\cos\alpha)^2}{(\varrho_\mathrm{E}-is)^2(2iD\sqrt{\rho(1+\rho)}+\varrho_\mathrm{E}-is)^2} \tag{A.46}$$

$$\Lambda_n(\alpha) = \frac{\cosh(2n\Delta)}{|\varrho_\mathrm{E}-is|^2|2iD\sqrt{\rho(1+\rho)}+\varrho_\mathrm{E}-is|^2} \tag{A.47}$$

$$\mathrm{K}_n^{'}(\alpha) = -\frac{(\sin 2\alpha+i\cos 2\alpha)^2}{(\varrho_\mathrm{E}-is)^4\Big(2iD\sqrt{\rho(1+\rho)}+\varrho_E-is\Big)^4} \tag{A.48}$$

$$\Lambda_n^{'}(\alpha) = \frac{\cosh(2n\Delta)+\frac{2D\sqrt{\rho(1+\rho)}-2(i\varrho_\mathrm{E}+s)}{2D\sqrt{\rho(1+\rho)}n}\sinh(2n\Delta)}{|\varrho_E-is|^4|2iD\sqrt{\rho(1+\rho)}+\varrho_\mathrm{E}-is|^4} \tag{A.49}$$

Power radiated by a quadrupole in 2D

From the minimal coupling Hamiltonian, quasistatic limit means that transversal fields are negligible. Only remain the velocities and the electrostatic potential. In its classical version, we write the energy of the interaction between a quasistatic potential and a distribution of charges as [251]

$$V_E = \int \rho(\mathbf{r})\phi(\mathbf{r})d^3\mathbf{r} \tag{A.50}$$

which reads as the purely electrostatic version since, in the quasistatic limit, the potential and the charges are assumed to have the same time dependence through a phase. The potential is the external stimuli and the integral runs over the charge distribution volume. If the potential slowly varies over the volume of the charge distribution, we can expand as a Taylor series

$$\phi(\mathbf{r}) \approx \phi(\mathbf{0}) + (\mathbf{r}\nabla)\phi|_\mathbf{0} + \frac{1}{2}(\mathbf{r}\nabla)^2\phi|_\mathbf{0} \tag{A.51}$$

where, in the xz-plane,

$$\int \rho(\mathbf{r})\phi(\mathbf{0})dV = q\phi(\mathbf{0}) \tag{A.52}$$

$$\int \rho(\mathbf{r})(\mathbf{r}\nabla)\phi|_{\mathbf{0}}dV = -\Big(\int \rho(\mathbf{r})\mathbf{r}dV\Big)\mathbf{E}(\mathbf{0}) = -\boldsymbol{\mu}\mathbf{E}(\mathbf{0}) \tag{A.53}$$

$$\begin{aligned}\int \frac{1}{2}\rho(\mathbf{r})(\mathbf{r}\nabla)^2\phi|_{\mathbf{0}}dV = \frac{1}{2}\int \rho(\mathbf{r})\Big(- x^2E_x|_{\mathbf{0}} - z^2\partial_z E_z|_{\mathbf{0}} - xz\partial_x E_z|_{\mathbf{0}} - zx\partial_z E_x|_{\mathbf{0}}\Big) = \\ -\frac{1}{2}\int \rho(\mathbf{r})\Big(\begin{bmatrix} x^2 & xz \\ xz & z^2\end{bmatrix}\begin{bmatrix}\partial_x \\ \partial_z\end{bmatrix}\begin{bmatrix}E_x(\mathbf{0}) \\ E_z(\mathbf{0})\end{bmatrix}\Big) = -\frac{1}{2}(\mathbf{Q}\nabla)\mathbf{E}|_{\mathbf{0}}\end{aligned} \tag{A.54}$$

The quadrupolar term is given by the $\mathbf{Q}$ tensor, defined in the form $\mathbf{Q} = \int \rho(\mathbf{r})\mathbf{r} \otimes \mathbf{r}$ in order to have $V_E^{(2)} = -\frac{1}{2}(\mathbf{Q}\nabla)\mathbf{E}$. This implies that the out-of-diagonal terms are in the form xy, consistent with our definition of the quadrupolar electrostatic potential. We have already presented the derivation of the quasistatic scattered quadrupolar fields, but the computation of the Purcell factor requires of the radiated power in free space, given by the purely electrodynamic component of the Green's function. Therefore, we just have to compute the imaginary part of the interaction Hamiltonian to get the radiated power as

$$P_0^Q = \frac{\omega}{4}\mathrm{Im}\Big([\mathbf{Q}\nabla]\,\mathbf{E}_{inc}(\mathbf{0})\Big). \tag{A.55}$$

To get the quadrupolar term, we take the 2nd order of the Taylor expansion of the two-dimensional Green's function of the Helmholtz equation

$$G_0^{2D} \approx \frac{-i}{4}\Big(\mathcal{H}_0^{(1)}(kr) + (\mathbf{r}'\nabla)\mathcal{H}_0^{(1)}(kr)\Big) \tag{A.56}$$

and we can write the quadrupolar order of the vector potential as

$$\mathbf{A}^1 = \mu_0 \int \frac{-i}{4}(\mathbf{r}'\nabla)\mathcal{H}_0^{(1)}(kr)\,\mathbf{j}(\mathbf{r}')\,d\mathbf{r}' = \frac{i\mu_0}{4}k\mathcal{H}_1^{(1)}(kr)\int (\mathbf{r}'\mathbf{n})\,\mathbf{j}\,d\mathbf{r}'. \tag{A.57}$$

Using the triple vector product and taking only the symmetric part (the antisymmetric is a vector product related to the magnetic dipole)

$$\text{Symmetric part of } \Big(\mathbf{r}'\mathbf{n}\Big)\,\mathbf{j} = \frac{1}{2}\Big[(\mathbf{n}\,\mathbf{r}')\,\mathbf{j} + (\mathbf{n}\,\mathbf{j})\,\mathbf{r}'\Big] \tag{A.58}$$

and integrating by parts plus using the continuity equation

$$\mathbf{A}^1 = \frac{i\mu_0}{4}k\mathcal{H}_1^{(1)}(kr)\int (\mathbf{r}'\mathbf{n})\,\mathbf{j}\,d\mathbf{r}' = \frac{i\mu_0\mu}{4}k\mathcal{H}_1^{(1)}(kr)\Big(\frac{-i\omega}{2}\int \mathbf{r}'\,(\mathbf{n}\mathbf{r}')\rho(\mathbf{r}')\,d\mathbf{r}'\Big) \tag{A.59}$$

so we can rewrite the full expresion

$$\frac{1}{2}\int \mathbf{r}'\,(\mathbf{n}\mathbf{r}')\rho(\mathbf{r}') = \frac{1}{2}\int \begin{bmatrix} x'^2 & x'z' \\ x'z' & z'^2 \end{bmatrix} \begin{bmatrix} x/r \\ z/r \end{bmatrix} \rho(\mathbf{r}') = \frac{1}{2}\mathbf{Q}\mathbf{n} \tag{A.60}$$

where it is clear that the quadrupole moment has the form $\mathbf{Q}$, satisfying both the definitions in both interaction Hamiltonian an the potential. The vector potential is just given by:

$$\mathbf{A}^1 = \frac{\mu_0 \omega k}{8}\mathcal{H}_1^{(1)}(kr)\,\mathbf{Q}\,\mathbf{n}. \tag{A.61}$$

The electric field $\mathbf{E}$ can be calculated as

$$\mathbf{E}^1 = i\omega\Big[1 + \frac{1}{k^2}\nabla\nabla\Big]\mathbf{A}^1 \tag{A.62}$$

Therefore, we have to find the imaginary part of the interaction Hamiltonian with our definition of $\mathbf{Q}$ at the emitter position

$$(\mathbf{Q}\nabla)\mathbf{E} = \frac{\omega^2 k \mu_0}{8}\Big(\mathbf{Q}\nabla\Big)\Big[1 + \frac{1}{k^2}\nabla\nabla\Big]\Big(i\mathcal{H}_1^{(1)}(kr)\Big)\,\mathbf{Q}\,\mathbf{n} \tag{A.63}$$

and

$$\mathrm{Im}\left(\Big(\mathbf{Q}\nabla\Big)\Big[1 + \frac{1}{k^2}\nabla\nabla\Big] i\mathcal{H}_1^{(1)}(kr)\,\mathbf{Q}\,\mathbf{n}\right)_{\mathbf{r}'=0} = \frac{1}{2}k(Q_{xx}^2 + Q_{xz}^2) \tag{A.64}$$

Arranging the whole set of results, we can write the imaginary part of the interaction Hamiltonian

$$\mathrm{Im}\Big\{\Big(\mathbf{Q}\nabla\Big)\mathbf{E}\Big\} = \frac{\omega^4\mu_0}{16c^2}(Q_{xx}^2 + Q_{xz}^2) = \frac{\omega^4 Q^2}{32\epsilon_0 c^4} \tag{A.65}$$

and so on, the power radiated in free space by a pure quadrupolar emitter

$$P_0^Q = \frac{\omega}{4}\mathrm{Im}\Big([\mathbf{Q}\nabla]\mathbf{E}\Big) = \frac{\omega^5 Q^2}{128\epsilon_0 c^4} \tag{A.66}$$

where we have used $Q^2 = 2(Q_{xx}^2 + Q_{xz}^2)$.

B

Spontaneous emission and far-field spectra derivations

In this appendix B, we provide the derivations related to the study of excited state population dynamics and scattering spectra used throughout chapters 2 and 3 in our study of light-allowed and light-forbidden transitions in a NPoM cavity. We will start with the derivation of the Wigner-Weisskopf problem for a three-level system with dipolar and quadrupolar excited states. Then, we will give details about the calculations of the scattering spectrum through the introduction of a coherent pumping term in the Hamiltonian.

Spontaneous decay of a three-level system (dipole and quadrupole)

In this section, we address the Wigner-Weisskopf approach for the calculation of the population dynamics when considering a single three-level system with two different excited states, as we did in chapter 3, coupled to a set of plasmonic modes. We start with the second quantization form of the Hamiltonian in terms of the energies and the couplings

$$\hat{H}_0 = \hbar\omega_\mu \hat{\sigma}_\mu^\dagger \hat{\sigma}_\mu + \hbar\omega_Q \hat{\sigma}_Q^\dagger \hat{\sigma}_Q + \sum_{n,\sigma} \hbar\omega_{n,\sigma} \hat{a}_{n,\sigma}^\dagger \hat{a}_{n,\sigma} + \sum_{n,\sigma} \hbar g_\mu^{n,\sigma} (\hat{a}_{n,\sigma}^\dagger \hat{\sigma}_\mu + \text{h.c.}) + \sum_{n,\sigma} \hbar g_Q^{n,\sigma} (\hat{a}_{n,\sigma}^\dagger \hat{\sigma}_Q + \text{h.c.}), \quad \text{(B.1)}$$

where both excitons, dipolar μ and quadrupolar Q, respectively, are coupled to the plasmonic fields but not direct coupling between excited states exists. The quantum state for this Hamiltonian within the single-excitation subspace reads

$$|\phi(t)\rangle = c_\mu(t)e^{-i\omega_\mu t}\left|e_\mu,0,\{0\}\right\rangle + c_Q(t)e^{-i\omega_Q t}\left|0,e_Q,\{0\}\right\rangle \tag{B.2}$$

$$+\sum_{n,\sigma} c_{n,\sigma}(t)e^{-i\omega_{n,\sigma}t}\left|0,0,\{1_{n,\sigma}\}\right\rangle . \tag{B.3}$$

In order to determine the dynamics of such an state, we apply the Hamiltonian operator in order to get the unitary evolution given by the Schrödinger Equation

$$\begin{aligned}\hat{H}_0\left|\phi(t)\right\rangle = {}& \hbar\omega_\mu c_\mu(t)e^{-i\omega_\mu t}\left|e_\mu,0,\{0\}\right\rangle + \hbar\omega_Q c_Q(t)e^{-i\omega_Q t}\left|0,e_Q,\{0\}\right\rangle \\ & +\sum_{n,\sigma}\hbar\omega_{n,\sigma}c_{n,\sigma}(t)e^{-i\omega_{n,\sigma}t}\left|0,0,\{1_{n,\sigma}\}\right\rangle \\ & +\sum_{n,\sigma}\hbar g_\mu^{n,\sigma}\Big(c_\mu(t)e^{-i\omega_\mu t}\left|0,0,\{1_{n,\sigma}\}\right\rangle + c_{n,\sigma}(t)e^{-i\omega_{n,\sigma}t}\left|e_\mu,0,\{0\}\right\rangle\Big) \\ & +\sum_{n,\sigma}\hbar g_Q^{n,\sigma}\Big(c_Q(t)e^{-i\omega_Q t}\left|0,0,\{1_{n,\sigma}\}\right\rangle + c_{n,\sigma}(t)e^{-i\omega_{n,\sigma}t}\left|0,e_Q,\{0\}\right\rangle\Big) = i\hbar\frac{d\left|\phi(t)\right\rangle}{dt}\end{aligned}$$

and we project onto the basis states on both sides, $\langle u|\,\hat{H}_0\left|\phi(t)\right\rangle = ih\,\langle u|\,\partial_t\left|\phi(t)\right\rangle$ with $|u\rangle = \left|e_\mu,0,\{0\}\right\rangle, \left|0,e_Q,\{0\}\right\rangle$ and $\left|0,0,\{1_{n,\sigma}\}\right\rangle$, respectively. Therefore, we obtain the following expressions

$$\hbar\omega_\mu c_\mu(t)e^{-i\omega_\mu t} + \sum_{n,\sigma}\hbar g_\mu^{n,\sigma}c_{n,\sigma}(t)e^{-i\omega_{n,\sigma}t} = i\hbar\Bigg(-i\omega_\mu c_\mu(t)e^{-i\omega_\mu t} + \dot{c}_\mu(t)e^{-i\omega_\mu t}\Bigg) \tag{B.4}$$

$$\hbar\omega_Q c_Q(t)e^{-i\omega_Q t} + \sum_{n,\sigma}\hbar g_Q^{n,\sigma}c_{n,\sigma}(t)e^{-i\omega_{n,\sigma}t} = i\hbar\Bigg(-i\omega_Q c_Q(t)e^{-i\omega_Q t} + \dot{c}_Q(t)e^{-i\omega_Q t}\Bigg) \tag{B.5}$$

$$\hbar\omega_{n,\sigma}c_{n,\sigma}(t)e^{-i\omega_{n,\sigma}t} + \hbar g_\mu^{n,\sigma}c_\mu(t)e^{-i\omega_\mu t} + \hbar g_Q^{n,\sigma}c_Q(t)e^{-i\omega_Q t} = i\hbar\Bigg(-i\omega_{n,\sigma}c_{n,\sigma}(t)e^{-i\omega_{n,\sigma}t} + \dot{c}_{n,\sigma}(t)e^{-i\omega_{n,\sigma}t}\Bigg) \tag{B.6}$$

where we have used the dot convention for denoting time derivatives. Then, the final form for the system of equations that define the dynamics reads

$$\dot{c}_\mu(t) = -i\sum_{n,\sigma} g_\mu^{n,\sigma}c_{n,\sigma}(t)e^{-i(\omega_{n,\sigma}-\omega_\mu)t} \tag{B.7}$$

$$\dot{c}_Q(t) = -i\sum_{n,\sigma} g_Q^{n,\sigma}c_{n,\sigma}(t)e^{-i(\omega_{n,\sigma}-\omega_Q)t} \tag{B.8}$$

$$\dot{c}_{n,\sigma}(t) = -i\Bigg(g_\mu^{n,\sigma}c_\mu(t)e^{-i(\omega_\mu-\omega_{n,\sigma})t} + g_Q^{n,\sigma}c_Q(t)e^{-i(\omega_Q-\omega_{n,\sigma})t}\Bigg) \tag{B.9}$$

The last equation provides a direct integration

$$c_{n,\sigma}(t) = -i\int_0^t\Big(g_\mu^{n,\sigma}c_\mu(t')e^{-i(\omega_\mu-\omega_{n,\sigma})t'} + g_Q^{n,\sigma}c_Q(t')e^{-i(\omega_Q-\omega_{n,\sigma})t'}\Big)dt' \tag{B.10}$$

where we directly assumed $c_{n,\sigma}(0) = 0$. Hence

$$\dot{c_\mu}(t) = -\int_0^t \sum_{n,\sigma} \left(\left(g_\mu^{n,\sigma}\right)^2 c_\mu(t') e^{-i(\omega_\mu - \omega_{n,\sigma})t'} + g_\mu^{n,\sigma} g_Q^{n,\sigma} c_Q(t') e^{-i(\omega_Q - \omega_{n,\sigma})t'} \right) dt' e^{-i(\omega_{n,\sigma} - \omega_\mu)t} \tag{B.11}$$

$$\dot{c_Q}(t) = -\int_0^t \sum_{n,\sigma} \left(\left(g_Q^{n,\sigma}\right)^2 c_Q(t') e^{-i(\omega_Q - \omega_{n,\sigma})t'} + g_\mu^{n,\sigma} g_Q^{n,\sigma} c_\mu(t') e^{-i(\omega_\mu - \omega_{n,\sigma})t'} \right) dt' e^{-i(\omega_{n,\sigma} - \omega_Q)t} \tag{B.12}$$

The next step is using a kernel equivalence expanding the sum as an integral[1]. As an example, considering no presence of the quadrupolar level and using

$$\delta(x - x_0) = \lim_{\gamma \to 0} \frac{1}{\pi} \frac{\gamma}{(x - x_0)^2 + \gamma^2} \tag{B.13}$$

for the limit of delta functions (and $\tau = t - t'$)

$$\begin{aligned} \sum_n \left(g_\mu^{n,\sigma}\right)^2 e^{i(\omega_\mu - \omega_n)\tau} &= \int_{-\infty}^{\infty} \sum_n \left(g_\mu^{n,\sigma}\right)^2 e^{i(\omega_\mu - \omega)\tau} \delta(\omega - \omega_n) d\omega \approx \\ &\approx \int_{-\infty}^{\infty} \sum_n \frac{\left(g_\mu^{n,\sigma}\right)^2}{\pi} \frac{\gamma/2}{(\omega - \omega_n)^2 + \gamma^2/4} e^{i(\omega_\mu - \omega)\tau} d\omega \approx \\ &\approx \int_0^{\infty} J_\mu(\omega) e^{i(\omega_\mu - \omega)\tau} d\omega \end{aligned} \tag{B.14}$$

that can be applied straightforward to the three-level case. Therefore, we can rewrite the dynamics equations as

$$\begin{aligned} \dot{c_\mu}(t) = &-\int_0^t \sum_{n,\sigma} \left(g_\mu^{n,\sigma}\right)^2 c_\mu(t') e^{i(\omega_\mu - \omega_{n,\sigma})(t-t')} dt' \\ &- \int_0^t \sum_{n,\sigma} g_\mu^{n,\sigma} g_Q^{n,\sigma} c_Q(t') e^{i(\omega_\mu - \omega_{n,\sigma})(t-t')} e^{i(\omega_\mu - \omega_Q)t'} dt' = \\ = &-\int_0^t \int_0^\infty J_\mu(\omega) e^{i(\omega_\mu - \omega)(t-t')} c_\mu(t') d\omega dt' - \int_0^t J_{\mu Q}(\omega) e^{i(\omega_\mu - \omega)(t-t')} e^{i(\omega_\mu - \omega_Q)t'} c_Q(t') d\omega dt' \end{aligned} \tag{B.15}$$

where we can define

$$K_{ij}(t - t') = \int_0^\infty J_{ij}(\omega) e^{i(\omega_i - \omega)(t-t')} d\omega \tag{B.16}$$

Scattering spectrum for a collection of N plasmonic modes and single emitter

In this section, we derive the approach based on an effective Hamiltonian to obtain the scattering cross-section of the hybrid emitter-cavity system under coherent illumination.

---

[1] This approach can be also done introducing imaginary parts in the energies of the Hamiltonian and using the equivalence between exponential functions and delta distributions [74, 252].

We start again with the the Hamiltonian just considering an emitter with a single excited dipolar state

$$\hat{H}_0 = \hbar\omega_\mu \hat{\sigma}_\mu^\dagger \hat{\sigma}_\mu + \sum_{n,\sigma} \hbar\omega_{n,\sigma} \hat{a}_{n,\sigma}^\dagger \hat{a}_{n,\sigma} \tag{B.17}$$

$$+ \sum_{n,\sigma} \hbar g_\mu^{n,\sigma} (\hat{a}_{n,\sigma}^\dagger \hat{\sigma}_\mu + \text{h.c.}) \tag{B.18}$$

where the exciton is coupled to the even and odd plasmonic fields. We add to the Hamiltonian the coherent driving part, representing the pumping of the system at a certain frequency. Then

$$\hat{H}_L = \hat{\Omega}^\dagger e^{-i\omega_L t} + \hat{\Omega} e^{i\omega_L t} \tag{B.19}$$

where the pumping is understood to affect both the emitter and the plasmonic modes. Due to the is a far-field character of the excitation, the only coupling is assumed to be given by the dipolar modes in the system as

$$\hat{\Omega} = \boldsymbol{\mu}\mathbf{E}_L \hat{\sigma}_\mu + \sum_{n,+1} \boldsymbol{\mu}_n \mathbf{E}_L \hat{a}_{n,+1} \tag{B.20}$$

where $\boldsymbol{\mu} = \mu\hat{\mathbf{n}}_\mu$ with μ being the transition dipole moment only even plasmonic modes, $\boldsymbol{\mu}_n = \mu_n \hat{\mathbf{n}}_n$, couple to the far-field, with $\mathbf{E}_L = E_L \hat{\mathbf{n}}_L$. The introduction of the coherent driving introduces time-dependences in our Hamiltonian. Then, it is useful to consider the transformation into another frame where the Hamiltonian does not show the explicit dependence (transformation to a rotating frame). The transformation is done by considering an unitary operator

$$\hat{\mathcal{U}} = e^{-i/\hbar \hat{\mathbf{A}} t} \longrightarrow \hat{H}_{RF} = \hat{\mathcal{U}}^\dagger(t)(\hat{H}_0 + \hat{H}_L)\hat{\mathcal{U}}(t) - \hat{\mathbf{A}} \tag{B.21}$$

where the operator $\hat{\mathbf{A}}$

$$\hat{\mathbf{A}} = \hbar\omega_L \Big(\hat{\sigma}_\mu^\dagger \hat{\sigma}_\mu + \sum_{n,\sigma} \hat{a}_{n,\sigma}^\dagger \hat{a}_{n,\sigma} \Big) \tag{B.22}$$

yielding the form for the operator $\hat{\mathcal{U}}$

$$\hat{\mathcal{U}} = e^{(-i\omega_L t)\left(\hat{\sigma}_\mu^\dagger \hat{\sigma}_\mu + \sum_{n,\sigma} \hat{a}_{n,\sigma}^\dagger \hat{a}_{n,\sigma}\right)} = e^{(-i\omega_L t)\hat{\sigma}_\mu^\dagger \hat{\sigma}_\mu} \prod_{n,\sigma} e^{(-i\omega_L t)\hat{a}_{n,\sigma}^\dagger \hat{a}_{n,\sigma}} \tag{B.23}$$

The application of this operator provides

$$\hat{\mathcal{U}}^\dagger(t)(\hat{H}_0)\hat{\mathcal{U}}(t) = \left(e^{(i\omega_L t)\hat{\sigma}_\mu^\dagger \hat{\sigma}_\mu} \prod_{n,\sigma} e^{(i\omega_L t)\hat{a}_{n,\sigma}^\dagger \hat{a}_{n,\sigma}} \right) \hat{H}_0 \left(e^{(-i\omega_L t)\hat{\sigma}_\mu^\dagger \hat{\sigma}_\mu} \prod_{n,\sigma} e^{(-i\omega_L t)\hat{a}_{n,\sigma}^\dagger \hat{a}_{n,\sigma}} \right) \tag{B.24}$$

We use the properties from the distinguishability of the states (orthogonality)

$$e^{\xi|\phi\rangle\langle\phi|}\,|\phi\rangle = e^{\xi}\,|\phi\rangle \tag{B.25}$$

$$e^{\xi|\phi\rangle\langle\phi|}\,|\nu\rangle = |\nu\rangle \tag{B.26}$$

so the energies of the emitter and plasmons provide

$$\hat{\mathcal{U}}^{\dagger}(t)\Big(\hbar\omega_{\mu}\hat{\sigma}^{\dagger}_{\mu}\hat{\sigma}_{\mu}\Big)\hat{\mathcal{U}}(t) = e^{(i\omega_L t)\hat{\sigma}^{\dagger}_{\mu}\hat{\sigma}_{\mu}}\Big(\hbar\omega_{\mu}\hat{\sigma}^{\dagger}_{\mu}\hat{\sigma}_{\mu}\Big)e^{(-i\omega_L t)\hat{\sigma}^{\dagger}_{\mu}\hat{\sigma}_{\mu}} = \hbar\omega_{\mu}\hat{\sigma}^{\dagger}_{\mu}\hat{\sigma}_{\mu} \tag{B.27}$$

where the orthogonality between exciton and plasmon states implies the not phase induction from $\hat{a}$ terms. On the other hand

$$\begin{aligned}&\hat{\mathcal{U}}^{\dagger}(t)\Big(\sum_{n,\sigma}\hbar\omega_{n\sigma}\hat{a}^{\dagger}_{n\sigma}\hat{a}_{n\sigma}\Big)\hat{\mathcal{U}}(t) = \\ &\qquad\prod_{n,\sigma}e^{(i\omega_L t)\hat{a}^{\dagger}_{n,\sigma}\hat{a}_{n,\sigma}}\Big(\sum_{n,\sigma}\hbar\omega_{n\sigma}\hat{a}^{\dagger}_{n\sigma}\hat{a}_{n\sigma}\Big)\prod_{n,\sigma}e^{(-i\omega_L t)\hat{a}^{\dagger}_{n,\sigma}\hat{a}_{n,\sigma}} = \sum_{n,\sigma}\hbar\omega_{n\sigma}\hat{a}^{\dagger}_{n\sigma}\hat{a}_{n\sigma}\end{aligned} \tag{B.28}$$

Due to orthogonality of states, from the product, only induces a phase the term corresponding to the same one in the summation. The last part of $\hat{H}_0$ is the coherent coupling

$$\begin{aligned}&\hat{\mathcal{U}}^{\dagger}(t)\Big(\sum_{n,\sigma}\hbar g_{n\sigma}\Big(\hat{a}^{\dagger}_{n\sigma}\hat{\sigma}_{\mu}+\hat{\sigma}^{\dagger}_{\mu}\hat{a}_{n\sigma}\Big)\Big)\hat{\mathcal{U}}(t) = \\ &e^{(i\omega_L t)\hat{\sigma}^{\dagger}_{\mu}\hat{\sigma}_{\mu}}\prod_{n,\sigma}e^{(i\omega_L t)\hat{a}^{\dagger}_{n,\sigma}\hat{a}_{n,\sigma}}\Big(\sum_{n,\sigma}\hbar g_{n\sigma}\Big(\hat{a}^{\dagger}_{n\sigma}\hat{\sigma}_{\mu}+\hat{\sigma}^{\dagger}_{\mu}\hat{a}_{n\sigma}\Big)\Big)e^{(-i\omega_L t)\hat{\sigma}^{\dagger}_{\mu}\hat{\sigma}_{\mu}}\prod_{n,\sigma}e^{(-i\omega_L t)\hat{a}^{\dagger}_{n,\sigma}\hat{a}_{n,\sigma}}\end{aligned}$$

Let's look carefully to the first term

$$e^{f_e|e\rangle\langle e|}e^{f_1|1\rangle\langle 1|}e^{f_2|2\rangle\langle 2|}e^{f_3|3\rangle\langle 3|}\Big(\hbar g_1\,|1\rangle\,\langle e|\,\Big)e^{-f_e|e\rangle\langle e|}e^{-f_1|1\rangle\langle 1|}e^{-f_2|2\rangle\langle 2|}e^{-f_3|3\rangle\langle 3|}$$

where we just expressed the productory in a simplified way. From the left, the only term that induces phase is e^{f_1} and from the right, e^{-f_e}. As those are the same, the term remains equal

$$\hat{\mathcal{U}}^{\dagger}(t)\Big(\sum_{n,\sigma}\hbar g_{n\sigma}\Big(\hat{a}^{\dagger}_{n\sigma}\hat{\sigma}_{\mu}+\hat{\sigma}^{\dagger}_{\mu}\hat{a}_{n\sigma}\Big)\Big)\hat{\mathcal{U}}(t) = \Big(\sum_{n,\sigma}\hbar g_{n\sigma}\Big(\hat{a}^{\dagger}_{n\sigma}\hat{\sigma}_{\mu}+\hat{\sigma}^{\dagger}_{\mu}\hat{a}_{n\sigma}\Big)\Big)$$

So, as expected, the independence of time of the original Hamiltonian provides that in the rotating frame

$$\hat{\mathcal{U}}^{\dagger}(t)\,\hat{H}_0\,\hat{\mathcal{U}}(t) = \hat{H}_0 \tag{B.29}$$

On the other hand, the unitary transformation of the pumping (first term)

$$\begin{aligned}&\hat{\mathcal{U}}^{\dagger}(t)\,\hat{H}_L\,\hat{\mathcal{U}}(t) = \\ &\quad e^{(i\omega_L t)\hat{\sigma}^{\dagger}_{\mu}\hat{\sigma}_{\mu}}\prod_{n,\sigma}e^{(i\omega_L t)\hat{a}^{\dagger}_{n,\sigma}\hat{a}_{n,\sigma}}\Big(\boldsymbol{\mu}\mathbf{E}_L\Big(e^{-i\omega_L t}\hat{\sigma}^{\dagger}_{\mu}+e^{+i\omega_L t}\hat{\sigma}_{\mu}\Big)\Big)e^{(-i\omega_L t)\hat{\sigma}^{\dagger}_{\mu}\hat{\sigma}_{\mu}}\prod_{n,\sigma}e^{(-i\omega_L t)\hat{a}^{\dagger}_{n,\sigma}\hat{a}_{n,\sigma}}\end{aligned}$$

yielding

$$\hat{\mathcal{U}}^\dagger(t)\,\hat{H}_L\,\hat{\mathcal{U}}(t) = \boldsymbol{\mu}\mathbf{E}_L\Big(\hat{\sigma}_\mu^\dagger + \hat{\sigma}_\mu\Big) \tag{B.30}$$

and exactly the same for the second term, where the summation runs over the **even** modes. Then, the Hamiltonian in the rotating frame reads (after subtracting the **A** terms)

$$\begin{aligned} \hat{H}_{RF} = {} & \hbar(\omega_\mu - \omega_L)\hat{\sigma}_\mu^\dagger\hat{\sigma}_\mu + \sum_{n,\sigma}\hbar(\omega_n - \omega_L)\hat{a}_{n,\sigma}^\dagger\hat{a}_{n,\sigma} \\ & + \sum_{n,\sigma}\hbar g_\mu^{n,\sigma}(\hat{a}_{n,\sigma}^\dagger\hat{\sigma}_\mu + \text{h.c.}) \\ & + \boldsymbol{\mu}\mathbf{E}_L(\hat{\sigma}_\mu^\dagger + \hat{\sigma}_\mu) + \sum_{n,+1}\boldsymbol{\mu}_n\mathbf{E}_L(\hat{a}_{n,+1}^\dagger + \hat{a}_{n,+1}) \end{aligned}$$

As our system presents losses (non-radiative and radiative), the dynamics is given by the master equation including the Lindblad terms

$$\partial_t\hat{\rho} = \frac{i}{\hbar}[\hat{\rho},\hat{H}_{RF}] + \frac{\gamma_\mu^r}{2}\mathcal{L}_{\hat{\sigma}}[\hat{\rho}] + \sum_{n,,\sigma}\frac{\gamma_{n,\sigma}^r + \gamma_{n,\sigma}^{nr}}{2}\mathcal{L}_{\hat{a}}[\hat{\rho}] \tag{B.31}$$

The refilling terms in the Lindblad operators ensure the normalization of the density matrix. In the limit of low-pumping regime, the population concentrates at the ground state, so the Lindblad operators can be approximated neglecting the refilling terms

$$\mathcal{L}_{\hat{a}} \approx -a^\dagger a\rho - \rho a^\dagger a \tag{B.32}$$

and so on in the σ-superoperator. Then, the master equation reduces to a Schrödinger equation with an effective non-hermitian Hamiltonian

$$\begin{aligned} \hat{H}_{\text{eff}} = {} & \hbar\Big(\omega_\mu - \omega_L - i\frac{\gamma_\mu}{2}\Big)\hat{\sigma}_\mu^\dagger\hat{\sigma}_\mu + \sum_{n,\sigma}\hbar\Big(\omega_n - \omega_L - i\frac{\gamma_{n,\sigma}^r + \gamma_{,\sigma}^{nr}}{2}\Big)\hat{a}_{n,\sigma}^\dagger\hat{a}_{n,\sigma} \\ & + \sum_{n,\sigma}\hbar g_\mu^{n,\sigma}(\hat{a}_{n,\sigma}^\dagger\hat{\sigma}_\mu + \text{h.c.}) + \boldsymbol{\mu}\mathbf{E}_L(\hat{\sigma}_\mu^\dagger + \hat{\sigma}_\mu) + \sum_{n,+1}\boldsymbol{\mu}_n\mathbf{E}_L(\hat{a}_n^\dagger + \hat{a}_n) \end{aligned} \tag{B.33}$$

The Schrödinger equation can be solved within perturbation theory for an small pumping

$$\hat{H}_{\text{eff}} = \hat{H}_{\text{eff}}^0 + E_L\hat{V} \tag{B.34}$$

The steady state can be expanded in a power series of the incident field E_L. Substituting this in the equation $\hat{H}_{\text{eff}}\,|\psi\rangle = 0$, we find the terms of the expansion. Zeroth order is $|\psi\rangle = |0\rangle$, and first order

$$|\psi\rangle = |0\rangle + E_L\,|\phi_1\rangle \tag{B.35}$$

Hence, the steady-state solution of the Schrödinger equation satisfies

$$\hat{H}_{\text{eff}} |\psi\rangle = 0 \longrightarrow \hat{H}^0_{\text{eff}} |\phi_1\rangle + \hat{V} |0\rangle = 0. \tag{B.36}$$

We solve the last identity in the basis $|e_\mu, 0\rangle, |0, 1_{n,\sigma}\rangle$ and once the state is known, $|\psi\rangle = |0\rangle + E_L |\phi_1\rangle$, we obtain the scattering intensity, given by the field operator in the far-field

$$\hat{\mathbf{E}}_{\text{FF}} = \frac{\omega^2}{c^2\epsilon_0} \mathbf{G}(\mathbf{r}_{\text{FF}}, \mathbf{r}_\mu, \omega) \boldsymbol{\mu} \hat{\sigma}_\mu + \frac{\omega^2}{c^2\epsilon_0} \sum_{n,+1} \mathbf{G}(\mathbf{r}_{\text{FF}}, \mathbf{r}_p, \omega) \boldsymbol{\mu}_{n,+1} \hat{a}_{n,+1} \tag{B.37}$$

where $\mathbf{r}_{\text{FF}}$ denotes the position where we calculate the field ans $\mathbf{r}_\mu, \mathbf{r}_p$ refer to the positions of the emitter and the particle in the NPoM system. As the difference in positions inside the cavity is negligible, $|\mathbf{r}_\mu - \mathbf{r}_p| \ll \mathbf{r}_{\text{FF}}$, we ignore the effects of retardation between the dyadic Green's functions, and simplify

$$\hat{\mathbf{E}}_{\text{FF}} \simeq \hat{M} = \boldsymbol{\mu} \hat{\sigma}_\mu + \sum_{n,+1} \boldsymbol{\mu}_{n,+1} \hat{a}_{n,+1} \tag{B.38}$$

to obtain

$$\sigma_{\text{sca}}(\omega) = \langle\psi| \hat{M} \hat{M}^\dagger |\psi\rangle \tag{B.39}$$

The introduction of a quadrupolar emitter in this scheme is trivial since, under our assumptions, the only coupling between the coherent pumping and the hybrid emitter-cavity system is mediated by the even plasmonic modes in that case.

C

Super- and subradiant lattice resonances derivations

In this appendix C, we review the coupled dipole model theoretical approach for the study of lattice resonances, providing a detailed derivation of the expressions given in Chapter 4.

Polarizability

The polarizability of the different metallic nanoparticles is calculated from the dipolar Mie scattering coefficient as [180, 183]

$$\alpha = -\frac{3c^3}{2\omega^3}\frac{-j_1(\kappa_0)[\kappa_m j_1(\kappa_m)]' - [\kappa_0 j_1(\kappa_0)]' j_1(\kappa_m)}{h_1(\kappa_0)[\kappa_m j_1(\kappa_m)] - [\kappa_0 h_1(\kappa_0)]' j_1(\kappa_m)} \tag{C.1}$$

where $j_1(x)$ and $h_1(x)$ are the spherical Bessel and Hankel functions of the first kind, repectively. Since in all of our calculations we consider metallic particles in vacuum, the corresponding $\kappa_0 = (\omega/c)D/2$ and $\kappa_m = \sqrt{\epsilon_m}(\omega/c)D/2$, with ϵ_m as the metallic dielectric function, taken from tabulated data [253] and D, the diameter of the spherical nanoparticle.

The coupled dipole model

Consider an square array of spherical particles, structured in N-particle unit cells that pattern infinitely in the xy plane. If we illuminate the array with an electromagnetic field $\mathbf{E}_{\text{ext}}$, the particles behave mainly as pure dipoles if the incident wavelength is larger than both their size and the array period. Then, the nanosphere response can be modeled through a frequency-dependent polarizability $\boldsymbol{\alpha}$. Within the coupled dipole model, the induced dipole moment in a particle placed at $\mathbf{r} = \mathbf{r}_i$ is written as

$$\mathbf{p}(\mathbf{r}_i) = \boldsymbol{\alpha}_i \mathbf{E}_{\text{ext}}(\mathbf{r}_i) + \frac{\boldsymbol{\alpha}_i}{4\pi\epsilon_0} \sum_{j \neq i} [k^2 \mathbf{I} + \nabla\nabla] \frac{e^{ik|\mathbf{r}_i - \mathbf{r}_j|}}{|\mathbf{r}_i - \mathbf{r}_j|} \mathbf{p}(\mathbf{r}_j), \tag{C.2}$$

where $k = 2\pi/\lambda = \omega/c$, with λ being the wavelength of light, $\mathbf{p}(\mathbf{r}_i)$ is the dipole induced in the particle located at $\mathbf{r}_i = (\mathbf{R}_i, 0)$, and $\mathbf{I}$ is the 3×3 identity matrix. As the array is periodic, the solutions can be Fourier-transformed and expanded in periodic functions $\mathbf{p}(\mathbf{r}_i) = \int d\mathbf{k}_\parallel \mathbf{p}_i(\mathbf{k}_\parallel) e^{i\mathbf{k}_\parallel \mathbf{r}_i}$, where we have used the fact that the array is placed in the xy plane, and $\mathbf{k}_\parallel$ has zero z-component.

If we assume plane wave illumination $\mathbf{E}_{\text{ext}}(\mathbf{r}) = \mathbf{E}_0 e^{i\mathbf{k}_\parallel \mathbf{r}}$ and we consider isotropic polarizabilities for the particle description ($\boldsymbol{\alpha} = \alpha \mathbf{I}$), we can write

$$\mathbf{p}_i(\mathbf{k}_\parallel) = \alpha_i \mathbf{E}_0 + \frac{\alpha_i}{4\pi\epsilon_0} \sum_{j \neq i} [k^2 \mathbf{I} + \nabla\nabla] \frac{e^{ik|\mathbf{r}_i - \mathbf{r}_j|}}{|\mathbf{r}_i - \mathbf{r}_j|} \mathbf{p}_j(\mathbf{k}_\parallel) e^{i\mathbf{k}_\parallel (\mathbf{r}_j - \mathbf{r}_i)}. \tag{C.3}$$

We can split the summation over the whole set of particles into two sums, one over the unit cells and another over the N particles in the unit cell, so we write

$$\mathbf{p}_i(\mathbf{k}_\parallel) = \alpha_i \mathbf{E}_0 + \frac{\alpha_i}{\epsilon_0} \sum_{\nu}{}' \sum_{j=1}^{N} \mathbf{G}_{ij,\nu 0} \mathbf{p}_j(\mathbf{k}_\parallel) e^{i\mathbf{k}_\parallel (\mathbf{r}_j - \mathbf{r}_i + \mathbf{T}_\nu)}, \tag{C.4}$$

where we are now defining $\mathbf{r}_i$ as the i-th particle position in the unit cell that we take as an origin of our coordinate system. $\mathbf{T}_\nu$ is the position vector of the ν-th unit cell with respect the cell chose as an origin. We have also used the definition of the dyadic Green's function

$$\mathbf{G}_{ij,\nu 0} = [k^2 \mathbf{I} + \nabla\nabla] \frac{e^{ik|\mathbf{r}_i - \mathbf{r}_j - \mathbf{T}_\nu|}}{4\pi |\mathbf{r}_i - \mathbf{r}_j - \mathbf{T}_\nu|}. \tag{C.5}$$

The latin indices refer now to the particle positions in the unit cell and the greek ones to the different unit cells over the whole system. The prime index in the sum indicates that we exclude the combinations for which $\mathbf{r}_i - \mathbf{r}_j - \mathbf{T}_\nu = 0$.

Bipartite arrays

In general, the tensor $\mathbf{G}_{ij,\nu 0}$ involves several components in the solution. Nevertheless, the solution under the specific illumination of a $\mathbf{E}_0 = (E_0, 0, 0)e^{ikz}$ provides $\mathbf{p}_i(\mathbf{k}_\parallel) = (p_{ix}, 0, 0)$ due to the system symmetry. Therefore, the only contribution from the $\mathbf{G}_{ij,\nu 0}$

tensor is $\mathbf{G}^{xx}_{ij,\nu 0} = G_{ij,\nu 0} = [k^2\mathbf{I} + \partial_x \partial_x]\frac{e^{ik|\mathbf{r}_i - \mathbf{r}_j - \mathbf{T}_\nu|}}{4\pi|\mathbf{r}_i - \mathbf{r}_j - \mathbf{T}_\nu|}$ [178]. As we are interested in the solution of the bipartite array where $N = 2$, Eq. (C.4) can be written as

$$\begin{bmatrix} p_1 \\ p_2 \end{bmatrix} = \begin{bmatrix} \alpha_1 \mathbf{I} & 0 \\ 0 & \alpha_2 \mathbf{I} \end{bmatrix} \begin{bmatrix} E_0 \\ E_0 \end{bmatrix} + \begin{bmatrix} \alpha_1 \mathbf{I} & 0 \\ 0 & \alpha_2 \mathbf{I} \end{bmatrix} \begin{bmatrix} \mathcal{G}_{11} & \mathcal{G}_{12} \\ \mathcal{G}_{21} & \mathcal{G}_{22} \end{bmatrix} \begin{bmatrix} p_1 \\ p_2 \end{bmatrix} \tag{C.6}$$

where p_i is the x-component of the induced dipole in the i-particle of the unit cell, described by the scalar polarizability α_i. $\mathcal{G}_{ij} = (1/\epsilon_0) \sum'_\nu G_{ij,\nu 0}$ are the components of the lattice sum for normal incidence. This sum, evaluated by using the Ewald's method, contains information about the interaction between i-th and j-th particles across the lattice.

The explicit solution for the induced dipole has the form

$$\begin{aligned} \begin{bmatrix} p_1 \\ p_2 \end{bmatrix} &= \begin{bmatrix} \alpha_1^{-1}\mathcal{I} - \mathcal{G}_{11} & -\mathcal{G}_{12} \\ -\mathcal{G}_{12} & \alpha_2^{-1}\mathcal{I} - \mathcal{G}_{11} \end{bmatrix}^{-1} \begin{bmatrix} E_0 \\ E_0 \end{bmatrix} = \\ &= \frac{E_0}{(\alpha_2^{-1} - \mathcal{G}_{11})(\alpha_2^{-1} - \mathcal{G}_{11}) - \left(\mathcal{G}_{12}\right)^2} \begin{bmatrix} \alpha_2^{-1} - \mathcal{G}_{11} - \mathcal{G}_{12} \\ \alpha_1^{-1} - \mathcal{G}_{11} - \mathcal{G}_{12} \end{bmatrix} \end{aligned} \tag{C.7}$$

and the total dipole induced in the unit cell becomes

$$p = p_1 + p_2 = \frac{\alpha_1^{-1} + \alpha_2^{-1} + 2(\mathcal{G}_{12} - \mathcal{G}_{11})}{(\alpha_1^{-1} - \mathcal{G}_{11})(\alpha_2^{-1} - \mathcal{G}_{11}) - (\mathcal{G}_{12})^2} E_0, \tag{C.8}$$

where it is clear that this solution for $N = 2$ provides the $N = 1$ just considering that there is no a second particle in the system ($\mathcal{G}_{12} = 0$). The equations decouple and the unique $p_1 = p$ has the form

$$p = \frac{E_0}{\alpha^{-1} - \mathcal{G}_{11}} \tag{C.9}$$

The total dipole p can be decomposed as a sum of two resonances if we use $2\beta^{-1} = \alpha_1^{-1} + \alpha_2^{-1}$ and $\delta = \alpha_1^{-1} - \alpha_2^{-1}$. Then

$$\alpha_1^{-1} = \beta^{-1} + \delta/2 \text{ and } \alpha_2^{-1} = \beta^{-1} - \delta/2 \tag{C.10}$$

and the denominator in Eq. (C.8) , can be expressed as

$$(\alpha_1^{-1} - \mathcal{G}_{11})(\alpha_2^{-1} - \mathcal{G}_{11}) - \mathcal{G}_{12}^2 = (\beta^{-1} - \Omega_+)(\beta^{-1} - \Omega_-) \tag{C.11}$$

where we defined $\Omega_\pm = \mathcal{G}_{11} \pm \sqrt{\mathcal{G}_{12}^2 + \left(\frac{\delta}{2}\right)^2}$. Thus, the expression for p reads

$$p = p_1 + p_2 = \frac{\alpha_1^{-1} + \alpha_2^{-1} + 2(\mathcal{G}_{12} - \mathcal{G}_{11})}{(\alpha_1^{-1} - \mathcal{G}_{11})(\alpha_2^{-1} - \mathcal{G}_{11}) - (\mathcal{G}_{12})^2} E_0 = \frac{\zeta_+ E_0}{\beta^{-1} - \Omega_+} + \frac{\zeta_- E_0}{\beta^{-1} - \Omega_-} \tag{C.12}$$

with

$$\zeta_+ = 1 + \frac{\mathcal{G}_{12}}{\sqrt{\mathcal{G}_{12}^2 + \left(\frac{\delta}{2}\right)^2}} \text{ and } \zeta_- = 1 - \frac{\mathcal{G}_{12}}{\sqrt{\mathcal{G}_{12}^2 + \left(\frac{\delta}{2}\right)^2}}. \tag{C.13}$$

Furthermore, since the resonant behaviour is related to the vanishing real part of the denominator in p, its imaginary part provides insight into the resonance linewidth. As shown in [178, 179], we can expand the tensor $\boldsymbol{\mathcal{G}}$ making use of the Weyl identity [55]

$$\begin{aligned}\boldsymbol{\mathcal{G}}_{11}(\mathbf{k}_\parallel) = \frac{1}{4\pi\epsilon_0}\sum_{\nu\neq 0} e^{i\mathbf{k}_\parallel \mathbf{T}_\nu}[k^2\mathbf{I} + \nabla\nabla]\frac{e^{ik|\mathbf{T}_\nu|}}{|\mathbf{T}_\nu|} = \\ = \frac{1}{4\pi\epsilon_0}\lim_{z\to 0}\sum_{\nu\neq 0} e^{i\mathbf{k}_\parallel \mathbf{T}_\nu}\frac{i}{2\pi}\int\int\frac{d\mathbf{k}'_\parallel}{k'_z}[k^2\mathbf{I} + \nabla\nabla]e^{-i\mathbf{k}'_\parallel \mathbf{T}_\nu}e^{ik'_z|z|}\end{aligned} \tag{C.14}$$

$$\begin{aligned}\boldsymbol{\mathcal{G}}_{12}(\mathbf{k}_\parallel) = \frac{1}{4\pi\epsilon_0}\sum_{\nu=0} e^{i\mathbf{k}_\parallel(\mathbf{r}_2-\mathbf{r}_1+\mathbf{T}_\nu)}[k^2\mathbf{I} + \nabla\nabla]\frac{e^{ik|\mathbf{r}_1-\mathbf{T}_\nu-\mathbf{r}_2|}}{|\mathbf{r}_1-\mathbf{T}_\nu-\mathbf{r}_2|} = \\ = \frac{1}{4\pi\epsilon_0}\lim_{z\to 0}\sum_{\nu=0} e^{i\mathbf{k}_\parallel(\mathbf{r}_2-\mathbf{r}_1+\mathbf{T}_\nu)}\frac{i}{2\pi}\int\int\frac{d\mathbf{k}'_\parallel}{k'_z}[k^2\mathbf{I} + \nabla\nabla]e^{-i\mathbf{k}'_\parallel \mathbf{T}_\nu}e^{i\mathbf{k}'_\parallel(\mathbf{r}_1-\mathbf{r}_2)}e^{ik'_z|z|}.\end{aligned} \tag{C.15}$$

By making use of $\sum_{\nu\neq 0} e^{i(\mathbf{k}'_\parallel-\mathbf{k}_\parallel)\mathbf{T}_\nu} = \frac{4\pi^2}{a^2}\sum_{\mathbf{q}}\delta(\mathbf{k}'_\parallel - \mathbf{k}_\parallel - \mathbf{q})$ and assuming normal incidence, the x-component of $\boldsymbol{\mathcal{G}}_{11}$ and $\boldsymbol{\mathcal{G}}_{12}$ can be written as

$$\mathcal{G}_{11} = \frac{1}{4\pi\epsilon_0}\left(\frac{2\pi i}{a^2}\sum_{\mathbf{q}}\frac{1}{k_{z\mathbf{q}}}[k^2 - q_x^2] - \frac{i}{2\pi}\int\frac{d\mathbf{k}_\parallel}{k}[k^2 - k^2_{\parallel,x}]\right), \tag{C.16}$$

$$\mathcal{G}_{12} = \frac{1}{4\pi\epsilon_0}\left(\frac{2\pi i}{a^2}\sum_{\mathbf{q}}\frac{1}{k_{z\mathbf{q}}}[k^2 - q_x]\right), \tag{C.17}$$

where we have used the reciprocal lattice vectors $\mathbf{q} = (\frac{2\pi m}{a}, \frac{2\pi n}{a})$ and $k_{z\mathbf{q}} = \sqrt{k^2 - q_x^2 - q_y^2}$. On the red side of the first Rayleigh anomaly ($\lambda > a$), we can neglect the sum and just take the first term due to the evancescent character of the higher order modes [178, 180] so the imaginary parts have the form

$$\mathrm{Im}\{\mathcal{G}_{11}\} = \frac{k}{2\epsilon_0 a^2} - \frac{k^3}{6\pi\epsilon_0},$$

$$\mathrm{Im}\{\mathcal{G}_{12}\} = \frac{k}{2\epsilon_0 a^2}.$$

On the other hand, the imaginary part of the polarizability can be written as

$$\mathrm{Im}\{\alpha^{-1}\} = -\frac{\mathrm{Im}\{\alpha\} - \frac{k^3}{6\pi\epsilon_0}|\alpha|^2}{|\alpha|^2} + \frac{k^3}{6\pi\epsilon_0} = -\frac{k^3}{6\pi\epsilon_0}\frac{\sigma^{\mathrm{abs}}}{\sigma^{\mathrm{sca}}} + \frac{k^3}{6\pi\epsilon_0} \tag{C.18}$$

where $\sigma^{\text{abs(sca)}}$ is the absorption (scattering) cross-section of the particle, described by α in the form $\sigma^{\text{abs}} = 4\pi k/\epsilon_0(\text{Im}\{\alpha\} - k^3/(6\pi\epsilon_0)|\alpha|^2)$ and $\sigma^{\text{sca}} = k^4/(6\pi\epsilon_0^2)|\alpha|^2$.

For the case $N = 1$, the imaginary part of the denominator in p can be written as:

$$\text{Im}\Big\{\alpha^{-1} - \mathcal{G}_{11}\Big\} = -\frac{k^3}{6\pi\epsilon_0}\frac{\sigma^{\text{abs}}}{\sigma^{\text{sca}}} - \frac{k}{2\epsilon_0 a^2} \tag{C.19}$$

while performing the same approach with the $N = 2$ case, the imaginary part of the denominators $[\text{Im}\Big\{\beta^{-1} - \Omega_\pm\Big\}]$ can be written in terms of the expressions above as

$$\text{Im}\{\beta^{-1} - \Omega_\pm\} \approx -\frac{k^3}{12\pi\epsilon_0}(\xi_1 + \xi_2) - \frac{k}{2\epsilon_0 a^2} \mp \text{Im}\Big\{\sqrt{\mathcal{G}_{12}^2 + \frac{\delta^2}{4}}\Big\}, \tag{C.20}$$

where as explained in the main text, we have assumed that $|\beta\delta| \ll 1$. We have also defined $\xi_i = \sigma_i^{\text{abs}}/\sigma_i^{\text{sca}}$ in terms of the cross section of particle i in isolation. We can distinguish that the first term (defined by $\xi_{1,2}$) is related to the non-radiative losses. The ± signs denote the different character for the radiative losses for each mode, compared to those in the $N = 1$ case.

Once $\mathbf{p}_l(\mathbf{k}_\parallel)$ and therefore $\mathbf{p}(\mathbf{r}_l)$ are known, we can obtain the explicit form of the electric field, at a position $\mathbf{r} = (\mathbf{R}, z)$, scattered by an square array of particles,

$$\mathbf{E}_{\text{scat}}(\mathbf{r}) = \frac{1}{4\pi\epsilon_0}\sum_l [k^2\mathbf{I} + \nabla\nabla]\frac{e^{ik|\mathbf{r}-\mathbf{r}_l|}}{|\mathbf{r}-\mathbf{r}_l|}\mathbf{p}(\mathbf{r}_l). \tag{C.21}$$

We can split the summation over the whole set of particles into two sums, one over the unit cells and another over the N particles in the unit cell. Then, using the Weyl identity [55], this expression can be rewritten as

$$\mathbf{E}_{\text{scat}}(\mathbf{r}) = \frac{1}{4\pi\epsilon_0}\sum_{\substack{j\in(1..N)\\ \nu}} [k^2\mathbf{I} + \nabla\nabla]\frac{i}{2\pi}\int \frac{d\mathbf{k}_\parallel}{k_z} e^{i\mathbf{k}_\parallel(\mathbf{R}-\mathbf{R}_j-\mathbf{T}_\nu)} e^{ik_z|z|}\mathbf{p}(\mathbf{R}_j + \mathbf{T}_\nu) \tag{C.22}$$

with $k_z = \sqrt{k^2 - (\mathbf{k}_\parallel)^2}$. The sum over $\mathbf{r}_l$ in the lattice is equivalent to sum $\mathbf{R}_j$ particle positions within the first unit cell and then a sum over unit cells with the translation vector $\mathbf{T}_\nu$. The periodicity of the array and the plane-wave illumination allows us to write $\mathbf{p}(\mathbf{R}_j + \mathbf{T}_\nu) = \mathbf{p}_j(\mathbf{k}_\parallel)e^{i\mathbf{k}_\parallel(\mathbf{R}_j+\mathbf{T}_\nu)}$.

$$\mathbf{E}_{\text{scat}}(\mathbf{r}) = \frac{1}{4\pi\epsilon_0}\sum_{\substack{j\in(1..N)\\ \nu}} [k^2\mathbf{I} + \nabla\nabla]\frac{i}{2\pi}\int \frac{d\mathbf{k}_\parallel}{k_z} e^{i\mathbf{k}_\parallel\mathbf{R}} e^{ik_z|z|}\mathbf{p}_j(\mathbf{k}_\parallel) e^{i(\mathbf{k}'_\parallel-\mathbf{k}_\parallel)(\mathbf{R}_j+\mathbf{T}_\nu)}. \tag{C.23}$$

Furthermore, thanks to the periodicity of the array, we have that [178]

$$\sum_\nu e^{i(\mathbf{k}'_\parallel-\mathbf{k}_\parallel)\mathbf{T}_\nu} = \frac{4\pi^2}{a^2}\sum_{\mathbf{q}}\delta(\mathbf{k}_\parallel - \mathbf{k}'_\parallel - \mathbf{q}), \tag{C.24}$$

where $\mathbf{q}$ are the reciprocal lattice vectors of the array and a is its period. Therefore, the expression for the electric field is given by the double sum $(j, \mathbf{q})$ where we have performed the integration involving the delta function and called the final $\mathbf{k}'_{\parallel}$ as $\mathbf{k}_{\parallel}$

$$\mathbf{E}_{\text{scat}}(\mathbf{r}) = \frac{i}{2\epsilon_0 a^2} \sum_{\substack{j\in(1..N)\\ \mathbf{q}}} [k^2\mathcal{I} + \nabla\nabla] \frac{1}{k_{z\mathbf{q}}} e^{i(\mathbf{k}_{\parallel}+\mathbf{q})\mathbf{R}} e^{ik_{z\mathbf{q}}|z|} \mathbf{p}_j(\mathbf{k}_{\parallel}) e^{-i\mathbf{q}\mathbf{R}_j}. \tag{C.25}$$

Then, we assume the conditions introduced in the main text. The array is defined in the xy plane and it is illuminated by a plane wave with amplitude $\mathbf{E}_0 = E_0\hat{\mathbf{x}}$, which propagates with wavevector $\mathbf{k} = (2\pi/\lambda)\hat{\mathbf{z}}$. Under this conditions, only the x-component of the dipole is excited $(\mathbf{p}_j(\mathbf{k}_{\parallel}) = p_{jx}(0) = p_j)$, and the scattered field can be written as

$$\begin{bmatrix} E_x(\mathbf{r}) \\ E_y(\mathbf{r}) \\ E_z(\mathbf{r}) \end{bmatrix} = \frac{i}{2\epsilon_0 a^2} \sum_{\mathbf{q}} \sum_{j=1}^{N} \begin{bmatrix} 1 - \frac{q_x^2}{k^2} \\ \frac{-q_x q_y}{k^2} \\ \pm\frac{q_x k_{z\mathbf{q}}}{k^2} \end{bmatrix} p_j \frac{k^2}{k_{z\mathbf{q}}} e^{ik_{z\mathbf{q}}|z|} e^{i\mathbf{q}(\mathbf{R}-\mathbf{R}_j)} = \sum_{\mathbf{q}} \sum_{j=1}^{2} \mathbf{E}_{\mathbf{q}}(\mathbf{r}), \tag{C.26}$$

where $k_{z\mathbf{q}} = \sqrt{k^2 - \mathbf{q}^2}$ and the upper (lower) signs apply for $z > 0$ $(z < 0)$.

The flux of energy through a surface parallel to the array plane can be written in terms of the time-averaged Poynting vector, $\mathbf{S}_{\text{sca}}$

$$\mathbf{S}_{\text{sca}} = \frac{c^2\epsilon_0}{2} \text{Re}\{\mathbf{E} \times \mathbf{B}^*\}, \tag{C.27}$$

where using $\mathbf{B} = \frac{i}{\omega}\nabla \times \mathbf{E}$

$$\frac{dP_{\text{sca}}}{dA} = \hat{\mathbf{z}} \cdot \mathbf{S}_{\text{sca}}(\mathbf{r}) = \frac{c\epsilon_0}{2k} \sum_{\mathbf{q}} k_{z\mathbf{q}} \Big| \sum_{j=1}^{N} \mathbf{E}_{\mathbf{q}}(\mathbf{r}) \Big|^2. \tag{C.28}$$

As we are interested in the contributions beyond the Rayleigh anomaly, the unique non-evanescent mode that contributes to the far field is the first term $(\mathbf{q} = 0)$. The normalization of the outcoming power flux with $dP_{\text{inc}}/dA = \epsilon_0 c E_0^2/2$ gives the reflectance

$$R = \frac{k^2}{4\epsilon_0^2 a^4 E_0^2} \left| \sum_{j=1}^{N} p_j \right|^2 = \frac{|p|^2}{(2\Pi_0)^2} \tag{C.29}$$

where we used p as the total dipole induced in the unit cell and $\Pi_0 = \epsilon_0 a^2 E_0/k$.

On the other hand, for the transmittance calculation we have to consider both the incident and the scattered fields

$$\mathbf{S}_{\text{tra}}(\mathbf{r}) = \frac{c\epsilon_0}{2k} \left(\text{Re}\Big\{\mathbf{k}\Big\}|E_0|^2 + \sum_{j,\mathbf{q}} k_{z\mathbf{q}} |\mathbf{E}_{\mathbf{q}}(\mathbf{r})|^2 + 2\mathbf{k}\text{Re}\Big\{\mathbf{E}_0\mathbf{E}_{\mathbf{q}=0}\Big\} \right) \tag{C.30}$$

Since our interest is in $\lambda > a$, we again restrict ourselves to the $\mathbf{q} = 0$. The first term is just the contribution of the incident field whereas the second is exactly the scattering considered just above. The correspondent normalization of $\hat{\mathbf{z}} \cdot \mathbf{S}_{\text{tra}}(\mathbf{r})$ with dP_{inc}/dA provides the transmittance, T

$$T = 1 + \frac{k^2}{4\epsilon_0^2 a^4 E_0^2}\Big|p\Big|^2 - \frac{k}{\epsilon_0 a^2 E_0}\text{Im}\Big\{p\Big\} \tag{C.31}$$

Just using energy conservation, the absorbance, $\mathcal{A}$ becomes

$$A = 1 - R - T = \frac{\text{Im}\Big\{p\Big\}}{\Pi_0} - \frac{2|p|^2}{(2\Pi_0)^2} \tag{C.32}$$

Finally, our interest in extinction efficiency arises from the fact that we can calculate the quality factor of the resonances based on the extinction description. For an infinite array, within the coupled dipole model, our array behaves as a thin layer in which the nanoparticles are point-like dipoles. The field scattered by this kind of system has to be symmetric, since no phase is gained by the field while crossing the dipole width [187]. Therefore, the total scattering has to be related to $2R$. Then, the extinction, defined as the combined effects of scattering and absorption, has to be described in terms of $2R+A$. Hence

$$\mathcal{E} = 2R + A = \frac{\text{Im}\Big\{p\Big\}}{\Pi_0}. \tag{C.33}$$

As shown in Ref. [191], the quality factor of lattice resonances can be extracted from the field enhancement produced by the resonances. In this way, as we have showed, the scattered field by an $N = 1$ array of particles is given by the induced dipole in the unit cell $p = E_0/(\alpha^-1 - \mathcal{G}_{11})$, so the enhancement is proportional to $|\alpha^-1 - \mathcal{G}_{11}|^{-2}$. Thus, the quality factor Q has the form:

$$Q \approx \left(1 + \frac{4\pi}{3}\xi\right)^{-1} \left(\frac{1}{2\left(\frac{\lambda_{\text{LR}}}{a} - 1\right)}\right)^{3/2} \tag{C.34}$$

which is valid for wavelengths around the resonance ($\lambda_{\text{LR}}/a \approx 1$). Furthermore, for $D << a$, $4\pi\xi/3 << 1$. Therefore, the quality factor reduces to $Q \sim (\lambda_{\text{LR}}/a - 1)^{-3/2}$. On the other hand, the lattice resonance is given by the condition $\text{Re}\Big\{\alpha^{-1}\Big\} = \text{Re}\Big\{\mathcal{G}_{11}\Big\}$. Those can be written as $\text{Re}\Big\{\alpha^{-1}\Big\} \sim D^{-3}$ and, as shown in Refs. [178] and [254], $\text{Re}\Big\{\mathcal{G}_{11}\Big\} \approx 4\pi^2/(a^3\sqrt{2})(\lambda_{\text{LR}}/a - 1)^{-1/2} - 118$, so we conclude $(\lambda_{\text{LR}}/a - 1) \sim (D/a)^6$, allowing us to write the scaling of the quality factor in terms of a/D as

$$Q \sim \left(\frac{a}{D}\right)^9. \tag{C.35}$$

Bibliography

[1] B. Taylor, W. Parker, and D. Langenberg. Determination of e h, using macroscopic quantum phase coherence in superconductors: Implications for quantum electrodynamics and the fundamental physical constants. Reviews of Modern Physics **41**, 375 (1969). (cited on p. 1)

[2] J. C. Maxwell. A dynamical theory of the electromagnetic field. Philosophical transactions of the Royal Society of London 459–512 (1865). (cited on p. 2)

[3] J. D. Jackson and L. B. Okun. Historical roots of gauge invariance. Reviews of Modern Physics **73**, 663 (2001). (cited on p. 2)

[4] H. Hertz. Ueber die ausbreitungsgeschwindigkeit der electrodynamischen wirkungen. Annalen der Physik **270**, 551 (1888). (cited on p. 2)

[5] R. Pathria. *Statistical mechanics* (Butterworth Heinemann, 1996). (cited on pages 2 and 9)

[6] N. Bohr. On the constitution of atoms and molecules. The London, Edinburgh, and Dublin Philosophical Magazine and Journal of Science **26**, 476 (1913). (cited on p. 2)

[7] P. A. M. Dirac. The quantum theory of the emission and absorption of radiation. Proceedings of the Royal Society of London. Series A, Containing Papers of a Mathematical and Physical Character **114**, 243 (1927). (cited on p. 2)

[8] E. M. Purcell, H. C. Torrey, and R. V. Pound. Resonance absorption by nuclear magnetic moments in a solid. Physical Review **69**, 37 (1946). (cited on pages 2 and 24)

[9] K. Drexhage. Influence of a dielectric interface on fluorescence decay time. Journal of

luminescence **1**, 693 (1970). (cited on p. 3)

[10] D. Kleppner. Inhibited spontaneous emission. Physical Review Letters **47**, 233 (1981). (cited on p. 3)

[11] T. H. Maiman *et al.* Stimulated optical radiation in ruby (1960). (cited on p. 3)

[12] C. Cohen-Tannoudji and S. Haroche. Absorption et diffusion de photons optiques par un atome en interaction avec des photons de radiofréquence. Journal de Physique **30**, 153 (1969). (cited on p. 3)

[13] P. Goy, J. Raimond, M. Gross, and S. Haroche. Observation of cavity-enhanced single-atom spontaneous emission. Physical Review Letters **50**, 1903 (1983). (cited on pages 3 and 28)

[14] S. Haroche. Nobel lecture: Controlling photons in a box and exploring the quantum to classical boundary. Reviews of Modern Physics **85**, 1083 (2013). (cited on p. 3)

[15] S. Haroche and D. Kleppner. Cavity quantum electrodynamics. Physics Today **42**, 24 (1989). (cited on p. 3)

[16] R. H. Ritchie. Plasma losses by fast electrons in thin films. Physical Review **106**, 874 (1957). (cited on p. 3)

[17] T. W. Ebbesen, H. J. Lezec, H. Ghaemi, T. Thio, and P. A. Wolff. Extraordinary optical transmission through sub-wavelength hole arrays. Nature **391**, 667 (1998). (cited on p. 3)

[18] D. K. Gramotnev and S. I. Bozhevolnyi. Plasmonics beyond the diffraction limit. Nature Photonics **4**, 83 (2010). (cited on p. 3)

[19] E. Yablonovitch. Inhibited spontaneous emission in solid-state physics and electronics. Physical Review Letters **58**, 2059 (1987). (cited on pages 3 and 28)

[20] S. John. Strong localization of photons in certain disordered dielectric superlattices. Physical Review Letters **58**, 2486 (1987). (cited on p. 3)

[21] D. R. Smith, W. J. Padilla, D. Vier, S. C. Nemat-Nasser, and S. Schultz. Composite medium with simultaneously negative permeability and permittivity. Physical Review Letters **84**, 4184 (2000). (cited on p. 3)

[22] H. Xu, E. J. Bjerneld, M. Käll, and L. Börjesson. Spectroscopy of single hemoglobin

molecules by surface enhanced raman scattering. Physical Review Letters **83**, 4357 (1999). (cited on p. 3)

[23] H. A. Atwater and A. Polman. Plasmonics for improved photovoltaic devices. Nature Materials 205–213 (2010). (cited on pages 3 and 20)

[24] C. Loo, A. Lowery, N. Halas, J. West, and R. Drezek. Immunotargeted nanoshells for integrated cancer imaging and therapy. Nano Letters **5**, 709 (2005). (cited on p. 3)

[25] D. W. Pohl, W. Denk, and M. Lanz. Optical stethoscopy: Image recording with resolution $\lambda/20$. Applied Physics Letters **44**, 651 (1984). (cited on p. 3)

[26] B. Yang, G. Chen, A. Ghafoor, Y. Zhang, Y. Zhang, Y. Zhang, Y. Luo, J. Yang, V. Sandoghdar, J. Aizpurua, *et al.* Sub-nanometre resolution in single-molecule photoluminescence imaging. Nature Photonics 1–7 (2020). (cited on p. 3)

[27] V. Sandoghdar. Nano-optics in 2020±20. Nano Letters **20**, 4721 (2020). (cited on p. 3)

[28] F. Hayee, L. Yu, J. L. Zhang, C. J. Ciccarino, M. Nguyen, A. F. Marshall, I. Aharonovich, J. Vučković, P. Narang, T. F. Heinz, *et al.* Revealing multiple classes of stable quantum emitters in hexagonal boron nitride with correlated optical and electron microscopy. Nature Materials **19**, 534 (2020). (cited on p. 3)

[29] I. Carusotto and C. Ciuti. Quantum fluids of light. Reviews of Modern Physics **85**, 299 (2013). (cited on p. 3)

[30] A. W. Elshaari, W. Pernice, K. Srinivasan, O. Benson, and V. Zwiller. Hybrid integrated quantum photonic circuits. Nature Photonics **14**, 285 (2020). (cited on p. 3)

[31] L. D. Landau and E. M. Lifshitz. *Mechanics and electrodynamics* (Elsevier, 2013). (cited on p. 4)

[32] G. Barton and G. Barton. *Elements of Green's functions and propagation: potentials, diffusion, and waves* (Oxford University Press, 1989). (cited on p. 7)

[33] G. Grynberg, A. Aspect, and C. Fabre. *Introduction to quantum optics: from the semi-classical approach to quantized light* (Cambridge University Press, 2010). (cited on pages 8, 10, and 21)

[34] D. A. Steck. *Quantum and atom optics* (2007). (cited on p. 8)

[35] G. W. Hanson, F. Lindel, and S. Y. Buhmann. Langevin noise approach for lossy

media and the lossless limit. J. Opt. Soc. Am. B **38**, 758 (2021). (cited on p. 8)

[36] S. Scheel and S. Y. Buhmann. Macroscopic QED - concepts and applications. Acta Physica Slovaca **58**, 675 (2008). (cited on p. 9)

[37] C. Sauvan, J.-P. Hugonin, I. Maksymov, and P. Lalanne. Theory of the spontaneous optical emission of nanosize photonic and plasmon resonators. Physical Review Letters **110**, 237401 (2013). (cited on pages 9 and 25)

[38] S. Franke, S. Hughes, M. K. Dezfouli, P. T. Kristensen, K. Busch, A. Knorr, and M. Richter. Quantization of quasinormal modes for open cavities and plasmonic cavity quantum electrodynamics. Physical Review Letters **122**, 213901 (2019). (cited on pages 9, 23, and 31)

[39] E. Waks and D. Sridharan. Cavity QED treatment of interactions between a metal nanoparticle and a dipole emitter. Physical Review A **82**, 043845 (2010). (cited on pages 9, 48, and 59)

[40] A. Delga, J. Feist, J. Bravo-Abad, and F. Garcia-Vidal. Quantum emitters near a metal nanoparticle: strong coupling and quenching. Physical Review Letters **112**, 253601 (2014). (cited on pages 9, 43, 44, and 53)

[41] S. Hughes, M. Richter, and A. Knorr. Quantized pseudomodes for plasmonic cavity QED. Optics Letters **43**, 1834 (2018). (cited on pages 9 and 31)

[42] I. Medina, F. J. García-Vidal, A. I. Fernández-Domínguez, and J. Feist. Few-mode field quantization of arbitrary electromagnetic spectral densities. Physical Review Letters **126**, 093601 (2021). (cited on pages 9, 23, 60, 90, and 147)

[43] A. Y. Khinchin. *Mathematical foundations of statistical mechanics* (Dover, 1949). (cited on p. 9)

[44] J. Mehra and H. Rechenberg. *The historical development of quantum theory* (Springer Science & Business Media, 2000). (cited on p. 9)

[45] K. E. Oughstun. *Electromagnetic and optical pulse propagation*, volume 1 (Springer, 2006). (cited on p. 9)

[46] M. Fox. *Optical properties of solids* (Oxford University Press, 2002). (cited on p. 9)

[47] J. Mehra. *The Solvay Conferences on physics: Aspects of the development of physics since 1911* (Springer Science & Business Media, 2012). (cited on p. 10)

[48] P. N. Prasad. *Nanophotonics* (John Wiley & Sons, 2004). (cited on p. 11)

[49] S. M. Reimann and M. Manninen. Electronic structure of quantum dots. Reviews of Modern Physics **74**, 1283 (2002). (cited on p. 11)

[50] G. D. Scholes and G. Rumbles. Excitons in nanoscale systems. Nature Materials 683–696 (2006). (cited on p. 11)

[51] D. Zhao, R. E. Silva, C. Climent, J. Feist, A. I. Fernández-Domínguez, and F. J. García-Vidal. Impact of vibrational modes in the plasmonic purcell effect of organic molecules. ACS Photonics **7**, 3369 (2020). (cited on p. 12)

[52] M. Dressel and G. Grüner. *Electrodynamics of solids: optical properties of electrons in matter* (Cambridge University Press, 2002). (cited on p. 13)

[53] S. I. Bozhevolnyi, L. Martin-Moreno, and F. Garcia-Vidal. *Quantum plasmonics* (Springer, 2017). (cited on p. 13)

[54] D. Pines. *Theory of Quantum Liquids: Normal Fermi Liquids* (CRC Press, 2018). (cited on p. 13)

[55] L. Novotny and B. Hecht. *Principles of Nano-Optics* (Cambridge University Press, 2012).
(cited on pages 17, 21, 22, 24, 38, 40, 76, 77, 78, 107, 108, 125, 134, 176, and 177)

[56] S. A. Maier. *Plasmonics: fundamentals and applications* (Springer Science & Business Media, 2007). (cited on pages 17, 18, 41, 48, 103, and 108)

[57] C. F. Bohren and D. R. Huffman. *Absorption and scattering of light by small particles* (John Wiley & Sons, 2008). (cited on p. 18)

[58] N. J. Halas, S. Lal, W.-S. Chang, S. Link, and P. Nordlander. Plasmons in strongly coupled metallic nanostructures. Chemical Reviews **111**, 3913 (2011).
(cited on pages 19 and 109)

[59] M. I. Stockman. Dark-hot resonances. Nature **467**, 541 (2010). (cited on p. 19)

[60] M. Liu, T.-W. Lee, S. K. Gray, P. Guyot-Sionnest, M. Pelton, *et al.* Excitation of dark plasmons in metal nanoparticles by a localized emitter. Physical Review Letters **102**, 107401 (2009). (cited on p. 19)

[61] E. Prodan, C. Radloff, N. J. Halas, and P. Nordlander. A hybridization model for the

plasmon response of complex nanostructures. Science **302**, 419 (2003). (cited on pages 19 and 109)

[62] P. Nordlander, C. Oubre, E. Prodan, K. Li, and M. Stockman. Plasmon hybridization in nanoparticle dimers. Nano Letters **4**, 899 (2004). (cited on p. 19)

[63] A. Aubry, D. Y. Lei, S. A. Maier, and J. Pendry. Interaction between plasmonic nanoparticles revisited with transformation optics. Physical Review Letters **105**, 233901 (2010). (cited on p. 20)

[64] A. Aubry, D. Y. Lei, S. A. Maier, and J. B. Pendry. Plasmonic hybridization between nanowires and a metallic surface: a transformation optics approach. ACS Nano **5**, 3293 (2011). (cited on pages 20, 31, 32, 41, 64, 65, 68, 92, and 98)

[65] A. Fernández-Domínguez, S. Maier, and J. Pendry. Collection and concentration of light by touching spheres: a transformation optics approach. Physical Review Letters **105**, 266807 (2010). (cited on pages 20 and 32)

[66] A. Aubry, D. Y. Lei, S. A. Maier, and J. Pendry. Broadband plasmonic device concentrating the energy at the nanoscale: The crescent-shaped cylinder. Physical Review B **82**, 125430 (2010). (cited on pages 20 and 32)

[67] A. Aubry, D. Y. Lei, S. A. Maier, and J. Pendry. Conformal transformation applied to plasmonics beyond the quasistatic limit. Physical Review B **82**, 205109 (2010). (cited on pages 20, 64, and 78)

[68] R. Loudon. *The Quantum Theory of Light* (OUP Oxford, 2000). (cited on pages 21 and 78)

[69] V. Weisskopf and E. Wigner. Berechnung der natürlichen linienbreite auf grund der diracschen lichttheorie. In *Part I: Particles and Fields. Part II: Foundations of Quantum Mechanics*, 30–49 (Springer, 1997). (cited on p. 21)

[70] P. Biagioni, J.-S. Huang, and B. Hecht. Nanoantennas for visible and infrared radiation. Reports on Progress in Physics **75**, 024402 (2012). (cited on p. 22)

[71] P. Bharadwaj, B. Deutsch, and L. Novotny. Optical antennas. Advances in Optics and Photonics **1**, 438 (2009). (cited on p. 22)

[72] L. Novotny and N. Van Hulst. Antennas for light. Nature Photonics **5**, 83 (2011). (cited on pages 22, 59, and 127)

[73] H. J. Carmichael. *Statistical Methods in Quantum Optics 1: Master Equations and Fokker-Planck Equations* (Springer Science & Business Media, 2013). (cited on p. 23)

[74] A. Imamoglu. Stochastic wave-function approach to non-markovian systems. Physical Review A **50**, 3650 (1994). (cited on pages 24 and 167)

[75] B. Garraway. Nonperturbative decay of an atomic system in a cavity. Physical Review A **55**, 2290 (1997). (cited on p. 24)

[76] H.-P. Breuer, F. Petruccione, *et al.* *The Theory of Open Quantum Systems* (Oxford University Press, 2002). (cited on p. 24)

[77] C. Carlson and S. Hughes. Dissipative modes, Purcell factors, and directional beta factors in gold bowtie nanoantenna structures. Physical Review B **102**, 155301 (2020). (cited on p. 25)

[78] K. H. Madsen, S. Ates, T. Lund-Hansen, A. Löffler, S. Reitzenstein, A. Forchel, and P. Lodahl. Observation of non-markovian dynamics of a single quantum dot in a micropillar cavity. Physical Review Letters **106**, 233601 (2011). (cited on p. 25)

[79] K. V. Nerkararyan and S. I. Bozhevolnyi. Relaxation dynamics of a quantum emitter resonantly coupled to a coherent state of a localized surface plasmon. Faraday Discussions **178**, 295 (2015). (cited on p. 25)

[80] A. Manjavacas, F. J. García de Abajo, and P. Nordlander. Quantum plexcitonics: strongly interacting plasmons and excitons. Nano Letters **11**, 2318 (2011). (cited on pages 26 and 69)

[81] R.-Q. Li, F. García-Vidal, and A. Fernández-Domínguez. Plasmon-exciton coupling in symmetry-broken nanocavities. ACS Photonics **5**, 177 (2018). (cited on pages 26, 31, and 34)

[82] A. F. Koenderink. On the use of purcell factors for plasmon antennas. Optics letters **35**, 4208 (2010). (cited on p. 27)

[83] S. A. Maier. Plasmonic field enhancement and sers in the effective mode volume picture. Optics Express **14**, 1957 (2006). (cited on p. 27)

[84] P. T. Kristensen and S. Hughes. Modes and mode volumes of leaky optical cavities and plasmonic nanoresonators. ACS Photonics **1**, 2 (2014). (cited on p. 28)

[85] Y. Kaluzny, P. Goy, M. Gross, J. Raimond, and S. Haroche. Observation of self-induced

rabi oscillations in two-level atoms excited inside a resonant cavity: The ringing regime of superradiance. Physical Review Letters **51**, 1175 (1983). (cited on p. 28)

[86] M.-K. Kim, H. Sim, S. J. Yoon, S.-H. Gong, C. W. Ahn, Y.-H. Cho, and Y.-H. Lee. Squeezing photons into a point-like space. Nano Letters **15**, 4102 (2015). (cited on p. 28)

[87] F. Benz, M. K. Schmidt, A. Dreismann, R. Chikkaraddy, Y. Zhang, A. Demetriadou, C. Carnegie, H. Ohadi, B. De Nijs, R. Esteban, *et al.* Single-molecule optomechanics in "picocavities". Science **354**, 726 (2016). (cited on pages 28, 34, 55, and 81)

[88] A. V. Kavokin, J. J. Baumberg, G. Malpuech, and F. P. Laussy. *Microcavities*, volume 21 (Oxford University Press, 2017). (cited on p. 28)

[89] G. Ramon, U. Mizrahi, N. Akopian, S. Braitbart, D. Gershoni, T. Reinecke, B. D. Gerardot, and P. Petroff. Emission characteristics of quantum dots in planar microcavities. Physical Review B **73**, 205330 (2006). (cited on p. 28)

[90] J. P. Reithmaier, G. Sek, A. Löffler, C. Hofmann, S. Kuhn, S. Reitzenstein, L. Keldysh, V. Kulakovskii, T. Reinecke, and A. Forchel. Strong coupling in a single quantum dot–semiconductor microcavity system. Nature **432**, 197 (2004). (cited on p. 28)

[91] D. Vernooy, V. S. Ilchenko, H. Mabuchi, E. Streed, and H. Kimble. High-Q measurements of fused-silica microspheres in the near infrared. Optics Letters **23**, 247 (1998). (cited on p. 28)

[92] J. D. Joannopoulos, P. R. Villeneuve, and S. Fan. Photonic crystals: putting a new twist on light. Nature **386**, 143 (1997). (cited on p. 28)

[93] E. Moreno, D. Erni, and C. Hafner. Modeling of discontinuities in photonic crystal waveguides with the multiple multipole method. Physical Review E **66**, 036618 (2002). (cited on p. 28)

[94] P. R. Villeneuve, S. Fan, and J. Joannopoulos. Microcavities in photonic crystals: Mode symmetry, tunability, and coupling efficiency. Physical Review B **54**, 7837 (1996). (cited on p. 28)

[95] D. Dzsotjan, B. Rousseaux, H. Jauslin, G. C. des Francs, C. Couteau, and S. Guerin. Mode-selective quantization and multimodal effective models for spherically layered systems. Physical Review A **94**, 023818 (2016). (cited on p. 31)

[96] R.-Q. Li, D. Hernángomez-Pérez, F. García-Vidal, and A. I. Fernández-Domínguez.

Transformation optics approach to plasmon-exciton strong coupling in nanocavities. Physical Review Letters **117**, 107401 (2016). (cited on pages 31, 34, 43, 44, 52, 60, 94, and 133)

[97] A. Cuartero-González and A. I. Fernández-Domínguez. Light-forbidden transitions in plasmon-emitter interactions beyond the weak coupling regime. ACS Photonics **5**, 3415 (2018). (cited on pages 31, 71, and 72)

[98] A. Demetriadou, J. M. Hamm, Y. Luo, J. B. Pendry, J. J. Baumberg, and O. Hess. Spatiotemporal dynamics and control of strong coupling in plasmonic nanocavities. ACS Photonics **4**, 2410 (2017). (cited on pages 31, 64, and 65)

[99] D. Schurig, J. Pendry, and D. R. Smith. Calculation of material properties and ray tracing in transformation media. Optics Express **14**, 9794 (2006). (cited on p. 32)

[100] D. Schurig, J. Pendry, and D. Smith. Transformation-designed optical elements. Optics Express **15**, 14772 (2007). (cited on p. 32)

[101] A. Ward and J. B. Pendry. Refraction and geometry in Maxwell's equations. Journal of modern optics **43**, 773 (1996). (cited on pages 32 and 33)

[102] J. B. Pendry, D. Schurig, and D. R. Smith. Controlling electromagnetic fields. Science **312**, 1780 (2006). (cited on p. 32)

[103] D. Schurig, J. J. Mock, B. Justice, S. A. Cummer, J. B. Pendry, A. F. Starr, and D. R. Smith. Metamaterial electromagnetic cloak at microwave frequencies. Science **314**, 977 (2006). (cited on p. 32)

[104] T. Bückmann, M. Kadic, R. Schittny, and M. Wegener. Mechanical cloak design by direct lattice transformation. Proceedings of the National Academy of Sciences **112**, 4930 (2015). (cited on p. 32)

[105] M. Brun, S. Guenneau, and A. B. Movchan. Achieving control of in-plane elastic waves. Applied physics letters **94**, 061903 (2009). (cited on p. 32)

[106] S. Brûlé, E. Javelaud, S. Enoch, and S. Guenneau. Experiments on seismic metamaterials: molding surface waves. Physical Review Letters **112**, 133901 (2014). (cited on p. 32)

[107] A. I. Fernández-Domínguez, Y. Luo, A. Wiener, J. Pendry, and S. A. Maier. Theory of three-dimensional nanocrescent light harvesters. Nano Letters **12**, 5946 (2012). (cited on p. 32)

[108] M. Kraft, J. Pendry, S. Maier, and Y. Luo. Transformation optics and hidden symmetries. Physical Review B **89**, 245125 (2014). (cited on p. 32)

[109] J. Pendry, A. Fernández-Domínguez, Y. Luo, and R. Zhao. Capturing photons with transformation optics. Nature Physics **9**, 518 (2013). (cited on p. 32)

[110] V. Pacheco-Peña, M. Beruete, A. I. Fernández-Domínguez, Y. Luo, and M. Navarro-Cía. Description of bow-tie nanoantennas excited by localized emitters using conformal transformation. ACS Photonics **3**, 1223 (2016). (cited on p. 32)

[111] V. Pacheco-Peña, A. I. Fernández-Domínguez, Y. Luo, M. Beruete, and M. Navarro-Cía. Aluminum nanotripods for light-matter coupling robust to nanoemitter orientation. Laser & Photonics Reviews **11**, 1700051 (2017). (cited on p. 32)

[112] L. V. Bewley. *Two-dimensional fields in electrical engineering* (Macmillan, 1948). (cited on p. 33)

[113] D. Knebl, A. Hörl, A. Trügler, J. Kern, J. R. Krenn, P. Puschnig, and U. Hohenester. Gap plasmonics of silver nanocube dimers. Physical Review B **93**, 081405 (2016). (cited on p. 34)

[114] P. Aravind and H. Metiu. Use of a perfectly conducting sphere to excite the plasmon of a flat surface. 1. calculation of the local field with applications to surface-enhanced spectroscopy. The Journal of Physical Chemistry **86**, 5076 (1982). (cited on p. 34)

[115] G.-C. Li, Q. Zhang, S. A. Maier, and D. Lei. Plasmonic particle-on-film nanocavities: a versatile platform for plasmon-enhanced spectroscopy and photochemistry. Nanophotonics **7**, 1865 (2018). (cited on p. 34)

[116] J. J. Baumberg, J. Aizpurua, M. H. Mikkelsen, and D. R. Smith. Extreme nanophotonics from ultrathin metallic gaps. Nature Materials **18**, 668 (2019). (cited on p. 34)

[117] T. B. Hoang, G. M. Akselrod, C. Argyropoulos, J. Huang, D. R. Smith, and M. H. Mikkelsen. Ultrafast spontaneous emission source using plasmonic nanoantennas. Nature Communications **6**, 1 (2015). (cited on p. 34)

[118] R. Chikkaraddy, B. De Nijs, F. Benz, S. J. Barrow, O. A. Scherman, E. Rosta, A. Demetriadou, P. Fox, O. Hess, and J. J. Baumberg. Single-molecule strong coupling at room temperature in plasmonic nanocavities. Nature **535**, 127 (2016). (cited on pages 34, 36, 50, 60, 70, 81, 82, 97, 98, and 146)

[119] C. Tserkezis, R. Esteban, D. O. Sigle, J. Mertens, L. O. Herrmann, J. J. Baumberg, and J. Aizpurua. Hybridization of plasmonic antenna and cavity modes: Extreme optics of nanoparticle-on-mirror nanogaps. Physical Review A **92**, 053811 (2015). (cited on p. 34)

[120] R. Chikkaraddy, X. Zheng, F. Benz, L. J. Brooks, B. De Nijs, C. Carnegie, M.-E. Kleemann, J. Mertens, R. W. Bowman, G. A. Vandenbosch, *et al.* How ultranarrow gap symmetries control plasmonic nanocavity modes: from cubes to spheres in the nanoparticle-on-mirror. ACS Photonics **4**, 469 (2017). (cited on p. 34)

[121] R. Esteban, G. Aguirregabiria, A. G. Borisov, Y. M. Wang, P. Nordlander, G. W. Bryant, and J. Aizpurua. The morphology of narrow gaps modifies the plasmonic response. ACS Photonics **2**, 295 (2015). (cited on p. 34)

[122] M. Urbieta, M. Barbry, Y. Zhang, P. Koval, D. Sánchez-Portal, N. Zabala, and J. Aizpurua. Atomic-scale lightning rod effect in plasmonic picocavities: a classical view to a quantum effect. ACS Nano **12**, 585 (2018). (cited on p. 34)

[123] N. Kongsuwan, A. Demetriadou, M. Horton, R. Chikkaraddy, J. J. Baumberg, and O. Hess. Plasmonic nanocavity modes: From near-field to far-field radiation. ACS Photonics **7**, 463 (2020). (cited on p. 34)

[124] A. Fernández-Domínguez, A. Wiener, F. García-Vidal, S. Maier, and J. Pendry. Transformation-optics description of nonlocal effects in plasmonic nanostructures. Physical Review Letters **108**, 106802 (2012). (cited on p. 34)

[125] N. Kongsuwan, A. Demetriadou, R. Chikkaraddy, F. Benz, V. A. Turek, U. F. Keyser, J. J. Baumberg, and O. Hess. Suppressed quenching and strong-coupling of purcell-enhanced single-molecule emission in plasmonic nanocavities. ACS Photonics **5**, 186 (2018). (cited on p. 36)

[126] E. Economou. Surface plasmons in thin films. Physical Review **182**, 539 (1969). (cited on p. 41)

[127] J. Dionne, L. Sweatlock, H. Atwater, and A. Polman. Planar metal plasmon waveguides: frequency-dependent dispersion, propagation, localization, and loss beyond the free electron model. Physical Review B **72**, 075405 (2005). (cited on p. 41)

[128] I. Kaminska, C. Vietz, Á. Cuartero-González, P. Tinnefeld, A. I. Fernández-Domínguez, and G. P. Acuna. Strong plasmonic enhancement of single molecule photostability in silver dimer optical antennas. Nanophotonics **7**, 643 (2018).

(cited on pages 43 and 129)

[129] V. Klimov and M. Ducloy. Quadrupole transitions near an interface: general theory and application to an atom inside a planar cavity. Physical Review A **72**, 043809 (2005). (cited on p. 47)

[130] M. L. Andersen, S. Stobbe, A. S. Sørensen, and P. Lodahl. Strongly modified plasmon–matter interaction with mesoscopic quantum emitters. Nature Physics **7**, 215 (2011). (cited on p. 55)

[131] T. Neuman, R. Esteban, D. Casanova, F. J. García-Vidal, and J. Aizpurua. Coupling of molecular emitters and plasmonic cavities beyond the point-dipole approximation. Nano Letters **18**, 2358 (2018). (cited on pages 55 and 70)

[132] A. González-Tudela, P. Huidobro, L. Martín-Moreno, C. Tejedor, and F. García-Vidal. Reversible dynamics of single quantum emitters near metal-dielectric interfaces. Physical Review B **89**, 041402 (2014). (cited on p. 60)

[133] C. Weisbuch, M. Nishioka, A. Ishikawa, and Y. Arakawa. Observation of the coupled exciton-photon mode splitting in a semiconductor quantum microcavity. Physical Review Letters **69**, 3314 (1992). (cited on p. 60)

[134] J. Baumberg, P. Savvidis, R. Stevenson, A. Tartakovskii, M. Skolnick, D. Whittaker, and J. Roberts. Parametric oscillation in a vertical microcavity: A polariton condensate or micro-optical parametric oscillation. Physical Review B **62**, R16247 (2000). (cited on p. 60)

[135] K. Daskalakis, S. Maier, R. Murray, and S. Kéna-Cohen. Nonlinear interactions in an organic polariton condensate. Nature Materials **13**, 271 (2014). (cited on p. 60)

[136] D. Y. Lei, A. I. Fernández-Domínguez, Y. Sonnefraud, K. Appavoo, R. F. Haglund Jr, J. B. Pendry, and S. A. Maier. Revealing plasmonic gap modes in particle-on-film systems using dark-field spectroscopy. ACS Nano **6**, 1380 (2012). (cited on p. 64)

[137] O. S. Ojambati, R. Chikkaraddy, W. D. Deacon, M. Horton, D. Kos, V. A. Turek, U. F. Keyser, and J. J. Baumberg. Quantum electrodynamics at room temperature coupling a single vibrating molecule with a plasmonic nanocavity. Nature Communications **10**, 1 (2019). (cited on p. 64)

[138] R. Sáez-Blázquez, J. Feist, A. I. Fernández-Domínguez, and F. J. García-Vidal. Enhancing photon correlations through plasmonic strong coupling. Optica **4**, 1363

(2017). (cited on pages 66, 68, and 69)

[139] R. Sáez-Blázquez, J. Feist, F. García-Vidal, and A. Fernández-Domínguez. Photon statistics in collective strong coupling: Nanocavities and microcavities. Physical Review A **98**, 013839 (2018). (cited on p. 66)

[140] P. Visser and G. Nienhuis. Solution of quantum master equations in terms of a non-hermitian hamiltonian. Physical Review A **52**, 4727 (1995). (cited on p. 68)

[141] C. Ciracì, R. Hill, J. Mock, Y. Urzhumov, A. Fernández-Domínguez, S. Maier, J. Pendry, A. Chilkoti, and D. Smith. Probing the ultimate limits of plasmonic enhancement. Science **337**, 1072 (2012). (cited on pages 69 and 125)

[142] S. Savasta, R. Saija, A. Ridolfo, O. Di Stefano, P. Denti, and F. Borghese. Nanopolaritons: vacuum rabi splitting with a single quantum dot in the center of a dimer nanoantenna. ACS Nano **4**, 6369 (2010). (cited on p. 69)

[143] G. Zengin, M. Wersäll, S. Nilsson, T. J. Antosiewicz, M. Käll, and T. Shegai. Realizing strong light-matter interactions between single-nanoparticle plasmons and molecular excitons at ambient conditions. Physical Review Letters **114**, 157401 (2015). (cited on p. 70)

[144] K. Santhosh, O. Bitton, L. Chuntonov, and G. Haran. Vacuum rabi splitting in a plasmonic cavity at the single quantum emitter limit. Nature Communications **7**, 1 (2016). (cited on p. 70)

[145] A. Ridolfo, O. Di Stefano, N. Fina, R. Saija, and S. Savasta. Quantum plasmonics with quantum dot-metal nanoparticle molecules: influence of the fano effect on photon statistics. Physical Review Letters **105**, 263601 (2010). (cited on p. 70)

[146] H. Leng, B. Szychowski, M.-C. Daniel, and M. Pelton. Strong coupling and induced transparency at room temperature with single quantum dots and gap plasmons. Nature Communications **9**, 1 (2018). (cited on pages 70 and 82)

[147] N. Rivera, I. Kaminer, B. Zhen, J. D. Joannopoulos, and M. Soljačić. Shrinking light to allow forbidden transitions on the atomic scale. Science **353**, 263 (2016). (cited on p. 76)

[148] S. Sanders, A. May, A. Alabastri, and A. Manjavacas. Extraordinary enhancement of quadrupolar transitions using nanostructured graphene. ACS Photonics **5**, 3282 (2018). (cited on p. 76)

[149] R. Carminati, J.-J. Greffet, C. Henkel, and J.-M. Vigoureux. Radiative and non-radiative decay of a single molecule close to a metallic nanoparticle. Optics Communications **261**, 368 (2006). (cited on p. 77)

[150] S. Albaladejo, R. Gómez-Medina, L. S. Froufe-Pérez, H. Marinchio, R. Carminati, J. Torrado, G. Armelles, A. García-Martín, and J. J. Sáenz. Radiative corrections to the polarizability tensor of an electrically small anisotropic dielectric particle. Optics Express **18**, 3556 (2010). (cited on p. 78)

[151] G. B. Arfken and H. J. Weber. *Mathematical methods for physicists* (American Association of Physics Teachers, 1999). (cited on p. 79)

[152] N. Passarelli, R. Bustos-Marún, and R. Depine. Lasing conditions of transverse electromagnetic modes in metallic-coated micro-and nanotubes. The Journal of Physical Chemistry C **123**, 13015 (2019). (cited on p. 79)

[153] G. Kewes, F. Binkowski, S. Burger, L. Zschiedrich, and O. Benson. Heuristic modeling of strong coupling in plasmonic resonators. ACS Photonics **5**, 4089 (2018). (cited on p. 81)

[154] J. Bohlen, Á. Cuartero-González, E. Pibiri, D. Ruhlandt, A. I. Fernández-Domínguez, P. Tinnefeld, and G. P. Acuna. Plasmon-assisted förster resonance energy transfer at the single-molecule level in the moderate quenching regime. Nanoscale **11**, 7674 (2019). (cited on p. 81)

[155] C. Gonzalez-Ballestero, J. Feist, E. Moreno, and F. J. Garcia-Vidal. Harvesting excitons through plasmonic strong coupling. Physical Review B **92**, 121402 (2015). (cited on pages 81 and 139)

[156] R. Sáez-Blázquez, J. Feist, F. J. García-Vidal, and A. I. Fernández-Domínguez. Theory of energy transfer in organic nanocrystals. Advanced Optical Materials **8**, 2001447 (2020). (cited on p. 81)

[157] A. Cuartero-González and A. I. Fernández-Domínguez. Dipolar and quadrupolar excitons coupled to a nanoparticle-on-mirror cavity. Physical Review B **101**, 035403 (2020). (cited on p. 84)

[158] B. Dalton, S. M. Barnett, and B. Garraway. Theory of pseudomodes in quantum optical processes. Physical Review A **64**, 053813 (2001). (cited on p. 90)

[159] S. Glutsch. Optical absorption of the fano model: General case of many resonances and

many continua. Physical Review B **66**, 075310 (2002). (cited on p. 90)

[160] S. Derom, R. Vincent, A. Bouhelier, and G. C. des Francs. Resonance quality, radiative/ohmic losses and modal volume of mie plasmons. EPL (Europhysics Letters) **98**, 47008 (2012). (cited on p. 104)

[161] B. Doiron, M. Mota, M. P. Wells, R. Bower, A. Mihai, Y. Li, L. F. Cohen, N. M. Alford, P. K. Petrov, R. F. Oulton, *et al.* Quantifying figures of merit for localized surface plasmon resonance applications: a materials survey. ACS Photonics **6**, 240 (2019). (cited on p. 104)

[162] A. Asenjo-Garcia, M. Moreno-Cardoner, A. Albrecht, H. Kimble, and D. E. Chang. Exponential improvement in photon storage fidelities using subradiance and "selective radiance" in atomic arrays. Physical Review X **7**, 031024 (2017). (cited on p. 104)

[163] S. J. Masson and A. Asenjo-Garcia. Universality of dicke superradiance in atomic arrays. arXiv preprint arXiv:2106.02042 (2021). (cited on p. 104)

[164] M. L. Brongersma, N. J. Halas, and P. Nordlander. Plasmon-induced hot carrier science and technology. Nature Nanotechnology **10**, 25 (2015). (cited on p. 104)

[165] J. N. Anker, W. P. Hall, O. Lyandres, N. C. Shah, J. Zhao, and R. P. Van Duyne. Biosensing with plasmonic nanosensors. Nanoscience and Technology: A Collection of Reviews from Nature Journals 308–319 (2010). (cited on p. 104)

[166] B. Luk'yanchuk, N. I. Zheludev, S. A. Maier, N. J. Halas, P. Nordlander, H. Giessen, and C. T. Chong. The fano resonance in plasmonic nanostructures and metamaterials. Nature Materials **9**, 707 (2010). (cited on pages 104 and 109)

[167] A. E. Miroshnichenko, S. Flach, and Y. S. Kivshar. Fano resonances in nanoscale structures. Reviews of Modern Physics **82**, 2257 (2010). (cited on p. 104)

[168] V. Giannini, Y. Francescato, H. Amrania, C. C. Phillips, and S. A. Maier. Fano resonances in nanoscale plasmonic systems: a parameter-free modeling approach. Nano Letters **11**, 2835 (2011). (cited on pages 104 and 109)

[169] L. Zhao, K. L. Kelly, and G. C. Schatz. The extinction spectra of silver nanoparticle arrays: influence of array structure on plasmon resonance wavelength and width. The Journal of Physical Chemistry B **107**, 7343 (2003). (cited on pages 104 and 105)

[170] S. Zou, N. Janel, and G. C. Schatz. Silver nanoparticle array structures that produce remarkably narrow plasmon lineshapes. The Journal of chemical physics **120**, 10871

(2004). (cited on pages 104 and 108)

[171] B. Auguié and W. L. Barnes. Collective resonances in gold nanoparticle arrays. Physical Review Letters **101**, 143902 (2008). (cited on p. 104)

[172] M. S. Bin-Alam, O. Reshef, Y. Mamchur, M. Z. Alam, G. Carlow, J. Upham, B. T. Sullivan, J.-M. Ménard, M. J. Huttunen, R. W. Boyd, *et al.* Ultra-high-q resonances in plasmonic metasurfaces. Nature Communications **12**, 1 (2021). (cited on pages 104 and 121)

[173] W. Zhou, M. Dridi, J. Y. Suh, C. H. Kim, D. T. Co, M. R. Wasielewski, G. C. Schatz, T. W. Odom, *et al.* Lasing action in strongly coupled plasmonic nanocavity arrays. Nature Nanotechnology **8**, 506 (2013). (cited on p. 104)

[174] G. Lozano, G. Grzela, M. A. Verschuuren, M. Ramezani, and J. G. Rivas. Tailor-made directional emission in nanoimprinted plasmonic-based light-emitting devices. Nanoscale **6**, 9223 (2014). (cited on p. 104)

[175] Y. Zakharko, M. Held, A. Graf, T. Rödlmeier, R. Eckstein, G. Hernandez-Sosa, B. Hähnlein, J. Pezoldt, and J. Zaumseil. Surface lattice resonances for enhanced and directional electroluminescence at high current densities. ACS Photonics **3**, 2225 (2016). (cited on p. 104)

[176] A. Väkeväinen, R. Moerland, H. Rekola, A.-P. Eskelinen, J.-P. Martikainen, D.-H. Kim, and P. Törmä. Plasmonic surface lattice resonances at the strong coupling regime. Nano Letters **14**, 1721 (2014). (cited on p. 104)

[177] T. K. Hakala, A. J. Moilanen, A. I. Väkeväinen, R. Guo, J.-P. Martikainen, K. S. Daskalakis, H. T. Rekola, A. Julku, and P. Törmä. Bose–einstein condensation in a plasmonic lattice. Nature Physics **14**, 739 (2018). (cited on p. 104)

[178] F. G. De Abajo. Colloquium: Light scattering by particle and hole arrays. Reviews of Modern Physics **79**, 1267 (2007). (cited on pages 105, 107, 110, 175, 176, 177, and 179)

[179] T. Teperik and A. Degiron. Design strategies to tailor the narrow plasmon-photonic resonances in arrays of metallic nanoparticles. Physical Review B **86**, 245425 (2012). (cited on pages 105, 106, 107, 108, 110, and 176)

[180] S. Baur, S. Sanders, and A. Manjavacas. Hybridization of lattice resonances. ACS Nano **12**, 1618 (2018). (cited on pages 107, 109, 110, 116, 173, and 176)

[181] M. Manzoni, M. Moreno-Cardoner, A. Asenjo-Garcia, J. V. Porto, A. V. Gorshkov, and

D. Chang. Optimization of photon storage fidelity in ordered atomic arrays. New Journal of Physics **20**, 083048 (2018). (cited on p. 107)

[182] K. Kambe. Theory of low-energy electron diffraction. Zeitschrift für Naturforschung A **23**, 1280 (1968). (cited on p. 107)

[183] F. G. De Abajo. Multiple scattering of radiation in clusters of dielectrics. Physical Review B **60**, 6086 (1999). (cited on pages 107 and 173)

[184] M. Hentschel, M. Saliba, R. Vogelgesang, H. Giessen, A. P. Alivisatos, and N. Liu. Transition from isolated to collective modes in plasmonic oligomers. Nano Letters **10**, 2721 (2010). (cited on p. 109)

[185] M. Hentschel, D. Dregely, R. Vogelgesang, H. Giessen, and N. Liu. Plasmonic oligomers: the role of individual particles in collective behavior. ACS Nano **5**, 2042 (2011). (cited on p. 109)

[186] G. Bachelier, I. Russier-Antoine, E. Benichou, C. Jonin, N. Del Fatti, F. Vallée, and P.-F. Brevet. Fano profiles induced by near-field coupling in heterogeneous dimers of gold and silver nanoparticles. Physical Review Letters **101**, 197401 (2008). (cited on p. 109)

[187] S. Thongrattanasiri, F. H. Koppens, and F. J. G. De Abajo. Complete optical absorption in periodically patterned graphene. Physical Review Letters **108**, 047401 (2012). (cited on pages 112, 119, 120, 121, and 179)

[188] D. R. Abujetas, N. van Hoof, S. ter Huurne, J. G. Rivas, and J. A. Sánchez-Gil. Spectral and temporal evidence of robust photonic bound states in the continuum on terahertz metasurfaces. Optica **6**, 996 (2019). (cited on p. 114)

[189] S. Tretyakov. Maximizing absorption and scattering by dipole particles. Plasmonics **9**, 935 (2014). (cited on p. 120)

[190] A. Alabastri, M. Malerba, E. Calandrini, A. Manjavacas, F. De Angelis, A. Toma, and R. Proietti Zaccaria. Controlling the heat dissipation in temperature-matched plasmonic nanostructures. Nano Letters **17**, 5472 (2017). (cited on p. 120)

[191] A. Manjavacas, L. Zundel, and S. Sanders. Analysis of the limits of the near-field produced by nanoparticle arrays. ACS Nano **13**, 10682 (2019). (cited on pages 121 and 179)

[192] T. J. Kucharski, Y. Tian, S. Akbulatov, and R. Boulatov. Chemical solutions for the

closed-cycle storage of solar energy. Energy & Environmental Science **4**, 4449 (2011). (cited on p. 124)

[193] M. Guentner, M. Schildhauer, S. Thumser, P. Mayer, D. Stephenson, P. J. Mayer, and H. Dube. Sunlight-powered khz rotation of a hemithioindigo-based molecular motor. Nature Communications **6**, 1 (2015). (cited on p. 124)

[194] B. Zietz, E. Gabrielsson, V. Johansson, A. M. El-Zohry, L. Sun, and L. Kloo. Photoisomerization of the cyanoacrylic acid acceptor group–a potential problem for organic dyes in solar cells. Physical Chemistry Chemical Physics **16**, 2251 (2014). (cited on p. 124)

[195] R. P. Sinha and D.-P. Häder. UV-induced DNA damage and repair: a review. Photochemical & Photobiological Sciences **1**, 225 (2002). (cited on p. 124)

[196] S. Shashkova and M. C. Leake. Single-molecule fluorescence microscopy review: shedding new light on old problems. Bioscience reports **37**, BSR20170031 (2017). (cited on p. 124)

[197] B. Lounis and M. Orrit. Single-photon sources. Reports on Progress in Physics **68**, 1129 (2005). (cited on p. 124)

[198] V. Balzani, P. Ceroni, and A. Juris. *Photochemistry and photophysics: concepts, research, applications* (John Wiley & Sons, 2014). (cited on pages 124 and 134)

[199] A. Nitzan, J. Jortner, and P. M. Rentzepis. Internal conversion in large molecules. Molecular Physics **22**, 585 (1971). (cited on p. 124)

[200] V. May and O. Kühn. *Charge and energy transfer dynamics in molecular systems* (John Wiley & Sons, 2008). (cited on p. 124)

[201] C. M. Marian. Spin–orbit coupling and intersystem crossing in molecules. Wiley Interdisciplinary Reviews: Computational Molecular Science **2**, 187 (2012). (cited on p. 124)

[202] G. M. Barrow. *The structure of molecules* (WA Benjamin, 1963). (cited on p. 124)

[203] M. Kuttge, F. J. García de Abajo, and A. Polman. Ultrasmall mode volume plasmonic nanodisk resonators. Nano Letters **10**, 1537 (2010). (cited on p. 125)

[204] A. Kinkhabwala, Z. Yu, S. Fan, Y. Avlasevich, K. Müllen, and W. Moerner. Large single-molecule fluorescence enhancements produced by a bowtie nanoantenna. Nature

Photonics **3**, 654 (2009). (cited on pages 125 and 127)

[205] A. F. Koenderink. Single-photon nanoantennas. ACS Photonics **4**, 710 (2017). (cited on p. 125)

[206] J. J. Mock, R. T. Hill, A. Degiron, S. Zauscher, A. Chilkoti, and D. R. Smith. Distance-dependent plasmon resonant coupling between a gold nanoparticle and gold film. Nano Letters **8**, 2245 (2008). (cited on p. 125)

[207] P. W. Rothemund. Folding DNA to create nanoscale shapes and patterns. Nature **440**, 297 (2006). (cited on pages 125 and 126)

[208] S. M. Douglas, H. Dietz, T. Liedl, B. Högberg, F. Graf, and W. M. Shih. Self-assembly of DNA into nanoscale three-dimensional shapes. Nature **459**, 414 (2009). (cited on p. 125)

[209] S. Nummelin, J. Kommeri, M. A. Kostiainen, and V. Linko. Evolution of structural DNA nanotechnology. Advanced Materials **30**, 1703721 (2018). (cited on p. 125)

[210] C. A. Mirkin, R. L. Letsinger, R. C. Mucic, and J. J. Storhoff. A DNA-based method for rationally assembling nanoparticles into macroscopic materials. Nature **382**, 607 (1996). (cited on p. 126)

[211] A. Kuzyk, R. Schreiber, H. Zhang, A. O. Govorov, T. Liedl, and N. Liu. Reconfigurable 3D plasmonic metamolecules. Nature Materials **13**, 862 (2014). (cited on p. 126)

[212] A. Kuzyk, Y. Yang, X. Duan, S. Stoll, A. O. Govorov, H. Sugiyama, M. Endo, and N. Liu. A light-driven three-dimensional plasmonic nanosystem that translates molecular motion into reversible chiroptical function. Nature Communications **7**, 1 (2016). (cited on p. 126)

[213] I. H. Stein, C. Steinhauer, and P. Tinnefeld. Single-molecule four-color FRET visualizes energy-transfer paths on DNA origami. Journal of the American Chemical Society **133**, 4193 (2011). (cited on p. 127)

[214] F. M. Möller, P. Holzmeister, T. Sen, G. P. Acuna, and P. Tinnefeld. Angular modulation of single-molecule fluorescence by gold nanoparticles on DNA origami templates. Nanophotonics **2**, 167 (2013). (cited on p. 127)

[215] P. Kühler, E.-M. Roller, R. Schreiber, T. Liedl, T. Lohmüller, and J. Feldmann. Plasmonic DNA–origami nanoantennas for surface-enhanced raman spectroscopy. Nano Letters **14**, 2914 (2014). (cited on p. 127)

[216] W. P. Klein, C. N. Schmidt, B. Rapp, S. Takabayashi, W. B. Knowlton, J. Lee, B. Yurke, W. L. Hughes, E. Graugnard, and W. Kuang. Multiscaffold DNA origami nanoparticle waveguides. Nano Letters **13**, 3850 (2013). (cited on p. 127)

[217] E. A. Hemmig, C. Creatore, B. Wünsch, L. Hecker, P. Mair, M. A. Parker, S. Emmott, P. Tinnefeld, U. F. Keyser, and A. W. Chin. Programming light-harvesting efficiency using DNA origami. Nano Letters **16**, 2369 (2016). (cited on p. 127)

[218] V. Giannini, A. I. Fernández-Domínguez, Y. Sonnefraud, T. Roschuk, R. Fernández-García, and S. A. Maier. Controlling light localization and light–matter interactions with nanoplasmonics. Small **6**, 2498 (2010). (cited on p. 127)

[219] M. Raab, C. Vietz, F. D. Stefani, G. P. Acuna, and P. Tinnefeld. Shifting molecular localization by plasmonic coupling in a single-molecule mirage. Nature Communications **8**, 1 (2017). (cited on p. 127)

[220] A. G. Curto, G. Volpe, T. H. Taminiau, M. P. Kreuzer, R. Quidant, and N. F. van Hulst. Unidirectional emission of a quantum dot coupled to a nanoantenna. Science **329**, 930 (2010). (cited on p. 127)

[221] H. Cang, Y. Liu, Y. Wang, X. Yin, and X. Zhang. Giant suppression of photobleaching for single molecule detection via the purcell effect. Nano Letters **13**, 5949 (2013). (cited on p. 128)

[222] K. Vasilev, F. D. Stefani, V. Jacobsen, W. Knoll, and M. Kreiter. Reduced photobleaching of chromophores close to a metal surface. The Journal of Chemical Physics **120**, 6701 (2004). (cited on p. 128)

[223] J. V. Pellegrotti, G. P. Acuna, A. Puchkova, P. Holzmeister, A. Gietl, B. Lalkens, F. D. Stefani, and P. Tinnefeld. Controlled reduction of photobleaching in DNA origami–gold nanoparticle hybrids. Nano Letters **14**, 2831 (2014). (cited on pages 128 and 129)

[224] I. Rasnik, S. A. McKinney, and T. Ha. Nonblinking and long-lasting single-molecule fluorescence imaging. Nature Methods **3**, 891 (2006). (cited on p. 128)

[225] Y. Avlasevich, C. Li, and K. Müllen. Synthesis and applications of core-enlarged perylene dyes. Journal of Materials Chemistry **20**, 3814 (2010). (cited on p. 128)

[226] P. Bharadwaj and L. Novotny. Robustness of quantum dot power-law blinking. Nano Letters **11**, 2137 (2011). (cited on p. 128)

[227] J. Enderlein. Single-molecule fluorescence near a metal layer. Chemical Physics **247**, 1

(1999). (cited on p. 128)

[228] I. H. Malitson. Interspecimen comparison of the refractive index of fused silica. JOSA **55**, 1205 (1965). (cited on p. 131)

[229] V. V. Thacker, L. O. Herrmann, D. O. Sigle, T. Zhang, T. Liedl, J. J. Baumberg, and U. F. Keyser. DNA origami based assembly of gold nanoparticle dimers for surface-enhanced raman scattering. Nature Communications **5**, 1 (2014). (cited on p. 131)

[230] E. D. Palik. *Handbook of optical constants of solids*, volume 3 (Academic press, 1998). (cited on p. 131)

[231] C. Tserkezis, N. A. Mortensen, and M. Wubs. How nonlocal damping reduces plasmon-enhanced fluorescence in ultranarrow gaps. Physical Review B **96**, 085413 (2017). (cited on p. 131)

[232] D. Punj, R. Regmi, A. Devilez, R. Plauchu, S. B. Moparthi, B. Stout, N. Bonod, H. Rigneault, and J. Wenger. Self-assembled nanoparticle dimer antennas for plasmonic-enhanced single-molecule fluorescence detection at micromolar concentrations. ACS Photonics **2**, 1099 (2015). (cited on p. 131)

[233] F. Todisco, S. D'Agostino, M. Esposito, A. I. Fernández-Domínguez, M. De Giorgi, D. Ballarini, L. Dominici, I. Tarantini, M. Cuscuná, F. Della Sala, *et al.* Exciton–plasmon coupling enhancement via metal oxidation. ACS Nano **9**, 9691 (2015). (cited on p. 133)

[234] R. Roy, S. Hohng, and T. Ha. A practical guide to single-molecule FRET. Nature Methods **5**, 507 (2008). (cited on p. 135)

[235] B. E. Hardin, E. T. Hoke, P. B. Armstrong, J.-H. Yum, P. Comte, T. Torres, J. M. Fréchet, M. K. Nazeeruddin, M. Grätzel, and M. D. McGehee. Increased light harvesting in dye-sensitized solar cells with energy relay dyes. Nature Photonics **3**, 406 (2009). (cited on p. 135)

[236] K. Werner, D. N. Wang, *et al.* Three-dimensional structure of plant light-harvesting complex determined by electron crystallography. Nature **350**, 130 (1991). (cited on p. 135)

[237] C. Blum, N. Zijlstra, A. Lagendijk, M. Wubs, A. P. Mosk, V. Subramaniam, and W. L. Vos. Nanophotonic control of the Förster resonance energy transfer efficiency. Physical

Review Letters **109**, 203601 (2012). (cited on p. 135)

[238] S. Bidault, A. Devilez, P. Ghenuche, B. Stout, N. Bonod, and J. Wenger. Competition between Förster resonance energy transfer and donor photodynamics in plasmonic dimer nanoantennas. ACS Photonics **3**, 895 (2016). (cited on p. 135)

[239] J. De Torres, M. Mivelle, S. B. Moparthi, H. Rigneault, N. F. Van Hulst, M. F. García-Parajó, E. Margeat, and J. Wenger. Plasmonic nanoantennas enable forbidden Förster dipole–dipole energy transfer and enhance the FRET efficiency. Nano Letters **16**, 6222 (2016). (cited on p. 135)

[240] N. Aissaoui, K. Moth-Poulsen, M. Käll, P. Johansson, L. M. Wilhelmsson, and B. Albinsson. FRET enhancement close to gold nanoparticles positioned in DNA origami constructs. Nanoscale **9**, 673 (2017). (cited on p. 135)

[241] A. A. Deniz, M. Dahan, J. R. Grunwell, T. Ha, A. E. Faulhaber, D. S. Chemla, S. Weiss, and P. G. Schultz. Single-pair fluorescence resonance energy transfer on freely diffusing molecules: observation of Förster distance dependence and subpopulations. Proceedings of the National Academy of Sciences **96**, 3670 (1999). (cited on p. 135)

[242] P. Ghenuche, J. de Torres, S. Moparthi, V. Grigoriev, and J. Wenger. Nanophotonic enhancement of Förster resonance energy–transfer rate with single nanoapertures. Nano Letters **14**, 4707 (2014). (cited on p. 135)

[243] P. Ghenuche, M. Mivelle, J. de Torres, S. B. Moparthi, H. Rigneault, N. F. Van Hulst, M. F. García-Parajó, and J. Wenger. Matching nanoantenna field confinement to FRET distances enhances Förster energy transfer rates. Nano Letters **15**, 6193 (2015). (cited on p. 135)

[244] G. P. Acuna, M. Bucher, I. H. Stein, C. Steinhauer, A. Kuzyk, P. Holzmeister, R. Schreiber, A. Moroz, F. D. Stefani, T. Liedl, *et al.* Distance dependence of single-fluorophore quenching by gold nanoparticles studied on DNA origami. ACS Nano **6**, 3189 (2012). (cited on p. 137)

[245] P. Anger, P. Bharadwaj, and L. Novotny. Enhancement and quenching of single-molecule fluorescence. Physical Review Letters **96**, 113002 (2006). (cited on p. 137)

[246] A. D. Rakić, A. B. Djurišić, J. M. Elazar, and M. L. Majewski. Optical properties of metallic films for vertical-cavity optoelectronic devices. Applied Optics **37**, 5271 (1998). (cited on p. 138)

[247] J. Enderlein. Modification of Förster resonance energy transfer efficiency at interfaces. International journal of molecular sciences **13**, 15227 (2012). (cited on p. 139)

[248] H. T. Dung, L. Knöll, and D.-G. Welsch. Intermolecular energy transfer in the presence of dispersing and absorbing media. Physical Review A **65**, 043813 (2002). (cited on p. 141)

[249] J. Ren, S. Franke, and S. Hughes. Quasinormal modes and purcell factors of coupled loss and gain resonators near an exceptional point. arXiv preprint arXiv:2101.07633 (2021). (cited on p. 147)

[250] S. Sanders and A. Manjavacas. Nanoantennas with balanced gain and loss. Nanophotonics **9**, 473 (2020). (cited on p. 147)

[251] J. D. Jackson. *Classical electrodynamics* (Wiley, 1999). (cited on p. 162)

[252] A. Bohm, N. Harshman, and H. Walther. Relating the lorentzian and exponential: Fermi's approximation, the fourier transform, and causality. Physical Review A **66**, 012107 (2002). (cited on p. 167)

[253] P. B. Johnson and R.-W. Christy. Optical constants of the noble metals. Physical Review B **6**, 4370 (1972). (cited on p. 173)

[254] F. G. De Abajo, R. Gómez-Medina, and J. Sáenz. Full transmission through perfect-conductor subwavelength hole arrays. Physical Review E **72**, 016608 (2005). (cited on p. 179)

List of publications

Publications related to the content of this thesis:

1. *Distortion of the local density of states in a plasmonic cavity by a quantum emitter.*
   A. Cuartero-González, A. Manjavacas and A. I. Fernández-Domínguez
   Accepted in New Journal of Physics (2021).

2. *Super- and Subradiant Lattice Resonances in Bipartite Nanoparticle Arrays.*
   A. Cuartero-González, S. Sanders, L. Zundel, A. I. Fernández-Domínguez and A. Manjavacas
   ACS Nano, 14, 9 (2020).

3. *Dipolar and quadrupolar excitons coupled to a nanoparticle-on-mirror-cavity.*
   A. Cuartero-González and A. I. Fernández-Domínguez
   Physical Review B 101, 035403 (2020).

4. *Plasmon-assisted Förster resonance energy transfer at the single-molecule level in the moderate quenching regime.*
   J. Bohlen*, **A. Cuartero-González***, E. Pibiri, D. Ruhlandt, A. I. Fernández-Domínguez, P. Tinnefeld and G. P. Acuna,
   Nanoscale, 11 (2019). **Equally contributing authors.*

5. *Light-Forbidden Transitions in Plasmon-Emitter Interactions beyond the Weak Coupling Regime.*
   A. Cuartero-González and A. I. Fernández-Domínguez,
   ACS Photonics, 5, 8 (2018).

6. *Strong plasmonic enhancement of single molecule photostability in silver dimer optical antennas.*
   I. Kaminska, C. Vietz, **A. Cuartero-González**, P. Tinnefeld, A. I. Fernández-Domínguez and G. P. Acuna,
   Nanophotonics, 7, 3 (2018).

Other publications

1. *Long-Range Dipole-Dipole Coupling Mediated by Lattice Resonances in Nanoparticle Arrays.*
   L. Zundel, **A. Cuartero-González**, S. Sanders, A. I. Fernández-Domínguez and A. Manjavacas,
   In preparation (2021)
2. *Photon Correlations in NPoM Cavities.*
   R. Sáez-Blázquez, **A. Cuartero-González**, J. Feist, F. J. García-Vidal and A. I. Fernández-Domínguez,
   In preparation (2021)